Numerically Efficient Theoretical Frameworks for Collective Spontaneous Emission

Dissertation
zur Erlangung des Doktorgrades
an der Fakultät für Mathematik, Informatik und Naturwissenschaften
Fachbereich Physik
der Universität Hamburg

vorgelegt von
Vladislav Sukharnikov

Hamburg
2025

Gutachter/innen der Dissertation:	Prof. Dr. Nina Rohringer Prof. Dr. Dieter Jaksch
Zusammensetzung der Prüfungskommission:	Prof. Dr. Nina Rohringer Prof. Dr. Dieter Jaksch Prof. Dr. Michael Potthoff Prof. Dr. Ralf Röhlsberger Prof. Dr. Markus Gühr
Vorsitzende/r der Prüfungskommission:	Prof. Dr. Michael Potthoff
Datum der Disputation:	23.05.2025
Vorsitzender des Fach-Promotionsausschusses PHYSIK:	Prof. Dr. Wolfgang J. Parak
Leiter des Fachbereichs PHYSIK:	Prof. Dr. Markus Drescher
Dekan der Fakultät MIN:	Prof. Dr.-Ing. Norbert Ritter

Contents

Abstract iii

Zusammenfassung iv

List of Publications v

Introduction 1
Experimental Demonstrations of Superradiance . . . 2
Theoretical Research of Superradiance . . . 3
Stochastic Methods in Quantum Mechanics . . . 4
Outline of Dissertation . . . 5

I Light-matter interaction 8
1 Classical Picture . . . 8
1.1 Reciprocal Space . . . 9
1.2 Longitudinal Field Energy . . . 10
1.3 Transverse Field Energy . . . 11
2 Quantized Picture . . . 12
2.1 System of Atoms . . . 13
2.2 Superradiance in Two-Level Emitters . . . 15
2.3 Tipping Angle Approach . . . 16
2.4 Phenomenological Stochastic Equations . . . 19
3 Conclusion: Limitations and Outlook . . . 21

II Second Quantization of Open Quantum Systems in Liouville Space 23
1 General Formalism . . . 24
1.1 Second Quantization of Bosons in Hilbert Space . . . 26
1.2 Occupation-Number Basis in Liouville-Hilbert Space . . . 27
1.3 Density Matrix Representation . . . 29
1.4 Examples of States . . . 30
1.5 Operators in Liouville-Hilbert space . . . 31
1.6 Bosonic Superoperators . . . 32
1.7 Representation of Many-Particle Operators . . . 33
1.8 Summary . . . 34
2 Applications . . . 35
2.1 Cooperative Emission of Two-Level Atoms . . . 36
2.2 Incoherently Pumped Two-Level Emitters . . . 41
2.3 Three-Level Systems: V-Type . . . 42
2.4 Three-Level Systems: Λ-Type . . . 48
2.5 Interaction with a Single-Mode Field . . . 51
3 Numerical Implementation . . . 53
3.1 Occupation-Number Basis . . . 53
3.2 Parameters . . . 55
3.3 Initial Density Matrix . . . 55
3.4 Set of Linear Differential Equations . . . 56

3.5 Generating Coefficient Matrix . . . 57
3.6 Solution of Differential Equations . . . 59
4 Supplementary Sections . . . 61
4.1 Fermionic Density Matrices . . . 61
4.2 Observables as Supervectors . . . 62
4.3 Coarse-Grained Description and Bose-Hubbard Model . . . 65
4.4 Partial Trace Operator . . . 66
5 Conclusion . . . 68

III Stochastic Methodology for Superradiance 69
1 General Formalism . . . 70
1.1 Fokker-Planck Equation . . . 71
1.2 Itô Stochastic Differential Equations . . . 72
1.3 Initial Conditions for Stochastic Variables . . . 73
1.4 Stochastic Variables for N Emitters . . . 75
1.5 Stochastic Differential Equations for Light-Matter Interaction . . . 77
1.6 Equations for Two-Level Emitters . . . 78
1.7 Diverging Trajectories and Stochastic Gauges . . . 80
1.8 Summary . . . 82
2 Applications . . . 84
2.1 Cooperative Emission of Two-Level Atoms . . . 85
2.2 Incoherently Pumped Two-Level Emitters . . . 87
2.3 Three-Level Systems: V-Type . . . 91
2.4 Three-Level Systems: Λ-Type . . . 96
2.5 Interaction with a Quantized Field . . . 100
3 Discussion . . . 107
3.1 Computational Effort . . . 108
3.2 Instabilities: small N . . . 108
3.3 Instabilities: weight function . . . 109
3.4 Importance of Gauging and Weight Function . . . 111
3.5 Stochastic Maxwell-Bloch Equations . . . 113
3.6 X-Ray Lasing in Neon . . . 115
3.7 Conclusion . . . 119
4 Numerical Implementation . . . 120
4.1 Stochastic Differential Equations on a Grid . . . 120
4.2 Algorithm for Solving Stochastic Differential Equations . . . 121
4.3 Parameters . . . 122
4.4 Drift Function . . . 123
4.5 Noise Function . . . 125
4.6 Single Trajectory Integration . . . 128
5 Supplementary Sections . . . 128
5.1 Properties of the Λ-Supervectors . . . 128
5.2 Non-Normalized Λ-Supervectors . . . 130
5.3 Elimination of η . . . 131
5.4 Stochastic Drift Gauges . . . 133

IV Conclusion and Outlook 135

Acknowledgment 137

Abstract

Cooperative spontaneous emission is a prominent example of a quantum many-body effect in which a group of initially uncorrelated atoms emits radiation coherently in a short, intense burst of light. This phenomenon can occur when a free-electron laser excites a solid or gaseous target, creating a population inversion within the atomic system. The excited atoms exchange spontaneously emitted photons, synchronizing their dipole moments through this interaction. Consequently, the atoms emit coherently, resulting in a photon avalanche known as superradiance. This process generates spatially and temporally coherent pulses with promising applications, for instance, in spectroscopy, metrology, and the development of high-brightness light sources.

Observing superradiance typically requires a large number of atoms. Therefore, theoretical modeling using conventional quantum-mechanical approaches often becomes impractical. This dissertation presents numerically efficient theoretical frameworks to model collective spontaneous emission in such computationally challenging cases. The study focuses on two primary directions: the adaptation of second quantization to open quantum systems and the formulation of a stochastic approach rooted in the positive P-representation. The developed methods address compact systems within the Dicke limit and extend to macroscopic pencil-shaped media.

The first part introduces second quantization in Liouville space, formulated for density matrices, facilitating efficient modeling of permutation-invariant systems with incoherent processes. The second part extends this approach by employing a phase-space description of quantum dynamics using stochastic differential equations for efficient, parallelizable sampling. By advancing the positive P framework, this methodology provides insights into systems where semiclassical methods are inadequate or traditional quantum-mechanical techniques are computationally infeasible.

For numerical illustrations, we examine compact systems of two- and three-level emitters under the influence of incoherent pumping and decoherence. Additionally, we investigate the impact of statistical mixing on their emission, revealing a class of many-body steady states. Our second-quantization approach serves as a benchmark for the stochastic methodology, determining its effectiveness and delineating its boundary of applicability.

This work also addresses limitations, including numerical instabilities, and proposes avenues for future research. Applications such as x-ray lasing, demonstrated through amplified spontaneous emission in neon, and cavity-mediated collective emission emphasize the importance of these frameworks in advancing the understanding of cooperative light-matter interactions.

Zusammenfassung

Kooperative spontane Emission ist ein herausragendes Beispiel für einen quantenmechanischen Vielteilcheneffekt, bei dem eine Gruppe zunächst unkorrelierter Atome kohärent einen kurzen, intensiven Lichtblitz emittieren. Dieses Phänomen tritt auf, wenn ein Freie-Elektronen-Laser ein festes oder gasförmiges Target anregt und dadurch eine Populationsinversion im atomaren System erzeugt. Die angeregten Atome tauschen spontan emittierte Photonen aus und synchronisieren über diese Wechselwirkung ihre Dipolmomente. Infolgedessen senden die Atome kohärente Strahlung aus, was zu einer Photonenlawine führt, die als Superradianz bekannt ist. Dieser Prozess erzeugt räumlich und zeitlich kohärente Pulse mit vielversprechenden Anwendungen, beispielsweise in der Spektroskopie, Metrologie und der Entwicklung hochbrillanter Lichtquellen.

Die Beobachtung von Superradianz erfordert in der Regel eine große Anzahl von Atomen. Daher wird die theoretische Modellierung mit konventionellen quantenmechanischen Methoden oft unpraktikabel. Diese Dissertation stellt numerisch effiziente theoretische Methoden zur Modellierung der kollektiven spontanen Emission in solchen rechnerisch herausfordernden Fällen vor. Die Untersuchung konzentriert sich auf zwei Hauptansätze: Die Anpassung der Zweiten Quantisierung an offene Quantensysteme sowie die Entwicklung eines stochastischen Ansatzes basierend auf der positiven P-Repräsentation. Die entwickelten Methoden erfassen sowohl kompakte Systeme im Dicke-Grenzfall als auch makroskopische, zylinderförmige Medien.

Der erste Teil führt die Zweite Quantisierung im Liouville-Raum ein, formuliert für Dichtematrizen, was eine effiziente Modellierung permutationsinvarianter Systeme mit inkohärenten Prozessen ermöglicht. Der zweite Teil erweitert diesen Ansatz durch eine Phasenraumbeschreibung der Quantendynamik unter Verwendung stochastischer Differentialgleichungen, die ein effizientes und parallelisierbares Sampling erlauben. Durch die Weiterentwicklung der positiven P-Repräsentation liefert diese Methodik neue Erkenntnisse über Systeme, in denen semi-klassische Methoden unzureichend sind oder traditionelle quantenmechanische Verfahren rechnerisch nicht durchführbar sind.

Zur numerischen Veranschaulichung analysieren wir kompakte Systeme von Zwei- und Drei-Niveau-Emittern unter dem Einfluss inkohärenter Pumpmechanismen und Dekohärenz. Zudem untersuchen wir den Einfluss statistischer Mischung auf ihre Emission, wobei eine Klasse von Vielteilchen-Gleichgewichtszuständen identifiziert wird. Unser Ansatz der Zweiten Quantisierung dient als Referenz für die stochastische Methodik, bestimmt deren Effektivität und grenzt ihren Anwendungsbereich ab.

Diese Arbeit diskutiert zudem Einschränkungen wie numerische Instabilitäten und schlägt mögliche Forschungsrichtungen für zukünftige Entwicklungen vor. Anwendungen wie Röntgen-Lasing, demonstriert durch verstärkte spontane Emission in Neon, sowie resonatorvermittelte kollektive Emission unterstreichen die Bedeutung dieser theoretischen Methoden für das tiefere Verständnis kooperativer Licht-Materie-Wechselwirkungen.

List of Publications

The results and most of the figures presented in this dissertation have been published in the following two publications:

1. **V. Sukharnikov**, S. Chuchurka, A. Benediktovitch, and N. Rohringer. "*Second Quantization of Open Quantum Systems in Liouville Space*." Physical Review A **107**, 053707 (2023). DOI: 10.1103/PhysRevA.107.053707.

2. S. Chuchurka,[1] **V. Sukharnikov**,[1] A. Benediktovitch, and N. Rohringer. "*Stochastic Modeling of Superfluorescence in Compact Systems*." Physical Review A **110**, 053703 (2024). DOI: 10.1103/PhysRevA.110.053703.

This dissertation goes beyond these publications by providing a more in-depth discussion, additional application cases, and exploring potential extensions.

Two other publications are cited in the main text but are not discussed in detail and do not form a substantial part of this dissertation:

3. A. C. LaForge,[2] A. Benediktovitch,[2] **V. Sukharnikov**,[2] et al. "*Time-Resolved Quantum Beats in the Fluorescence of Helium Resonantly Excited by XUV Radiation*." Journal of Physics B: Atomic, Molecular and Optical Physics **53**, 244012 (2020). DOI: 10.1088/1361-6455/abc660.

4. S. Chuchurka, **V. Sukharnikov**, and N. Rohringer. "*Hermitian Stochastic Methodology for X-Ray Superfluorescence*." Physical Review A **109**, 063705 (2024). DOI: 10.1103/PhysRevA.109.063705.

Here are the author's contributions to all of the publications mentioned above:

1. V. S. developed the published formalism, handled the mathematical formalization, contextualized it within the literature, developed the codes, analyzed the application cases, and wrote the manuscript. V. S. and S. C. worked together on the conceptual development of the theoretical framework. S. C., A. B., and N. R. assisted with manuscript writing and offered conceptual support.

2. V. S. and S. C. jointly worked on the numerical implementation and theory development. V. S. finalized and optimized the code, which is presented in this dissertation. S. C. developed the theoretical framework presented in the manuscript (in this dissertation, the final equations are derived using a different method, published in the previous article). V. S. authored the section on Numerical Analysis and assisted in writing other parts. A. B. and N. R. provided support with manuscript writing and conceptual guidance.

3. V. S. was a part of a large experimental team and contributed by gathering and analyzing data on-site. Under the supervision of A. B., V. S. later conducted data analysis and theoretical modeling, and co-wrote the manuscript with A. C. L. and A. B.

4. V. S. contributed by visualizing numerical results, assisting with manuscript writing, and supporting the publication process.

[1] These authors contributed equally to the work.
[2] These authors contributed equally to the work.

Introduction

Cooperative spontaneous emission is a phenomenon in which the emission properties of a group of atoms or molecules differ significantly from those of isolated particles. In typical fluorescence experiments, a dilute gas of excited particles emits photons isotropically, with intensity decaying exponentially over time. However, as the density of emitters increases, emission occurs much more rapidly, often in a single, intense burst. In some cases, the geometry of the radiating medium dictates the directional properties of the emission.

The theoretical work of R. Dicke in 1954 [1] investigated collective interactions between identical two-level particles confined within a volume much smaller than the resonant wavelength. Using the formula for electric dipole radiation, which states that radiation intensity is proportional to the mean square of the dipole moment, Dicke analyzed how collective states of particles influence the emission rate. Dicke found that the emission rate is maximized in symmetric states, where approximately half of the atoms are excited; these were termed *superradiant*. These states can be reached either through excitation or by transitioning down a ladder of states from the fully excited state. Dicke also examined the directional characteristics of emission in extended systems and later proposed the concept of the coherence-brightened laser [2].

Superradiance, as introduced by Dicke, exhibits many classical aspects, as highlighted in Ref. [3]. Its quantum nature lies in the fact that individual atoms, on average, have no dipole moments, and coherence emerges from quantum fluctuations. Initially uncorrelated emitters generate spontaneous photons independently. These photons are subsequently absorbed and re-emitted by other atoms, enhancing decay and leading to the emergence of coherent emission. Some authors have referred to this process as a *photon avalanche* [4] or as *superfluorescence* [5–7].

Furthermore, Refs. [6, 7] distinguish between *superfluorescence* and *superradiance*. According to these works, *superradiance* is an emission process in which emitters start from a strongly correlated state with a dipole moment created by coherent excitation. In contrast, *superfluorescence* involves initially uncorrelated emitters producing incoherent spontaneous emission, which eventually phase-lock due to interactions. Additionally, some authors differentiate between cooperative emission from compact and extended systems [8], both of which are often referred to as superradiance. In this dissertation, we adopt the terminology used by M. Gross and S. Haroche in their 1982 essay [9], where *superradiance* and *superfluorescence* are used synonymously.

Cooperative emission phenomena are challenging to analyze in detail since numerous factors shape the process. The dynamics is initiated by creating an active medium with a significant population inversion. Most experiments realize pencil-shaped geometries, whose dimensions influence field propagation and can be characterized by the Fresnel number, $F \sim \theta_G/\theta_D$ [9]. The angle θ_D is the characteristic diffraction angle, given by $\theta_D = \lambda_0/\sqrt{S^\perp}$, where $S^\perp$ is the cross-sectional area of the sample, L is its length, and λ_0 is the emission wavelength. The angle θ_G is the characteristic geometrical angle, given by $\theta_G = \sqrt{S^\perp}/L$. When $F \gg 1$, transverse field dynamics involves multiple diffraction modes within the geometrical angle. In the opposite case, when $F \ll 1$, the geometrical angle is small compared to the diffraction angle, causing diverging emission that escapes the active medium due to diffraction.

We can estimate a characteristic superradiant emission time for a sample with $F \sim 1$. In this case, only atoms emitting within the solid angle of $\Delta o \sim \lambda_0^2/S^\perp$ participate in the cooperative emission, enhancing the spontaneous decay rate of an isolated atom γ to approximately $\gamma \times (n\lambda_0^2 L)$, where n is the concentration of atoms. A realistic analysis should also consider various dissipation channels that incoherently de-excite atoms and compete with the emission process.

Notably, Dicke superradiance—cooperative emission from compact systems—should not be confused with the Dicke model [10, 11], which describes the interaction of atoms with a few quantized field modes in an ideal cavity. The Dicke model is a variant of the Tavis-Cummings model [12], with some authors distinguishing it by the presence of counter-rotating terms, typically neglected under the rotating-wave approximation [13]. Since light remains trapped in the cavity, photons are always present, making the system's equilibrium properties and phase transitions a subject of extensive study [10, 11, 13–15].

This dissertation develops numerically tractable methods to model superradiance in scenarios where standard quantum-mechanical techniques become impractical. We will focus on compact systems and propose extensions to macroscopic pencil-shaped media.

The significance of this research is highlighted by the sustained interest in cooperative emission phenomena from both experimental and theoretical perspectives, tracing its origins to the pioneering work of R. Dicke in 1954 [1]. Interest in this area gained further momentum in the 1970s, following the first experimental demonstration by N. Skribanowitz, I. P. Herman, J. C. MacGillivray, and M. S. Feld in 1973 [16]. More recently, renewed attention has been driven by the development of novel light sources, such as x-ray free-electron lasers, and advances in experimental techniques that enable the precise arrangement of ordered atomic arrays that interact collectively. The following sections provide a brief overview of key advancements.

Experimental Demonstrations of Superradiance

Early experiments successfully realized pencil-shaped active media, leading to the observation of superradiance in the axial modes of the sample. In Ref. [16], superradiance was demonstrated in the rotational transitions of hydrogen fluoride (HF) gas in the far-infrared range, with wavelengths between 50 and 250 μm. The observed superradiant emission lasted for hundreds of nanoseconds and was characterized by a delay before the first emission peak, followed by multiple oscillations or ringings. The authors supported their experimental findings with an analysis based on the semiclassical Maxwell-Bloch equations [17].

Superradiance was also demonstrated in atomic sodium gas in the near-infrared range [18]. After sodium atoms were excited to the $5S_{1/2}$ state, a cascade of transitions was observed at wavelengths of 3.41 μm, 2.21 μm, and 9.10 μm. The superradiant emission exhibited characteristics such as delay time and ringing, lasting for tens of nanoseconds.

Additionally, superradiance was observed in the visible lines of europium atoms at a wavelength of 605.7 nm [19]. In the millimeter-wave range, superradiance was reported, for example, in Ref. [20], where a sample of Na atoms in a cavity was excited to the $29S_{1/2}$ level. Subsequently, superradiance at a wavelength of 1.86 mm was observed (corresponding to the transition $29S_{1/2} \to 28P_{1/2}$). The measured evolution of atomic populations agreed with the predictions of the fundamental Dicke model.

Beyond gaseous media, superradiance also occurs in solids [21]. (Quasi)particles confined within a specific region of a solid exhibit atomic-like behavior, allowing the application of Dicke's concepts. For example, superradiance was observed in molecular centers of O_2^- in KCl [22–24]. The possibility of cooperative emission in molecular aggregates has been explored both theoretically [25] and experimentally [26, 27]. The main obstacle is the presence of inhomogeneous broadening, which quenches superradiance.

More recent experimental advancements include the study of cooperative emission in perovskite nanocrystals [28], nitrogen-vacancy centers in nanodiamonds [29], and quantum dots [30–32]. Furthermore, superradiance has been investigated in distributed systems within nanophotonic waveguides, which mediate long-range interatomic interactions [33]. Superradiance from Rydberg atoms in free space was reported in Ref. [34].

The development of free-electron lasers has enabled new experimental approaches. Notably, superradiance has been observed in helium pumped by XUV pulses from a free-electron laser, resulting in emissions in the visible [35] and far-ultraviolet [36] domains. Evidence of superfluorescence in the extreme ultraviolet region of xenon was reported in Ref. [37].

Furthermore, x-ray free-electron lasers can create population inversion through rapid photoionization of inner shells, leading to cooperative $K\alpha$ emission. This mechanism has been demonstrated, for example, in neon [38], solid copper [39], and solutions of Mn(II) and Mn(VII) complexes [40]. Initiated by an incoherent x-ray SASE pulse, the superradiant mechanism generates coherent x-ray pulses with a narrower bandwidth, centered at a frequency determined by the target material. Free-electron laser and synchrotron pulses also provide opportunities to explore cooperative emission in nuclei, as discussed in Refs. [41, 42].

In summary, the superradiant mechanism has been demonstrated across various systems and spectral domains, generating coherent, intense pulses. These pulses may be particularly valuable for spectroscopic purposes in the x-ray domain [43, 44], as they offer greater stability and coherence compared to x-ray SASE light sources. A notable example of a system potentially capable of producing coherent x-ray pulses is the x-ray laser oscillator [45].

The superradiant mechanism has also been employed to realize a steady-state superradiant laser [46] and plays a crucial role in developing a continuous-wave superradiant laser [47], both of which are promising tools for metrology and atomic clocks due to their high coherence. Additionally, cavity-mediated collective emission offers possibilities for generating multiphoton quantum states, as discussed in Ref. [48].

Theoretical Research of Superradiance

Theoretical research in this field has made significant progress, analyzing the conditions necessary for observing superradiance, exploring its evidence in various media, and developing both phenomenological and first-principles models.

For example, in 1971, R. Bonifacio, P. Schwendimann, and F. Haake presented a theory of cooperative emission for a pencil-shaped active medium in a low-Q cavity [49, 50]. They showed that cooperative emission could be realistically modeled as a "single-mode" laser when the sample length is smaller than the maximum distance over which atoms can coherently interact. The transition to other modes was treated phenomenologically as a dissipation channel. Assuming instantaneous excitation of the entire sample, they demonstrated that all atoms cooperate when the sample length is smaller than the so-called cooperation length. This condition ensures that the pulse envelope varies slowly across the sample, thereby allowing propagation effects to be neglected. This work links superradiance with laser theory, demonstrating that it can be practically used to produce laser-like radiation.

F. T. Arrecchi and E. Courtens investigated an extended pencil-shaped active medium in which propagation effects cannot be neglected [51]. They assumed the entire medium was instantaneously excited. The medium was modeled by equations analogous to the Bloch equations [52]. The propagation of emission leads to the concept of limited cooperation, as only a finite number of atoms can cooperate. The concept of limited cooperation is crucial for understanding superradiance, as it reflects limitations encountered in practical realizations of the amplification mechanism. When the sample is not excited instantaneously and the pump is transient, its duration, attenuation, and propagation restrict the number of atoms that can effectively cooperate. Cooperation can be further influenced by the sample's geometry and decoherence channels.

Models for cooperative spontaneous emission have also been constructed from first principles. Notably, in 1970, R. H. Lehmberg developed a fully quantum-mechanical treatment [53, 54]. Applied to compact systems, a crucial restriction of this model is that the sample length must be smaller than the emission pulse length, ensuring that all atoms experience the same field and interact cooperatively. This theory also describes the frequency shifts resulting from interatomic interactions. The influence of these frequency shifts and the sample's geometry on superradiance has been discussed in Refs. [55, 56].

In 1974, G. Banfi and R. Bonifacio introduced a first-principles theory [5], deriving the master equation in the Born-Markov approximation under the assumption that the sample length is much smaller than the cooperation length. Applied to a pencil-shaped medium, this theory confirmed the qualitative conclusions of the phenomenological approach from Refs. [49, 50].

G. S. Agarwal adopted a different approach in Ref. [57] by reformulating the dynamics using the Fokker-Planck equation. This formulation was then used to derive a hierarchy of equations for the expectation values, which required appropriate truncation. Importantly, this work explores the problem of cooperative emission through a phase-space description.

Recent studies investigate directional superradiance in ultracold gases of dipole-dipole interacting atoms [58] and in ordered structures [59]. Another prominent area is single-photon superradiance, in which a single excitation is coherently shared by the entire ensemble [60–62]. These systems provide a platform for studying the collective Lamb shift, which is highly sensitive to atomic spatial arrangement [41, 56, 63]. Another intriguing direction is the study of superradiant mechanisms in free electrons, particularly the role of entanglement in shaping emission properties [64].

In summary, while a comprehensive review of superradiance is beyond the scope of this dissertation, existing theoretical work has greatly advanced the field, inspiring both experimental and conceptual progress. We will now focus on theoretical models of superradiance that allow for feasible numerical solutions.

When a system has an initial dipole moment or is driven, its dynamics can be described using semiclassical methods. In this case, the dynamics is governed by a coupled set of Maxwell-Bloch equations [9,65]. In this framework, atoms are modeled as dipoles that de-excite according to the pendulum equation [6, 7]. However, when superradiance is triggered by spontaneous emission, it becomes essential to accurately model the initial stage of the process, where the production of spontaneous photons is critical. This generally requires quantum-mechanical approaches, which can become increasingly complex depending on the number of emitters. Although complexity can be reduced if the system exhibits permutation symmetry, incoherent processes may render standard techniques such as second quantization inapplicable.

Therefore, there is a need for theoretical methods applicable to open systems of identical emitters that are subject to incoherent processes such as incoherent pumping or incoherent decay.

For instantaneously excited two-level emitters, fluctuations that trigger the collective effect can be effectively modeled by assuming random initial conditions for their dipole moments [9,66]. While effective in certain cases, this approach may become unreliable when excitation is achieved through pumping or when incoherent dissipation channels are present.

An alternative method for modeling these fluctuations involves the use of stochastic processes. This idea can be traced back to the 1970s when the role of quantum fluctuations in triggering emission was already recognized [66–68]. For instance, in 1979, D. Polder, M. F. H. Schuurmans, and Q. H. F. Vrehen [67] introduced a Langevin force to model these fluctuations. Stochastic sources have also been used to model the effects of spontaneous emission in laser theory [69].

More recent stochastic approaches build on these early concepts, providing phenomenological and numerically efficient frameworks, as detailed in Refs. [70–75]. These studies extend the semiclassical Maxwell-Bloch equations by adding noise terms designed to approximate spontaneous emission. However, these approaches are not derived from first principles and may introduce inaccuracies. For example, the commonly used method proposed in Ref. [70] can yield an incorrect temporal profile of spontaneous emission, as noted in Ref. [76].

These inaccuracies highlight the need for developing stochastic methods based on first principles, which offer a numerically tractable and reliable solution for many-level atoms subject to incoherent processes.

Stochastic Methods in Quantum Mechanics

The representation of quantum dynamics using stochastic equations has been widely studied. A notable example is quantum-state diffusion. In the Markovian approximation, the system's dynamics is typically described by a master equation for the density matrix. This density matrix can be sampled by averaging over a statistical ensemble of state vectors, which are solutions to the stochastic Schrödinger equation [77–81].

In non-Markovian regimes, environmental degrees of freedom cannot be averaged out and replaced with effective dissipation rates. Instead, the influence of the environment is typically treated stochastically, while the system is described quantum-mechanically [82]. One example is the coherent-state unraveling approach, in which the bath's degrees of freedom are expanded in the multimode coherent-state basis. By treating coherent-state amplitudes as random variables, it is possible to derive a non-Markovian stochastic Schrödinger equation [82–86].

In these approaches, the system's state vector is driven by stochastic processes representing the environment. When the system has a large number of degrees of freedom, this approach may become impractical. Another stochastic approach to quantum mechanics develops the concept of quantum noise and quantum Langevin equations [87, 88]. While this method is exact and, in many cases, provides analytical solutions [89], it is numerically challenging to implement for macroscopically large quantum systems.

Consequently, we opt for methods that describe all degrees of freedom using stochastic variables determined by conventional stochastic processes, making the problem's complexity comparable to that of semiclassical approaches.

Such methods are closely related to the phase-space description of quantum mechanics, where density matrices are mapped to phase-space distribution functions. This approach replaces operators with functions, allowing quantum dynamics to be described within a quasi-classical framework and enabling numerically tractable simulations [90–92]. Two notable examples of phase-space representations are the Wigner function [93] and the Husimi Q-representation [94].

In quantum optics, the Glauber-Sudarshan P-representation has received significant attention [95,96]. In this representation, the expectation values of operators are obtained by integrating their matrix elements in the coherent-state basis with the P-function. However, since the P-function can be negative, it cannot be interpreted as a true probability density function [97].

The problem of negativity of the P function was solved in Ref. [97] by introducing a class of positive P functions, known as the positive P representation. This representation found numerous applications across quantum optics and related fields [97–102]. In many applications, positive P functions satisfy a Fokker-Planck equation, allowing the statistical properties of the phase-space variables to be reproduced through Itô stochastic differential equations [103].

While well-established for bosonic systems, extending the positive P representation to systems of emitters with incoherent processes remains an open challenge.

Outline of Dissertation

The primary objective of this dissertation is to develop and test methods for modeling superradiance in scenarios where traditional approaches become impractical. As discussed in previous sections, there are two potential research directions:

1. Formulating a method for open quantum systems of emitters that utilizes permutation symmetry in the presence of incoherent processes.

2. Adapting the positive P framework to describe open quantum systems of emitters. This adaptation enables a formulation based on the Fokker-Planck equation and associated Itô stochastic differential equations, thus providing the potential to describe macroscopically large systems.

Both objectives point to establishing *the method of second quantization of density matrices.* If a system begins in a permutation-invariant state and evolves according to a permutation-invariant Liouvillian, the density matrix retains its symmetry throughout its evolution [104–107]. Furthermore, by formulating second quantization directly for density matrices, we can adapt the standard positive P formalism by properly defining generalized coherent states.

While our numerical illustrations primarily focus on systems of identical emitters, we also explore extensions to non-identical emitters and more realistic, spatially distributed configurations. A key potential application of the developed formalisms is cavity-mediated collective emission and x-ray superradiance.

This dissertation is based on two publications, [108] and [109], and naturally divides into two main parts: Chapter II and Chapter III, each corresponding to a publication. However, its scope extends beyond these works, incorporating additional applications, extensions, and deeper discussions. Both chapters conclude with numerical implementations of the developed frameworks in `Julia`,[1] as well as essential benchmarks and discussions.

The final chapter, Chapter IV, provides a comprehensive outlook on potential applications and reviews unresolved issues that still need to be addressed.

Below is a brief outline of the first three chapters.

Chapter I: Light-Matter Interaction

In the first chapter, we provide basic information on light-matter interaction and superradiance. Readers already familiar with superradiance may choose to skip this chapter.

We begin with Maxwell's equations, identifying the independent dynamical variables before proceeding to their quantization. Next, we introduce a fundamental quantum master equation in the Born-Markov approximation that describes the superradiance of two-level atoms.

As part of our discussion, we review well-established phenomenological approaches. For instance, we examine semiclassical equations with random initial conditions, which are effective for systems with a large number of particles. Additionally, we introduce the simplest phenomenological stochastic equations. Both approaches provide accurate expectation values only when the system is excited instantaneously and consists of a large number of atoms.

However, these phenomenological approaches fail to accurately model systems with an arbitrary number of multilevel atoms undergoing incoherent processes. This limitation underscores the need for the advanced methods developed in the subsequent chapters.

Chapter II: Second Quantization of Open Quantum Systems in Liouville Space

The foundational framework of this dissertation is presented in Chapter II, where we develop a formalism for density matrices using the principles of second quantization. Specifically, we extend the framework of second quantization directly to density matrices, treating them as supervectors in the extended Liouville-Hilbert space [110, 111].

Our approach is closely related to the methods presented in Refs. [105–107, 112], as it introduces an occupation-number representation for density matrices [105–107] and employs bosonic superoperators to construct generalized Fock states [112]. The results of this work were published in Ref. [108]. The key advantage of our framework is its ability to accommodate incoherent processes while extending the widely used second quantization formalism to density matrices.

To summarize the findings of Chapter II, we draw an analogy with standard second quantization. State vectors are (anti)symmetrized combinations of many-particle tensor product states:

$$|\psi\rangle \sim \sum_{\text{(anti)sym.}} |i_1\rangle_1 \otimes \ldots \otimes |i_N\rangle_N,$$

where $|i\rangle_\mu$ denotes the μ-th particle in state i. These permutation-invariant states are characterized by the occupation numbers n_i, which indicate the number of particles occupying each single-particle state $|i\rangle$. These occupation-number states can be manipulated using either fermionic or bosonic annihilation and creation operators, $\hat{b}_i$ and $\hat{b}_i^\dagger$.

Density matrices for identical emitters are permutation-invariant; more specifically, they are symmetric. They are constructed from bra and ket states, $\hat{\rho} = |\psi\rangle\langle\psi|$, or their statistical mixtures. Both components can be expanded in terms of many-particle tensor product states:

$$\hat{\rho} \sim \sum_{\text{sym.}} |i_1\rangle_1\langle j_1|_1 \otimes \ldots \otimes |i_N\rangle_N\langle j_N|_N.$$

[1] Official documentation is available at https://docs.julialang.org.

Consequently, symmetric density matrices can be parameterized by occupation numbers with two indices, n_{ij}, indicating the number of particles represented by the operator $|i\rangle\langle j|$ in the density matrix expansion.

The corresponding generalized Fock states can be constructed and manipulated using bosonic superoperators, $\hat{b}_{ij}$ and $\hat{b}^\dagger_{ij}$. In Chapter II, we employ this formalism to examine the effects of statistical mixing of emitter states and incoherent processes on their collective emission, identifying a class of subradiant states across various systems.

While the established formalism reduces the number of basis states from exponential to polynomial in the number of particles, this remains a significant limitation. Additionally, we encountered numerical instabilities when solving equations for relatively large particle numbers ($N \gtrsim 150$) using explicit methods. These constraints limit the practical application of this approach to medium-sized systems. Nevertheless, this framework provides a foundation for the phase-space description of the dynamics, which is explored in the subsequent chapter.

Chapter III: Stochastic Methodology for Superradiance

This chapter begins by defining generalized coherent states for density matrices using bosonic superoperators. These states form a basis for the density matrix, with the expansion coefficients defining a phase-space distribution, denoted by P.

We derive the Fokker-Planck equation for the P function and the corresponding Itô stochastic differential equations, assuming a model Liouvillian with at most two-particle interactions. This approach allows us to describe the open system dynamics through stochastic equations. The deterministic terms characterize semiclassical behavior, while noise-induced correlations capture quantum effects such as spontaneous emission.

The number of stochastic variables for emitters is independent of the number of particles and scales as M^2, where M is the number of levels. In contrast, the quantum-mechanical method scales as N^{M^2}. As a result, the complexity of the stochastic approach aligns with that of the semiclassical approach combined with statistical sampling, which can be parallelized. By design, statistical averages accurately reproduce quantum-mechanical expectation values.

Emitters are described by a stochastic density matrix, which is not necessarily Hermitian in individual stochastic realizations. This presents a significant issue, as its anti-Hermiticity can lead to the unbounded growth of the deterministic part of the stochastic equations. Such instabilities are well known within the positive P formalism [103]. To regularize these divergences, we apply the method of stochastic gauges, which exploits so-called stochastic freedom [100,101]. Our regularization strategy and the benchmarking of this method were published in Ref. [109].

We present a detailed, step-by-step derivation and examine various application cases previously discussed in Chapter II. By comparing our results with the exact solution, we assess the effectiveness of the derived stochastic approach and determine its limits of applicability. For compact systems, the stochastic method performs well as long as the influence of subradiant states remains weak. However, when these states have a significant impact, the solution becomes highly unstable, even with the use of stochastic gauges.

We also explore various extensions involving systems that interact with few-mode quantized fields, non-identical particle systems, and distributed systems where propagation effects are significant. As an illustration, we present a one-dimensional analysis of x-ray lasing from the $K\alpha$ transition in neon using experimental parameters from Ref. [38].

Chapter I

Light-matter interaction

This chapter provides a concise overview of electromagnetic field quantization within the framework of non-relativistic quantum optics, beginning with Maxwell's equations in Sec. 1. We identify the independent dynamical variables for a system of non-relativistic charges and the electromagnetic field, which are heuristically quantized in Sec. 2. Readers familiar with these concepts may skip ahead to Sec. 2.2, where we analyze the superradiance of two-level atoms. The analysis includes several semi-phenomenological approaches, such as one based on random initial conditions (Sec. 2.3) and another employing phenomenological stochastic equations (Sec. 2.4).

1 Classical Picture

We begin by outlining Maxwell's equations, which govern the evolution of the electromagnetic field influenced by a system of point charges q_i in a vacuum. This system is characterized by the charge density $\rho(\mathbf{r},t)$ and the current density $\mathbf{j}(\mathbf{r},t)$, which are related through the continuity equation that expresses the principle of local charge conservation:

$$\frac{\partial\rho(\mathbf{r},t)}{\partial t}+\boldsymbol{\nabla}\cdot\mathbf{j}(\mathbf{r},t)=0, \tag{I.1}$$

where $\boldsymbol{\nabla}$ denotes the nabla operator, $\boldsymbol{\nabla}=\mathbf{e}_x\frac{\partial}{\partial x}+\mathbf{e}_y\frac{\partial}{\partial y}+\mathbf{e}_z\frac{\partial}{\partial z}$.

In Maxwell's equations, the charge and current densities serve as sources of the electromagnetic field. In the CGS (centimeter-gram-second) system, these equations are expressed as follows:

$$\boldsymbol{\nabla}\cdot\mathbf{E}(\mathbf{r},t)=4\pi\rho(\mathbf{r},t), \qquad \text{(Gauss's law)} \tag{I.2a}$$

$$\boldsymbol{\nabla}\cdot\mathbf{B}(\mathbf{r},t)=0, \qquad \text{(Gauss's law for magnetism)} \tag{I.2b}$$

$$\boldsymbol{\nabla}\times\mathbf{E}(\mathbf{r},t)+\frac{1}{c}\frac{\partial\mathbf{B}(\mathbf{r},t)}{\partial t}=0, \qquad \text{(Faraday's law)} \tag{I.2c}$$

$$\boldsymbol{\nabla}\times\mathbf{B}(\mathbf{r},t)-\frac{1}{c}\frac{\partial\mathbf{E}(\mathbf{r},t)}{\partial t}=\frac{4\pi}{c}\mathbf{j}(\mathbf{r},t). \qquad \text{(Ampère's law)} \tag{I.2d}$$

These equations govern the dynamics of the electromagnetic field. The charge and current densities depend on the positions and velocities of the charges, $\mathbf{r}_i(t)$ and $\dot{\mathbf{r}}_i(t)$, which influence the field according to Maxwell's equations. We assume that the charges move at velocities much smaller than the speed of light.

To obtain a self-consistent system of equations, Newton's equations for the charges must be solved, incorporating the forces exerted by the electromagnetic field. The force acting on the i-th charge, known as the Lorentz force, is given by:

$$\mathbf{F}(\mathbf{r}_i,\dot{\mathbf{r}}_i,t)=q_i\,\mathbf{E}(\mathbf{r}_i,t)+\frac{q_i}{c}\,\dot{\mathbf{r}}_i\times\mathbf{B}(\mathbf{r}_i,t), \tag{I.3}$$

where q_i is the charge of the i-th particle. Together, Maxwell's equations and the Newton-Lorentz equations form a self-consistent framework that describes the dynamics of the entire

system. Although the charges do not interact directly, they influence each other indirectly through the electromagnetic field.

Maxwell's equations involve two unknown vector fields: the electric field $\mathbf{E}(\mathbf{r},t)$ and the magnetic field $\mathbf{B}(\mathbf{r},t)$. These equations possess a symmetry that reduces the number of independent variables. Specifically, we can introduce the vector potential $\mathbf{A}(\mathbf{r},t)$ and the scalar potential $\varphi(\mathbf{r},t)$, and express the electric and magnetic fields as follows:

$$\mathbf{E}(\mathbf{r},t) = -\boldsymbol{\nabla}\varphi(\mathbf{r},t) - \frac{1}{c}\frac{\partial \mathbf{A}(\mathbf{r},t)}{\partial t}, \tag{I.4a}$$

$$\mathbf{B}(\mathbf{r},t) = \boldsymbol{\nabla} \times \mathbf{A}(\mathbf{r},t). \tag{I.4b}$$

These representations automatically satisfy Gauss's law for magnetism (I.2b) and Faraday's law (I.2c). Moreover, the potentials $\mathbf{A}(\mathbf{r},t)$ and $\varphi(\mathbf{r},t)$ are not uniquely defined. The following transformation, known as a gauge transformation, leaves the electromagnetic field unchanged:

$$\mathbf{A}'(\mathbf{r},t) = \mathbf{A}(\mathbf{r},t) + \boldsymbol{\nabla} f(\mathbf{r},t), \qquad \varphi'(\mathbf{r},t) = \varphi(\mathbf{r},t) - \frac{1}{c}\frac{\partial f(\mathbf{r},t)}{\partial t}. \tag{I.5}$$

Choosing an appropriate gauge can simplify the equations. However, not all components of the electromagnetic potentials represent independent dynamical variables, a fact that becomes more evident in reciprocal space.

1.1 Reciprocal Space

Assuming the fields are confined within a large box of volume V, we express all quantities in Maxwell's equations using their Fourier transforms, under the assumption of periodic boundary conditions:

$$\mathrm{X}(\mathbf{r},t) = \frac{1}{V}\sum_{\mathbf{k}} \mathrm{X}(\mathbf{k},t)\, e^{i\mathbf{k}\cdot\mathbf{r}}.$$

If the function X represents a physical observable, it must be real-valued, which imposes the condition $\mathrm{X}^*(\mathbf{k},t) = \mathrm{X}(-\mathbf{k},t)$ on its Fourier components.

The Fourier transform simplifies Maxwell's equations by converting local spatial derivatives into algebraic operations in reciprocal space, specifically:

$$\boldsymbol{\nabla} \times \mathbf{X}(\mathbf{r},t) \longrightarrow i\mathbf{k} \times \mathbf{X}(\mathbf{k},t), \qquad \boldsymbol{\nabla} \cdot \mathbf{X}(\mathbf{r},t) \longrightarrow i\mathbf{k} \cdot \mathbf{X}(\mathbf{k},t).$$

This transformation decouples the evolution of each Fourier component, making them independent of one another. Additionally, the orientation of the vector fields relative to $\mathbf{k}$ becomes significant. Any vector $\mathbf{X}(\mathbf{k},t)$ can be decomposed into two orthogonal components:

$$\mathbf{X}(\mathbf{k},t) = \mathbf{X}^{\perp}(\mathbf{k},t) + \mathbf{X}^{\parallel}(\mathbf{k},t),$$

where $\mathbf{X}^{\perp}(\mathbf{k},t)$ is the transverse component (orthogonal to $\mathbf{k}$), and $\mathbf{X}^{\parallel}(\mathbf{k},t)$ is the longitudinal component (parallel to $\mathbf{k}$).

In real space, the transverse and longitudinal components are computed as integrals involving transverse and longitudinal delta functions [113]. While this decomposition is geometrically intuitive in reciprocal space, in real space, the transverse and longitudinal components become complex, nonlocal functions of the original fields.

Let's represent the electric and magnetic fields from Eqs. (I.4) in reciprocal space. The magnetic field is purely transverse, while the electric field has both longitudinal and transverse components:

$$\mathbf{B}(\mathbf{k},t) = i\mathbf{k} \times \mathbf{A}^{\perp}(\mathbf{k},t), \tag{I.6a}$$

$$\mathbf{E}^{\perp}(\mathbf{k},t) = -\frac{1}{c}\frac{\partial \mathbf{A}^{\perp}(\mathbf{k},t)}{\partial t}, \tag{I.6b}$$

$$\mathbf{E}^{\parallel}(\mathbf{k},t) = -i\mathbf{k}\,\varphi(\mathbf{k},t) - \frac{1}{c}\frac{\partial \mathbf{A}^{\parallel}(\mathbf{k},t)}{\partial t}. \tag{I.6c}$$

The longitudinal electric field can be derived directly from Gauss's law (I.2a), which links it to the charge density:[1]

$$\mathbf{E}^{\parallel}(\mathbf{k},t) = -\frac{4\pi i\mathbf{k}}{\mathbf{k}^2}\rho(\mathbf{k},t). \tag{I.7}$$

This demonstrates that the longitudinal electric field is fully determined by the charge positions and does not constitute an independent dynamical variable. Furthermore, Ampère's law (I.2d) written for the longitudinal components simplifies to the continuity equation (I.1).

The remaining fields, the magnetic field and the transverse electric field, are governed by the transverse form of Ampère's law (I.2d):

$$i\mathbf{k}\times\mathbf{B}^{\perp}(\mathbf{k},t) - \frac{1}{c}\frac{\partial\mathbf{E}^{\perp}(\mathbf{k},t)}{\partial t} = \frac{4\pi}{c}\mathbf{j}^{\perp}(\mathbf{k},t), \tag{I.8}$$

where $\mathbf{j}^{\perp}(\mathbf{k},t)$ is the transverse part of the current density.[2] Notably, the transverse electric and magnetic fields, as well as the transverse component of the vector potential, are gauge-invariant.

To simplify the equations further, we eliminate the longitudinal vector potential using a gauge transformation.[3] This choice, known as the Coulomb gauge, is commonly used in quantum optics when relativistic effects are negligible. In this gauge, the vector potential becomes purely transverse. We keep the original notation for the gauge-transformed potentials, $\mathbf{A}(\mathbf{k},t)$ and $\varphi(\mathbf{k},t)$, where $\mathbf{A}(\mathbf{k},t)$ is purely transverse.

Returning to the reciprocal Ampère's law in Eq. (I.8), we rewrite it in terms of the gauge-transformed vector potential:

$$\frac{\partial^2\mathbf{A}(\mathbf{k},t)}{\partial t^2} + \nu_{\mathbf{k}}^2\,\mathbf{A}(\mathbf{k},t) = 4\pi c\,\mathbf{j}^{\perp}(\mathbf{k},t). \tag{I.9}$$

Here, $\nu_{\mathbf{k}} = c|\mathbf{k}|$ is the frequency associated with the wave vector $\mathbf{k}$. This equation describes the dynamics of a driven harmonic oscillator, indicating that each Fourier component of the transverse vector potential acts as an independent harmonic oscillator. This interpretation will be further explored in Sec. 1.3.

1.2 Longitudinal Field Energy

In the Coulomb gauge, the longitudinal electric field is fully determined by the scalar potential $\varphi(\mathbf{k},t)$. For completeness, we provide the expression for its contribution in real space:

$$-\boldsymbol{\nabla}\varphi(\mathbf{r},t) = \sum_i q_i \frac{\mathbf{r}-\mathbf{r}_i(t)}{|\mathbf{r}-\mathbf{r}_i(t)|^3}, \tag{I.10}$$

for $\mathbf{r}\neq\mathbf{r}_i(t)$. This component of the electric field responds instantaneously to changes in charge positions, seemingly violating causality. However, the total field also includes a contribution from the vector potential that cancels the instantaneous part, thereby restoring causality [113].

The contribution of the longitudinal electric field to the electromagnetic field energy depends on the positions of the charges $\mathbf{r}_i$ and is given by:

$$H_{\text{long.}}(\{\mathbf{r}_i\}) = \frac{1}{2}\sum_{\substack{i,j\\ i\neq j}}\frac{q_iq_j}{|\mathbf{r}_i-\mathbf{r}_j|} + \sum_i \frac{q_i^2}{\pi}\int_0^{\infty} dk. \tag{I.11}$$

The second term is an infinite Coulomb self-energy, which, in the non-relativistic regime, can be regularized by introducing a cutoff to the integral [113]. In this dissertation, we omit this term and consider only the finite contribution, which describes electrostatic interactions between all charged particles.

[1] In reciprocal space, the charge density for point charges is given by $\rho(\mathbf{k},t) = \sum_i q_i e^{-i\mathbf{k}\cdot\mathbf{r}_i(t)}$.

[2] In reciprocal space, the current density for point charges is given by $\mathbf{j}(\mathbf{k},t) = \sum_i q_i\,\dot{\mathbf{r}}_i(t)\,e^{-i\mathbf{k}\cdot\mathbf{r}_i(t)}$.

[3] This requires defining the gauge function as:

$$f(\mathbf{k},t) = i\frac{\mathbf{k}\cdot\mathbf{A}^{\parallel}(\mathbf{k},t)}{\mathbf{k}^2}.$$

1.3 Transverse Field Energy

In the Coulomb gauge, the vector potential is purely transverse and satisfies Eq. (I.9), which describes a driven harmonic oscillator. In this section, we introduce normal harmonic oscillator variables, following the approach similar to that described in Ref. [113].

The dynamics can be reformulated as a first-order differential equation. By combining Faraday's law (I.2c) with Ampère's law (I.2d) in reciprocal space, we derive the following equation:

$$\frac{d\mathbf{A}_{\mathbf{k}}(t)}{dt} + i\nu_{\mathbf{k}}\mathbf{A}_{\mathbf{k}}(t) = \frac{2\pi i}{C_{\mathbf{k}}}\,\mathbf{j}^{\perp}(\mathbf{k},t), \tag{I.12}$$

where $\nu_{\mathbf{k}} = c|\mathbf{k}|$. The variables $\mathbf{A}_{\mathbf{k}}(t)$ are the following combinations of the transverse electric and magnetic fields:

$$\mathbf{A}_{\mathbf{k}}(t) = \frac{1}{2iC_{\mathbf{k}}}\Big\{\mathbf{E}^{\perp}(\mathbf{k},t) - \frac{c}{\nu_{\mathbf{k}}}\,\mathbf{k}\times\mathbf{B}(\mathbf{k},t)\Big\}.$$

In these expressions, we introduced a phenomenological scaling factor, $C_{\mathbf{k}}$, that does not affect the dynamics. The variables $\mathbf{A}_{\mathbf{k}}(t)$ represent normal harmonic oscillator modes, serving as independent dynamical variables that fully characterize the physical fields: the transverse electric field, magnetic field, and vector potential.

> Indeed, by combining the normal oscillator variables, we derive the following expressions for the transverse components of the electric and magnetic fields:
>
> $$\mathbf{E}^{\perp}(\mathbf{k},t) = iC_{\mathbf{k}}\,\mathbf{A}_{\mathbf{k}}(t) - iC^{*}_{-\mathbf{k}}\,\mathbf{A}_{-\mathbf{k}}(t),$$
> $$\mathbf{B}(\mathbf{k},t) = i\mathbf{k}\times\Big[\frac{c}{\nu_{\mathbf{k}}}\{C_{\mathbf{k}}\,\mathbf{A}_{\mathbf{k}}(t) + C^{*}_{-\mathbf{k}}\,\mathbf{A}^{*}_{-\mathbf{k}}(t)\}\Big].$$
>
> By comparing the expression for the magnetic field with Eq. (I.6a), the term in square brackets is identified as the transverse vector:
>
> $$\mathbf{A}(\mathbf{k},t) = \frac{c}{\nu_{\mathbf{k}}}\{C_{\mathbf{k}}\,\mathbf{A}_{\mathbf{k}}(t) + C^{*}_{-\mathbf{k}}\,\mathbf{A}^{*}_{-\mathbf{k}}(t)\}.$$
>
> Furthermore, the expression for the transverse electric field coincides with Eq. (I.6b), provided that $\mathbf{A}_{\mathbf{k}}(t)$ satisfy Eq. (I.12).

Each vector $\mathbf{A}_{\mathbf{k}}(t)$ lies in the plane orthogonal to the wave vector $\mathbf{k}$, possessing two independent degrees of freedom. For each wave vector $\mathbf{k}$, we introduce a basis of polarization vectors $\mathbf{e}_{\mathbf{k},\lambda}$, where $\lambda = 1, 2$, defined by the following relations:

$$\mathbf{e}_{\mathbf{k},\lambda}\cdot\mathbf{e}^{*}_{\mathbf{k},\lambda'} = \delta_{\lambda\lambda'}, \qquad\qquad \mathbf{k}\cdot\mathbf{e}_{\mathbf{k},\lambda} = 0.$$

In this basis, the normal variables $\mathbf{A}_{\mathbf{k}}(t)$ are expressed as:

$$\mathbf{A}_{\mathbf{k}}(t) = \sum_{\lambda}\mathbf{e}_{\mathbf{k},\lambda}\,\alpha_{\mathbf{k},\lambda}(t).$$

The new scalar variables $\alpha_{\mathbf{k},\lambda}(t)$ satisfy the following equation, derived from Eq. (I.12):

$$\frac{d\alpha_{\mathbf{k},\lambda}(t)}{dt} = -i\nu_{\mathbf{k}}\alpha_{\mathbf{k},\lambda}(t) + \frac{2\pi i}{C_{\mathbf{k}}}\,\mathbf{e}^{*}_{\mathbf{k},\lambda}\cdot\mathbf{j}(\mathbf{k},t). \tag{I.13}$$

This equation can be formally solved and substituted into the expressions for the total electric and magnetic fields. The resulting solutions, expressed in the retarded time framework, are known as Jefimenko's equations [114, 115]. These equations can also be derived directly from Maxwell's equations without using electromagnetic potentials, ensuring their gauge independence.

The contribution of the transverse electric and magnetic fields to the electromagnetic field energy is described by the following functional of the variables $\alpha_{\mathbf{k},\lambda}$ and $\alpha^{*}_{\mathbf{k},\lambda}$:

$$H_{\text{trans.}}(\{\alpha_{\mathbf{k},\lambda},\alpha^{*}_{\mathbf{k},\lambda}\}) = \sum_{\mathbf{k},\lambda}\frac{|C_{\mathbf{k}}|^2}{2\pi V}\alpha^{*}_{\mathbf{k},\lambda}\,\alpha_{\mathbf{k},\lambda}. \tag{I.14}$$

After quantization, the field should be represented by quanta with energy $\hbar\nu_{\mathbf{k}}$. Therefore, when quantizing, we set the scaling coefficient to $|C_{\mathbf{k}}|^2 = 2\pi V\hbar\nu_{\mathbf{k}}$ as a phenomenological condition.

2 Quantized Picture

We have identified the following independent dynamical variables: the positions and momenta of the charged particles (not velocities, as momenta are conjugate to positions) and the normal oscillator modes of the electromagnetic field, $\alpha_{\mathbf{k},\lambda}$ and $\alpha^*_{\mathbf{k},\lambda}$. The free motion of the particles is quantized by replacing classical dynamical variables $\mathbf{p}_i$, $\mathbf{r}_i$ with the quantum operators $\hat{\mathbf{p}}_i$, $\hat{\mathbf{r}}_i$, which satisfy the fundamental canonical commutation relations.

For the quantization of the electromagnetic field, a rigorous approach first requires identifying the field's canonical dynamical variables [113, 116]. It is necessary to find the Lagrangian that reproduces the equations of motion. The redundant degrees of freedom are eliminated: the longitudinal component of the vector potential is removed by fixing the Coulomb gauge, while the scalar potential depends on the charges' positions. The Hamiltonian is then derived via the Legendre transformation.

Assuming a free electromagnetic field, we can identify the following canonically conjugated variables: the vector potential (generalized position) and, up to a factor of $-1/(4\pi c)$, the transverse electric field (generalized momentum). By postulating the canonical commutation relations between these variables in reciprocal space, we obtain the quantized description of the electromagnetic field.

As a result of quantization, the classical variables $\alpha_{\mathbf{k},\lambda}$ and $\alpha^*_{\mathbf{k},\lambda}$ are replaced by operators $\hat{a}_{\mathbf{k},\lambda}$ and $\hat{a}^\dagger_{\mathbf{k},\lambda}$, which satisfy the bosonic commutation relations:

$$[\hat{a}_{\mathbf{k},\lambda},\, \hat{a}^\dagger_{\mathbf{k}',\lambda'}] = \delta_{\lambda\lambda'}\, \delta_{\mathbf{k}\mathbf{k}'}. \tag{I.15}$$

These operators annihilate and create quanta of the field—photons—with energy $\hbar\nu_{\mathbf{k}}$. This provides a heuristic method for transitioning from a classical to a quantum description. Specifically, in all classical expressions in Sec. 1.3, the classical normal oscillator variables are replaced with bosonic operators. Returning to Eq. (I.14), we choose the scaling coefficient $|C_{\mathbf{k}}|^2 = 2\pi V \hbar\nu_{\mathbf{k}}$ to support the interpretation of photons [113].

This approach is not entirely rigorous and introduces some inaccuracies. For example, when replacing the transverse field energy with the operator

$$\hat{H}_{\text{trans.}} = \sum_{\mathbf{k},\lambda} \hbar\nu_{\mathbf{k}}\, \hat{a}^\dagger_{\mathbf{k},\lambda}\, \hat{a}_{\mathbf{k},\lambda}, \tag{I.16}$$

the zero-point energy associated with quantum harmonic oscillators is omitted. However, this divergent term is often disregarded in practical applications where it has no observable effect. Nevertheless, changes in the zero-point energy can have physical consequences, such as the Casimir force; see Ref. [117] for a more detailed discussion. In other respects, this approach yields results consistent with rigorous quantization.

Let us now introduce the interaction terms. The energy contribution from the longitudinal electric field in Eq. (I.11) represents the electrostatic interactions between charges. Replacing the classical charge positions with their quantum operator counterparts yields the following operator:

$$\hat{H}_{\text{long.}} = \frac{1}{2} \sum_{\substack{i,j \\ i\neq j}} \frac{q_i q_j}{|\hat{\mathbf{r}}_i - \hat{\mathbf{r}}_j|}.$$

To correctly reproduce the quantum analogs of Eq. (I.13) and the Newton-Lorentz equation, we must start from the classical Hamiltonian for light-matter interaction. For brevity, we present only the final expressions here. The canonical momenta in the Hamiltonian for free particles are replaced with the following kinetic momenta:

$$\hat{\mathbf{p}}_i \longrightarrow \hat{\mathbf{p}}_i - \frac{q_i}{c}\, \hat{\mathbf{A}}(\hat{\mathbf{r}}_i).$$

After performing this transformation and including the longitudinal field energy, we arrive at the minimal coupling Hamiltonian, which describes a system of charges interacting with the

quantized electromagnetic field:

$$\hat{H} = \sum_i \frac{\left[\hat{\mathbf{p}}_i - \frac{q_i}{c}\hat{\mathbf{A}}(\hat{\mathbf{r}}_i)\right]^2}{2m_i} + \hat{H}_{\text{long.}} + \hat{H}_{\text{trans.}}. \tag{I.17}$$

This Hamiltonian is written in the Coulomb gauge, which ensures that the vector potential operator commutes with the particle momentum operators.

The Schrödinger picture operators for the transverse electric field, magnetic field, and vector potential retain the same structure as their classical counterparts (see Sec. 1.3), with the distinction that the normal field modes are now expressed through the bosonic operators. In real space, the expressions are the following:

$$\hat{\mathbf{E}}^{\perp}(\mathbf{r}) = i\sqrt{\frac{2\pi\hbar}{V}} \sum_{\mathbf{k},\lambda} \sqrt{\nu_{\mathbf{k}}} \{\mathbf{e}_{\mathbf{k},\lambda}\, \hat{a}_{\mathbf{k},\lambda}\, e^{i\mathbf{k}\cdot\mathbf{r}} - \mathbf{e}^*_{\mathbf{k},\lambda}\, \hat{a}^\dagger_{\mathbf{k},\lambda}\, e^{-i\mathbf{k}\cdot\mathbf{r}}\}, \tag{I.18a}$$

$$\hat{\mathbf{B}}(\mathbf{r}) = i\sqrt{\frac{2\pi c^2\hbar}{V}} \sum_{\mathbf{k},\lambda} \frac{\mathbf{k}}{\sqrt{\nu_{\mathbf{k}}}} \times \{\mathbf{e}_{\mathbf{k},\lambda}\, \hat{a}_{\mathbf{k},\lambda}\, e^{i\mathbf{k}\cdot\mathbf{r}} + \mathbf{e}^*_{\mathbf{k},\lambda}\, \hat{a}^\dagger_{\mathbf{k},\lambda}\, e^{-i\mathbf{k}\cdot\mathbf{r}}\}, \tag{I.18b}$$

$$\hat{\mathbf{A}}(\mathbf{r}) = \sqrt{\frac{2\pi c^2\hbar}{V}} \sum_{\mathbf{k},\lambda} \frac{1}{\sqrt{\nu_{\mathbf{k}}}} \{\mathbf{e}_{\mathbf{k},\lambda}\, \hat{a}_{\mathbf{k},\lambda}\, e^{i\mathbf{k}\cdot\mathbf{r}} + \mathbf{e}^*_{\mathbf{k},\lambda}\, \hat{a}^\dagger_{\mathbf{k},\lambda}\, e^{-i\mathbf{k}\cdot\mathbf{r}}\}. \tag{I.18c}$$

Here, $\nu_{\mathbf{k}} = c|\mathbf{k}|$; V represents the quantization volume, and $\mathbf{e}_{\mathbf{k},\lambda}$ are polarization vectors orthogonal to $\mathbf{k}$, with $\lambda = 1, 2$. The total electric field is obtained by adding the operator for the longitudinal component.

2.1 System of Atoms

Consider a system of N neutral atoms, indexed by μ, where the charges consist of nuclei and electronic shells. Since the electron-to-proton mass ratio is approximately 5×10^{-4}, we assume that the center of mass of each atom coincides with the position of its nucleus, denoted by $\mathbf{R}_\mu$. Furthermore, we neglect the dynamics of the nuclei, treating them as motionless. This implies that the evolution of the electronic shells occurs with fixed nuclear positions. The relevant dynamical variables are the internal positions of the electrons relative to their nuclei:

$$\hat{\mathbf{x}}_{\mu,a} = \hat{\mathbf{r}}_{\mu,a} - \mathbf{R}_\mu, \tag{I.19}$$

where $\hat{\mathbf{r}}_{\mu,a}$ is the position of the a-th electron within the μ-th atom, and $\hat{\mathbf{x}}_{\mu,a}$ denotes the electron's position relative to the nucleus of the atom. We assume that the μ-th atom contains Z_μ electrons. Additionally, we neglect the $\mathbf{A}^2$-term at nuclear positions, focusing solely on the electronic dynamics.

Next, we apply the dipole approximation, which neglects the spatial variation of the electromagnetic field within each atom:

$$e^{i\mathbf{k}\cdot\hat{\mathbf{r}}_{\mu,a}} = e^{i\mathbf{k}\cdot(\hat{\mathbf{x}}_{\mu,a}+\mathbf{R}_\mu)} \approx e^{i\mathbf{k}\cdot\mathbf{R}_\mu}.$$

For emission processes, this approximation holds as long as the spatial overlap of the orbitals involved in transitions is much smaller than the characteristic emission wavelength.

Now, consider the ensemble of atoms as a whole. We assume that the distances between atoms are much greater than their sizes. For reference, the characteristic linear size of an atom is approximately $a_0 \sim 10^{-8}$ cm. For an atomic gas, this implies that the atomic concentration must remain well below $1/a_0^3$, which is roughly 10^{24} cm^{-3}.

Within each atom, the maximum distance between any electron and its nucleus is much smaller than the distances between atoms. This allows the electrostatic interaction between atoms to be expanded as a Taylor series, known as a multipolar expansion. The zero- and first-order terms correspond to charge-charge and charge-dipole interactions, but these vanish

since atoms are electrically neutral. The first non-zero contribution arises from the second-order term, which corresponds to the interaction between atomic dipole moments:

$$\hat{\mathbf{d}}_\mu = \sum_{a=1}^{Z_\mu} e\hat{\mathbf{r}}_{\mu,a} + Q_\mu \mathbf{R}_\mu = \sum_{a=1}^{Z_\mu} e\hat{\mathbf{x}}_{\mu,a}, \tag{I.20}$$

where $Q_\mu = -eZ_\mu$ is the nuclear charge, and e is the electron charge (with $e < 0$). The longitudinal energy can then be decomposed into two leading components: the intra-atomic Coulomb potentials and the dipole-dipole interactions between atoms.[4]

Under these approximations, it is convenient to express the Hamiltonian in the length gauge, derived using the Power-Zienau-Woolley transformation [118, 119], neglecting additional terms such as contact interactions and self-energy contributions. The resulting Hamiltonian is:

$$\hat{H} = \sum_{\mu=1}^{N} \hat{H}_\mu + \sum_{\mathbf{k},\lambda} \hbar\nu_{\mathbf{k}}\, \hat{a}^\dagger_{\mathbf{k},\lambda}\, \hat{a}_{\mathbf{k},\lambda} - \sum_{\mu=1}^{N} \hat{\mathbf{d}}_\mu \cdot \hat{\mathbf{E}}(\mathbf{r}_\mu), \tag{I.21}$$

where, for simplicity, the atomic positions have been re-notated by replacing $\mathbf{R}_\mu$ with $\mathbf{r}_\mu$, and the superscript $^\perp$ has been omitted from the transverse electric field operator. The term $\hat{H}_\mu$ represents the free Hamiltonian of the μ-th atom, which includes the kinetic energy of its electrons and the intra-atomic Coulomb potentials.

To simplify the model, we replace real atoms, which have an infinite number of energy levels, with effective objects called *quantum emitters* or *pseudospins*. Each quantum emitter is characterized by M distinct energy levels, relevant for the phenomena under consideration. The free Hamiltonian takes the diagonal form:

$$\hat{H}_\mu = \sum_{i=1}^{M} \hbar\omega_i\, \hat{\sigma}_{\mu,ii}. \tag{I.22}$$

Here, $\hat{\sigma}_{\mu,ij} = |i\rangle_\mu\langle j|_\mu$, where $|i\rangle_\mu$ denotes the i-th state of the μ-th emitter, and $\hbar\omega_i$ is the energy associated with this state. We assume that all emitters share the same energy level structure.

The Hamiltonian in Eq. (I.21) serves as a foundation for describing light-matter interactions. Using the associated Heisenberg equations, one can derive propagation equations for the radiation field, which can be treated within a semiclassical framework [9, 65]. This approach is widely employed in the modeling of distributed systems and allows for the derivation of analytical qualitative solutions [65]. However, the semiclassical approach inherently neglects quantum fluctuations arising from interactions with a vacuum, which are responsible for spontaneous emission. Consequently, in the absence of external driving and without an initial dipole moment, the semiclassical theory predicts no dynamics. This underscores the need to incorporate at least some treatment of quantum fluctuations, if not a fully quantum mechanical approach.

When the system is compact, meaning its linear size is much smaller than any characteristic emission wavelengths (the Dicke limit [1]), it is more common to exclude the field variables in the Born-Markov approximation [5, 9, 120–122]. This approximation assumes that the buildup of correlations between the atoms and the field can be neglected and that the atom-field correlation time is negligibly short relative to the atomic system's evolution time [9].

The Born-Markov quantum master equation for the reduced density matrix *of the emitters* is given by:

$$\frac{d\hat{\rho}(t)}{dt} = -\frac{1}{\hbar^2}\,\mathrm{Tr}_{\mathrm{field}} \int_0^\infty d\tau\, \big[\hat{V}(t), \big[\hat{V}(t-\tau),\, \hat{\rho}(t) \otimes \hat{\rho}_{\mathrm{field}}(0)\big]\big],$$

[4] For completeness, the explicit expressions are:

$$\hat{H}_{\mathrm{long.}} \approx \sum_{\mu=1}^{N} \left\{ \sum_{a=1}^{Z_\mu} \frac{eQ_\mu}{|\hat{\mathbf{x}}_{\mu,a}|} + \frac{1}{2} \sum_{\substack{a,b=1 \\ a\neq b}}^{Z_\mu} \frac{e^2}{|\hat{\mathbf{x}}_{\mu,a} - \hat{\mathbf{x}}_{\mu,b}|} \right\} + \frac{1}{2} \sum_{\substack{\mu,\nu=1 \\ \mu\neq\nu}}^{N} \frac{(\hat{\mathbf{d}}_\mu \cdot \hat{\mathbf{d}}_\nu)\, R^2_{\mu\nu} - 3\,(\hat{\mathbf{d}}_\mu \cdot \mathbf{R}_{\mu\nu})\,(\hat{\mathbf{d}}_\nu \cdot \mathbf{R}_{\mu\nu})}{R^5_{\mu\nu}},$$

where $\mathbf{R}_{\mu\nu} = \mathbf{R}_\mu - \mathbf{R}_\nu$ and $R_{\mu\nu} = |\mathbf{R}_{\mu\nu}|$.

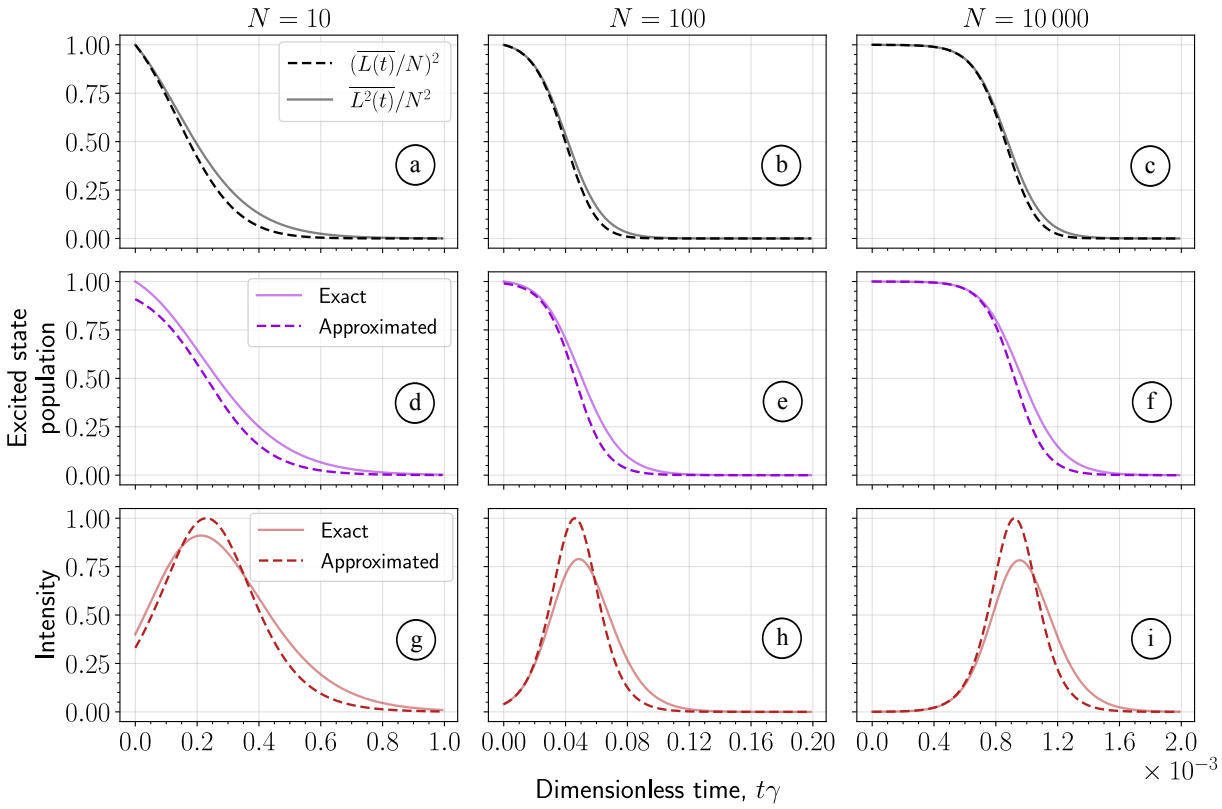

Figure I.1: Comparison of the exact solution of Eq. (I.23) with the approximate solutions from Eqs. (I.25) and (I.26) for various values of N. Panels (a)-(c) display $\overline{L^2(t)}$ and $\overline{L(t)}^2$ based on the exact solution. Panels (d)-(f) and (g)-(i) show the excited state population and emission intensity, respectively. Intensities are normalized to the maximum value of the exact solution.

where all operators are written in the interaction picture, and the operator $\hat{V}(t)$ describes the light-matter interaction. The density operator $\hat{\rho}_{\text{field}}(0)$ represents the field's initial state, which we assume to be the vacuum.

When deriving the master equation, we employ the rotating-wave approximation and disregard the dipole-dipole interactions that have a dephasing effect on the cooperative emission [123–125]. This approximation holds for atoms within a cavity [20, 126], as non-resonant interactions are suppressed and the dipole-dipole interaction is modified [127]. The resulting master equation for *two-level emitters* is given by [53]:

$$\frac{d\hat{\rho}(t)}{dt} = \gamma \hat{J}_{12}\,\hat{\rho}(t)\,\hat{J}_{21} - \frac{\gamma}{2}\hat{J}_{21}\,\hat{J}_{12}\,\hat{\rho}(t) - \frac{\gamma}{2}\hat{\rho}(t)\,\hat{J}_{21}\,\hat{J}_{12}. \tag{I.23}$$

Here, $\gamma = 4\omega_0^3|\mathbf{d}_{12}|^2/(3\hbar c^3)$ is the spontaneous decay rate, where ω_0 is the emission frequency, and $\mathbf{d}_{12} = \langle 1|\hat{\mathbf{d}}|2\rangle$ is the transition dipole moment. The collective operators are defined as:

$$\hat{J}_{pq} = \sum_{\mu=1}^{N} \hat{\sigma}_{\mu,pq}.$$

In the next section, we examine the exact and approximate solutions of this master equation.

2.2 Superradiance in Two-Level Emitters

In the absence of external fields and nonradiative dissipation channels, and assuming all atoms are instantaneously excited, the density matrix is expressed as a statistical mixture of Dicke states:

$$\hat{\rho}(t) = \sum_{L=0}^{N} \rho_L(t)\,|L\rangle\langle L|.$$

Here, $|L\rangle$ denotes a symmetrized state where L out of N atoms are excited. The coefficient $\rho_L(t)$ is the probability of finding L atoms excited at time t. These probabilities are governed by the following rate equations:

$$\frac{d\rho_L(t)}{dt} = -\gamma_L\,\rho_L(t) + \gamma_{L+1}\,\rho_{L+1}(t), \tag{I.24}$$

where $\gamma_L = \gamma L\,(N - L + 1)$. These equations indicate that the ensemble evolves through a ladder of Dicke states, starting from the highest state and cascading through transitions $N \to (N-1) \to \ldots \to 1 \to 0$, until reaching complete relaxation.

The emission of the first photon occurs at a characteristic rate of γN, which is N times faster than the decay rate of an isolated atom. The emission of the second photon is governed by the depopulation rate of the coefficient $\rho_{N-1}(t)$, which is roughly $\gamma(N-1)$, and so on.

The system of linear equations in Eq. (I.24) contains only $N+1$ unknown variables. However, the inclusion of incoherent processes or external driving increases the complexity of the problem from linear to higher-degree polynomial. For macroscopic ensembles ($N \gg 1$), this can become a significant limitation. These challenges highlight the need for approximate methods that either yield analytical solutions or maintain complexity independent of N.

The probabilities $\rho_L(t)$ determine the average number of excited atoms, $\overline{L(t)}$, through:

$$\overline{L(t)} = \sum_{L=0}^{N} L\rho_L(t).$$

Assuming the distribution $\rho_L(t)$ satisfies $\overline{L^2(t)} \approx \overline{L(t)}^2$ for all t, a simplified solution can be derived. In Fig. I.1 (a)-(c), the averages $\overline{L^2(t)}$ and $\overline{L(t)}^2$ are shown for different values of N using the exact solution. These averages converge closely only for larger N.

Under this approximation, the mean number of excited atoms is expressed as [9]:

$$\overline{L(t)} \approx \frac{N}{2} - \frac{N}{2}\tanh\left[\frac{\gamma N(t - t_D)}{2}\right], \tag{I.25}$$

where $t_D = \tau_{\text{sp.}} \ln N/N$, and $\tau_{\text{sp.}} = 1/\gamma$. This solution resembles a smooth step function, transitioning from N to 0 around $t \approx t_D$ over a characteristic timescale of $\tau_{\text{sp.}}/N$. The delay time t_D defines the interval between instantaneous excitation and the peak emission intensity.

The emission is characterized by the rate of emitted photons per unit time, expressed as:

$$I(t) = -\frac{d\overline{L(t)}}{dt} = \frac{\gamma N^2}{4}\operatorname{sech}^2\left[\frac{\gamma N(t - t_D)}{2}\right]. \tag{I.26}$$

The total number of emitted photons is found by integrating this intensity over time.

Figures I.1 (d)-(f) and (g)-(i) compare the excited state population and emission intensity for different N, using both exact and approximate solutions. For a large number of atoms, the approximate solution qualitatively resembles the exact solution. However, it predicts shorter delay times and faster decay, and the approximate intensity curves are narrower than the exact ones. The approximation $\overline{L^2(t)} \approx \overline{L(t)}^2$ significantly distorts the averages, emphasizing the importance of fluctuations.

2.3 Tipping Angle Approach

Another approximate approach derives semiclassical equations and reintroduces the effects of quantum fluctuations via random initial conditions [9]. Using the master equation in Eq. (I.23), we derive equations for the averages:

$$\rho_{pq}(t) = \frac{1}{N}\sum_{\mu=1}^{N} \text{Tr}\left[\hat{\sigma}_{\mu,qp}\,\hat{\rho}(t)\right],$$

which represent a single-particle reduced density matrix. These averages evolve according to the following equations:

$$\frac{d\rho_{11}(t)}{dt} = \gamma\rho_{22}(t) + \gamma \sum_{\mu\neq\nu} \mathrm{Tr}\left[\hat{\sigma}_{\mu,21}\,\hat{\sigma}_{\nu,12}\,\hat{\rho}(t)\right], \tag{I.27a}$$

$$\frac{d\rho_{12}(t)}{dt} = -\frac{\gamma}{2}\rho_{12}(t) + \frac{\gamma}{2} \sum_{\mu\neq\nu} \mathrm{Tr}\left[\hat{\sigma}_{\mu,12}\left(\hat{\sigma}_{\nu,22} - \hat{\sigma}_{\nu,11}\right)\hat{\rho}(t)\right], \tag{I.27b}$$

$$\frac{d\rho_{21}(t)}{dt} = -\frac{\gamma}{2}\rho_{21}(t) + \frac{\gamma}{2} \sum_{\mu\neq\nu} \mathrm{Tr}\left[\hat{\sigma}_{\mu,21}\left(\hat{\sigma}_{\nu,22} - \hat{\sigma}_{\nu,11}\right)\hat{\rho}(t)\right], \tag{I.27c}$$

$$\frac{d\rho_{22}(t)}{dt} = -\gamma\rho_{22}(t) - \gamma \sum_{\mu\neq\nu} \mathrm{Tr}\left[\hat{\sigma}_{\mu,21}\,\hat{\sigma}_{\nu,12}\,\hat{\rho}(t)\right]. \tag{I.27d}$$

Here, μ and ν are distinct indices ranging from 1 to N. The first term in each equation represents spontaneous decay, while the second term captures interparticle interactions.

The equations for $\rho_{pq}(t)$ contain averages of two-particle operators. Similarly, the equations for mean two-particle operators include mean three-particle operators, and so forth. Writing equations for all possible averages quickly becomes intractable as the number of atoms increases.

Alternatively, we can truncate this hierarchy by factorizing the averages beyond a certain order and proposing an ansatz that expresses higher-order averages in terms of lower-order ones. This approach simplifies the system and makes it tractable. Let us factorize the second-order averages for different particles as follows:

$$\mathrm{Tr}\left[\hat{\sigma}_{\mu,ij}\,\hat{\sigma}_{\nu,pq}\,\hat{\rho}(t)\right] \approx \mathrm{Tr}\left[\hat{\sigma}_{\mu,ij}\,\hat{\rho}(t)\right]\,\mathrm{Tr}\left[\hat{\sigma}_{\nu,pq}\,\hat{\rho}(t)\right], \qquad \mu \neq \nu. \tag{I.28}$$

This approximation allows us to derive a closed system of equations while avoiding the exponential growth in complexity. However, it disregards all quantum correlations between particles. With this simplification, Eqs. (I.27) reduce to:

$$\frac{d\rho_{11}(t)}{dt} = \gamma\rho_{22}(t) + \gamma(N-1)\,\rho_{12}(t)\,\rho_{21}(t), \tag{I.29a}$$

$$\frac{d\rho_{12}(t)}{dt} = -\frac{\gamma}{2}\rho_{12}(t) + \frac{\gamma(N-1)}{2}\rho_{12}(t)\left[\rho_{22}(t) - \rho_{11}(t)\right], \tag{I.29b}$$

$$\frac{d\rho_{21}(t)}{dt} = -\frac{\gamma}{2}\rho_{21}(t) + \frac{\gamma(N-1)}{2}\rho_{21}(t)\left[\rho_{22}(t) - \rho_{11}(t)\right], \tag{I.29c}$$

$$\frac{d\rho_{22}(t)}{dt} = -\gamma\rho_{22}(t) - \gamma(N-1)\,\rho_{12}(t)\,\rho_{21}(t). \tag{I.29d}$$

If the emitters are initially excited without a dipole moment, the coherences remain static, and the system evolves solely according to the rate equations. To induce non-trivial dynamics, either an external field must be applied, or the emitters must have an initial nonzero dipole moment. In both cases, the system's dynamics is semiclassical.

However, it is possible to *phenomenologically* reintroduce the effects of quantum fluctuations lost due to the truncation in Eq. (I.28) without modifying the equations themselves. This is achieved by appropriately selecting initial conditions for the semiclassical variables [9], assuming that $\rho_{pq}(0)$ are treated as random variables.

Random Initial Conditions

Initially, all emitters are excited, forming the Dicke state $|N\rangle$. In this state, the average collective dipole moment—expressed as a linear combination of $\hat{J}_x$ and $\hat{J}_y$—is zero.[5] However,

[5] All emitters are identical, meaning that the matrix elements of the dipole moment operator, $\mathbf{d}_{ij} = \langle i|_\mu \hat{\mathbf{d}}_\mu |j\rangle_\mu$, are also identical for each emitter. Using this assumption, we can express:

$$\sum_{\mu=1}^{N} \hat{\mathbf{d}}_\mu = \sum_{\mu=1}^{N} \sum_{i,j=1}^{2} |i\rangle_\mu\langle i|_\mu \hat{\mathbf{d}}_\mu |j\rangle_\mu\langle j|_\mu = \hat{J}_{12}\,\mathbf{d}_{12} + \hat{J}_{21}\,\mathbf{d}_{21} = \hat{J}_x\,\mathrm{Re}\,\mathbf{d}_{12} + \hat{J}_y\,\mathrm{Im}\,\mathbf{d}_{12},$$

since Dicke states are eigenstates of the operator $\hat{J}_z$, other components of the angular momentum do not have definite values. Individual measurements of these components yield random values, which average to zero. To estimate their statistical moments, we compute:

$$\frac{\langle N|\hat{J}_{21}^{K}\,\hat{J}_{12}^{K'}|N\rangle}{N^{K+K'}} = \delta_{KK'} \times \begin{cases} \dfrac{N!\,K!}{N^{2K}\,(N-K)!}, & 0 \le K \le N, \\ 0, & K > N. \end{cases} \tag{I.30}$$

We can *phenomenologically* assume that the initial values $\rho_{ij}(0)$ are random variables, denoted by $\widetilde{\rho}_{ij}$, selected to reproduce these statistical moments. On average, the coherences $\widetilde{\rho}_{12}$ and $\widetilde{\rho}_{21}$ remain zero but take nonzero values in individual statistical realizations. This leads to non-trivial dynamics in Eqs. (I.29).

This reformulation alters the interpretation of the variables $\rho_{ij}(t)$. They correspond to the single-particle reduced density matrix only after statistical averaging. The averages of many-particle operators reflect the collective properties of the entire ensemble.

By definition, the random variables $\widetilde{\rho}_{ij}$ must reproduce the expectation value in Eq. (I.30):

$$\langle \widetilde{\rho}_{12}^{K}\,\widetilde{\rho}_{21}^{K'}\rangle = \delta_{KK'} \times \begin{cases} \dfrac{N!\,K!}{N^{2K}\,(N-K)!}, & 0 \le K \le N, \\ 0, & K > N. \end{cases}$$

Here, $\langle \ldots \rangle$ denotes statistical averaging over the distribution of $\widetilde{\rho}_{ij}$. Determining this distribution in general is challenging. However, in the limit as $N \to \infty$, the statistical moments simplify to:

$$\langle \widetilde{\rho}_{12}^{K}\,\widetilde{\rho}_{21}^{K'}\rangle \approx \delta_{KK'}\,\frac{K!}{N^{K}}. \tag{I.31}$$

A further simplification can be made by assuming that $\widetilde{\rho}_{ij}$ corresponds to a pure state on the Bloch sphere. In this case, these variables can be parameterized using two angles that define the orientation of the Bloch vector: the polar angle θ and the azimuthal angle ϕ:

$$\widetilde{\rho}_{11} = \sin^2\frac{\theta}{2}, \quad \widetilde{\rho}_{12} = \frac{\sin\theta}{2}\,e^{i\phi}, \quad \widetilde{\rho}_{21} = \frac{\sin\theta}{2}\,e^{-i\phi}, \quad \widetilde{\rho}_{22} = \cos^2\frac{\theta}{2}.$$

We interpret the angles θ and ϕ as new random variables, with their distribution functions to be determined shortly.

Averages involving unequal numbers of variables $\widetilde{\rho}_{12}$ and $\widetilde{\rho}_{21}$ must vanish. For example, $\langle\widetilde{\rho}_{12}\rangle$, $\langle\widetilde{\rho}_{12}\,\widetilde{\rho}_{22}\rangle$, and $\langle\widetilde{\rho}_{12}\,\widetilde{\rho}_{12}\,\widetilde{\rho}_{21}\rangle$ are all zero. This condition is satisfied by assuming the azimuthal angle ϕ is uniformly distributed over the interval from 0 to 2π.

Fluctuations in the polar angle θ correspond to small deviations of the Bloch vector around the north pole of the sphere, where $\theta = 0$. Assuming these fluctuations are sufficiently small, we can approximate $\sin\theta \approx \theta$. From the statistical moments in Eq. (I.31), we directly obtain:

$$\langle\theta^{2K}\rangle = \frac{K!}{(N/4)^K}.$$

These moments correspond to the even moments of a random variable that follows a Rayleigh distribution with a scale parameter $\sqrt{2/N}$:

$$\langle\theta^{k}\rangle = \int_0^\infty d\theta\,\theta^k\,\frac{N\theta}{2}\,e^{-N\theta^2/4} = \frac{\Gamma\,(1+k/2)}{(N/4)^{k/2}}.$$

Alternatively, the real and imaginary parts of the coherences can be sampled as Gaussian normal variables.

---

where the components of the angular momentum operator are defined as $\hat{J}_x = \hat{J}_{21} + \hat{J}_{12}$, $\hat{J}_y = -i\hat{J}_{21} + i\hat{J}_{12}$, and $\hat{J}_z = \hat{J}_{22} - \hat{J}_{11}$. From this expression, it follows that all powers of the collective dipole moment are proportional to combinations of $\hat{J}_{12}$ and $\hat{J}_{21}$, as in Eq. (I.30).

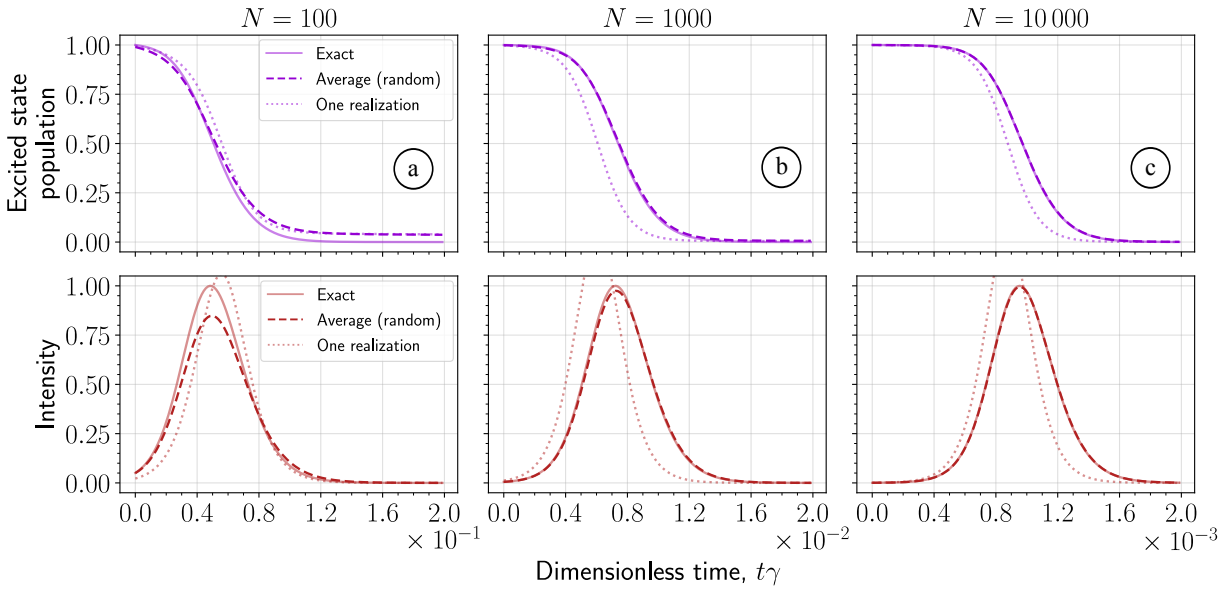

Figure I.2: Solutions of the semiclassical equations (I.29) with randomly distributed initial conditions are compared to the exact solutions. Intensities are normalized to the maximum of the exact solution. Statistical averages were computed using 10^5 realizations.

In Fig. I.2, we compare the exact solutions to the solutions of the semiclassical equations (I.29) with random initial conditions. For a small number of atoms, the discrepancy between the solutions is substantial. However, as the number of atoms increases to $N \sim 10^4$, the curves converge closely to the exact solution, as demonstrated in panels (b) and (c). Single realizations are also plotted to illustrate fluctuations around the mean curves.

In summary, fluctuations in the collective Bloch vector are sufficient to initiate the collective effect. The deviation from the north pole of the Bloch sphere that triggers the process is commonly referred to as the *tipping angle*. Experimental efforts have been made to measure this angle directly. For example, in the study by Q. Vrehen and M. Schuurmans [66], the mean tipping angle was measured to be on the order of $2/\sqrt{N}$, which aligns well with the theoretical model presented here.

The tipping angle approach, however, has several limitations. First, it is primarily applicable to systems with a large number of atoms. Second, it relies on the assumption that the system becomes fully excited instantaneously, whereas in realistic scenarios, excitation typically occurs through continuous pumping. Lastly, extending this approach to many-level atoms introduces additional complexity, requiring more sophisticated distribution models. These constraints motivate the development of alternative frameworks to describe cooperative emission.

2.4 Phenomenological Stochastic Equations

We have demonstrated that fluctuations in the tipping angle can activate the interaction terms in the semiclassical equations (I.29). To understand why this mechanism works, it is essential to examine how these fluctuations influence the equations.

Let us focus on the early stages of the dynamics, where the populations remain nearly constant. By assuming a fixed population inversion in Eq. (I.29b)—a regime we refer to as *linear*—we can compute the average $\langle \rho_{12}(t)\, \rho_{21}(t) \rangle$ for a large number of atoms:

$$\langle \rho_{12}(t)\, \rho_{21}(t) \rangle \approx \frac{\exp\left(N t \gamma\right)}{N}.$$

At approximately the delay time $t_D = \tau_{\text{sp.}} \ln N/N$, this average reaches unity, causing the interaction term in Eq. (I.29d) to dominate, thereby invalidating the assumption of a linear regime.

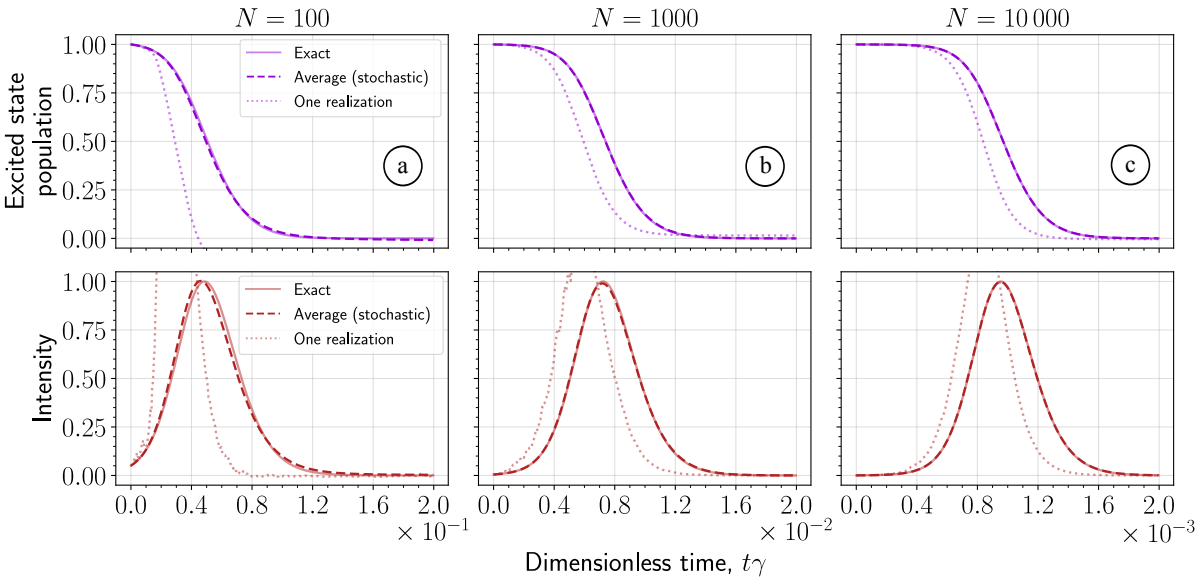

Figure I.3: Solutions of the stochastic equations in Eq. (I.32) compared to the exact solution for different numbers of atoms. Intensities are normalized to the maximum of the exact solution. Statistical averages were computed using 10^5 stochastic realizations.

For times $t \ll \tau_{\text{sp.}}/N$, the expression for this average predicts linear growth:

$$\langle \rho_{12}(t)\, \rho_{21}(t) \rangle \approx \frac{1}{N} + \gamma t.$$

The first term originates from the initial conditions and can be seen as a remnant of the tipping angle approach, vanishing as $N \to \infty$. Most importantly, there is a linear growth in the second term, which is activated by the fluctuations in the initial conditions.

Let us consider an alternative approach, where fluctuations in the coherences are introduced *phenomenologically* by adding an extra term to the equations for them (I.29b). These additional terms are modeled as stochastic processes:

$$\frac{d\rho_{12}(t)}{dt} = \ldots + \sqrt{\gamma}\, \mathscr{D}(t)\, \mathrm{S}(t), \qquad \frac{d\rho_{21}(t)}{dt} = \ldots + \sqrt{\gamma}\, \mathscr{D}^*(t)\, \mathrm{S}^*(t),$$

where $\mathscr{D}(t)$ is an undetermined multiplier, and $\mathrm{S}(t)$ is a complex Gaussian white noise process satisfying $\langle \mathrm{S}(t)\, \mathrm{S}^*(t') \rangle = \delta(t - t')$, with all other first- and second-order averages equal to zero.

According to Itô's lemma, these stochastic terms contribute an additional term to the equation for the composition of the coherences:

$$\frac{d}{dt}\left[\rho_{12}(t)\, \rho_{21}(t)\right] = \ldots + \gamma\, |\mathscr{D}(t)|^2.$$

To reproduce the initial linear growth, the function $|\mathscr{D}(t)|^2$ must remain near unity during the early stages and then rapidly drop to zero around the delay time.

A suitable candidate for this function is the excited-state population, which remains nearly constant at the beginning and then quickly decays to zero. Therefore, our *guess* for $\mathscr{D}(t)$ is:

$$\mathscr{D}(t) = \sqrt{\rho_{22}(t)}\,.$$

This approach is phenomenological, and the effectiveness of this choice cannot be guaranteed a priori. The equations governing the dynamics become:

$$\frac{d\rho_{11}(t)}{dt} = \gamma \rho_{22}(t) + \gamma(N-1)\rho_{12}(t)\, \rho_{21}(t), \tag{I.32a}$$

$$\frac{d\rho_{12}(t)}{dt} = -\frac{\gamma}{2}\rho_{12}(t) + \frac{\gamma(N-1)}{2}\, \rho_{12}(t)\, [\rho_{22}(t) - \rho_{11}(t)] + \sqrt{\gamma \rho_{22}(t)}\, \mathrm{S}(t), \tag{I.32b}$$

$$\frac{d\rho_{21}(t)}{dt} = -\frac{\gamma}{2}\rho_{21}(t) + \frac{\gamma(N-1)}{2}\,\rho_{21}(t)\,[\rho_{22}(t) - \rho_{11}(t)] + \sqrt{\gamma\rho_{22}(t)}\;\mathrm{S}^*(t), \tag{I.32c}$$

$$\frac{d\rho_{22}(t)}{dt} = -\gamma\rho_{22}(t) - \gamma(N-1)\,\rho_{12}(t)\,\rho_{21}(t). \tag{I.32d}$$

Only two variables are independent since $\rho_{21}(t) = \rho_{12}^*(t)$ and $\rho_{11}(t) + \rho_{22}(t) = 1$. The initial conditions $\rho_{ij}(0)$ are deterministic, with $\rho_{22}(0) = 1$ and $\rho_{12}(0) = \rho_{21}(0) = 0$.

Figure I.3 illustrates the simulation results. Remarkably, the agreement with the exact solution is excellent in panels (b)-(c) and surpasses the results shown in Fig. I.2. Notably, in Fig. I.3 (a), the excited-state population can dip below zero in individual realizations. For a small number of atoms (around $N = 10$, not shown in the figure), even the average probability can drop below zero.

This approach successfully reproduces the dynamics for instantaneously excited two-level atoms. The approximation relies heavily on the assumption that the noise terms are significant only during the initial stage. However, realistic scenarios require the inclusion of pumping, additional dissipation channels, multiple polarizations, and lasing between multiple levels. Because these noise terms are introduced heuristically rather than derived from first principles, their effectiveness in other scenarios is uncertain.

3 Conclusion: Limitations and Outlook

To conclude this chapter, we test the system of phenomenological stochastic equations (I.32) for incoherently pumped, identical atoms with two lasing transitions and dissipation, as illustrated in Fig. I.4 (a). The atoms begin in the state $|0\rangle$ and are subsequently excited to the state $|2\rangle$. The excitation process is modeled via the following Lindblad operator:

$$\mathcal{L}_{0\to2}[\hat{\rho}(t)] = \frac{J_0(t)}{2}\sum_{\mu=1}^{N}\{2\hat{\sigma}_{\mu,20}\,\hat{\rho}(t)\,\hat{\sigma}_{\mu,02} - \hat{\sigma}_{\mu,00}\,\hat{\rho}(t) - \hat{\rho}(t)\,\hat{\sigma}_{\mu,00}\}.$$

Note that this Lindblad operator is symmetrized over the atomic labels, meaning it does not distinguish between particles. The pump flux $J_0(t)$ is modeled with a Gaussian envelope:

$$J_0(t) = \frac{I_p}{\sqrt{2\pi\tau^2}}\exp\Big[-\frac{(t-t_0)^2}{2\tau^2}\Big],$$

where t_0 signifies the time of the peak, τ denotes the pulse duration, and I_p corresponds to the pulse area.

The excited state can relax either through a radiative transition to the state $|1\rangle$, governed by Eq. (I.23), or via nonradiative decay to the state $|3\rangle$, described by the Lindblad operator:

$$\mathcal{L}_{2\to3}[\hat{\rho}(t)] = \frac{\Gamma}{2}\sum_{\mu=1}^{N}\{2\hat{\sigma}_{\mu,32}\,\hat{\rho}(t)\,\hat{\sigma}_{\mu,23} - \hat{\sigma}_{\mu,22}\,\hat{\rho}(t) - \hat{\rho}(t)\,\hat{\sigma}_{\mu,22}\}.$$

This Lindblad operator also preserves permutation symmetry, as it does not distinguish between particles.

The master equation thus incorporates three contributions:

$$\frac{d\hat{\rho}(t)}{dt} = \mathcal{L}_{0\to2}[\hat{\rho}(t)] + \mathcal{L}_{2\to3}[\hat{\rho}(t)] + \gamma\hat{J}_{12}\,\hat{\rho}(t)\,\hat{J}_{21} - \frac{\gamma}{2}\hat{J}_{21}\,\hat{J}_{12}\,\hat{\rho}(t) - \frac{\gamma}{2}\hat{\rho}(t)\,\hat{J}_{21}\,\hat{J}_{12}. \tag{I.33}$$

The Liouvillian is permutation-invariant. As a result, if the system starts in a permutationally invariant state, this symmetry is preserved. However, the presence of Lindblad operators precludes describing the dynamics solely in terms of fully symmetric Dicke states, even though permutation symmetry is preserved. *This requires the development of a more general method that accounts for the symmetry while accommodating the dissipative dynamics.* Chapter II of the dissertation is devoted to this method.

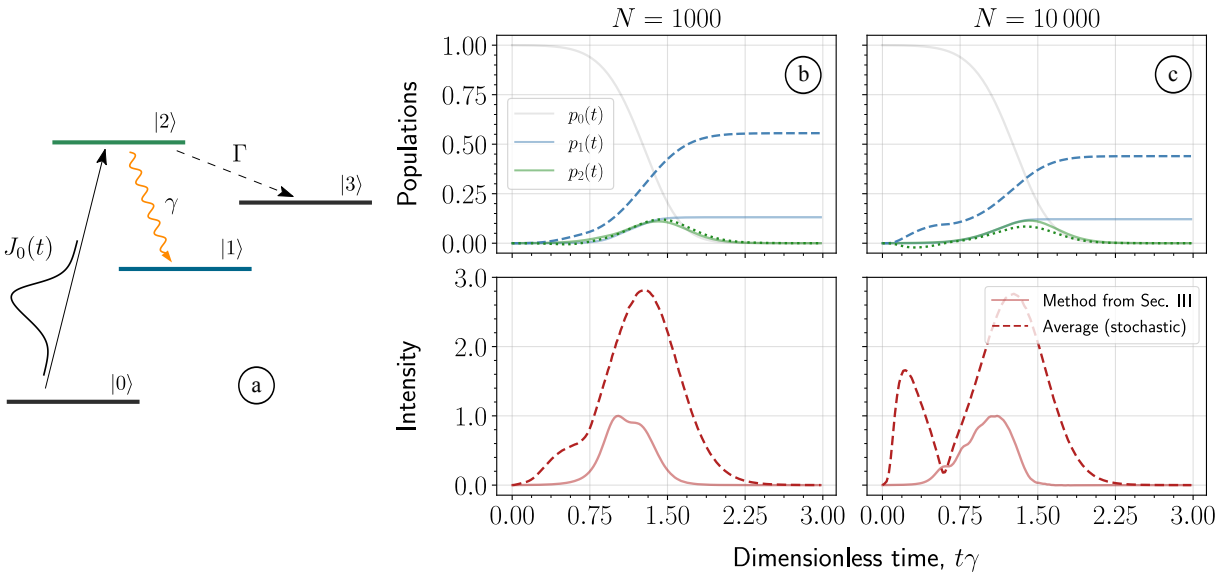

Figure I.4: Panel (a) illustrates the level structure of pumped emitters with dissipation. Panels (b) and (c) compare the solutions of the phenomenological stochastic equations (I.32) with the exact solutions for $N = 10^3$ and $N = 10^4$, respectively. Intensities are normalized to the maximum of the exact solution. Statistical averages are calculated using 10^5 stochastic realizations. We set the parameters $\Gamma = 10\gamma$, $I_p = 10$, $t_0 = 2/\gamma$, and $\tau = 0.5/\gamma$.

We derive the semiclassical equations corresponding to the master equation in Eq. (I.33), and supplement them by the phenomenological noise terms from Eqs. (I.32):

$$\frac{d\rho_{00}(t)}{dt} = -J_0(t)\,\rho_{00}(t), \tag{I.34a}$$

$$\frac{d\rho_{11}(t)}{dt} = \gamma\rho_{22}(t) + \gamma(N-1)\rho_{12}(t)\,\rho_{21}(t), \tag{I.34b}$$

$$\frac{d\rho_{12}(t)}{dt} = -\frac{(\gamma+\Gamma)}{2}\rho_{12}(t) + \frac{\gamma(N-1)}{2}\,\rho_{12}(t)\,[\rho_{22}(t)-\rho_{11}(t)] + \sqrt{\gamma\rho_{22}(t)}\,\mathrm{S}(t), \tag{I.34c}$$

$$\frac{d\rho_{21}(t)}{dt} = -\frac{(\gamma+\Gamma)}{2}\rho_{21}(t) + \frac{\gamma(N-1)}{2}\,\rho_{21}(t)\,[\rho_{22}(t)-\rho_{11}(t)] + \sqrt{\gamma\rho_{22}(t)}\,\mathrm{S}^*(t), \tag{I.34d}$$

$$\frac{d\rho_{22}(t)}{dt} = J_0(t)\,\rho_{00}(t) - (\gamma+\Gamma)\rho_{22}(t) - \gamma(N-1)\,\rho_{12}(t)\,\rho_{21}(t). \tag{I.34e}$$

and $\rho_{33}(t) = 1 - \rho_{00}(t) - \rho_{11}(t) - \rho_{22}(t)$.

The solutions to these equations are depicted with dashed lines in Fig. I.4 (b)-(c). For comparison, we also include the solution obtained using the method introduced in Chapter III, which will later be shown to be reliable. These results are represented by semi-transparent lines. Panels (b) and (c) demonstrate that the phenomenological noise terms yield entirely incorrect results. For $N = 10^4$, the average excited-state population even drops below zero. In both cases presented, the qualitative behavior is also incorrect. This issue cannot be easily resolved because the proposed noise terms were not derived from a systematic approach.

Based on these observations, this dissertation pursues the following goals:

1. Develop an efficient quantum-mechanical approach to solve quantum master equations with Lindblad operators *exactly*.

2. Establish a theoretical framework for deriving stochastic differential equations for such systems from *first principles*.

The results from Step 1 provide benchmarks for assessing the method developed in Step 2. This benchmarking is crucial, as the primary motivation for the stochastic approach is its use in cases where fully quantum-mechanical descriptions are computationally infeasible.

Chapter II

Second Quantization of Open Quantum Systems in Liouville Space

In this chapter, we explore permutation symmetry in Liouville space. While the findings have been published in Ref. [108], we present the formalism differently here and include additional examples of its application. This chapter begins with a brief introduction and an explanation of the motivation behind the research presented in Ref. [108].

In closed quantum systems of *identical* emitters, the Hilbert space framework and state vectors are typically sufficient for analysis. However, the inclusion of dissipation requires the use of the density matrix formalism [128], as open quantum systems cannot be fully described by standard Heisenberg or Schrödinger equations [129]. When the coupling to the environment is collective—identical for all emitters—the dynamics can be effectively represented using the basis of symmetric states [130].

The second quantization formalism offers a convenient means to construct and manipulate symmetric states, reducing the exponentially growing number of states to a polynomial in the number of emitters. However, when emitters interact with independent reservoirs—disrupting the collective nature of dissipation—the standard second-quantization framework becomes inapplicable.

The basis for identical two-level particles can be parameterized by two quantum numbers: the total angular momentum J and its projection M (or equivalently, the cooperation number, r, and m, as described in Ref. [1]). Fully symmetric states correspond to the maximum angular momentum $J = N/2$, where N is the number of particles. For collective interactions with the environment, it suffices to use symmetric states ($J = N/2$). However, systems with incoherent processes require the full basis, including antisymmetric states and states with mixed symmetry [131–135]. Due to the mixed symmetry, the standard second-quantization framework does not apply to such systems. Moreover, the generalization of the Dicke basis to many-level emitters is not straightforward.

Our work directly exploits permutation symmetry at the level of Liouville space and density matrices. Significant progress has already been made in this area. For example, Refs. [105–107] employed occupation numbers to parameterize a symmetric basis for density matrices. Furthermore, Refs. [112, 136] introduced bosonic superoperators in Liouville space via the Jordan-Schwinger representation [137]. In our study [108], we adopted the apparatus of second quantization [138], yielding a similar representation applicable to the same class of problems, including solutions to master equations with Lindblad operators [121, 128, 139–141].

In contrast to the recent study in Ref. [130], which also examined a system of identical many-level emitters using a second-quantization approach, our formalism accommodates incoherent processes and is not confined to the subspace of fully symmetric states.

The quantization of density matrices developed in our work should not be confused with approaches from Refs. [142–145]. These studies utilized the Fock state basis $|n\rangle$ for representing density matrices in the basis formed by $|n\rangle\langle m|$. This leads to a doubling of the degrees of freedom, as bra and ket components are independent. However, this approach imposes certain

symmetry restrictions and can address non-unitary dynamics in the form of collective dissipation or particle loss. In contrast, our approach applies second quantization directly to density matrices, preserving the number of emitters and incorporating incoherent processes.

This chapter is organized as follows. In Sec. 1, we present a step-by-step derivation of the second-quantization representation for density matrices, starting with establishing the isomorphism between density matrices and vectors in the extended Liouville-Hilbert space [110, 111]. For a concise summary of the essential points, readers may refer to Sec. 1.8.

Section 2 demonstrates the formalism's application in modeling various systems exhibiting cooperative emission. Specifically, we investigate two-level emitters (Sec. 2.1 and 2.2), three-level V emitters (Sec. 2.3), three-level Λ emitters (Sec. 2.4), and the Tavis-Cummings model (Sec. 2.5). These examples explore cases where emitters begin in statistically mixed states, are excited by incoherent pumping, or undergo incoherent dissipation. In many cases, ensembles evolve into dark many-body steady states, achieving equilibrium with their environments.

Section 3 outlines a numerical implementation of our formalism in `Julia`, complete with code details and performance benchmarks.

In Sec. 4, we provide supplementary sections discussing possible extensions and applications of the formalism.

The chapter concludes with Sec. 5, where we discuss the limitations of the formalism and introduce a potential extension toward a phase-space description, which is further elaborated in Chapter III.

1 General Formalism

We begin by introducing permutation symmetry and the framework of second quantization. Consider a system of particles, or emitters (e.g., atoms, ions, etc.), that can occupy M distinct states, as illustrated schematically in Fig. II.1 (a). The notation $|i\rangle_\mu$ indicates that the μ-th emitter is in state $|i\rangle$, where $i = 1, \ldots, M$. These states form the basis of a single-particle Hilbert space and are assumed to be eigenstates of the corresponding free emitter Hamiltonian (I.22).

The states of N particles are represented by vectors in an N-particle Hilbert space, constructed as a tensor product of N single-particle spaces. Consequently, the basis of this space comprises tensor products of all possible combinations of single-particle states. A general N-particle state, $|\psi\rangle$, can be expressed as a linear combination of these basis states:

$$|\psi\rangle = \sum_{\boldsymbol{i}} C_{\boldsymbol{i}} \, |i_1\rangle_1 \otimes |i_2\rangle_2 \otimes \ldots \otimes |i_N\rangle_N, \tag{II.1}$$

where $\boldsymbol{i} = (i_1, i_2, \ldots, i_N)$ is a multi-index. The summation over $\boldsymbol{i}$ is understood as a sum over all its components i_1, i_2, …, i_N. The coefficients $C_{\boldsymbol{i}}$ must satisfy normalization.

In general, the state in Eq. (II.1) describes distinguishable particles, as the multi-index $\boldsymbol{i}$ is an ordered sequence where each position specifies the state of a particular emitter. When emitters are identical, it means that exchanging any pair of them does not alter observable quantities. For example, this invariance can be ensured if any permutation of particles results in a global phase shift of the state in Eq. (II.1):

$$|\psi\rangle \longrightarrow e^{i\phi} \, |\psi\rangle, \tag{II.2}$$

where $\phi = 0$ for symmetric states (bosons) and $\phi = \pi$ for antisymmetric states (fermions).[1] This dissertation does not specifically focus on bosons or fermions. Instead, we examine quantum emitters, often referred to as pseudospins, for which the collective states can exhibit mixed symmetry. The symmetry properties of such states cannot generally be characterized by a simple global phase shift.

[1] The cases $\phi = 0$ and $\phi = \pi$ imply that a double permutation leaves the state unchanged. However, in two-dimensional quantum materials, quasiparticles known as anyons [146] exhibit behavior where a double permutation introduces an uncompensated phase shift. In quantum-statistical terms, these particles obey neither Bose-Einstein nor Fermi-Dirac statistics. This dissertation does not address such quasiparticles.

The indistinguishability of particles implies that measurement outcomes must remain unchanged under particle permutations. Since identical particles cannot be distinguished by any experiment, only symmetric operators—those invariant under particle label exchange—can represent observables. Consequently, the measurement outcome of an observable, represented by a symmetric operator $\hat{\mathcal{O}}$, must remain invariant under particle exchange:

$$\langle\psi|\hat{\mathcal{O}}|\psi\rangle \longrightarrow \langle\psi|\hat{\mathcal{O}}|\psi\rangle.$$

As a result, the system's density matrix $|\psi\rangle\langle\psi|$ is symmetric. If the system begins in a permutationally invariant state, and this symmetry is preserved over time, then the density matrix always remains *symmetric*.

The density matrix formalism is particularly useful for describing quantum systems interacting with their environment under the Markovian approximation. The environment is typically modeled as a bath with an infinite number of degrees of freedom. Averaging over these degrees of freedom introduces effective dissipation, rendering the system open. As a result, the state of an open quantum system is generally not a pure state.

Consider a composite closed quantum system comprising identical emitters and their environment. The general state of this system can be seen as an extension of Eq. (II.1):

$$|\psi'\rangle = \sum_{\boldsymbol{i},\text{env}} C_{\boldsymbol{i},\text{env}}\ |i_1\rangle_1 \otimes |i_2\rangle_2 \otimes \ldots \otimes |i_N\rangle_N \otimes |\text{env}\rangle, \tag{II.3}$$

where $|\text{env}\rangle$ denotes the state of the environment, and the summation over "env" accounts for all environmental degrees of freedom. This expansion suggests that all emitters collectively interact with the same environment.

In many applications, providing a detailed description of environmental dynamics is either infeasible or unnecessary. Instead, the environmental degrees of freedom can be excluded by tracing over them, yielding the reduced density matrix for the emitters:

$$\hat{\rho} = \text{Tr}_{\text{env.}}|\psi'\rangle\langle\psi'| = \sum_{\boldsymbol{i},\boldsymbol{j}} \overline{C_{\boldsymbol{ij}}}\ \hat{\sigma}_{1,i_1j_1}\ \hat{\sigma}_{2,i_2j_2}\ \ldots\ \hat{\sigma}_{N,i_Nj_N}. \tag{II.4}$$

Here, the multi-indices are $\boldsymbol{i} = (i_1, i_2, \ldots, i_N)$ and $\boldsymbol{j} = (j_1, j_2, \ldots, j_N)$, and $\hat{\sigma}_{\mu,ij} = |i\rangle_\mu\langle j|_\mu$. The decomposition coefficients $\overline{C_{\boldsymbol{ij}}}$ are averages over the environmental degrees of freedom:

$$\overline{C_{\boldsymbol{ij}}} = \sum_{\text{env}} C_{\boldsymbol{i},\text{env}}\, C^*_{\boldsymbol{j},\text{env}}.$$

Under the Markovian approximation, the reduced density matrix can be shown to evolve according to a quantum master equation in Lindblad form [128, 139].

We assume that, after averaging over the environmental degrees of freedom, the effective interaction with the environment does not distinguish between particles, thereby preserving permutation symmetry. A more general scenario might involve particles interacting with independent reservoirs, but if all particles interact identically with their respective environments, permutation symmetry is restored after averaging.

The density matrix in Eq. (II.4) generally describes a mixed state, where the ensemble's statistical properties are no longer evident. Such a density matrix can represent a statistical mixture of symmetric and antisymmetric states, making it impossible to assign specific quantum statistics to the ensemble. For example, consider the following mixed state of two pseudospin-1/2 particles:

$$\frac{|\uparrow\downarrow\rangle\,\langle\uparrow\downarrow| + |\downarrow\uparrow\rangle\,\langle\downarrow\uparrow|}{2} \equiv \frac{1}{2}\,\frac{|\uparrow\downarrow\rangle + |\downarrow\uparrow\rangle}{\sqrt{2}}\,\frac{\langle\uparrow\downarrow| + \langle\downarrow\uparrow|}{\sqrt{2}} + \frac{1}{2}\,\frac{|\uparrow\downarrow\rangle - |\downarrow\uparrow\rangle}{\sqrt{2}}\,\frac{\langle\uparrow\downarrow| - \langle\downarrow\uparrow|}{\sqrt{2}}.$$

This density matrix is a statistical mixture of the symmetric and antisymmetric states.

Ensembles of N two-level pseudospins are described by angular momentum states $|J, M\rangle$, which can exhibit mixed statistics. As a result, the dynamics of an open quantum system is

not restricted to a subspace with a specific symmetry, making it impossible to fully describe the system using only bosonic or fermionic states and operators.

Nevertheless, it has been established that density matrices of identical emitters are always symmetric. By defining an isomorphism between Liouville space and Hilbert space, density matrices can be treated as analogous to symmetric state vectors [110, 111]. This approach allows us to adapt the bosonic second-quantization approach to symmetric density matrices, resulting in a general theory applicable to open systems of emitters.

The next subsection, Sec. 1.1, reviews the basics of second quantization for bosons in Hilbert space. Readers already familiar with this material may skip it. The discussion on Liouville-Hilbert space begins in Sec. 1.2, with a concise summary provided in Sec. 1.8.

1.1 Second Quantization of Bosons in Hilbert Space

When the state vector in Eq. (II.1) describes a system of bosons, the phase shift in Eq. (II.2) is zero ($\phi = 0$). Consequently, the expansion coefficients are symmetric under the exchange of any two particles:

$$C_{i_1 \ldots i_\mu \ldots i_\nu \ldots i_N} \equiv C_{i_1 \ldots i_\nu \ldots i_\mu \ldots i_N}.$$

These coefficients depend only on the values of the indices $i_1, \ldots, i_N$, not their order. Therefore, the decomposition coefficients can be parameterized by occupation numbers—the number of particles in each single-particle state.

For any sequence of indices $(i_1, \ldots, i_N)$, we count the number of times each state $|i\rangle$ appears, denoting these counts as n_i. The corresponding decomposition coefficient $C_{i_1 \ldots i_N}$ can then be parameterized as:

$$C_{i_1 \ldots i_N} \sim C(\{n_i\}),$$

where $\{n_i\}$ is an ordered set of occupation numbers $\{n_1, n_2, \ldots, n_M\}$. We also introduce a new basis of symmetric states parameterized by these numbers, denoted as $|\{n_i\}\rangle$.

This basis is constructed by starting with an arbitrary product state:

$$|i_1\rangle_1 \otimes \ldots \otimes |i_N\rangle_N,$$

counting the corresponding occupation numbers $\{n_i\}$, and summing over all possible permutations of the labels $i_1, \ldots, i_N$. After normalization, the resulting superposition becomes $|\{n_i\}\rangle$. This symmetrization can be conveniently expressed by summing over N additional indices μ_1, $\ldots$, μ_N, which don't overlap and range between 1 and N:

$$|\{n_i\}\rangle = \sqrt{\frac{1}{N! \prod_i n_i!}} \sum_{\mu_1 \neq \ldots \neq \mu_N} |i_{\mu_1}\rangle_1 \otimes \ldots \otimes |i_{\mu_N}\rangle_N. \tag{II.5}$$

Any symmetric state vector can be represented in this basis. The total number of basis states is determined by the number of ways N identical objects (particles) can be distributed among M bins (states), as illustrated schematically in Fig. II.1 (b). Each distribution corresponds to a specific occupation-number state.

After representing symmetric states in the occupation-number basis, we can examine the action of symmetric operators on these states. Consider a symmetric single-particle operator of the form:

$$\hat{J}_{pq} = \sum_{\mu=1}^{N} \hat{\sigma}_{\mu,pq}, \tag{II.6}$$

with $\hat{\sigma}_{\mu,pq} = |p\rangle_\mu \langle q|_\mu$. Let's find how this operator transforms the basis vectors. When $p = q$, we have:

$$\hat{J}_{pp} |\{n_i\}\rangle = n_p |\{n_i\}\rangle.$$

This shows that this operator counts the number of particles in state p, and the occupation-number states are its eigenvectors.

When the indices are distinct, $p \neq q$, the collective operator acts as follows:

$$\hat{J}_{pq} \, |\{n_i\}\rangle = \sqrt{n_q(n_p+1)} \, |\{\ldots, n_q - 1, \ldots, n_p + 1, \ldots\}\rangle.$$

This transformation corresponds to the annihilation of one particle in state q and the creation of one particle in state p. This interpretation leads to the introduction of bosonic annihilation and creation operators, $\hat{b}_p$ and $\hat{b}_p^\dagger$, which change occupation numbers according to:

$$\hat{b}_p \, |\{n_i\}\rangle = \sqrt{n_p} \, |\{\ldots, n_p - 1, \ldots\}\rangle, \qquad \hat{b}_p^\dagger \, |\{n_i\}\rangle = \sqrt{n_p + 1} \, |\{\ldots, n_p + 1, \ldots\}\rangle, \tag{II.7}$$

and satisfy the commutation relations $[\hat{b}_p, \, \hat{b}_q^\dagger] = \delta_{pq}$.

As a result, operator $\hat{J}_{pq}$, when applied to symmetric states, can be bosonized as follows:

$$\hat{J}_{pq} = \hat{b}_p^\dagger \, \hat{b}_q. \tag{II.8}$$

This bosonization preserves the commutation relations of $\hat{J}_{pq}$. Since the total number of particles N is fixed, the sum $\hat{n}_1 + \hat{n}_2 + \ldots + \hat{n}_M$, where $\hat{n}_p = \hat{b}_p^\dagger \, \hat{b}_p$, is also constant and equals N. In a sense, such system of identical emitters can be described as M harmonic oscillators sharing N excitations [130]. This representation is known as the Schwinger representation, and the corresponding bosonization of symmetric operators as the Jordan-Schwinger transformation [57, 137, 147–153].

It is important to note that this description is complete only if the system's state remains within the subspace of symmetric states. If the system is prepared in a statistical mixture of states with mixed symmetry or undergoes incoherent processes, this representation may fail to fully capture its dynamics. The formulation of second quantization in Liouville space overcomes these limitations, as discussed in the next section.

1.2 Occupation-Number Basis in Liouville-Hilbert Space

In this section, we adapt the principles of bosonic second quantization, outlined in the previous section, to symmetric density matrices.

An analogy with bosons becomes apparent once we establish an isomorphism between the Liouville space and an extended Hilbert space [110, 111]. To clarify this isomorphism, we begin with the simplest case: a single two-level particle.

For a single two-level particle, the state vectors reside in a two-dimensional Hilbert space and can be represented as two-component column vectors. In Liouville space—the Cartesian product of Hilbert space and its dual—the basis consists of 2×2 matrices denoted by $\hat{\sigma}_{ij} = |i\rangle\langle j|$.

Since finite-dimensional vector spaces of the same dimension are isomorphic, a one-to-one correspondence exists between the space of 2×2 matrices in Liouville space and a four-dimensional vector space. For a single two-level particle, we define a specific vectorization map from the Liouville space to a four-dimensional vector space as follows:

$$\hat{\sigma}_{11} = \begin{pmatrix} 1 & 0 \\ 0 & 0 \end{pmatrix} \longleftrightarrow \begin{pmatrix} 1 \\ 0 \\ 0 \\ 0 \end{pmatrix} \equiv |11\rangle\!\rangle, \qquad \hat{\sigma}_{12} = \begin{pmatrix} 0 & 1 \\ 0 & 0 \end{pmatrix} \longleftrightarrow \begin{pmatrix} 0 \\ 1 \\ 0 \\ 0 \end{pmatrix} \equiv |12\rangle\!\rangle,$$

$$\hat{\sigma}_{21} = \begin{pmatrix} 0 & 0 \\ 1 & 0 \end{pmatrix} \longleftrightarrow \begin{pmatrix} 0 \\ 0 \\ 1 \\ 0 \end{pmatrix} \equiv |21\rangle\!\rangle, \qquad \hat{\sigma}_{22} = \begin{pmatrix} 0 & 0 \\ 0 & 1 \end{pmatrix} \longleftrightarrow \begin{pmatrix} 0 \\ 0 \\ 0 \\ 1 \end{pmatrix} \equiv |22\rangle\!\rangle.$$

The basis vectors in this representation are denoted $|ij\rangle\!\rangle$ and are commonly referred to as *superkets* [110–112, 141, 154].

The scalar product in the space of superkets is defined using the dual space of *superbras*, $\langle\!\langle pq|$, as:

$$\langle\!\langle pq|ij\rangle\!\rangle = \delta_{pi} \, \delta_{qj}. \tag{II.9}$$

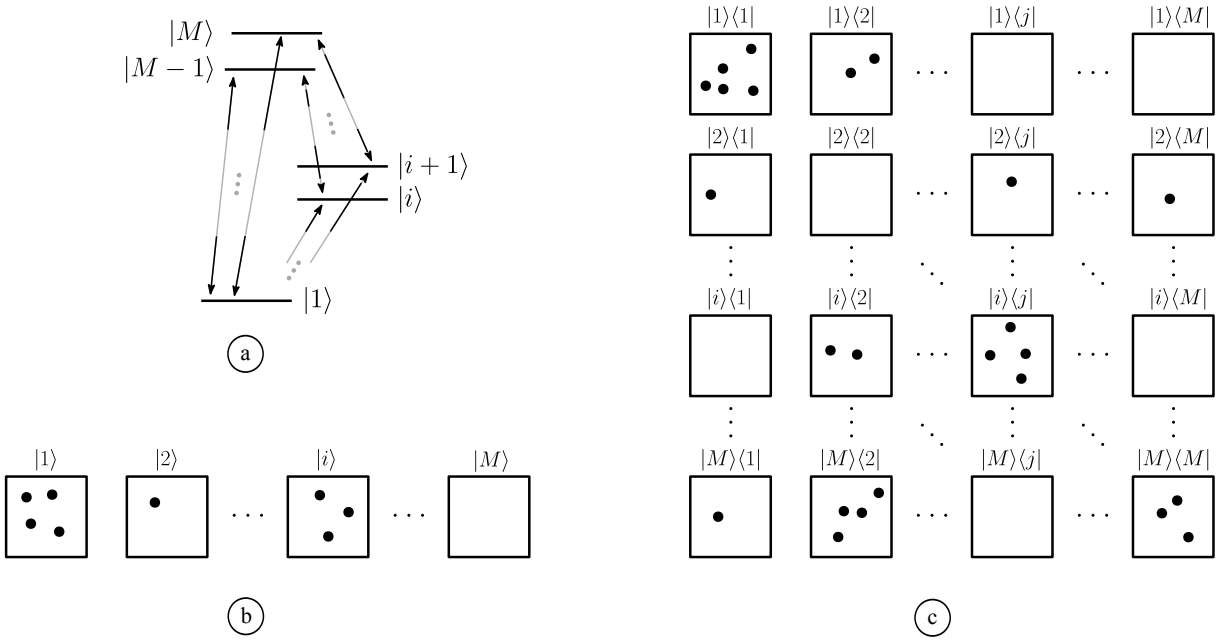

Figure II.1: Symmetric states of ensembles of M-level identical particles, schematically depicted in panel (a). Panel (b) visualizes the states in Eq. (II.5), which are constructed by distributing N identical particles (objects) across M states (bins). Panel (c) depicts the superstates in Eq. (II.11), where N identical objects (particles) are distributed among M^2 bins (superstates).

With these constructs, the vector representation of Liouville space can be identified with an extended Hilbert space [154], which we call the *Liouville-Hilbert space*.

To generalize this framework to M-level systems, the index range is simply extended to M. Multi-particle superstates are constructed using a tensor-product basis of superkets, analogous to state vectors in Hilbert space, as shown in Eq. (II.1).

The density matrix $\hat{\rho}$ from Eq. (II.4), which describes N identical M-level particles, is represented as a supervector $|\rho\rangle\!\rangle$ in the Liouville-Hilbert space:

$$|\rho\rangle\!\rangle = \sum_{\boldsymbol{i},\boldsymbol{j}} C_{\boldsymbol{ij}}\, |i_1 j_1\rangle\!\rangle_1 \otimes |i_2 j_2\rangle\!\rangle_2 \otimes \ldots \otimes |i_N j_N\rangle\!\rangle_N. \tag{II.10}$$

By assumption, the coefficients $C_{\boldsymbol{ij}}$ are symmetric under the exchange of any two particles. Since each particle is represented by a pair of indices ij, this symmetry can be expressed as:

$$C_{i_1 j_1 \ldots i_\mu j_\mu \ldots i_\nu j_\nu \ldots i_N j_N} \equiv C_{i_1 j_1 \ldots i_\nu j_\nu \ldots i_\mu j_\mu \ldots i_N j_N}.$$

This property implies that the coefficients $C_{\boldsymbol{ij}}$ depend only on the number of times each superket $|ij\rangle\!\rangle$ appears in the expansion. Let n_{ij} denote the number of occurrences of each superket $|ij\rangle\!\rangle$. The decomposition coefficients can then be parameterized by these *occupation numbers*:

$$C_{\boldsymbol{ij}} \sim \rho(\{n_{ij}\}),$$

where $\{n_{ij}\}$ is the ordered set of M^2 occupation numbers $\{n_{11}, n_{12}, \ldots, n_{1M}, n_{21}, \ldots, n_{MM}\}$.

The occupation-number basis, parameterized by the numbers $\{n_{ij}\}$, is constructed analogously to Eq. (II.5). For any sequence of superket indices $i_1 j_1$, …, $i_N j_N$, we count how often each pair ij appears, denoted n_{ij}. The basis element $|\{n_{ij}\}\rangle\!\rangle$ is then formed by summing over all tensor-product superstates corresponding to the set $\{n_{ij}\}$:

$$|\{n_{ij}\}\rangle\!\rangle = \sqrt{\frac{1}{N! \prod_{i,j} n_{ij}!}} \sum_{\mu_1 \neq \ldots \neq \mu_N} |i_{\mu_1} j_{\mu_1}\rangle\!\rangle_1 \otimes \ldots \otimes |i_{\mu_N} j_{\mu_N}\rangle\!\rangle_N. \tag{II.11}$$

This construction can be interpreted as distributing N identical objects among M^2 bins, as illustrated in Fig. II.1 (c). The total number of basis superstates corresponds to the number of possible distributions, given by:

$$\binom{N+M^2-1}{N} = \frac{(N+M^2-1)!}{N!\,(M^2-1)!}. \tag{II.12}$$

This reduction from exponential to polynomial complexity has been explored in numerous studies [105–107, 112, 131–133, 135].

Any symmetric density matrix can be expressed in the symmetric basis defined in Eq. (II.11). In essence, the bosonization strategy outlined in this section extends the results of Sec. 1.1 by treating indices (i) as two-component multi-indices (ij). However, the interpretation of the expansion coefficients $\rho(\{n_{ij}\})$ and the procedure for calculating expectation values differ significantly, because the density matrix is a statistical object.

1.3 Density Matrix Representation

Expectation values of observables are determined by taking the trace of the product of the corresponding operator and the density matrix. This process is straightforward when density matrices are treated as operators in the traditional Hilbert space. However, extending this operation to the Liouville-Hilbert space requires additional clarification.

In the supervector representation, when a symmetric operator acts on a basis element $|\{n_{ij}\}\rangle\!\rangle$, the resulting state can still be expressed within this basis. Consequently, calculating the expectation values of observables reduces to computing the trace of the basis states $|\{n_{ij}\}\rangle\!\rangle$.

The superstates $|\{n_{ij}\}\rangle\!\rangle$ are constructed from superkets (Eq. (II.11)), which are vectorized representations of the σ-operators. Assuming the trace should be independent of the representation, we have:

$$\mathrm{Tr}\left[|ij\rangle\!\rangle\right] \equiv \mathrm{Tr}\,\hat{\sigma}_{ij} = \langle j|i\rangle = \delta_{ij}.$$

Thus, the trace of a many-particle tensor-product superstate is zero if at least one superket $|ij\rangle\!\rangle$ has distinct indices, $i \neq j$. Similarly, the trace of $|\{n_{ij}\}\rangle\!\rangle$ is zero if any $n_{ij} \neq 0$ for $i \neq j$. Otherwise, if all numbers with distinct indices are zero, the trace is:

$$\mathrm{Tr}\big[|\{n_{ij}\}\rangle\!\rangle\big] = \sqrt{\frac{N!}{\prod_i n_{ii}!}}, \qquad (\text{all } n_{i\neq j} = 0). \tag{II.13}$$

This factor appears in all expectation value calculations. To simplify expressions, we incorporate its inverse into the expansion of density matrices in the occupation-number basis:

$$|\rho\rangle\!\rangle = \sum_{\{n_{ij}\}} \sqrt{\frac{\prod_{i,j} n_{ij}!}{N!}}\, \rho(\{n_{ij}\})\, |\{n_{ij}\}\rangle\!\rangle. \tag{II.14}$$

The sum is taken over all possible sets of occupation numbers that sum to N. This representation is analogous to that found in Refs. [105–107], which also incorporate this multinomial factor for numerical convenience and more compact expressions.

In this representation, the trace of the density matrix simplifies to the sum of its decomposition coefficients:

$$\mathrm{Tr}\left[|\rho\rangle\!\rangle\right] = \sum_{\{n_{ii}\}} \rho(\{n_{ii}\}) = 1,$$

where the summation includes only "diagonal" occupations with $n_{i\neq j} = 0$. Such sets are denoted as $\{n_{ii}\}$. Coefficients $\rho(\{n_{ii}\})$ represent the joint probabilities of finding n_{11} particles in state $|1\rangle$, n_{22} in state $|2\rangle$, and so forth. While the trace of a density matrix is always one, some applications introduce incomplete density matrices—where not all states are accounted for explicitly. In such cases, their trace may be less than one. However, in this dissertation, we do not consider such cases.

Not every supervector expressed in the form of Eq. (II.14) corresponds to a physical density matrix. For a supervector to qualify as a density matrix, it must meet additional criteria.

First, it must represent a Hermitian operator. In the occupation-number representation, this requirement translates to:

$$\rho^*(\{n_{ij}\}) = \rho(\{n_{ji}\}),$$

where $\{n_{ji}\}$ denotes the set $\{m_{ij}\}$, with $m_{ij} = n_{ji}$. This constraint reduces the number of basis elements required to construct physical states. For instance, the total number of basis elements for two-level emitters, as specified in (II.12), is:

$$\frac{(N+1)(N+2)(N+3)}{3!} \sim \frac{N^3}{3!}.$$

When the Hermiticity condition is considered, this number decreases to:

$$\left[\frac{(N+2)(N+4)(2N+3)}{4!}\right] \sim \frac{1}{2}\frac{N^3}{3!},$$

which is about half of the original number of basis elements. Here, $[A/B]$ denotes the integer division of A by B.

Furthermore, physical density matrices must have non-negative eigenvalues. Determining these eigenvalues within the Liouville-Hilbert space is not straightforward. To avoid possible complications, we assume the system begins in a physical state and evolves according to master equations that maintain the positive semidefiniteness of the density matrix.

1.4 Examples of States

Let us examine a few examples of quantum states and their representations as given by Eq. (II.14), starting with a density matrix describing uncorrelated emitters sharing the same state:

$$\hat{\rho} = \prod_{\mu=1}^{N} \left\{ \sum_{p,q=1}^{M} \rho_{pq}\, \hat{\sigma}_{\mu,pq} \right\}. \tag{II.15}$$

The parameters ρ_{pq} must satisfy the following conditions: $\rho^*_{pq} = \rho_{qp}$, $\sum_i \rho_{ii} = 1$, and the matrix formed by ρ_{pq} must have non-negative eigenvalues. These conditions ensure that ρ_{pq} represents a single-particle reduced density matrix. Using the multinomial theorem, we can derive the occupation-number representation (II.14) for this state:

$$\rho(\{n_{ij}\}) = N! \prod_{p,q=1}^{M} \frac{(\rho_{pq})^{n_{pq}}}{n_{pq}!}, \tag{II.16}$$

which resembles a multinomial distribution parameterized by ρ_{pq}.

To illustrate states with a non-trivial tensor structure, consider the Dicke states of two-level emitters, denoted by $|L\rangle$. The state $|L\rangle$ is symmetric, with L atoms in the excited state and $N-L$ atoms in the ground state. The corresponding density matrix is denoted by $|L\rangle\!\rangle = |L\rangle\langle L|$. In the occupation-number representation, this density matrix is expressed as:

$$|L\rangle\!\rangle = \sum_{\{n_{ij}\}} \sqrt{\frac{\prod_{i,j} n_{ij}!}{N!}}\, \rho_L(\{n_{ij}\})\, |\{n_{ij}\}\rangle\!\rangle.$$

The coefficients $\rho_L(\{n_{ij}\})$ are given by:

$$\rho_L(\{n_{ij}\}) = \frac{(N-L)!\, L!}{n_{11}!\, n_{12}!\, n_{21}!\, n_{22}!}, \tag{II.17}$$

with the following two constraints: $n_{22} - n_{11} = 2L - N$ and $n_{12} = n_{21}$. These coefficients are zero unless both conditions are satisfied.

1.5 Operators in Liouville-Hilbert space

At the beginning of Sec. 1.3, we briefly mentioned that symmetric operators possess a matrix representation in the Liouville-Hilbert space. The algebraic structure of operators acting on supervectors requires additional discussion.

Consider a single two-level particle. In Hilbert space, the algebra of operators is formed by the σ-operators, represented as 2×2 matrices. These operators act on 2×2 density matrices or two-dimensional state vectors. However, in the Liouville-Hilbert space, density matrices are represented as 4-dimensional supervectors. Consequently, the σ-operators must be represented not as 2×2 matrices but as 4×4 matrices.

Let us find the representation of the σ-operators in the Liouville-Hilbert space. To understand how they transform superkets, consider the following expression:

$$\hat{\sigma}_{pq}\,\hat{\sigma}_{ij} = \delta_{qi}\,\hat{\sigma}_{pj}.$$

We interpret the left-hand side as the action of the operator $\hat{\sigma}_{pq}$ on the basis element $|ij\rangle\!\rangle$, which results in the transformed basis element $|pj\rangle\!\rangle$ on the right-hand side:

$$\hat{\sigma}_{pq}\,|ij\rangle\!\rangle = \delta_{qi}\,|pj\rangle\!\rangle.$$

Here, the operator $\hat{\sigma}_{pq}$ acts as a 4×4 matrix on a 4-component supervector. For simplicity, we use the same notation for $\hat{\sigma}_{pq}$, relying on context to specify its algebraic properties.

From this, we can explicitly derive the matrix representation of each σ-operator in the Liouville-Hilbert space:

$$\hat{\sigma}_{11}\,|\rho\rangle\!\rangle = \left(\begin{array}{cc|cc} 1 & 0 & 0 & 0 \\ 0 & 1 & 0 & 0 \\ \hline 0 & 0 & 0 & 0 \\ 0 & 0 & 0 & 0 \end{array}\right)|\rho\rangle\!\rangle, \qquad \hat{\sigma}_{12}\,|\rho\rangle\!\rangle = \left(\begin{array}{cc|cc} 0 & 0 & 1 & 0 \\ 0 & 0 & 0 & 1 \\ \hline 0 & 0 & 0 & 0 \\ 0 & 0 & 0 & 0 \end{array}\right)|\rho\rangle\!\rangle,$$

$$\hat{\sigma}_{21}\,|\rho\rangle\!\rangle = \left(\begin{array}{cc|cc} 0 & 0 & 0 & 0 \\ 0 & 0 & 0 & 0 \\ \hline 1 & 0 & 0 & 0 \\ 0 & 1 & 0 & 0 \end{array}\right)|\rho\rangle\!\rangle, \qquad \hat{\sigma}_{22}\,|\rho\rangle\!\rangle = \left(\begin{array}{cc|cc} 0 & 0 & 0 & 0 \\ 0 & 0 & 0 & 0 \\ \hline 0 & 0 & 1 & 0 \\ 0 & 0 & 0 & 1 \end{array}\right)|\rho\rangle\!\rangle.$$

Vertical and horizontal lines have been added to highlight the block structure of these matrices.

The matrix representations above can be generalized to an M-level particle. Since the operator $\hat{\sigma}_{pq}$ transforms any supervector $|qt\rangle\!\rangle$ into $|pt\rangle\!\rangle$, we can express this transformation as:

$$\hat{\sigma}_{pq}\,|\rho\rangle\!\rangle = \sum_{t=1}^{M} |pt\rangle\!\rangle\langle\!\langle qt|\rho\rangle\!\rangle. \tag{II.18a}$$

The sum on the right-hand side defines the representation of this operator in the Liouville-Hilbert space.

Note that the operators considered in Eq. (II.18a) act only on the ket side of density matrices, specifically on the first index of the superkets, $|\overset{\downarrow}{i}j\rangle\!\rangle$.

To act on the bra side of density matrices, $|i\rangle\langle\overset{\downarrow}{j}|$, operators should be applied from the right. However, in supervector representation, all operators are conventionally applied from the left. Therefore, both bra and ket sides should be accessible from the left, meaning right-acting operators in Liouville space correspond to left-acting operators in Liouville-Hilbert space.

We denote an operator acting from the right with a superscript $^\intercal$:

$$\hat{\rho}\,\hat{\sigma}_{k\ell} \longleftrightarrow \hat{\sigma}^{\intercal}_{k\ell}\,|\rho\rangle\!\rangle.$$

Operators with the superscript $^\intercal$ affect the second index of supervectors, $\hat{\sigma}^{\intercal}_{k\ell}\,|i\overset{\downarrow}{j}\rangle\!\rangle$. Applying such an operator to the superket basis yields:

$$\hat{\sigma}^{\intercal}_{k\ell}\,|ij\rangle\!\rangle = \delta_{jk}\,|i\ell\rangle\!\rangle.$$

When the second index of the superket is k, it is transformed to ℓ, while the first index remains unchanged. This gives the following representation for these operators:

$$\hat{\sigma}^{\mathsf{T}}_{k\ell}\,|\rho\rangle\!\rangle = \sum_{s=1}^{M} |s\ell\rangle\!\rangle\langle\!\langle sk|\rho\rangle\!\rangle. \tag{II.18b}$$

Up to this point, we have discussed operators acting either from the left or from the right. However, operators can also be applied simultaneously from both sides. For example, consider the following transformation:

$$\hat{\sigma}_{pq}\,\hat{\rho}\,\hat{\sigma}_{k\ell} \longleftrightarrow \hat{\sigma}_{pq}\,\hat{\sigma}^{\mathsf{T}}_{k\ell}\,|\rho\rangle\!\rangle.$$

This transformation converts the supervector $|qk\rangle\!\rangle$ into $|p\ell\rangle\!\rangle$, allowing us to formulate the following representation:

$$\hat{\sigma}_{pq}\,\hat{\sigma}^{\mathsf{T}}_{k\ell}\,|\rho\rangle\!\rangle = |p\ell\rangle\!\rangle\langle\!\langle qk|\rho\rangle\!\rangle. \tag{II.18c}$$

Summing over $k = \ell$ or $p = q$ results in Eqs. (II.18a) and (II.18b), respectively.

The generalization to N particles is straightforward. Similar to symmetric operators in Hilbert space, any collective superoperator is constructed by symmetrizing over particle labels. For instance, the symmetrized form of the operator in Eq. (II.18c) for N particles is given by:

$$\sum_{\mu=1}^{N} \hat{\sigma}_{\mu,pq}\,\hat{\sigma}^{\mathsf{T}}_{\mu,k\ell}. \tag{II.19}$$

Summing over $k = \ell$ or $p = q$ yields the collective operator applied from the left or the right, respectively.

1.6 Bosonic Superoperators

Now, let us examine how symmetric superoperators transform the occupation-number basis, specifically how they modify the occupation numbers n_{ij}. Consider the collective operator from Eq. (II.19) with $p = q$ and $k = \ell$. It turns out that the supervectors $|\{n_{ij}\}\rangle\!\rangle$ are eigenstates of such operators:

$$\sum_{\mu=1}^{N} \hat{\sigma}_{\mu,pp}\,\hat{\sigma}^{\mathsf{T}}_{\mu,kk}\,|\{n_{ij}\}\rangle\!\rangle = n_{pk}\,|\{n_{ij}\}\rangle\!\rangle.$$

When this superoperator has distinct pairs of indices, $p \neq q$ and $k \neq \ell$, its action alters the occupation numbers as follows:

$$\sum_{\mu=1}^{N} \hat{\sigma}_{\mu,pq}\,\hat{\sigma}^{\mathsf{T}}_{\mu,k\ell}\,|\{n_{ij}\}\rangle\!\rangle = \sqrt{n_{qk}(n_{p\ell}+1)}\,|\{\ldots,n_{qk}-1,\ldots,n_{p\ell}+1,\ldots\}\rangle\!\rangle,$$

specifically, one particle in state $|qk\rangle\!\rangle$ is annihilated, while one particle in $|p\ell\rangle\!\rangle$ is created. The superoperators in Eq. (II.19) have been used in Refs. [105–107], where they are denoted as $\hat{\Gamma}^{k\ell}_{pq}$, to modify the occupation numbers for density matrices.

Drawing an analogy with bosonization in Hilbert space (see Eqs. (II.7)), we introduce annihilation and creation superoperators, $\hat{b}_{pq}$ and $\hat{b}^{\dagger}_{pq}$, defined by the relations:

$$\hat{b}_{pq}\,|\{n_{ij}\}\rangle\!\rangle = \sqrt{n_{pq}}\,|\{\ldots,n_{pq}-1,\ldots\}\rangle\!\rangle, \tag{II.20a}$$

$$\hat{b}^{\dagger}_{pq}\,|\{n_{ij}\}\rangle\!\rangle = \sqrt{n_{pq}+1}\,|\{\ldots,n_{pq}+1,\ldots\}\rangle\!\rangle, \tag{II.20b}$$

with commutation relations $[\hat{b}_{ij}, \hat{b}^{\dagger}_{pq}] = \delta_{ip}\,\delta_{jq}$. Analogous bosonic superoperators with double indices were introduced in Ref. [112] as a Jordan-Schwinger representation of the operators in Eq. (II.19), preserving their commutation relations.

All symmetric operators that act on symmetric density matrices can be expressed in terms of these bosonic superoperators. For instance, the collective operator (II.19) becomes:

$$\sum_{\mu=1}^{N} \hat{\sigma}_{\mu,pq}\, \hat{\sigma}^{\intercal}_{\mu,k\ell}\, |\rho\rangle\!\rangle = \hat{b}^{\dagger}_{p\ell}\, \hat{b}_{qk}\, |\rho\rangle\!\rangle. \tag{II.21}$$

By summing over the indices $k = \ell$ or $p = q$, we obtain the following representations for collective operators applied from the left and the right:

$$\hat{J}_{pq}\, |\rho\rangle\!\rangle = \sum_{t=1}^{M} \hat{b}^{\dagger}_{pt}\, \hat{b}_{qt}\, |\rho\rangle\!\rangle, \qquad \hat{J}^{\intercal}_{k\ell}\, |\rho\rangle\!\rangle = \sum_{s=1}^{M} \hat{b}^{\dagger}_{s\ell}\, \hat{b}_{sk}\, |\rho\rangle\!\rangle. \tag{II.22}$$

The total number of bosonic superoperators is M^2. Since the number of particles N is fixed, the sum of all operators $\hat{n}_{ij} = \hat{b}^{\dagger}_{ij}\, \hat{b}_{ij}$ remains constant and equals N. Effectively, after bosonization, an ensemble of N identical M-level particles is described as a system of M^2 harmonic oscillators collectively sharing N excitations.

The occupation-number basis can be constructed by applying creation superoperators to the vacuum superstate, denoted by $|\mathrm{vac}\rangle\!\rangle$:

$$|\{n_{ij}\}\rangle\!\rangle = \sum_{p,q=1}^{M} \frac{(\hat{b}^{\dagger}_{pq})^{n_{pq}}}{\sqrt{n_{pq}!}}\, |\mathrm{vac}\rangle\!\rangle,$$

where the numbers n_{pq} are taken from the set $\{n_{ij}\}$. The vacuum superstate does not correspond to any physical system but serves as a foundation for constructing physical states. For instance, density matrices of fermions, which are symmetric, can be constructed using creation superoperators. As shown in Sec. 4.1, a collective fermionic state can be generated by applying a determinant of creation superoperators to the vacuum superstate.

Using the vacuum superstate, we can construct a basis for any number of particles, naturally leading to the concept of a Fock space for density matrices. This Fock space differs, however, from the Liouville-Fock space commonly discussed in the context of second quantization [142–145]. In these references, bosonic and fermionic systems are second quantized in Hilbert space, and density matrices are then expressed using Fock states. In contrast, our method applies second quantization directly within the Liouville-Hilbert space, bypassing the intermediate step of second quantization in Hilbert space.

1.7 Representation of Many-Particle Operators

So far, we have considered only one-particle symmetric operators of the form given in Eq. (II.19). In general, a K-particle operator involves symmetrization over K particle labels. For simplicity, we will discuss operators applied from the left side only.

A symmetric K-particle operator, $\hat{\mathcal{O}}^{(K)}$, can be expressed as:

$$\hat{\mathcal{O}}^{(K)} = \sum_{\boldsymbol{p},\boldsymbol{q}} \mathcal{O}^{(K)}_{\boldsymbol{pq}} \sum_{\mu_1 \neq \ldots \neq \mu_K} \hat{\sigma}_{\mu_1,p_1q_1}\, \ldots\, \hat{\sigma}_{\mu_K,p_Kq_K}. \tag{II.23}$$

Here, $\boldsymbol{p} = (p_1, \ldots, p_K)$ and $\boldsymbol{q} = (q_1, \ldots, q_K)$ are K-element multi-indices, with $K \leq N$. The matrix elements $\mathcal{O}^{(K)}_{\boldsymbol{pq}}$ are identical for any selection of K distinct particle labels.

When the operator in Eq. (II.23) is applied to a symmetric density matrix $|\rho\rangle\!\rangle$, it can be expressed using bosonic superoperators as follows:

$$\hat{\mathcal{O}}^{(K)} |\rho\rangle\!\rangle = \sum_{\boldsymbol{p},\boldsymbol{q}} \mathcal{O}^{(K)}_{\boldsymbol{pq}} \sum_{\boldsymbol{t}} \hat{b}^{\dagger}_{p_1t_1}\, \ldots\, \hat{b}^{\dagger}_{p_Kt_K} \hat{b}_{q_1t_1}\, \ldots\, \hat{b}_{q_Kt_K}\, |\rho\rangle\!\rangle, \tag{II.24}$$

where $\boldsymbol{t} = (t_1, \ldots, t_K)$, and the bosonic superoperators are arranged in normal order.

Notably, there is an alternative interpretation of operators. Symmetric operators in the Liouville space can also be treated as supervectors in the Liouville-Hilbert space. This representation is discussed in Sec. 4.2.

1.8 Summary

In summary, we utilized the fact that density matrices for identical particles are always symmetric and constructed a second-quantized representation for such density matrices.

First, we established a one-to-one correspondence between density matrices, $\hat{\rho}$, and supervectors, $|\rho\rangle\!\rangle$, by leveraging the isomorphism between the vector space of $d \times d$ matrices and the space of d^2-dimensional vectors (Sections 1.2 and 1.5). We then introduced the occupation-number basis through an analogy with second quantization in Hilbert space. In Hilbert space, particles can occupy M states, $|i\rangle_\mu$, with occupation numbers n_i representing the occupancy of each state (Sec. 1.1). For density matrices, however, each particle is represented by a bra and a ket, $|i\rangle_\mu\langle j|_\mu$, leading to occupation numbers with two indices, n_{ij} (Sec. 1.2, Eq. (II.11)). These numbers parameterize the basis for symmetric density matrices, $|\{n_{ij}\}\rangle\!\rangle$:

$$\hat{\rho} \longleftrightarrow |\rho\rangle\!\rangle = \sum_{\{n_{ij}\}} \sqrt{\frac{\prod_{i,j} n_{ij}!}{N!}}\, \rho(\{n_{ij}\})\, |\{n_{ij}\}\rangle\!\rangle,$$

where the multinomial prefactor is chosen for convenience (Sec. 1.3 and Sec. 1.4, Eq. (II.14)). The summation is over all occupation-number sets whose elements sum to N.

Since symmetric operators do not distinguish between particles, their action on symmetric density matrices can be expressed as changes in occupation numbers (Sec. 1.6). These transformations can be conveniently written using bosonic superoperators, $\hat{b}_{ij}$ and $\hat{b}^\dagger_{ij}$, which satisfy the commutation relations $[\hat{b}_{ij}, \hat{b}^\dagger_{pq}] = \delta_{ip}\,\delta_{jq}$ and are defined by (Eq. (II.20)):

$$\begin{aligned}
\hat{b}_{pq}\, |\{n_{ij}\}\rangle\!\rangle &= \sqrt{n_{pq}}\, |\{\ldots, n_{pq}-1, \ldots\}\rangle\!\rangle, \\
\hat{b}^\dagger_{pq}\, |\{n_{ij}\}\rangle\!\rangle &= \sqrt{n_{pq}+1}\, |\{\ldots, n_{pq}+1, \ldots\}\rangle\!\rangle.
\end{aligned}$$

These operators enable the bosonization of superoperators acting on the density matrix. For example, the bosonized form of a general one-particle symmetric superoperator is (Eq. (II.21)):

$$\sum_{\mu=1}^{N} \hat{\sigma}_{\mu.pq}\, \hat{\rho}\, \hat{\sigma}_{\mu,k\ell} \longleftrightarrow \hat{b}^\dagger_{p\ell}\, \hat{b}_{qk}\, |\rho\rangle\!\rangle,$$

where $\hat{\sigma}_{\mu,ij} = |i\rangle_\mu\langle j|_\mu$ (Sections 1.6 and 1.7). The application of this formalism to cooperative emission will be explored in Sec. 2.

The framework can be generalized to systems with local symmetry. Consider a medium of emitters divided into smaller subregions, each sufficiently small for particles within it to be indistinguishable. By performing second quantization independently for each subregion, the occupation numbers and bosonic superoperators acquire additional indices to label the subregions. Similarly, the theory can be applied to a Bose-Hubbard model, where particles are localized at lattice sites and may hop between them. Both generalizations will be discussed in Sec. 4.3.

Although bosonic superoperators formally alter the particle number, conservation of the total particle number implies that annihilation operators always appear paired with creation operators. However, unpaired annihilation operators can still have physical significance, particularly in excluding particles by tracing out their degrees of freedom. When applied to a symmetric density matrix, the following operator:

$$\hat{T} = \frac{1}{\sqrt{\hat{N}+1}} \sum_{i=1}^{M} \hat{b}_{ii},$$

traces out a single particle, yielding a reduced density matrix with one particle excluded. This operator provides a convenient tool for analyzing the structure of the density matrix and probing correlations between particles. A detailed discussion, along with examples, will be presented in Sec. 4.4.

2 Applications

We now demonstrate how the derived formalism can be applied to solve quantum master equations. Typically, the density matrix satisfies a master equation of the form:

$$\frac{d\hat{\rho}(t)}{dt} = \mathcal{L}\big[\hat{\rho}(t)\big], \tag{II.25}$$

where $\mathcal{L}\big[\dots\big]$ denotes the Liouville operator. We do not represent it as a standard operator applied from the left, as it generally involves operators acting simultaneously from both the left and the right. The Liouvillian comprises a unitary part, represented by the Hamiltonian, and a non-unitary dissipative part. Under the Markovian approximation, incoherent processes are described by the general Lindblad operator:

$$\mathcal{L}_{\text{incoh.}}\big[\hat{\rho}(t)\big] = \sum_{i,j,p,q=1}^{M} \frac{\Gamma_{ijpq}}{2} \sum_{\mu=1}^{N} \big\{2\hat{\sigma}_{\mu,ij}\,\hat{\rho}(t)\,\hat{\sigma}_{\mu,qp} - \delta_{ip}\big[\hat{\sigma}_{\mu,qj}\,\hat{\rho}(t) + \hat{\rho}(t)\,\hat{\sigma}_{\mu,qj}\big]\big\}, \tag{II.26}$$

where Γ_{ijpq} represents interaction rates with the environment.

We assume the Liouvillian is symmetric and conserves the number of particles, meaning it commutes with both particle permutation and particle number operators. Consequently, it can be bosonized following Sections 1.6 and 1.7. After bosonization, the Liouvillian $\mathcal{L}\big[\dots\big]$ becomes a superoperator $\hat{\mathcal{L}}$ acting on $|\rho\rangle\!\rangle$ from the left. For example, the Lindbladian in Eq. (II.26) is bosonized as follows:

$$\hat{\mathcal{L}}_{\text{incoh.}}|\rho(t)\rangle\!\rangle = \sum_{i,j,p,q=1}^{M} \frac{\Gamma_{ijpq}}{2}\{2\hat{b}^{\dagger}_{ip}\,\hat{b}_{jq} - \delta_{ip}\sum_{t=1}^{M}(\hat{b}^{\dagger}_{qt}\,\hat{b}_{jt} + \hat{b}^{\dagger}_{tj}\,\hat{b}_{tq})\}|\rho(t)\rangle\!\rangle.$$

The density matrix is expressed as in Eq. (II.14), with time-dependent expansion coefficients $\rho(\{n_{ij}\},t)$. The quantum master equation generates a system of linear differential equations for these coefficients:

$$\frac{d\rho(\{n_{ij}\},t)}{dt} = \sum_{\{n'_{ij}\}} \sqrt{\frac{\prod_{i,j} n'_{ij}!}{\prod_{i,j} n_{ij}!}}\; \langle\!\langle\{n_{ij}\}|\hat{\mathcal{L}}\,|\{n'_{ij}\}\rangle\!\rangle\, \rho(\{n'_{ij}\},t)\ . \tag{II.27}$$

In other words, the equations are determined by the matrix elements of the Liouvillian in the occupation-number basis.

The master equation for collective emission of two-level atoms, discussed in Eq. (I.23) of Chapter I, was derived within the Born-Markov approximation. Similarly, a master equation can be derived for multilevel atoms with a two-band level structure, where the radiative states are divided into upper and lower states. The energy separation between bands is much larger than separations within each band, leading to nearly equal transition energies.

We introduce a characteristic radiative decay rate, γ, and account for polarization effects using effective transition dipole moments, $\overline{\mathbf{d}}_{ij}$. The magnitude of these vectors scales the corresponding decay rate. For example, for the $e \to g$ transition the rate is $\gamma|\overline{\mathbf{d}}_{ge}|^2$.

In this notation, the Born-Markov equation for collective emission from emitters with a two-band structure is [109]:

$$\mathcal{L}_{\text{coll.}}\big[\hat{\rho}(t)\big] = -i\sum_{i=1}^{M}\omega_i\big[\hat{\rho}(t),\,\hat{J}_{ii}\big] + \frac{\gamma}{2}\big[\hat{\mathbf{P}}^{(+)}\,\hat{\rho}(t),\,\hat{\mathbf{P}}^{(-)}\big] + \frac{\gamma}{2}\big[\hat{\mathbf{P}}^{(+)},\,\hat{\rho}(t)\,\hat{\mathbf{P}}^{(-)}\big], \tag{II.28}$$

where "coll." stands for collective, $\hbar\omega_i$ is the energy of the i-th atomic state, and $\hat{\mathbf{P}}^{(\pm)}$ are the positive- and negative-frequency components of the collective polarization operator:

$$\hat{\mathbf{P}}^{(+)} = \sum_{i,j=1}^{M}\overline{\mathbf{d}}_{i<j}\,\hat{J}_{ij}, \qquad\qquad \hat{\mathbf{P}}^{(-)} = \sum_{i,j=1}^{M}\overline{\mathbf{d}}_{i>j}\,\hat{J}_{ij}. \tag{II.29}$$

The summations are restricted by the conditions in the subscripts of the dipole moments.

Although the field appears absent in the master equation, its properties are encoded in the atomic variables. For example, the electric field operator is directly related to the atomic polarization operator:

$$\hat{\mathbf{E}}^{(\pm)} \sim \hat{\mathbf{P}}^{(\pm)}.$$

Up to a multiplier, the emission intensity along the $\mathbf{e}_\alpha$-axis is given by:

$$I_\alpha = \langle \hat{P}_\alpha^{(-)}\, \hat{P}_\alpha^{(+)} \rangle = \sum_{i,j,q=1}^{M} \overline{d}_{i<j}^{(\alpha)}\, \overline{d}_{q>i}^{(\alpha)}\, \langle \hat{b}_{qq}^\dagger\, \hat{b}_{jq} \rangle + \sum_{i,j,p,q=1}^{M} \overline{d}_{i<j}^{(\alpha)}\, \overline{d}_{q>p}^{(\alpha)}\, \langle \hat{b}_{qq}^\dagger\, \hat{b}_{ii}^\dagger\, \hat{b}_{pq}\, \hat{b}_{ji} \rangle. \tag{II.30}$$

Summing over all polarization components yields the total intensity.

The bosonized Liouvillian for the master equation in Eq. (II.28) is:

$$\begin{aligned} \hat{\mathcal{L}}_{\text{coll.}} = &-i \sum_{i,j=1}^{M} \omega_{ij}\, \hat{n}_{ij} + \gamma \sum_{i,j,p,q=1}^{M} \frac{\overline{\mathbf{d}}_{i<j} \cdot \overline{\mathbf{d}}_{q>p}}{2} \{ 2\hat{b}_{ip}^\dagger\, \hat{b}_{jq} - \delta_{ip} \sum_{t=1}^{M} (\hat{b}_{qt}^\dagger\, \hat{b}_{jt} + \hat{b}_{tj}^\dagger\, \hat{b}_{tq}) \} \\ &+\gamma \sum_{i,j,p,q=1}^{M} \frac{\overline{\mathbf{d}}_{i<j} \cdot \overline{\mathbf{d}}_{q>p}}{2} \sum_{s,t=1}^{M} \{ 2\hat{b}_{is}^\dagger\, \hat{b}_{tp}^\dagger\, \hat{b}_{js}\, \hat{b}_{tq} - \hat{b}_{qt}^\dagger\, \hat{b}_{is}^\dagger\, \hat{b}_{pt}\, \hat{b}_{js} - \hat{b}_{sj}^\dagger\, \hat{b}_{tp}^\dagger\, \hat{b}_{si}\, \hat{b}_{tq} \}. \end{aligned} \tag{II.31}$$

Here, $\hat{n}_{ij} = \hat{b}_{ij}^\dagger\, \hat{b}_{ij}$. The first term represents free oscillations, with $\omega_{ij} = \omega_i - \omega_j$. The second term describes spontaneous decay. The last term accounts for interactions between atoms, which vanish if $N = 1$.

In subsequent sections, we analyze collective emission in two-level atoms, systems with pumping, and three-level atoms (V and Λ configurations). Additionally, in Sec. 3, we provide an example of a numerical implementation.

2.1 Cooperative Emission of Two-Level Atoms

We begin with the simplest model: two-level atoms interacting collectively with a common environment. By rearranging terms in Eq. (II.31) and assuming $|\overline{\mathbf{d}}_{12}|^2 = 1$, we derive the collective Liouvillian for two-level atoms:[2]

$$\begin{aligned} \hat{\mathcal{L}}_{\text{coll.}} = &-i\omega_{21}(\hat{n}_{21} - \hat{n}_{12}) - \gamma \hat{n}_{22} - \frac{\gamma}{2}(\hat{n}_{21} + \hat{n}_{12})(\hat{n}_{11} + \hat{n}_{22} + 1) \\ &+\gamma(\hat{n}_{12} + \hat{n}_{21} + 1)\, \hat{b}_{11}^\dagger\, \hat{b}_{22} - \gamma(\hat{b}_{22}^\dagger - \hat{b}_{11}^\dagger)\, \hat{b}_{11}^\dagger\, \hat{b}_{21}\, \hat{b}_{12} + \gamma\, \hat{b}_{21}^\dagger\, \hat{b}_{12}^\dagger\, \hat{b}_{22}\, (\hat{b}_{22} - \hat{b}_{11}). \end{aligned} \tag{II.32}$$

The second and third terms determine the decay rate of the coefficient $\rho(\{n_{ij}\}, t)$. The fourth term describes population increase, while the last two terms capture the interplay between coherences (n_{12} and n_{21}) and populations (n_{11} and n_{22}) due to atomic interactions.

Notably, the numbers n_{12} and n_{21} change simultaneously, preserving $n_{12} - n_{21}$. In fact, the Liouvillian commutes with the corresponding operator:

$$[\hat{\mathcal{L}}_{\text{coll.}},\, \hat{n}_{12} - \hat{n}_{21}] = 0,$$

indicating that this quantity is an integral of motion.

The density matrix at $t = 0$ can be represented as a sum of contributions with different values of $n_{12} - n_{21}$. Because the master equation is linear, each contribution evolves independently, allowing for parallelization. However, processes such as interactions with an external classical field or the inclusion of counter-rotating terms can disrupt the conservation of $\hat{n}_{12} - \hat{n}_{21}$.

[2] The corresponding master equation in the occupation-number representation is given by:

$$\begin{aligned} \dot{\rho}(\{n_{11}, n_{12}, n_{21}, n_{22}\}, t) = &\Big\{ -i\omega_{21}(n_{21} - n_{12}) - \gamma n_{22} - \frac{\gamma}{2}(n_{21} + n_{12})\,(n_{11} + n_{22} + 1) \Big\} \rho(\{n_{11}, n_{12}, n_{21}, n_{22}\}, t) \\ &+\gamma(n_{22} + 1)(n_{12} + n_{21} + 1)\, \rho(\{n_{11} - 1, n_{12}, n_{21}, n_{22} + 1\}, t) \\ &+\gamma(n_{12} + 1)(n_{21} + 1) \Big\{ \rho(\{n_{11} - 2, n_{12} + 1, n_{21} + 1, n_{22}\}, t) - \rho(\{n_{11} - 1, n_{12} + 1, n_{21} + 1, n_{22} - 1\}, t) \Big\} \\ &+\gamma(n_{22} + 1) \Big\{ (n_{22} + 2)\, \rho(\{n_{11}, n_{12} - 1, n_{21} - 1, n_{22} + 2\}, t) - (n_{11} + 1)\, \rho(\{n_{11} + 1, n_{12} - 1, n_{21} - 1, n_{22} + 1\}, t) \Big\}. \end{aligned}$$

Initial Conditions

We consider the following initial state for the atoms, which is a specific case of Eq. (II.15):

$$\hat{\rho}(0) = \prod_{\mu=1}^{N} \left\{ \sum_{q=1}^{2} p_q \, \hat{\sigma}_{\mu,qq} \right\}, \tag{II.33}$$

where $p_1 + p_2 = 1$, and $p_1, p_2 \geq 0$. This state is pure only if $p_1 = 0$ or $p_1 = 1$. Otherwise, each atom is described by a mixed density matrix with no off-diagonal elements. This mixed state can be prepared as a statistical combination of the following pure states:

$$\prod_{\mu=1}^{N} \left\{ \sqrt{p_1} \, |1\rangle_\mu + \sqrt{p_2} \, e^{i\phi_\mu} \, |2\rangle_\mu \right\},$$

where ϕ_μ are independent random phases uniformly distributed between 0 and 2π. These phases determine the azimuthal orientation of each atom's Bloch vector. Averaging over ϕ_μ eliminates off-diagonal matrix elements, resulting in the mixed state in Eq. (II.33). Importantly, this mixed state cannot be expressed as a combination of fully symmetric states from Eq. (II.5).

In the occupation-number representation, the initial state in Eq. (II.33) is described by the coefficients:

$$\rho(\{n_{11}, 0, 0, n_{22}\}, 0) = \frac{N!}{n_{11}! \, n_{22}!} \, p_1^{n_{11}} \, p_2^{n_{22}}, \tag{II.34}$$

where $n_{11}+n_{22} = N$, and all other coefficients are zero. This state is characterized by a zero value of the integral of motion $\hat{n}_{12} - \hat{n}_{21}$, which is conserved during the evolution. Consequently, only the decomposition coefficients $\rho(\{n_{11}, n_{12}, n_{21}, n_{22}\}, t)$ with $n_{12} = n_{21} \equiv \ell$ evolve non-trivially. Compared to Eq. (II.12), this reduces the number of unknown variables by one power of N:[3]

$$\left[\frac{(N+2)^2}{4} \right] \sim \frac{1}{2} \frac{N^2}{2!},$$

where $[a/b]$ denotes integer division of a by b.

Observables of Two-Level Atoms

To visualize the atomic properties, we will present plots of the populations of atomic states, $p_q(t)$, calculated as follows:

$$p_q(t) = \frac{1}{N} \sum_{\substack{n_{11}, n_{22} \\ n_{11}+n_{22}=N}} n_{qq} \, \rho(\{n_{11}, 0, 0, n_{22}\}, t), \tag{II.35a}$$

where $q = 1$ (ground state) or $q = 2$ (excited state).

We will also present plots of the normalized emission intensity. Since only a single transition is involved, the general expression in Eq. (II.30) simplifies to:

$$I = \langle \hat{n}_{22} \rangle + \langle \hat{b}_{22}^\dagger \, \hat{b}_{11}^\dagger \, \hat{b}_{12} \, \hat{b}_{21} \rangle.$$

In terms of time-dependent decomposition coefficients, the intensity is expressed as:

$$I(t) = N p_2(t) + \sum_{\substack{n_{11}, n_{22} \\ n_{11}+n_{22}+2=N}} \rho(\{n_{11}, 1, 1, n_{22}\}, t). \tag{II.35b}$$

This expression represents the normalized negative rate of relaxation of the atomic ensemble, in accordance with the energy conservation law:

$$I(t) = -\frac{N}{\gamma} \frac{dp_2(t)}{dt}.$$

The calculation of the emission spectral line shape is discussed in the supplementary section, specifically in Sec. 4.2.

[3] The corresponding sequence $1, 2, 4, 6, 9, 12, 16, 20, \ldots$ appears in other mathematical tasks; see, for example, https://oeis.org/A002620.

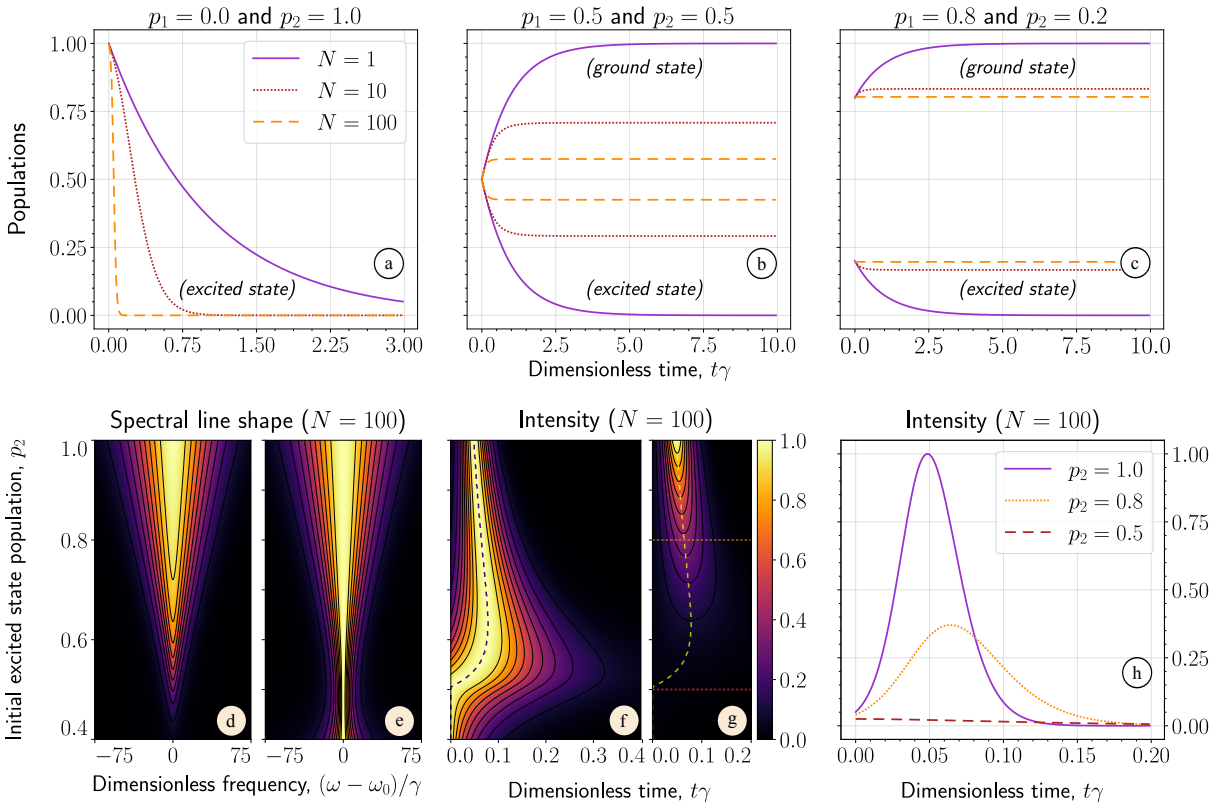

Figure II.2: Dynamics of an ensemble of N two-level atoms, initially prepared in the mixed state in Eq. (II.33) with (a) $p_1 = 0.0$, $p_2 = 1.0$; (b) $p_1 = 0.5$, $p_2 = 0.5$; and (c) $p_1 = 0.8$, $p_2 = 0.2$; calculated for different particle numbers N. Panel (d) presents the spectral line shape for varying initial excited-state populations for $N = 100$, normalized to the overall maximum. Panel (e) shows the same plot normalized for each row (for each p_2). Panel (f) displays the emission intensity for different values of p_2, normalized row-wise, with the dashed line marking the peak position; panel (g) shows the same plot normalized to the overall maximum. Panel (h) shows the normalized emission intensities for $p_2 = 1.0$, 0.8, and 0.5.

Results

When the system begins in a fully excited state ($p_2 = 1$, $p_1 = 0$), the master equation describes the phenomenon of superradiance. Figure II.2 (a) illustrates the evolution of the excited-state population for $N = 1$, 10, 100. The case with $N = 100$ decays significantly faster, demonstrating a strong cooperative effect. This scenario can be effectively modeled using traditional Hilbert space techniques, which offer greater computational efficiency.

For mixed initial states, traditional Hilbert space techniques are not applicable. Figures II.2 (b) and (c) show the populations for $N = 1$, 10, 100, with initial conditions $p_1 = 0.5$ ($p_2 = 0.5$) and $p_1 = 0.8$ ($p_2 = 0.2$), respectively. A single atom still relaxes exponentially to the ground state. However, an ensemble with many atoms reaches the steady state in which the excited-state population remains nonzero, $p_2^{(ss)} > 0$, with (ss) denoting the steady state.

Figure II.2 (d) shows the spectral line shape for $N = 100$ atoms with varying initial conditions. In Fig. II.2 (e), the spectrum is normalized for each row (for each value of p_2), revealing line narrowing as p_2 decreases.

Figures II.2 (f) and (g) depict the intensity curves for the same parameters. A reduction in p_2 shifts the emission peak, as marked by the vertical dashed line. In panel (f), the intensity is normalized row-wise, while in panel (g) it is normalized to the overall maximum. For clarity, Figure II.2 (h) highlights the intensities for selected values of p_2.

During our numerical studies, we observed instability when employing explicit integration methods for $N \gtrsim 150$, as shown in Fig. II.3. Although implicit methods improve stability, they

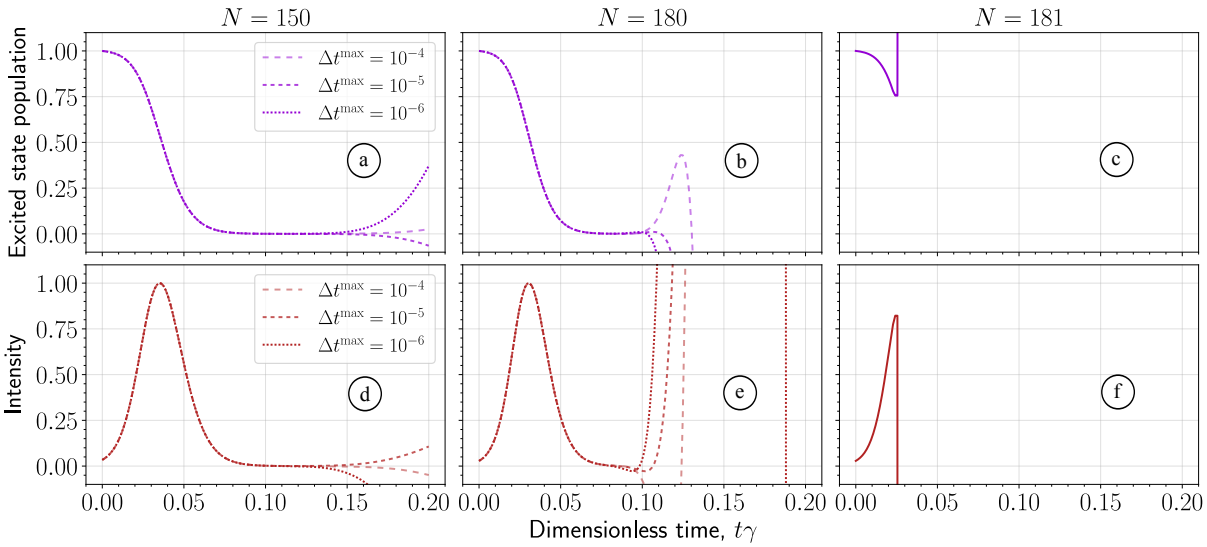

Figure II.3: Solutions for different values of N using the `Tsit5` method [155] with a maximum step size constrained by $\Delta t^{\max}$. For $N > 180$, the solution becomes unstable for any $\Delta t^{\max}$.

become computationally impractical for large N.

Let us examine the final state of the ensemble. The emission intensity approaches zero as $t \to \infty$. Substituting this limit into Eq. (II.35b), we find

$$0 = N p_2^{(ss)} + \sum_{\substack{n_{11},n_{22} \\ n_{11}+n_{22}=N-2}} \rho^{(ss)}(\{n_{11},1,1,n_{22}\}).$$

Since the steady-state excited population $p_2^{(ss)}$ is nonzero, the second term on the right-hand side must also be nonzero and negative. This indicates the existence of non-vanishing atomic correlations, described by $\rho^{(ss)}(\{n_{11},1,1,n_{22}\})$. Furthermore, as intensity-intensity correlations vanish when $t \to \infty$, higher-order atomic correlations, such as $\rho^{(ss)}(\{n_{11},2,2,n_{22}\})$, must also exist, and so forth.

We derived an analytical expression for the steady-state density matrix, represented as a power series in the parameter $p_1 p_2$:

$$\rho^{(ss)}(\{n_{11},\ell,\ell,n_{22}\}) = \frac{(n_{11}-n_{22}+1)\,N!}{n_{22}!\,(n_{11}+\ell+1)!\,\ell!} \sum_{k=n_{22}+\ell}^{[N/2]} (-1)^{k+n_{22}}\,(p_1\,p_2)^k \binom{n_{11}+\ell-k}{k-n_{22}-\ell}. \quad \text{(II.36a)}$$

Here, $[N/2]$ denotes integer division of N by 2. The sum over k can be evaluated analytically. When $n_{11} \geq n_{22}$, the density matrix takes the form:

$$\rho^{(ss)}(\{n_{11},\ell,\ell,n_{22}\}) = (-1)^\ell (p_1 p_2)^{n_{22}+\ell} \frac{(n_{11}-n_{22}+1)\,N!}{n_{22}!\,(n_{11}+\ell+1)!\,\ell!} \sum_{K=0}^{n_{11}-n_{22}} p_1^{n_{11}-n_{22}-K}\,p_2^K. \quad \text{(II.36b)}$$

For $n_{11} < n_{22}$, the coefficients are zero.

The steady-state density matrix depends solely on the product $p_1 p_2$, indicating that interchanging the initial populations does not affect the final state. For example, a system prepared with $p_1 = 0.2$ ($p_2 = 0.8$) evolves into the same final state as one initialized with $p_1 = 0.8$ ($p_2 = 0.2$). In this sense, the specific case $p_1 = p_2 = 0.5$ is particularly symmetric, leading to a simplified form of the density matrix:

$$\rho^{(ss)}(\{n_{11},\ell,\ell,n_{22}\}) = \frac{(-1)^\ell}{2^N} \frac{(n_{11}-n_{22}+1)^2\,N!}{n_{22}!\,(n_{11}+\ell+1)!\,\ell!}, \qquad p_1 = p_2 = 0.5, \quad \text{(II.36c)}$$

when $n_{11} \geq n_{22}$, and zero otherwise.

Using the density matrix from Eq. (II.36a), we derive an analytical expression for the steady-state excited population:

$$p_2^{(ss)} = \sum_{k=1}^{[N/2]} C_{k-1}\,(p_1\,p_2)^k\,\frac{N-2k+1}{N},$$

where $C_k = (2k)!/(k!\,(k+1)!)$ are the Catalan numbers. For a large number of atoms, this expression approaches $\min(p_1, p_2)$. This implies that if the system starts with $p_2 \leq 1/2$, the change in populations is negligible, meaning a full suppression of relaxation. This population trapping results from a balance between emission and absorption due to the special initial state. However, in realistic systems, dissipation and dipole-dipole interactions disrupt this balance, causing the ensemble to eventually relax.

Discussion on Steady States

The density matrix in Eq. (II.36a) is a non-trivial eigenstate of the Liouvillian $\hat{\mathcal{L}}_{\text{coll.}}$ with zero eigenvalue. It is also an eigenstate of the lowering operator with zero value, $\hat{J}_{12}\,|\rho^{(ss)}\rangle\!\rangle = 0$, linking it to dark states [156]. This indicates that this state is decoupled from the environment and resides in the decoherence-free subspace [157].

The steady-state density matrix in Eq. (II.36a) is complex and challenging to analyze directly. However, it simplifies significantly in the case of two atoms. To clarify the analysis, we use the angular momentum basis, which consists of four states: the triplet states $|0\rangle$, $|1_+\rangle$, and $|2\rangle$; and the singlet state $|1_-\rangle$:

$$|0\rangle = |1\rangle_1 \otimes |1\rangle_2, \qquad |1_\pm\rangle = \frac{|1\rangle_1 \otimes |2\rangle_2 \pm |2\rangle_1 \otimes |1\rangle_2}{\sqrt{2}}, \qquad |2\rangle = |2\rangle_1 \otimes |2\rangle_2.$$

Expanding the initial state from Eq. (II.33) in this basis yields the statistical mixture:

$$\hat{\rho}(0) = p_1^2\,|0\rangle\langle 0| + 2p_1p_2\,\frac{|1_+\rangle\langle 1_+| + |1_-\rangle\langle 1_-|}{2} + p_2^2\,|2\rangle\langle 2|.$$

The antisymmetric state $|1_-\rangle$ does not participate in collective emission, while the symmetric states fully relax. As a result, the final state in Eq. (II.36a) is a statistical mixture of the fully relaxed state $|0\rangle$ and the antisymmetric state $|1_-\rangle$:

$$\hat{\rho}^{(ss)} = (1 - p_1p_2)\,|0\rangle\langle 0| + p_1p_2\,|1_-\rangle\langle 1_-|.$$

The symmetry properties of the initial state enable destructive interference in atom-atom interactions, which leads to the emergence of this steady state and links it to the phenomenon of superradiance [158–160].

For a system of N two-level atoms, the initial state represents a statistical mixture of states with different total angular momenta $J = \frac{N}{2}, \frac{N}{2} - 1, \ldots$, and their projections. These states define orthogonal subspaces in the N-particle Hilbert space [1]. It can be conjectured that during evolution, all contributions that couple to the field relax to the lowest energy state within their respective subspaces, leading to the steady state in Eq. (II.36a).

Although a detailed description of the entire process is complex, we can show that the final state contains only the lowest state from the subspace with $J = \frac{N}{2}$ by computing the corresponding projection:

$$\langle\!\langle L|\rho^{ss}\rangle\!\rangle = \delta_{L0} \sum_{K=0}^{N} p_1^{N-K}\,p_2^K.$$

As expected, the only contribution comes from the fully relaxed state with $L = 0$. Here, $|L\rangle\!\rangle$ denotes the Dicke state with L excited atoms (see Sec. 1.4). Interestingly, this projection matches that of the initial density matrix onto the subspace with $J = \frac{N}{2}$. By calculating the projection

$$\langle\!\langle L|\rho(0)\rangle\!\rangle = p_1^{N-L}\,p_2^L,$$

and summing over L from 0 to N, we recover the same result.

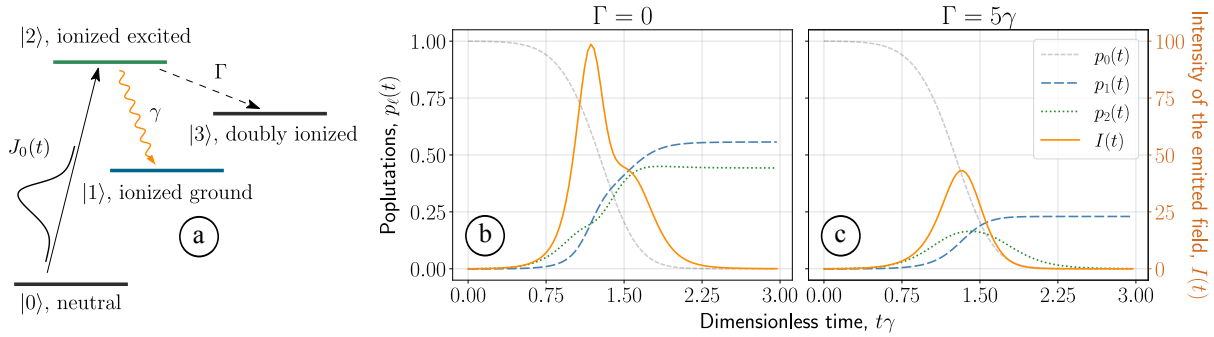

Figure II.4: Dynamics of an ensemble of $N = 100$ atoms with the level structure depicted in (a). Neutral atoms are ionized by a photon flux with the Gaussian temporal envelope $J_0(t) = I_p\, e^{-\frac{(t-t_0)^2}{2\tau^2}}/\sqrt{2\pi\tau^2}$, with parameters $I_p = 10$, $t_0 = 2/\gamma$, $\tau = 0.5/\gamma$. (b) Without the Auger effect, a pronounced emission burst is observed. (c) With fast Auger decay ($\Gamma = 5\gamma$), the burst is significantly suppressed.

2.2 Incoherently Pumped Two-Level Emitters

In realistic scenarios, excitation of the ensemble is not instantaneous. The system's initial state may be prepared through continuous incoherent pumping, as in x-ray lasing experiments [38, 161]. A pump pulse ionizes inner-shell electrons, opening a lasing transition in the ionized atoms, see Fig. II.4 (a) for a level structure. Ref. [108] demonstrated that incoherently pumped two-level atoms reach a steady state after emission.

The ensemble relaxes to the ground state via emission, while incoherent pumping maintains the population of the excited state without inducing coherences. This highlights the similarity with steady states discussed in the previous section. However, continuous pumping results in more complex states, for which we were unable to derive analytical expressions.

When modeling photoionization, we neglect plasma effects and assume no depletion of the pump. Under these conditions, ionization can be described using a simple Lindblad operator. Atoms in the neutral state, denoted by $|0\rangle$, are ionized by an incoming pump pulse, modeled as a photon flux with a time envelope $J_0(t)$. The Lindbladian for this process is:

$$\begin{aligned}\mathcal{L}_{0\to2}[\hat{\rho}(t)] &= \frac{J_0(t)}{2}\sum_{\mu=1}^{N}\{2\hat{\sigma}_{\mu,20}\,\hat{\rho}(t)\,\hat{\sigma}_{\mu,02} - \hat{\sigma}_{\mu,00}\,\hat{\rho}(t) - \hat{\rho}(t)\,\hat{\sigma}_{\mu,00}\},\\ \hat{\mathcal{L}}_{0\to2}\,|\rho(t)\rangle\!\rangle &= J_0(t)(\hat{b}_{22}^{\dagger}\,\hat{b}_{00} - \hat{n}_{00})|\rho(t)\rangle\!\rangle.\end{aligned} \tag{II.37}$$

This operator describes the transition from the neutral state $|0\rangle$ to the ionized excited state $|2\rangle$.

Since there are no coherences between the neutral and ionized states, the neutral state is described by a single occupation number n_{00}, while n_{01}, n_{10}, n_{20} and n_{02} remain zero. The density matrix is therefore expanded over the sets $\{n_{00}, n_{11}, n_{12}, n_{21}, n_{22}\}$ with $n_{12} = n_{21}$ because the Liouvillian still commutes with $\hat{n}_{12} - \hat{n}_{21}$. The basis size scales as:[4]

$$\left[\frac{(N+2)\,(N+4)\,(2N+3)}{4!}\right] \sim \frac{1}{2}\frac{N^3}{3!},$$

reflecting that there are only three independent occupation numbers.

The radiative transition $2 \to 1$ may correspond, for example, to the emission of a $K\alpha$ line as an electron from a higher orbital fills an inner-shell vacancy. However, Auger-Meitner decay often competes with this radiative process, releasing energy via the autoionization of a second electron. The system then transitions to a doubly ionized state, denoted by $|3\rangle$. Neglecting plasma effects, we assume only the excited state relaxes via Auger-Meitner decay, described by

[4] The corresponding sequence $1, 3, 7, 13, 22, 34, 50, 70, \ldots$ is described in https://oeis.org/A173196.

the Lindblad operator with rate Γ:

$$\begin{aligned}\mathcal{L}_{2\to3}[\hat{\rho}(t)] &= \frac{\Gamma}{2}\sum_{\mu=1}^{N}\{2\hat{\sigma}_{\mu,32}\,\hat{\rho}(t)\,\hat{\sigma}_{\mu,23} - \hat{\sigma}_{\mu,22}\,\hat{\rho}(t) - \hat{\rho}(t)\,\hat{\sigma}_{\mu,22}\},\\ \hat{\mathcal{L}}_{2\to3}\,|\rho(t)\rangle\!\rangle &= \frac{\Gamma}{2}\,\{2\hat{b}_{33}^{\dagger}\,\hat{b}_{22} - \sum_{t=1}^{2}(\hat{n}_{2t}+\hat{n}_{t2})\}|\rho(t)\rangle\!\rangle.\end{aligned} \tag{II.38}$$

The doubly ionized state is described by a single occupation number n_{33}, with no coherences between this state and others. Thus, the density matrix is expanded in an extended basis $\{n_{00}, n_{11}, n_{12}, n_{21}, n_{22}, n_{33}\}$ with $n_{12} = n_{21}$. This increases the basis size scaling to:[5]

$$\left[\frac{(N+2)\,(N+4)\,(N^2+6N+6)}{48}\right] \sim \frac{1}{2}\frac{N^4}{4!},$$

since there are now four independent occupation numbers.

The full master equation includes three terms:

$$\hat{\mathcal{L}}\,|\rho(t)\rangle\!\rangle = (\hat{\mathcal{L}}_{0\to2} + \hat{\mathcal{L}}_{2\to3} + \hat{\mathcal{L}}_{\text{coll.}})|\rho(t)\rangle\!\rangle,$$

where $\hat{\mathcal{L}}_{\text{coll.}}$ is given in Eq. (II.32). We model the pump flux as a Gaussian pulse. Figure II.4 (b) illustrates the dynamics for $N = 100$ atoms without Auger-Meitner decay. The ensemble reaches a steady state with a nonzero excited-state population. The emission intensity shows a pronounced peak followed by a "shoulder." During the shoulder formation, the population inversion $p_2(t) - p_1(t)$ remains nearly constant. Including Auger decay ($\Gamma = 5\gamma$) disrupts the balance and significantly suppresses emission intensity, as shown in Fig. II.4 (c).

2.3 Three-Level Systems: V-Type

Up to this point, we have focused on models with lasing between two levels. However, our approach generalizes naturally to energy structures with multiple levels. In this section, we examine a V-type configuration with two excited states, $|2\rangle$ and $|3\rangle$, and a single ground state, $|1\rangle$, as depicted in Fig. II.5 (a). The energy gap between the excited states Δ is assumed to be much smaller than the center frequency, $\Delta \ll \omega_0$.

Fluorescence from emitters with this level structure can exhibit quantum beating—a fundamental phenomenon observed across various spectral ranges [162–166]. In the context of collective emission, quantum beating combines with superfluorescence behavior [167, 168]. Here, we study superfluorescence in a gas placed in a magnetic field, which induces the Zeeman splitting Δ of the upper states, similar to the experimental situation in Ref. [165].

We consider transitions $2 \to 1$ and $3 \to 1$, with orthogonal transition dipole moments of slightly different magnitudes:

$$\begin{aligned}\overline{\mathbf{d}}_{31} &= \frac{\overline{d}_{31}}{\sqrt{2}}(\mathbf{e}_x - i\mathbf{e}_y),\\ \overline{\mathbf{d}}_{21} &= \frac{\overline{d}_{21}}{\sqrt{2}}(\mathbf{e}_x + i\mathbf{e}_y),\end{aligned}$$

where $|\overline{d}_{31}|^2 = 1$ and $|\overline{d}_{21}|^2 = 0.75$. Transitions between the excited states are forbidden: $\overline{\mathbf{d}}_{32} = \overline{\mathbf{d}}_{23} = 0$. Assuming each atom is initially prepared in a coherent superposition of the excited states:

$$\frac{|2\rangle_\mu - |3\rangle_\mu}{\sqrt{2}}, \tag{II.39}$$

quantum beats can be observed in the intensity of both the x- and y-components of the field [169]. Experimentally, this can be achieved by applying a magnetic field and using a pump polarized in a plane orthogonal to the field's orientation, as demonstrated in Ref. [165].

[5] The corresponding sequence $1, 4, 11, 24, 46, 80, 130, 200, \ldots$ is described in https://oeis.org/A001752.

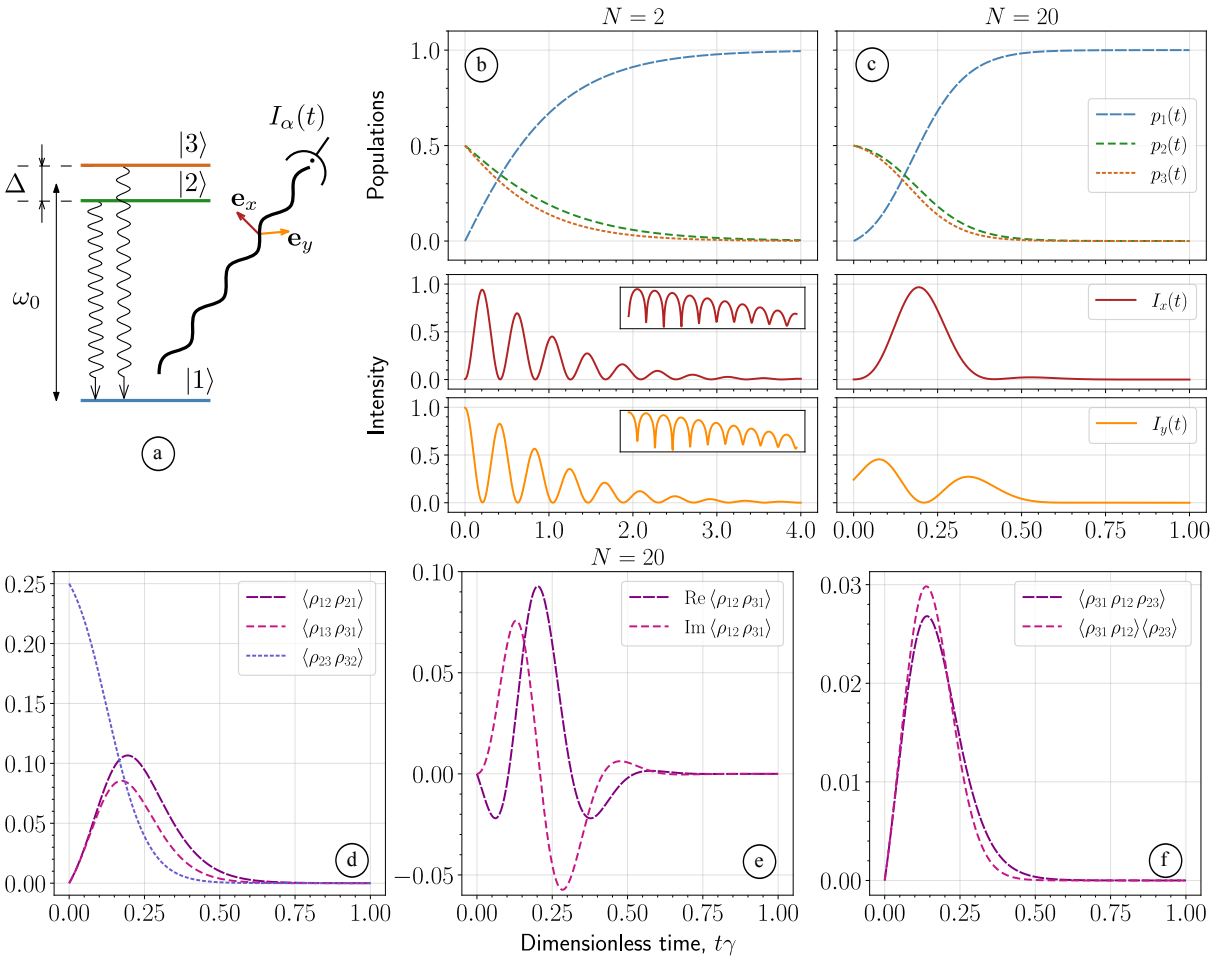

Figure II.5: Quantum beats in V-type systems, depicted in panel (a), calculated for $N = 2$ (b) and $N = 20$ (c) atoms. In both cases, $\Delta = 15\gamma$. Panels show populations and normalized intensities of both polarization components. For $N = 2$ (b), intensity curves are also shown on a logarithmic scale in the inset. Intensity components are normalized to the maximum full intensity. Panels (d) and (e) depict non-trivial two-particle correlators. Panel (f) depicts three-particle correlator and its factorization.

The collective Liouvillian in Eq. (II.31) for V systems has the following integrals of motion:

$$\hat{n}_{12} - \hat{n}_{21} + \hat{n}_{32} - \hat{n}_{23} = \text{const},$$
$$\hat{n}_{13} - \hat{n}_{31} + \hat{n}_{23} - \hat{n}_{32} = \text{const},$$
$$\hat{n}_{12} - \hat{n}_{21} + \hat{n}_{13} - \hat{n}_{31} = \text{const}.$$

Only two expressions are independent. These conserved quantities are lost if counter-rotating terms or external classical driving are introduced.

For the initial state in Eq. (II.39), there are no coherences between the ground and excited states, leading to non-trivial dynamics only for decomposition coefficients where $n_{12} - n_{21} + n_{13} - n_{31} \equiv 0$. However, coherences between the excited states are present, and the second integral of motion can still be utilized through parallelization. The decomposition of the initial state can be grouped by different values of $n_{12} - n_{21} + n_{32} - n_{23}$, with states in different groups evolving independently. This enables parallel computation and overall reduces the number of independent basis states from approximately $N^8/8!$ to $N^6/6!$.

Pure Initial State: Quantum Beats

In Fig. II.5 (b, c), we present the populations and emission intensities for $N = 2$ (b) and $N = 20$ (c) atoms, initially prepared in the pure state in Eq. (II.39).

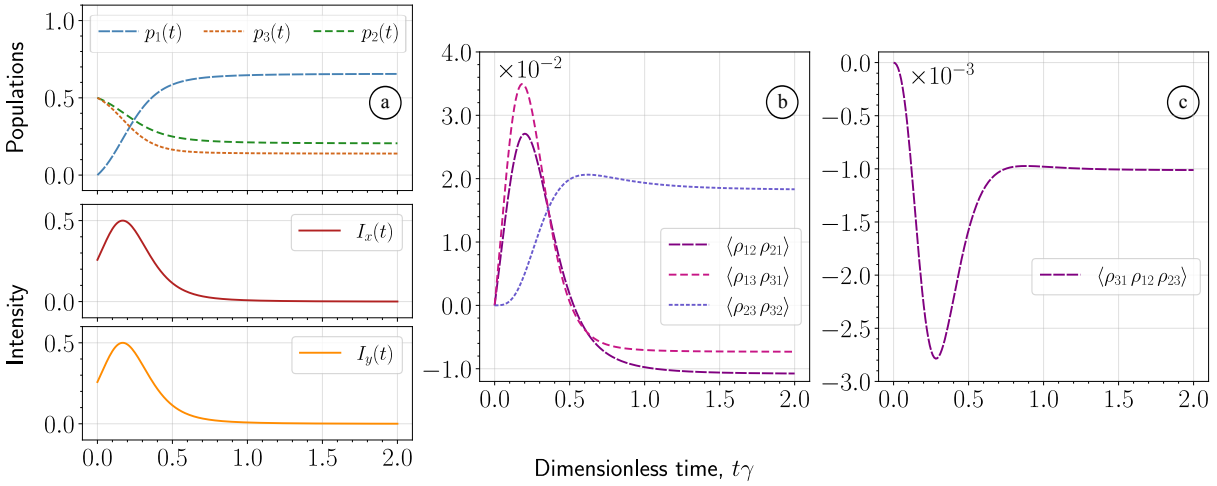

Figure II.6: Dynamics of an ensemble of $N = 20$ atoms with a V-type level configuration. Each atom is initially prepared in the mixed state in Eq. (II.42). Panel (a) shows the populations and normalized intensity components. The area under the full intensity curve is approximately 13.1 before normalization. Panel (b) depicts non-trivial two-particle correlators. Panel (c) illustrates the dynamics of three-particle correlator. The labels $\times 10^{-n}$ indicate the corresponding values should be multiplied by these factors.

Quantum beats are observed in the intensity components, with the modulation frequency determined by the energy difference between the excited states. For $N = 20$ in panel (c), there are fewer oscillations, as collective processes enhance the decay rate by approximately a factor of N, making the decay time comparable to the oscillation period.

To analyze interatomic correlations, we introduce the following notation for two-particle correlators:

$$\langle \rho_{ij}\,\rho_{pq}\rangle = \frac{\sum\limits_{\mu_1\neq\mu_2} \langle \hat{\sigma}_{\mu_1,ji}\,\hat{\sigma}_{\mu_2,qp}\rangle}{N(N-1)} = \frac{\langle \hat{b}^\dagger_{jj}\,\hat{b}^\dagger_{qq}\,\hat{b}_{ij}\,\hat{b}_{pq}\rangle}{N(N-1)}. \tag{II.40}$$

For $i \neq j$ and $p \neq q$, contributions come only from occupation-number sets where $n_{i\neq j} = n_{p\neq q} = 1$, with all other non-diagonal numbers being zero.

Figure II.5 (d) shows different two-particle correlators for $N = 20$. The correlator $\langle \rho_{23}\,\rho_{32}\rangle$, which describes coherence between the excited states, starts at a nonzero value (determined by the initial conditions) and gradually decays to zero as the system relaxes. Correlators $\langle \rho_{13}\,\rho_{31}\rangle$ and $\langle \rho_{23}\,\rho_{32}\rangle$, which contribute to the emission intensity, start from zero and rise to peak values before relaxation.

In Fig. II.5 (e), we plot the real and imaginary parts of $\langle \rho_{31}\,\rho_{12}\rangle$. Both components oscillate at a frequency determined by the energy gap between the excited states.

Figure II.5 (f) shows a three-particle correlator, calculated as:

$$\langle \rho_{31}\,\rho_{12}\,\rho_{23}\rangle = \frac{\sum\limits_{\mu_1\neq\mu_2\neq\mu_3} \langle \hat{\sigma}_{\mu_1,32}\,\hat{\sigma}_{\mu_2,21}\,\hat{\sigma}_{\mu_3,13}\rangle}{N(N-1)(N-2)} = \frac{\langle \hat{b}^\dagger_{33}\,\hat{b}^\dagger_{22}\,\hat{b}^\dagger_{11}\,\hat{b}_{31}\,\hat{b}_{12}\,\hat{b}_{23}\rangle}{N(N-1)(N-2)}. \tag{II.41}$$

Such correlators are often factorized in semiclassical and approximate approaches [76]. However, in the absence of initial coherence, any factorization of this operator results in zero. For comparison, we also plot the factorized correlator $\langle \rho_{31}\,\rho_{12}\rangle\langle \rho_{23}\rangle$. Here, the mean coherence $\langle \rho_{23}\rangle$ is defined analogously to other expectation values:

$$\langle \rho_{23}\rangle = \frac{\sum\limits_{\mu} \langle \hat{\sigma}_{\mu,32}\rangle}{N} = \frac{\langle \hat{b}^\dagger_{33}\,\hat{b}_{23}\rangle}{N}.$$

While the factorized correlator does not exactly replicate the original, it qualitatively captures similar behavior.

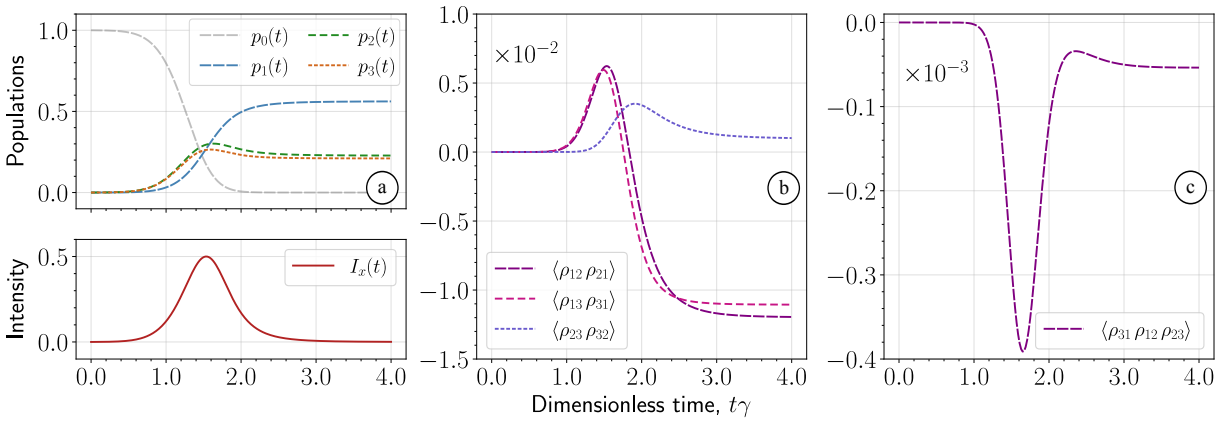

Figure II.7: Dynamics of an ensemble of $N = 20$ atoms with a V-type level configuration. Each atom starts from the additional level $|0\rangle$, and is then excited by the Gaussian pulse according to Eq. (II.44), with $J_0(t)$ chosen as in Fig. II.4. Panel (a) displays the populations and normalized intensity of the x-component. The area under the full intensity curve is approximately 11.2 before normalization. Panel (b) depicts non-trivial two-particle correlators. Panel (c) illustrates the dynamics of the three-particle correlator. The labels $\times 10^{-n}$ indicate the corresponding values should be multiplied by these factors.

Mixed Initial State: Steady States

Quantum beats arise due to an initially nonzero coherence between the excited states. In the absence of initial coherence, as in the mixed state:

$$\frac{|2\rangle_\mu\langle 2|_\mu}{2} + \frac{|3\rangle_\mu\langle 3|_\mu}{2}, \tag{II.42}$$

quantum beats vanish, as illustrated in Fig. II.6 (a). The intensities of both polarization components evolve identically. Notably, the system reaches a steady state, as in previous sections.

Figure II.6 (b) shows two-particle correlators. The steady-state correlators describing transitions between the ground and excited states are negative: $\langle \rho_{13}^{(ss)}\,\rho_{31}^{(ss)} \rangle < 0$ and $\langle \rho_{12}^{(ss)}\,\rho_{21}^{(ss)} \rangle < 0$. The steady-state correlator for the excited states is positive: $\langle \rho_{23}^{(ss)}\,\rho_{32}^{(ss)} \rangle > 0$. The correlator $\langle \rho_{31}\,\rho_{12} \rangle$ shows no dynamics and is not included in the figure.

The three-particle correlator $\langle \rho_{31}\,\rho_{12}\,\rho_{23} \rangle$ remains negative throughout the entire evolution, eventually reaching a nonzero negative value, as shown in Fig. II.6 (c). Any attempt to factorize this correlator results in zero, highlighting the importance of many-particle correlations. The fact that excited states are not empty after the evolution in the absence of initial coherence was also noted in Ref. [170].

Numerical analysis indicates that the decomposition coefficients $\rho(\{n_{ij}\}, t)$, where any occupation number involving the ground state is zero (namely $n_{1j} = 0$ and $n_{j1} = 0$), exhibit non-trivial dynamics only when $n_{23} = n_{32} = 0$. In a sense, this indicates the absence of direct correlations between the excited states.

Furthermore, all previously mentioned conserved quantities are zero for the initial state in Eq. (II.42):

$$n_{12} - n_{21} + n_{32} - n_{23} = 0, \tag{II.43a}$$
$$n_{13} - n_{31} + n_{23} - n_{32} = 0, \tag{II.43b}$$
$$n_{12} - n_{21} + n_{13} - n_{31} = 0. \tag{II.43c}$$

Defining $n_{12} - n_{21} \equiv \Delta\ell$, it follows from the first and third relations that $n_{23} - n_{32} = \Delta\ell$ and $n_{31} - n_{13} = \Delta\ell$. Hence, only four independent variables exist among $n_{i\neq j}$, with the absolute difference between any pair $n_{i\neq j}$ and $n_{j\neq i}$ being the same.

The steady-state density matrix can be derived analytically when the transition dipole moments have identical magnitudes ($|\overline{\mathbf{d}}_{12}|^2 = |\overline{\mathbf{d}}_{13}|^2 = 1$) and the excited states are equally populated initially, as in Eq. (II.42).

The steady-state density matrix is nonzero when $n_{11} \geq n_{22} + n_{33} + n_{23} + n_{32}$ and occupation numbers satisfy all three conditions in Eqs. (II.43). It is expressed as:

$$\begin{aligned}\rho^{(ss)}(\{n_{ij}\}) = &\frac{(-1)^{\ell_{12}+\ell_{13}+\Delta\ell}}{2^N} \\ &\times \frac{(\ell_{12}+\ell_{13}+\Delta\ell)!}{\ell_{13}!\,\ell_{12}!\,\Delta\ell!}\,\frac{\ell_{23}!\,\Delta\ell!}{(\ell_{23}+\Delta\ell)!}\,\frac{(n_{22}+\ell_{12}+\ell_{23}+\Delta\ell)!}{n_{22}!\,(\ell_{12}+\Delta\ell)!\,\ell_{23}!}\,\frac{(n_{33}+\ell_{13}+\ell_{23}+\Delta\ell)!}{n_{33}!\,(\ell_{13}+\Delta\ell)!\,\ell_{23}!} \\ &\times \frac{(n_{11}-n_{22}-2\ell_{23}-n_{33}-\Delta\ell+1)^2 N!}{(n_{22}+n_{33}+\ell_{12}+\ell_{13}+2\ell_{23}+2\Delta\ell+1)!\,(n_{11}+\ell_{12}+\ell_{13}+\Delta\ell+1)!}.\end{aligned}$$

Here, $\Delta\ell = |n_{12}-n_{21}| = |n_{13}-n_{31}| = |n_{23}-n_{32}|$, $\ell_{12} = \min(n_{12}, n_{21})$, $\ell_{13} = \min(n_{13}, n_{31})$, and $\ell_{23} = \min(n_{23}, n_{32})$. All terms in the second line represent multinomial distributions. Notably, there is asymmetry between different coherences: ℓ_{12} and ℓ_{13} directly affect the sign of the matrix elements, while ℓ_{23} does not.

Setting all occupation numbers with distinct indices to zero gives the diagonal elements of the density matrix:

$$\rho^{(ss)}(\{n_{ii}\}) = \frac{1}{2^N}\frac{(n_{11}-n_{22}-n_{33}+1)^2\,N!}{(n_{22}+n_{33}+1)!\,(n_{11}+1)!},$$

where $n_{11} \geq n_{22} + n_{33}$. The excited states enter this expression only as the sum $n_{22} + n_{33}$. This expression resembles the steady-state solution found for two-level systems in Eq. (II.36c) with $\ell = 0$.

If the occupation numbers involving one of the excited states, e.g., state 3, are set to zero, the density matrix remains nonzero for $n_{12} = n_{21} = \ell_{12}$ and $n_{11} \geq n_{22}$:

$$\rho(\{n_{11}, \ell_{12}, 0, \ell_{12}, n_{22}, 0, 0, 0, 0\}) = \frac{1}{(n_{22}+\ell_{12}+1)}\frac{(-1)^{\ell_{12}}}{2^N}\frac{(n_{11}-n_{22}+1)^2\,N!}{n_{22}!\,(n_{11}+\ell_{12}+1)!\,\ell_{12}!},$$

which, up to a factor of $(n_{22}+\ell_{12}+1)^{-1}$, reproduces Eq. (II.36c).

The similarity to two-level systems offers insights into the symmetry properties of the steady states discussed here. The initial state in Eq. (II.42) may also be represented as a statistical mixture of states with different symmetries. While more complex due to the three levels, parts of the steady-state density matrix involving an excited state and the ground state share the mixed symmetry structure observed in two-level systems.

Incoherently Pumped V-Systems

Let us consider the scenario where the ensemble is not excited instantaneously. Instead, each atom starts in the ground state $|0\rangle$ and transitions to the excited states via incoherent pumping. The population transfer from the state $|0\rangle$ to the mixture of excited states (II.42) is modeled using the Lindblad operator:

$$\begin{aligned}\mathcal{L}_{0\to 2,3}\left[\hat{\rho}(t)\right] &= \frac{J_0(t)}{4}\sum_{\mu=1}^{N}\sum_{e=2,3}\{2\hat{\sigma}_{\mu,e0}\,\hat{\rho}(t)\,\hat{\sigma}_{\mu,0e} - \hat{\sigma}_{\mu,00}\,\hat{\rho}(t) - \hat{\rho}(t)\,\hat{\sigma}_{\mu,00}\}, \\ \hat{\mathcal{L}}_{0\to 2,3}\,|\rho(t)\rangle\!\rangle &= \frac{J_0(t)}{2}(\hat{b}_{22}^\dagger\,\hat{b}_{00} + \hat{b}_{33}^\dagger\,\hat{b}_{00} - 2\hat{n}_{00})|\rho(t)\rangle\!\rangle.\end{aligned} \tag{II.44}$$

The results are presented in Fig. II.7. A comparison of panels (a), (b), and (c) with the corresponding panels in Fig. II.6 reveals only quantitative differences; the overall qualitative behavior remains similar. Since both polarization components of the emission evolve identically, only one is displayed.

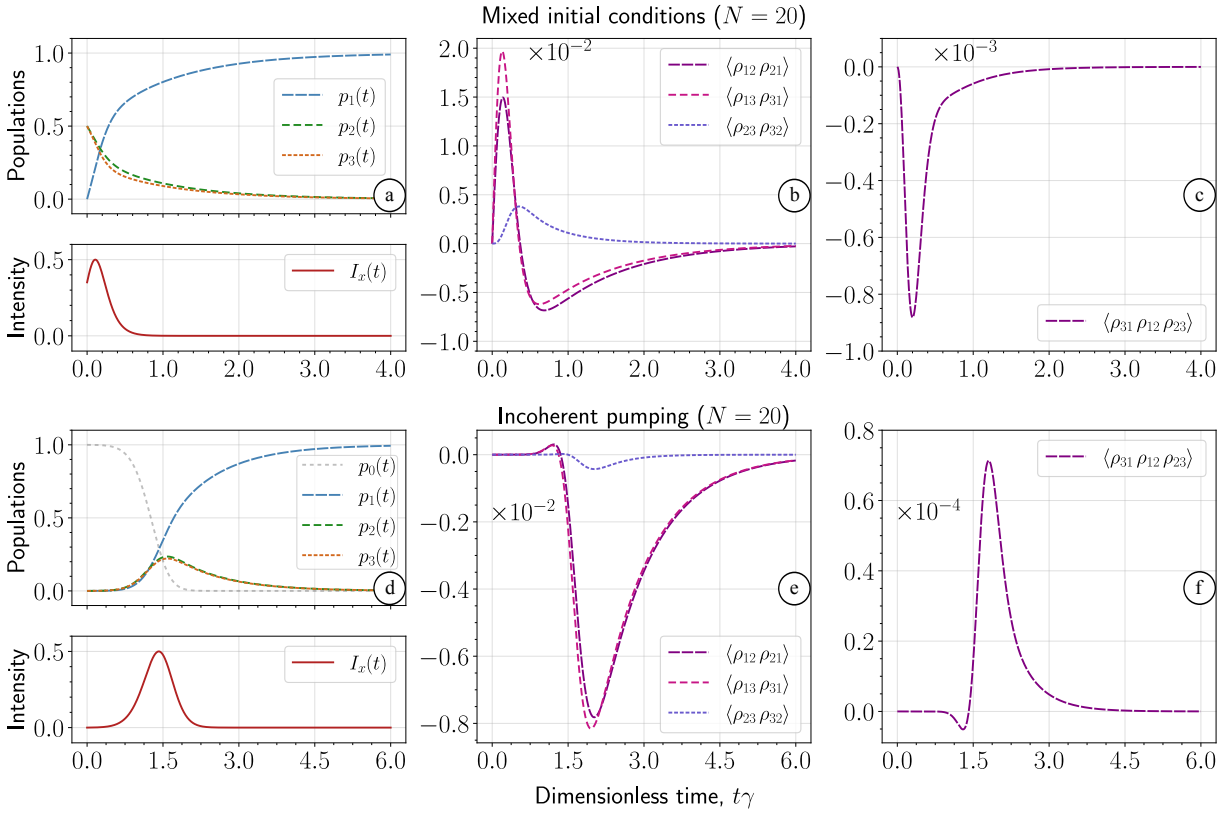

Figure II.8: Dynamics of an ensemble of $N = 20$ atoms with a V-type level structure with the additional dissipation channel described by Eq. (II.45) with $\Gamma = \gamma$. In the upper row (a)-(c), atoms start from the state in Eq. (II.42). In the lower row (d)-(f), atoms are incoherently excited according to Eq. (II.44), with $J_0(t)$ as in Fig. II.4. Panels (a) and (d) display the populations and normalized intensities of the x-component. The area under the full intensity curve is approximately 7.6 (a) and 5.0 (d) before normalization. Panels (b) and (e) show the dynamics of two-particle correlators, while panels (c) and (f) depict three-particle correlator. The labels $\times 10^{-n}$ indicate the corresponding values should be multiplied by these factors.

Inclusion of Dissipation

Introducing an additional dissipation channel disrupts the equilibrium of the steady state, causing the ensemble to release energy.

We incorporate dissipation channels from both excited states to the ground state, corresponding to the transitions $3 \to 1$ and $2 \to 1$. Both decays take place with a rate Γ. These channels describe nonradiative decay and do not contribute to spontaneous emission. The corresponding Lindblad operator, similar to Eq. (II.38), is given by:

$$\hat{\mathcal{L}}_{e\to 1}\,|\rho(t)\rangle\!\rangle = \frac{\Gamma}{2}\{2\hat{b}_{11}^{\dagger}\,\hat{b}_{ee} - \sum_{t=1}^{3}(\hat{n}_{et} + \hat{n}_{te})\}|\rho(t)\rangle\!\rangle, \qquad e = 1, 2. \tag{II.45}$$

In the numerical analysis, we set $\Gamma = \gamma$. The results are presented in Fig. II.8. Panels (a), (b), and (c) illustrate the dynamics of the ensemble initially prepared in the mixed state in Eq. (II.42). In contrast to Fig. II.6, all correlators decay to zero, indicating the breakdown of the steady state. Again, only one of the polarization components is displayed due to their identical evolution.

Panels (d), (e), and (f) of Fig. II.8 show the dynamics when the ensemble is incoherently excited according to Eq. (II.44). In contrast to Fig. II.7, dissipation introduces several qualitative differences. In panel (e), the correlator between the excited states $\langle\rho_{23}\,\rho_{32}\rangle$ now exhibits negative values. Additionally, the three-particle correlator in panel (f) exhibits positive values. All correlators eventually decay to zero.

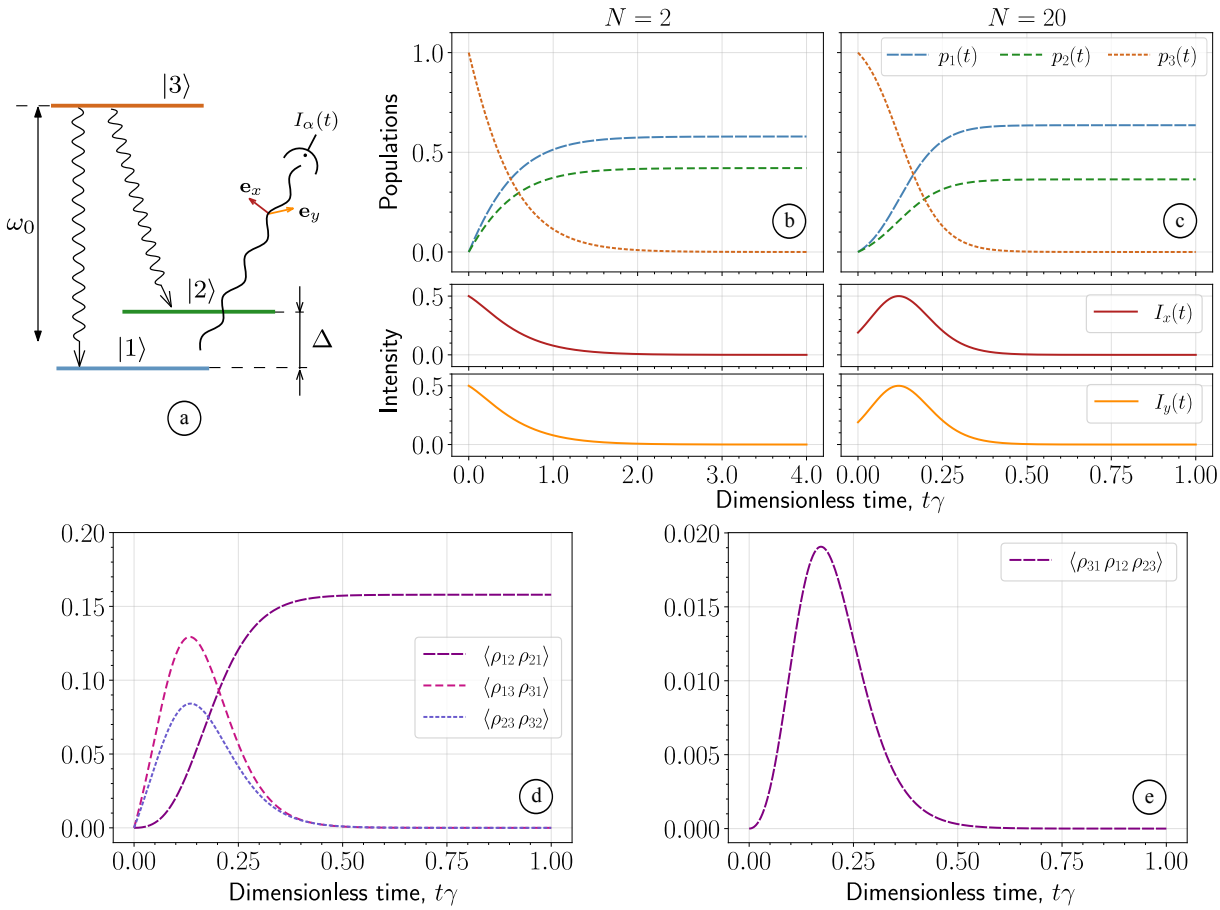

Figure II.9: Dynamics of an ensemble of atoms with a Λ-type level configuration, depicted in panel (a). Panels (b) and (c) display the populations and emission intensities of both polarization components, for $N = 2$ (b) and $N = 20$ (c). Intensities are normalized to the maximum of full intensity. Panels (d) and (e) show non-trivial two-particle and three-particle correlators for $N = 20$.

2.4 Three-Level Systems: Λ-Type

Another possible configuration for three-level atoms is the Λ configuration, where a single excited state can relax into one of two ground states, as shown in Fig. II.9 (a). Unlike V systems, Λ systems do not exhibit quantum beats in the intensity components [119].

In this section, we analyze an ensemble of atoms with a Λ configuration and orthogonal transition dipole moments:

$$\overline{\mathbf{d}}_{31} = \frac{\overline{d}_{31}}{\sqrt{2}}(\mathbf{e}_x - i\mathbf{e}_y), \qquad \overline{\mathbf{d}}_{32} = \frac{\overline{d}_{32}}{\sqrt{2}}(\mathbf{e}_x + i\mathbf{e}_y).$$

Transitions between the ground states are forbidden. Similar to the V systems discussed earlier, we assume slightly different transition rates, namely $|\overline{d}_{31}|^2 = 1$ and $|\overline{d}_{32}|^2 = 0.75$.

The Liouvillian in Eq. (II.31) for Λ systems has the same integrals of motion as the V systems:

$$\begin{aligned}
\hat{n}_{12} - \hat{n}_{21} + \hat{n}_{32} - \hat{n}_{23} &= \text{const}, \\
\hat{n}_{13} - \hat{n}_{31} + \hat{n}_{23} - \hat{n}_{32} &= \text{const}, \\
\hat{n}_{12} - \hat{n}_{21} + \hat{n}_{13} - \hat{n}_{31} &= \text{const}.
\end{aligned}$$

Only two of these relations are independent. For an initial state with no coherences, all these quantities are zero, leaving only six independent occupation numbers. Consequently, the computational complexity is reduced from approximately $N^8/8!$ to $N^6/6!$.

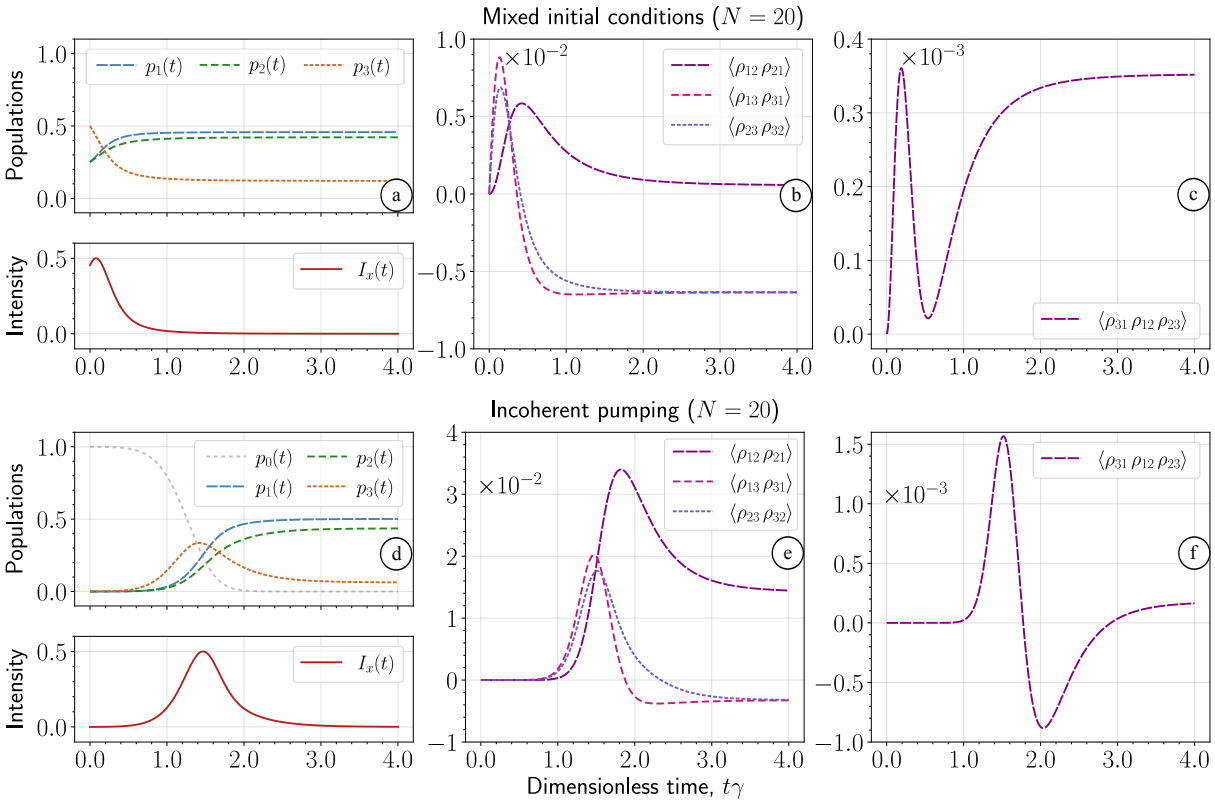

Figure II.10: Dynamics of the ensemble of $N = 20$ atoms with a Λ-type level configuration. In the upper row (a)-(c), atoms start from the mixed state in Eq. (II.47). In the lower row (d)-(f), atoms are incoherently excited according to Eq. (II.48) with $J_0(t)$ as in Fig. II.4. Panels (a) and (d) display populations and normalized intensities. The area under the full intensity curve is approximately 7.7 (a) and 18.7 (d) before normalization. Panels (b) and (e) show the dynamics of the two-particle correlators, while panels (c) and (f) depict the three-particle correlator. The labels $\times 10^{-n}$ indicate the corresponding values should be multiplied by these factors.

Figures II.9 (b) and (c) illustrate the evolution of populations and intensity components for $N = 2$ and $N = 20$ atoms. Both polarization components evolve identically, with no beatings observed. Due to the distinct dipole moments of the transitions $3 \to 2$ and $3 \to 1$, the final populations of the ground states are not equal.

Panel (d) shows non-trivial two-particle correlators for $N = 20$. In the final state, the correlator $\langle\rho_{12}\,\rho_{21}\rangle$ is nonzero, reflecting correlations between the ground states. While general analytical expressions are challenging to derive, some analytical expressions can be found when the transition dipole moments are equal, $|\bar{d}_{31}|^2 = |\bar{d}_{32}|^2 = 1$. In this case, the final state is described by the following density matrix:

$$\rho^{(ss)}(\{n_{11}, \ell, 0, \ell, n_{22}, 0, 0, 0, 0\}) = \frac{1}{N+1} \frac{(n_{11}+\ell)!\,(n_{22}+\ell)!}{n_{11}!\,\ell!\,\ell!\,n_{22}!},$$

where $n_{11} + 2\ell + n_{22} = N$. If this condition is not met, the decomposition coefficients are zero. Setting $\ell = 0$ gives diagonal matrix elements, each equal to $1/(N+1)$.

This steady state is a statistical mixture of fully symmetric states, where atoms are distributed among the ground states:

$$\hat{\rho}^{(ss)} = \frac{1}{N+1} \sum_{L=0}^{N} |L\rangle\langle L|, \tag{II.46}$$

where $|L\rangle$ denotes the state with $N - L$ atoms in the first ground state and L atoms in the second ground state. This structure reflects a simple fact: if L atoms transition to state $|2\rangle$, the remaining atoms relax into state $|1\rangle$.

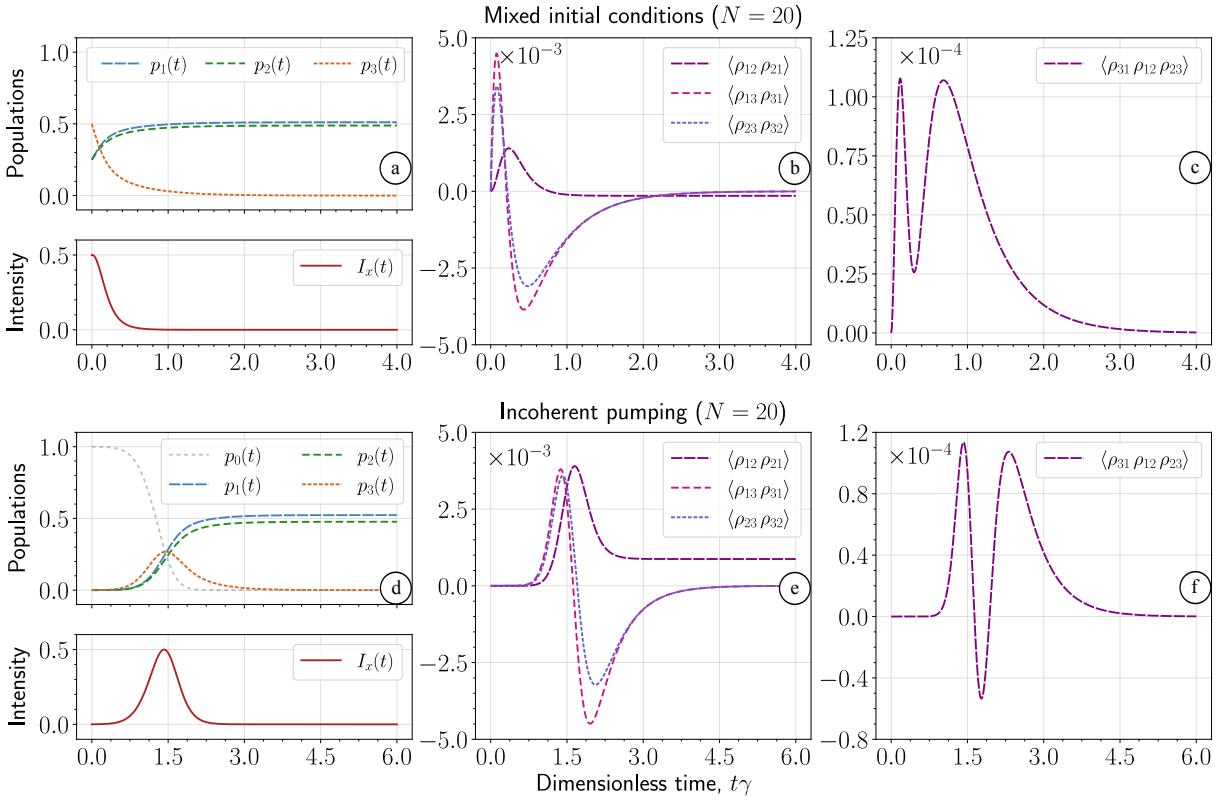

Figure II.11: Dynamics of an ensemble of $N = 20$ atoms with a Λ-type level configuration with the additional dissipation channel described by Eq. (II.49) with $\Gamma = \gamma$. In the top row (a)-(c), atoms start from the mixed state in Eq. (II.47). In the lower row (d)-(f), atoms are incoherently excited according to Eq. (II.48) with $J_0(t)$ as in Fig. II.4. Panels (a) and (d) display populations and normalized intensities. The area under the full intensity curve is approximately 3.9 (a) and 8.6 (d) before normalization. Panels (b) and (e) show the dynamics of two-particle correlators, while panels (c) and (f) depict three-particle correlator. The labels $\times 10^{-n}$ indicate the corresponding values should be multiplied by these factors.

It is worth noting that the analogy with Dicke states is purely mathematical. The equal population of each Dicke state suggests that the relaxations of individual atoms are not independent. Independent relaxation would make it highly improbable for all atoms to decay into the same ground state—this probability is $1/2^N$ for independent transitions. If the transitions have different decay rates, the system favors the faster decay channel, breaking the symmetry between the ground states.

Mixed Initial State

In this subsection, we investigate the effects of statistical mixing of the initial state. We assume that each atom is initially prepared in the following mixed state:

$$\frac{|1\rangle_\mu\langle 1|_\mu + |2\rangle_\mu\langle 2|_\mu}{4} + \frac{|3\rangle_\mu\langle 3|_\mu}{2}, \tag{II.47}$$

Here, the ground states are equally populated with probabilities $p_1 = p_2 = 0.25$, and the rest of the probability remains in the excited state, $p_3 = 0.5$.

Numerical simulations show that the ensemble does not relax to the ground states but reaches a steady state with some population remaining in the excited state, as illustrated in Fig. II.10 (a). This steady state exhibits nonzero two-particle correlations. As shown in panel (b), correlators involving the excited state $\langle\rho_{13}^{(ss)}\,\rho_{31}^{(ss)}\rangle$ and $\langle\rho_{23}^{(ss)}\,\rho_{32}^{(ss)}\rangle$ are negative, while the ground-state correlator $\langle\rho_{12}^{(ss)}\,\rho_{21}^{(ss)}\rangle$ remains positive. Additionally, the three-particle correlator $\langle\rho_{31}^{(ss)}\,\rho_{12}^{(ss)}\,\rho_{23}^{(ss)}\rangle$, shown in panel (c), evolves to a positive value.

Incoherently Pumped Λ-Systems

To study the effect of continuous incoherent pumping, we introduce an additional state $|0\rangle$, as done for V systems from the previous section. The excited state is populated according to the Lindbladian:

$$\hat{\mathcal{L}}_{0\to 3}\,|\rho(t)\rangle\rangle = J_0(t)\,(\hat{b}^\dagger_{33}\,\hat{b}_{00} - \hat{n}_{00})|\rho(t)\rangle\rangle. \tag{II.48}$$

The results are shown in Fig. II.10 (d)-(f). The system evolves into a steady state with nonzero two-particle (e) and three-particle (f) correlators. Qualitatively, the dynamics in panels (d) and (e) is similar to the case of statistically mixed state in Fig. II.10 (a) and (b). However, the three-particle correlator in panel (f) has negative values.

Inclusion of Dissipation

When analyzing V systems, we examined the effects of dissipation. Dissipation disrupted the formation of steady states, driving the ensemble to relax to the ground state and introducing several qualitative changes to the dynamics.

We conduct the same analysis for Λ systems, incorporating nonradiative decay from the excited state to the ground states at a rate Γ. The corresponding Lindbladian operators are given by

$$\hat{\mathcal{L}}_{3\to g}\,|\rho(t)\rangle\rangle = \frac{\Gamma}{2}\{2\hat{b}^\dagger_{gg}\,\hat{b}_{33} - \sum_{t=1}^{3}(\hat{n}_{3t} + \hat{n}_{t3})\}|\rho(t)\rangle\rangle, \tag{II.49}$$

where $g = 1, 2$. As a result, the excited state is depleted at a total rate of 2Γ, while the coherences between the excited and ground states are damped at a rate of Γ. For the numerical examples presented, we set $\Gamma = \gamma$.

Figures II.11 (a)-(c) illustrate the dynamics when the system is prepared in the mixed state in Eq. (II.47). Notably, the correlators $\langle\rho_{13}\,\rho_{31}\rangle$ and $\langle\rho_{23}\,\rho_{32}\rangle$ decay to zero (b), as does the three-particle correlator (c). However, the correlator between the ground states, $\langle\rho_{12}\,\rho_{21}\rangle$ stabilizes at a constant negative value instead of decaying to zero. In contrast, without dissipation, this correlator remained positive.

Panels (d)-(f) of the same figure depict the dynamics when the system is incoherently pumped, following Eq. (II.48). Similarly, the correlator between the ground states does not decay to zero but instead reaches a positive value (e).

In both scenarios, the steady states involve only the ground states. Formation of these steady states can be disrupted by direct damping of the coherences between the ground states.

2.5 Interaction with a Single-Mode Field

In previous examples, we averaged over the electromagnetic field degrees of freedom in the Born-Markov approximation. However, in certain physical situations, these approximations break down. For instance, in the presence of a cavity, the interaction between an atomic ensemble and the resonant modes of the electromagnetic field can be studied. If the light does not rapidly escape the cavity, allowing the ensemble to exchange excitations with the field, memory effects become significant, requiring the retention of photonic degrees of freedom. This section discusses key aspects of applying our formalism to such contexts, focusing on how the statistical mixing of the initial states of two-level emitters influences their interaction with a cavity mode.

The interaction of two-level emitters with a single-mode field, in the rotating-wave approximation, is governed by the Tavis-Cummings Hamiltonian [10, 12, 13, 15]:

$$\hat{V} = \hbar g(\hat{J}_+\,\hat{a} + \hat{a}^\dagger\,\hat{J}_-). \tag{II.50}$$

This Hamiltonian leads to the quantum master equation with the following Liouvillian:

$$\mathcal{L}\,[\hat{\rho}(t)] = \frac{i}{\hbar}[\hat{\rho}(t),\,\hat{V}]. \tag{II.51}$$

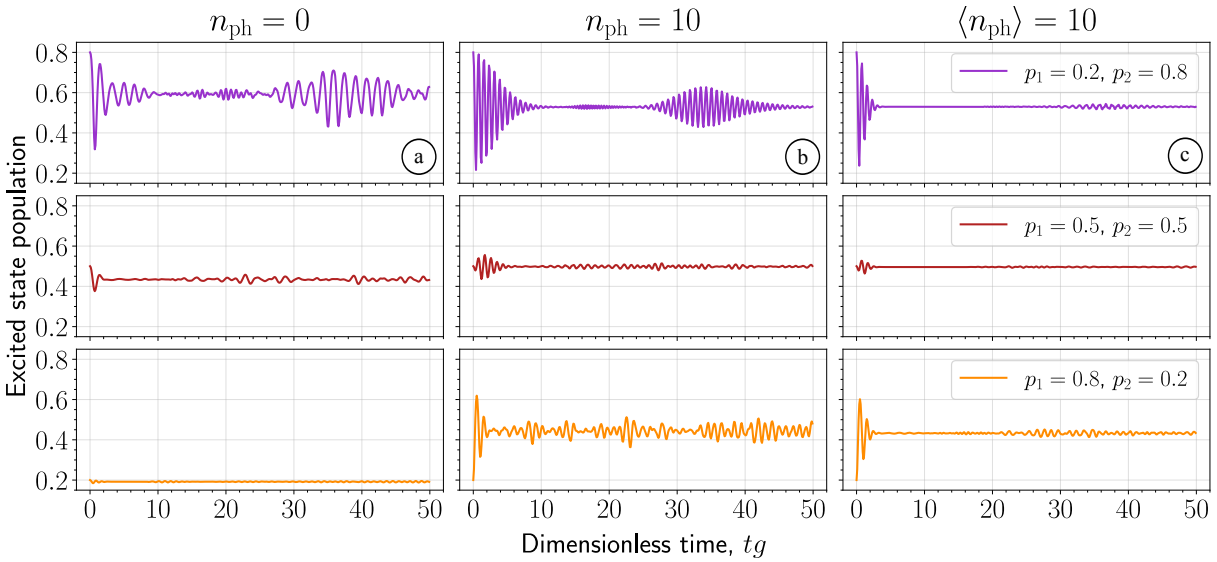

Figure II.12: Excited-state population in a compact system of $N = 20$ atoms, initially prepared in a mixed state (II.33), calculated for different initial conditions and initial field states: (a) vacuum state; (b) Fock state with $n_{\rm ph} = 10$ photons; (c) coherent state with $\langle n_{\rm ph} \rangle = 10$.

All operators are expressed in the interaction picture. The interaction term is time-independent because the cavity mode is assumed to be resonant with the atomic transition.

The composite density matrix encompasses both atomic and photonic degrees of freedom, residing in a space that is the direct product of the Liouville-Hilbert space for atoms and the Fock space for photons. Basis vectors for this composite space are:

$$|\{n_{ij}\}\rangle\!\rangle \otimes |n_L\rangle\langle n_R|, \tag{II.52}$$

where $|m\rangle$ denotes the photon Fock state with m quanta. We can compactly denote this basis as $|\{n_{ij}, n_L, n_R\}\rangle\!\rangle$, enabling density matrices to be treated as supervectors in the extended space.

The Liouvillian for the Tavis-Cummings model can now be bosonized, yielding the superoperator $\hat{\mathcal{L}}$:

$$\hat{\mathcal{L}}\,|\rho(t)\rangle\!\rangle = ig \sum_{t=1}^{2} \{\hat{a}^{\dagger\intercal}\,\hat{b}_{t2}^{\dagger}\,\hat{b}_{t1} - \hat{a}^{\dagger}\,\hat{b}_{1t}^{\dagger}\,\hat{b}_{2t} + \hat{b}_{t1}^{\dagger}\,\hat{b}_{t2}\,\hat{a}^{\intercal} - \hat{b}_{2t}^{\dagger}\,\hat{b}_{1t}\,\hat{a}\}|\rho(t)\rangle\!\rangle.$$

Here, the superscript $^\intercal$ on the photonic annihilation and creation operators indicates that these operators act on the bra side, specifically modifying the number n_R. This Liouvillian possesses two integrals of motion:

$$(\hat{n}_{22} - \hat{n}_{11}) + (\hat{n}_R + \hat{n}_L) = \text{const},$$
$$(\hat{n}_{12} - \hat{n}_{21}) + (\hat{n}_R - \hat{n}_L) = \text{const},$$

as these operators commute with the Liouvillian. Here, $\hat{n}_L = \hat{a}^{\dagger}\,\hat{a}$ and $\hat{n}_R = (\hat{a}^{\dagger}\,\hat{a})^{\intercal}$. As before, the initial state can be divided into distinct groups based on these conserved quantities, allowing for independent evolution and parallelization. Note that dissipation, such as photon leakage from the cavity, may violate the first relation.

We assume the atoms are initially in the statistically mixed state from Eq. (II.33). Figure II.12 shows the excited-state population after tracing over the photonic degrees of freedom. For interaction with the vacuum state in panel (a), instead of vacuum Rabi oscillations [171], the dynamics resemble a collapse phenomenon. Injecting $n_{\rm ph.} = 10$ photons in a Fock state results in more pronounced collapse-revival dynamics for $p_1 = 0.2$ ($p_2 = 0.8$), as shown in Fig. II.12 (b). The revival effect is weaker and collapse occurs earlier when the field is initially in the coherent state with $\langle n_{\rm ph.} \rangle = 10$, as shown in Fig. II.12 (c).

In summary, when the emitters start from a statistically mixed state, collapse-revival dynamics is observed, even when the field is initially in a vacuum or a Fock state.

3 Numerical Implementation

This section outlines the numerical implementation for solving the quantum master equation within our formalism. Readers who are not interested in the numerical aspects may skip to Sec. 4, where we discuss possible extensions of the formalism.

The basis vectors are parameterized by M^2 occupation numbers, resulting in a state space that scales polynomially with N. This introduces two primary objectives:

1. Establishing a vectorized representation of the occupation-number basis.
2. Efficiently solving a system of linear ordinary differential equations with a sparse coefficient matrix, and computing selected observables.

To achieve the first objective, we must define a one-to-one mapping between occupation-number sets and integers. In subsequent sections, we focus on implementation for two-level atoms (as discussed in Sec. 2.1) and propose a numerical implementation in `Julia v1.8.5`.[6]

3.1 Occupation-Number Basis

Occupation-number sets can be represented as tuples and mapped to integers using dictionaries. These tuples, composed of occupation numbers, serve as dictionary keys and are assigned a unique integer value.

In Sec. 2.1, we discussed the cooperative emission of two-level atoms initially prepared in the state described by Eq. (II.33). In this case, the dynamics is fully captured using occupation-number sets of the form $\{n_{11}, \ell, \ell, n_{22}\}$.

The first two numbers in the set fully determine the state since $n_{22} = N - n_{11} - 2\ell$. Therefore, tuples of type `NTuple{2, Int16}` are suitable as dictionary keys. The `Int16` type is chosen to minimize memory usage since N is not expected to be large ($N \sim 100$). The following structure can be employed to map occupation-number sets to integers and vice versa:

```
mutable struct TLS
    N      :: Int16
    dim    :: Int32
    sets   :: Vector{NTuple{2, NTuple{2, Int16}}}
    dict   :: Dict{NTuple{2, Int16}, Int32}
    ρii    :: Vector{Int32}
    ρ12ρ21 :: Vector{Int32}
    function TLS(N)
        self        = new()
        self.N      = Int16(N)
        self.dim    = Int32(0)
        self.sets   = NTuple{2, NTuple{2, Int16}}[]
        self.dict   = Dict{NTuple{2, Int16}, Int32}()
        self.ρii    = Int32[]
        self.ρ12ρ21 = Int32[]
        for n11 in Int16(0):self.N
            for ℓ in Int16(0):Int16((self.N-n11)÷2)
                self.dim += 1
                n22 = Int16(self.N-n11-ℓ-ℓ)
                push!(self.sets, ((n11,ℓ),(ℓ,n22)))
                self.dict[(n11,ℓ)] = self.dim
                if ℓ == 0
                    push!(self.ρii, self.dim)
                elseif ℓ == 1
                    push!(self.ρ12ρ21, self.dim)
                end
            end
        end
        return self
    end
end
```

A new object of type `TLS` can be created using the following snippet:

[6] Official documentation is available at https://docs.julialang.org.

```
N = 200;   # number of atoms
OccupationNumbers = TLS(N)
```

For reference, creating the object with $N = 200$ takes about 265 microseconds, with total allocations of around 541 kilobytes, as measured by `BenchmarkTools.jl`. The total size of the `OccupationNumbers` object is 231 kilobytes. To access the specific occupation number n_{ij} from the set indexed by `item`, one can use the command `OccupationNumbers.sets[item][i][j]`.

The `OccupationNumbers` object contains six fields:

1. `OccupationNumbers.N`: the number of atoms N.
2. `OccupationNumbers.dim`: the number of generated occupation-number sets.
3. `OccupationNumbers.sets`: an array containing all generated occupation-number sets.
4. `OccupationNumbers.dict`: a dictionary mapping each set to a unique integer.
5. `OccupationNumbers.ρ₁₁`: integers corresponding to sets of the form $\{n_{11}, 0, 0, n_{22}\}$.
6. `OccupationNumbers.ρ₁₂ρ₂₁`: integers corresponding to sets of the form $\{n_{11}, 1, 1, n_{22}\}$.

The last two fields are particularly important for computing expectation values.

To check if a specific key exists in the dictionary, the `get` method can be used. The efficiency of this operation can be benchmarked with the following code:

```
using BenchmarkTools
key     = (Int16(136),Int16(10));
dict    = deepcopy(OccupationNumbers.dict);
default = Int32(0);
@benchmark item = get($dict, $key, $default)
```

The third argument of the `get` method specifies the value to return if the key is not found in the dictionary. We use the `Int32` type to match the dictionary's entry format. The `@benchmark` macro reports an execution time of approximately 5.3 nanoseconds, with no additional memory allocations. For $N = 200$, the returned value of `item` is `9123`, and accessing `OccupationNumbers.sets[9123]` yields the tuple `((136, 10), (10, 44))`.

In the subsequent sections, occupation-number sets will be represented as matrices to facilitate the generation of the coefficient matrix for the differential equations. To support this, two supplementary functions are introduced.

The first function copies the values of a given tuple from `OccupationNumbers.sets` into a matrix:

```
function tupletomatrix!(matrix, set)
    @inbounds for i in eachindex(set), j in eachindex(set)
        matrix[i,j] = set[i][j]
    end
    return nothing
end
```

Benchmarking this function shows no additional memory allocations, with an execution time of around 2.2 nanoseconds.

The second function converts a matrix of occupation numbers into a corresponding tuple formatted as a dictionary key:

```
function matrixtokey(matrix)
    return NTuple{2, Int16}(transpose(matrix))
end
```

This function also creates no additional memory allocations and executes in approximately 2.5 nanoseconds.

3.2 Parameters

We define all parameters involved in the master equation, particularly the effective dipole moments $\overline{\mathbf{d}}_{ij}$ and the transition frequencies ω_{ij}. The dipole moments contribute to the master equation via scalar products, which are precomputed and stored in the following form:

$$\gamma_{ijqp} = \frac{\overline{\mathbf{d}}_{ij} \cdot \overline{\mathbf{d}}_{qp}}{2},$$

represented in the code as `γ[i,j,q,p]`. All parameters, including the `OccupationNumbers` structure and initial conditions, are collected into a named tuple `parameters`:

```
using Einsum, Parameters
M  = 2;                    # number of levels involved in emission
nᵅ = 1;                    # number of polarizations
d = zeros(Float64,M,M,nᵅ); # dipole moments; third index is a polarization axis
ω = zeros(Float64,M,M);    # transition frequencies; in our case not important
d[2,1,1] = 1.0;            # dipole moment has only x-component
d[1,2,1] = conj(d[2,1,1]);
@einsum γ[i,j,q,p] := d[i,j,α]*d[q,p,α]/2;
p₁ = 0.2;          # initial ground state population
p₂ = 1.0-p₁;       # initial excited state population
parameters = (; OccupationNumbers, M, nᵅ, d, ω, γ, p₁, p₂);
```

The parameters p_1 and p_2 represent the initial populations of the ground and excited states, respectively, and will be used to construct the initial density matrix.

3.3 Initial Density Matrix

The initial density matrix is defined in Eq. (II.34). To avoid unnecessary calculations of factorials, we notice that for $n_{11} \geq 1$ these coefficients can be computed recursively:

$$\rho(\{n_{11}, 0, 0, N - n_{11}\}, 0) = \frac{p_1}{p_2} \frac{n_{22} + 1}{n_{11}} \rho(\{n_{11} - 1, 0, 0, N - n_{11} + 1\}, 0).$$

To prevent division by zero, we should first verify that p_2 is nonzero. The following function efficiently generates the initial density matrix in the occupation-number basis:

```
function initialconditions(parameters)
    @unpack p₁, p₂       = parameters
    @unpack N, dict, dim = parameters.OccupationNumbers
    ρ₀ = zeros(Float64, dim)
    if p₁ == 1.0
        item = dict[Int16.((N,0))]
        ρ₀[item] += 1.0
    elseif p₂ == 1.0
        item = dict[Int16.((0,0))]
        ρ₀[item] += 1.0
    else
        item = dict[Int16.((0,0))]
        ρ₀[item] += p₂^N
        for n₁₁ in 1:N
            item = dict[Int16.((n₁₁,0))]
            item′ = dict[Int16.((n₁₁-1,0))]
            ρ₀[item] += ρ₀[item′]*p₁/p₂*(N-n₁₁+1)/n₁₁
        end
    end
    return ρ₀
end
```

Applying the `@benchmark` macro to the `initialconditions` function yields an average execution time of around 12 microseconds and 82 kilobytes of allocations, which is mostly the size of the created `ρ₀` object.

3.4 Set of Linear Differential Equations

For two-level atoms, the equation for the expansion coefficient $\rho(\{n_{ij}\},t)$ (provided in the footnote following Eq. (II.32)), has at most six terms on the right-hand side. The number of terms does not depend on N, while the number of variables grows as a polynomial of N. Consequently, directly implementing the differential equations as a matrix-vector product:

$$\frac{dx_i(t)}{dt} = \sum_j a_{ij}\, x_j(t),$$

is inefficient due to the sparsity of the coefficient matrix a_{ij}.

Instead, we optimize the computation by exploiting sparsity. For each row i, we define two sets: a set b_i, containing the column indices j such that $a_{ij} \neq 0$, and a set c_i of corresponding nonzero values:

$$b_i = \{j_1, j_2, \ldots, j_k, \ldots\}, \qquad c_i = \{a_{ij_1}, a_{ij_2}, \ldots, a_{ij_k}, \ldots\}.$$

In this notation, $b_i[k] = j_k$ and $c_i[k] = a_{ij_k} \neq 0$.

Using these two sets, the differential equations are expressed as:

$$\frac{dx_i(t)}{dt} = \sum_{k=1}^{\mathrm{len}(b_i)} c_i[k]\, x_{b_i[k]}(t), \tag{II.53}$$

where $\mathrm{len}(b_i)$ is the number of nonzero entries in row i. This approach significantly reduces the number of operations. In particular, in the case of two-level atoms, instead of handling matrices of size proportional to $N^2 \times N^2$, we now work with two lists, each containing a number of elements proportional to N^2.

Now, let's discuss how to determine the elements of $\{b_i\}$ and $\{c_i\}$ for the general master equation (II.31). The equation for the decomposition coefficient $\rho(\{n_{ij}\},t)$ is determined by the matrix elements of the Liouvillian, as given by Eq. (II.27), which is:

$$\frac{d\rho(\{n_{ij}\},t)}{dt} = \sum_{\{n'_{ij}\}} \underbrace{\sqrt{\frac{\prod_{i,j} n'_{ij}!}{\prod_{i,j} n_{ij}!}}\, \langle\!\langle \{n_{ij}\}|\hat{\mathcal{L}}_{\text{coll.}}|\{n'_{ij}\}\rangle\!\rangle}_{\text{analogous to } a_{ij}}\, \rho(\{n'_{ij}\},t).$$

The sets $\{n_{ij}\}$ and $\{n'_{ij}\}$ are mapped to the integers i and j using the dictionary. Accordingly, $\rho(\{n_{ij}\},t)$ corresponds to $x_i(t)$, while $\rho(\{n'_{ij}\},t)$ corresponds to $x_j(t)$.

Let's consider a specific contribution to the equation for $\rho(\{n_{ij}\},t)$, for example, the following:

$$\frac{d\rho(\{n_{ij}\},t)}{dt} = \ldots + \gamma \sum_{i,j,p,q=1}^{M} \frac{\overline{\mathbf{d}}_{i<j} \cdot \overline{\mathbf{d}}_{q>p}}{2} \sum_{\{n'_{ij}\}} \sqrt{\frac{\prod_{i,j} n'_{ij}!}{\prod_{i,j} n_{ij}!}} \times \sum_{s,t=1}^{M} \langle\!\langle \{n_{ij}\}|\, \hat{b}^\dagger_{is}\, \hat{b}^\dagger_{tp}\, \hat{b}_{js}\, \hat{b}_{tq}\, |\{n'_{ij}\}\rangle\!\rangle\, \rho(\{n'_{ij}\},t) + \ldots$$

The combination of bosonic superoperators induces different changes on the set $\{n'_{ij}\}$, depending on the indices. Consider the case when $t = j$ and $s = q$. The combination of bosonic superoperators then becomes $\hat{b}^\dagger_{iq}\, \hat{b}^\dagger_{jp}\, \hat{b}_{jq}\, \hat{b}_{jq}$, and the corresponding term is given by:

$$\gamma \frac{\overline{\mathbf{d}}_{i<j} \cdot \overline{\mathbf{d}}_{q>p}}{2}\, (n_{jq}+1)(n_{jq}+2)\, \rho(\underbrace{\{\ldots, n_{iq}-1, \ldots, n_{jp}-1, \ldots, n_{jq}+2, \ldots\}}_{=\{m_{ij}\}}, t).$$

As we can see, when a creation operator is applied, it decreases the corresponding occupation number in the density matrix argument, leaving the coefficient in front unchanged. Conversely, applying an annihilation operator increases the corresponding occupation number and introduces a coefficient based on this updated value. Following these simple rules, we can determine $\{m_{ij}\}$ and the associated multiplier for any term.

3.5 Generating Coefficient Matrix

In our implementation, the sets $\{b_i\}$ and $\{c_i\}$ are represented by the arrays `indices` and `values`. Both arrays contain `OccupationNumbers.dim` elements, where each element is a list:

```
indices = [Int32[] for _ in 1:OccupationNumbers.dim];
values  = [Float64[] for _ in 1:OccupationNumbers.dim];
```

The elements `indices[i][k]` and `values[i][k]` correspond to $b_i[k]$ and $c_i[k]$, respectively. To fill these arrays for a given i, we need to identify all variables that contribute to the equation for $x_i(t)$.

Suppose we identify a contribution from a specific occupation-number set, represented by the dictionary key, denoted by `key`, with a corresponding value, denoted by `value`. We then use the function `pushvalues!` to store the position and value in the lists `indices` and `values`, respectively:

```
function pushvalues!(indices, values, value, dict, key)
    if value != 0.0
        index = get(dict, key, Int32(0))
        if index != 0
            index′ = findfirst(isequal(index), indices)
            if isnothing(index′)
                push!(indices, index)
                push!(values, value)
            else
                values[index′] += value
            end
        end
    end
    return nothing
end
```

The function first verifies that `value` is nonzero. It then checks if `key` exists in the dictionary `dict`. If it does, the corresponding entry `index` is retrieved. Next, the function determines whether `index` is already in the incoming list `indices`. If it is, the existing value is updated by adding the incoming `value`. Otherwise, the new elements are appended to the lists using the `push!` method.

Let's consider the equation for the variable $\rho(\{n_{ij}\}, t)$. In the code, the occupation-number set $\{n_{ij}\}$ is stored in a matrix denoted by `n`. To determine all contributions, we implement the summations according to the master equation (II.31) and analyze each term individually.

When a specific combination of bosonic superoperators is encountered, the entries of the `n` matrix are modified following the rules outlined in the previous section. Additionally, a local variable `value` is introduced and updated whenever any occupation number increases. These modifications to `n` result in a modified matrix of occupation numbers, corresponding to the set $\{m_{ij}\}$ in the notation used above. Using the `matrixtokey(n)` function, we obtain the corresponding tuple, which is then passed as `key` to the `pushvalues!` function, along with the other necessary arguments.

Once these steps are completed, the `n` matrix is restored to its original form and is used to compute the remaining terms. The `fillrow!` function completes this process for a single row (indexed by i, corresponding to the occupation-number set n_{ij}):

```
function fillrow!(indices, values, n, parameters)
    @unpack M, ω, γ = parameters
    @unpack N, dict = parameters.OccupationNumbers
    @inbounds for i in 1:M, p in 1:M
        # uncomment if frequencies are relevant
        # additionally change the type of ρ₀ and values to ComplexF64
        # value = -im*ω[i,p]*float(n[i,p])
        # pushvalues!(indices, values, value, dict, matrixtokey(n))
        for j in i+1:M
            for q in i+1:M
                n[q,p] -= 1; n[j,p] += 1
                value = -γ[i,j,q,i]*float(n[j,p])
                pushvalues!(indices, values, value, dict, matrixtokey(n))
                n[q,p] += 1; n[j,p] -= 1

                n[p,j] -= 1; n[p,q] += 1
                value = -γ[i,j,q,i]*float(n[p,q])
                pushvalues!(indices, values, value, dict, matrixtokey(n))
                n[p,j] += 1; n[p,q] -= 1
            end
            for q in p+1:M
                n[i,p] -= 1; n[j,q] += 1
                value = 2*γ[i,j,q,p]*float(n[j,q])
                pushvalues!(indices, values, value, dict, matrixtokey(n))
                n[i,p] += 1; n[j,q] -= 1
                for s in 1:M, t in 1:M
                    n[i,s] -= 1; n[t,p] -= 1; n[j,s] += 1
                    value = float(n[j,s])
                    n[t,q] += 1
                    value *= 2*γ[i,j,q,p]*float(n[t,q])
                    pushvalues!(indices, values, value, dict, matrixtokey(n))
                    n[i,s] += 1; n[t,p] += 1; n[j,s] -= 1; n[t,q] -= 1

                    n[q,t] -= 1; n[i,s] -= 1; n[p,t] += 1
                    value = float(n[p,t])
                    n[j,s] += 1
                    value *= -γ[i,j,q,p]*float(n[j,s])
                    pushvalues!(indices, values, value, dict, matrixtokey(n))
                    n[q,t] += 1; n[i,s] += 1; n[p,t] -= 1; n[j,s] -= 1

                    n[s,j] -= 1; n[t,p] -= 1; n[s,i] += 1
                    value = float(n[s,i])
                    n[t,q] += 1
                    value *= -γ[i,j,q,p]*float(n[t,q])
                    pushvalues!(indices, values, value, dict, matrixtokey(n))
                    n[s,j] += 1; n[t,p] += 1; n[s,i] -= 1; n[t,q] -= 1
                end
            end
        end
    end
    return nothing
end
```

This function fills the sets b_i and c_i for a single value of i.

The complete lists are filled by the function `fillmatrix!`, which is defined below:

```
function fillmatrix!(indices, values, container, parameters)
    @unpack dim, sets = parameters.OccupationNumbers
    @inbounds for item in 1:dim
        empty!(indices[item])
        empty!(values[item])
        tupletomatrix!(container, sets[item])
        fillrow!(indices[item], values[item], container, parameters)
    end
    return nothing
end

indices   = [Int32[] for _ in 1:OccupationNumbers.dim];
values    = [Float64[] for _ in 1:OccupationNumbers.dim];
container = Matrix{Int16}(undef, 2, 2);
fillmatrix!(indices, values, container, parameters);
```

Here, we use the auxiliary object `container` to store the occupation-number sets in matrix form. Benchmarking shows that the execution takes approximately 3.65 milliseconds with no additional memory allocations. The combined size of the generated arrays `indices` and `values` is 1.7 megabytes.

For each basis element, there are at most 17 dictionary lookups. Assuming an average lookup time of 5.3 nanoseconds and multiplying this by 17 and `OccupationNumbers.dim`, we estimate the overall lookup time to be 0.92 milliseconds. The code also performs nearly the same number of matrix-to-tuple conversions, amounting to 0.43 milliseconds. Benchmarking the function `findfirst!` shows a search time of 4.7 nanoseconds, leading to a total of 0.82 milliseconds. Converting occupation-number tuples to matrix form adds 0.02 milliseconds. Altogether, these operations total 2.19 milliseconds.

The remaining execution time is due to the `push!` method, which runs about 6 times per basis element.

3.6 Solution of Differential Equations

We employ the `DifferentialEquations.jl` library for solving differential equations [155],[7] adhering to its conventions.

The right-hand side of the differential equations can be implemented via the `rhs!` function, defined as follows:

```
function sparseproduct!(dx, x, indices, values)
    @inbounds for item in 1:lastindex(dx)
        subindices = view(indices[item], :)
        subvalues  = view(values[item], :)
        for item′ in 1:lastindex(subindices)
            dx[item] += subvalues[item′]*x[subindices[item′]]
        end
    end
    return nothing
end

function rhs!(dx, x, parameters, time)
    @. dx = 0.0
    indices = parameters[1]
    values  = parameters[2]
    sparseproduct!(dx, x, indices, values)
    return nothing
end
```

The first argument, `dx`, stores the right-hand side, while `x` contains the variables. The function `sparseproduct!` numerically implements the product in Eq. (II.53). To assess the efficiency of `rhs!`, we benchmark its application to the initial density matrix. The execution time is approximately 54 microseconds, with no additional memory allocation.

We additionally define a named tuple called `parameters_ode` containing the information required to integrate the differential equations:

```
T     = 0.2;        # last time point
Nᵗ    = 150;        # number of points to save
gridᵗ = range(0.0, T, Nᵗ);
Δtᵐᵃˣ = T/1000;     # upper limit for the time stepsize
parameters_ode = (; T, Nᵗ, gridᵗ, Δtᵐᵃˣ, indices, values);
```

Since the number of variables grows polynomially with N, storing the entire density matrix at each time step becomes inefficient. Instead, we specify which elements to extract at each step and define a function to compute specific observables.

We focus on two observables: (1) the populations of the emitters' states, computed according

[7] Documentation is available at https://docs.sciml.ai/DiffEqDocs/stable/.

to Eq. (II.35a), and (2) the emission intensity, defined by Eq. (II.35b), which additionally requires elements from the list `OccupationNumbers.ρ₁₂ρ₂₁`.

To implement this, we use the tools provided by the `DiffEqCallbacks.jl` library.[8] First, we define the object `saved_values`, which specifies the data type for storage:

```
using OrdinaryDiffEq, DiffEqCallbacks
saved_values = SavedValues(Float64, Tuple{Float64, Float64, Float64});
```

At each step, data is saved as a tuple containing the ground state population, excited state population, and intensity.

The following function extracts data from the solution at a given time t:

```
cb = SavingCallback((u, t, integrator) ->
    begin
        @unpack N, sets, ρᵢᵢ, ρ₁₂ρ₂₁ = integrator.p[3]
        p₁ = 0.0
        p₂ = 0.0
        Iᵃ = 0.0
        @inbounds for item in ρᵢᵢ
            n₁₁ = sets[item][1][1]
            n₂₂ = sets[item][2][2]
            p₁ += u[item]*n₁₁/N
            p₂ += u[item]*n₂₂/N
        end
        @inbounds for item in ρ₁₂ρ₂₁
            Iᵃ += u[item]
        end
        Iᵃ += N*p₂
        return (p₁, p₂, Iᵃ)
    end, saved_values, saveat = parameters_ode.gridᵗ);
```

We use the adaptive step size method `Tsit5` to solve differential equations [155]. The function `solve_ode!` function solves the equations:

```
using RecursiveArrayTools

function solve_ode!(saving_tools, parameters_ode, parameters)
    @unpack T, Nᵗ, Δtᵐᵃˣ, indices, values = parameters_ode
    @unpack OccupationNumbers = parameters
    results, saved_values, cb = saving_tools
    parameters_rhs = (indices, values, OccupationNumbers)
    tspan = (0.0, T)
    u0 = initialconditions(parameters)
    prob = ODEProblem(rhs!, u0, tspan, parameters_rhs)

    solve(prob, Tsit5(), adaptive=true, callback=cb, dtmax=Δtᵐᵃˣ, save_everystep
     =false, save_start=false, save_end=false)

    p₁, p₂, Iᵃ = results.x
    @inbounds for time in 1:Nᵗ
        p₁[time] = saved_values.saveval[time][1]
        p₂[time] = saved_values.saveval[time][2]
        Iᵃ[time] = saved_values.saveval[time][3]
    end
    return nothing
end

p₁ = zeros(Float64, parameters_ode.Nᵗ); # array for ground state population
p₂ = zeros(Float64, parameters_ode.Nᵗ); # array for excited state population
Iᵃ = zeros(Float64, parameters_ode.Nᵗ); # array for intensity
results = ArrayPartition(p₁, p₂, Iᵃ);

saving_tools = (results, saved_values, cb);
solve_ode!(saving_tools, parameters_ode, parameters);
```

[8] Documentation is available at https://docs.sciml.ai/DiffEqCallbacks/stable/.

Benchmarking the `solve_ode!` function provides the following estimates: the mean evaluation time is approximately 418 milliseconds, with total memory allocations of around 1.4 megabytes. For the given parameters, the `rhs!` function was called 6543 times. Multiplying this by the average execution time of 54 microseconds, the total time spent on calling `rhs!` amounts to about 353 milliseconds. This suggests that most of the `solve_ode!` execution time is spent on repeated right-hand side evaluations.

For completeness, we provide the code snippet for plotting the observables:

```
using Plots
ρ₁₁, ρ₂₂, Iᵃ = results.x
plot(gridᵗ, [p₁, p₂])
plot(gridᵗ, Iᵃ)
```

For a system with $N = 200$ atoms, the total execution time is approximately (440 ± 19) milliseconds, with a memory allocation reaching 7.5 megabytes. For $N = 100$, these characteristics reduce to (105 ± 4) milliseconds and 2.6 megabytes. For $N = 50$ atoms, they further reduce to (29 ± 1) milliseconds and 1.1 megabytes. This reduction in execution time by a factor of approximately 4, when decreasing the number of atoms by a factor of 2, agrees with the expected complexity scaling of N^2.

4 Supplementary Sections

This section includes additional topics that, while not essential to the main flow of the text, are still valuable as they demonstrate further applications of the formalism. Readers interested in these extensions will find discussions on constructing fermionic density matrices (Sec. 4.1), treating operators as supervectors (Sec. 4.2), extending the theory to systems with local symmetry or the Bose-Hubbard models (Sec. 4.3), and analyzing the interparticle correlations (Sec. 4.4). Those not interested in these topics may proceed directly to the conclusion in Sec. 5.

4.1 Fermionic Density Matrices

This section presents an example of constructing collective antisymmetric states, useful in applications involving electronic shells. This possibility was briefly mentioned at the end of Sec. 1.6, when the vacuum superstate was introduced.

The Pauli exclusion principle requires that the number of available states, M, must exceed the number of particles, N. The antisymmetric state of N fermions occupying N distinct states $i_1, i_2, \ldots, i_N$ can be expressed as a Slater determinant:

$$|i_1,\ldots,i_N\rangle_A = \frac{1}{\sqrt{N!}} \begin{vmatrix} |i_1\rangle_1 & |i_1\rangle_2 & \ldots & |i_1\rangle_N \\ |i_2\rangle_1 & |i_2\rangle_2 & \ldots & |i_2\rangle_N \\ \vdots & \vdots & \ddots & \vdots \\ |i_N\rangle_1 & |i_N\rangle_2 & \ldots & |i_N\rangle_N \end{vmatrix} = \frac{1}{\sqrt{N!}} \sum_{\substack{p_1,\ldots,p_N \\ \in\{i_1,\ldots,i_N\}}} \epsilon_{p_1\ldots p_N} |p_1\rangle_1 \otimes \ldots \otimes |p_N\rangle_N .$$

Here, the determinant is expanded using the Leibniz formula, with the antisymmetric Levi-Civita symbol $\epsilon_{i_1 i_2 \ldots i_N} = 1$. The indices $p_1, \ldots, p_N$ take distinct values from the set $\{i_1, \ldots, i_N\}$. The subscript A denotes "antisymmetric."

A general pure state is a superposition of the states $|i_1, \ldots, i_N\rangle_A$. Correspondingly, density matrices are linear combinations of operators $|i_1, \ldots, i_N\rangle_A \langle j_1, \ldots, j_N|_A$, which can also be

expressed using the Levi-Civita symbol:

$$|i_1,\dots,i_N\rangle_A\,\langle j_1,\dots,j_N|_A = \frac{1}{N!}\sum_{\substack{p_1,\dots,p_N\\ \in\{i_1,\dots,i_N\}}}\ \sum_{\substack{q_1,\dots,q_N\\ \in(j_1,\dots,j_N)}} \epsilon_{p_1\dots p_N}\,\epsilon_{q_1\dots q_N}\,\hat{\sigma}_{1,p_1q_1}\dots\hat{\sigma}_{N,p_Nq_N} = \dots$$

Permuting any pair of particles on the right-hand side changes the sign twice, maintaining symmetry. Consequently, symmetrizing over particle labels only yields a factor of $N!$. The resulting symmetrized combination of σ-operators can be constructed by applying creation superoperators to the vacuum superstate:

$$\dots \longleftrightarrow \frac{1}{N!\sqrt{N!}}\sum_{\substack{p_1,\dots,p_N\\ \in\{i_1,\dots,i_N\}}}\ \sum_{\substack{q_1,\dots,q_N\\ \in\{j_1,\dots,j_N\}}} \epsilon_{p_1\dots p_N}\,\epsilon_{q_1\dots q_N}\,\hat{b}^\dagger_{p_1q_1}\dots\hat{b}^\dagger_{p_Nq_N}\,|\mathrm{vac}\rangle\rangle = \dots$$

In this representation, one sum is redundant because summing over the q-indices yields identical terms for any selection of p-indices. This is due to the exchange symmetry of bosonic superoperators, allowing them to be freely permuted. The first sum merely contributes a factor of $N!$, resulting in:

$$\dots = \frac{1}{\sqrt{N!}}\sum_{\substack{q_1,\dots,q_N\\ \in\{j_1,\dots,j_N\}}} \epsilon_{q_1\dots q_N}\,\hat{b}^\dagger_{i_1q_1}\dots\hat{b}^\dagger_{i_Nq_N}\,|\mathrm{vac}\rangle\rangle.$$

The right-hand side has a determinant structure. By applying the Leibniz formula once more, we obtain the following representation:

$$|i_1,\dots,i_N\rangle_A\,\langle j_1,\dots,j_N|_A \longleftrightarrow \frac{1}{\sqrt{N!}}\begin{vmatrix} \hat{b}^\dagger_{i_1j_1} & \hat{b}^\dagger_{i_1j_2} & \dots & \hat{b}^\dagger_{i_1j_N}\\ \hat{b}^\dagger_{i_2j_1} & \hat{b}^\dagger_{i_2j_2} & \dots & \hat{b}^\dagger_{i_2j_N}\\ \vdots & \vdots & \ddots & \vdots\\ \hat{b}^\dagger_{i_Nj_1} & \hat{b}^\dagger_{i_Nj_2} & \dots & \hat{b}^\dagger_{i_Nj_N}\end{vmatrix}|\mathrm{vac}\rangle\rangle. \tag{II.54}$$

A general fermionic density matrix is a linear combination of such superstates.

4.2 Observables as Supervectors

At the end of Sec. 1.7, we mentioned an alternative interpretation of superoperators as supervectors in the Liouville-Hilbert space [110, 111, 154]. In this section, we expand on this concept and demonstrate how to derive the occupation-number representation of symmetric superoperators.

The trace of an operator $\hat{\mathcal{O}}$ acting on a density matrix $\hat{\rho}$ can be understood as an inner product in the Liouville-Hilbert space [110, 111, 154]:

$$\langle\mathcal{O}\rangle = \mathrm{Tr}\left[\hat{\mathcal{O}}\,\hat{\rho}\right] = \langle\langle\rho|\mathcal{O}\rangle\rangle. \tag{II.55}$$

Here, $|\mathcal{O}\rangle\rangle$ denotes the supervector corresponding to the operator $\hat{\mathcal{O}}$. Such a supervector exists because every operator in the Liouville space has a corresponding representation in the Liouville-Hilbert space. This section focuses on identifying the rules for determining the components of these supervectors in the occupation-number basis.

Consider a general K-particle operator defined in Eq. (II.23):

$$\hat{\mathcal{O}}^{(K)} = \sum_{\boldsymbol{p},\boldsymbol{q}}\mathcal{O}^{(K)}_{\boldsymbol{pq}}\sum_{\mu_1\neq\dots\neq\mu_K}\hat{\sigma}_{\mu_1,p_1q_1}\,\dots\,\hat{\sigma}_{\mu_K,p_Kq_K}.$$

This operator has the same structure as the density matrix in Eq. (II.4), except that it is not normalized and seemingly involves only K particles. The remaining $N-K$ particles are represented by identity operators. By explicitly inserting these identity operators, the right-hand side transforms into an N-particle symmetric operator, which can then be expressed in the occupation-number basis, analogous to density matrices.

We propose the following representation for symmetric operators in the occupation-number basis:

$$|\mathcal{O}\rangle\!\rangle = \sum_{\{n_{pq}\}} \sqrt{\frac{N!}{\prod_{i,j} n_{ij}!}}\, \mathcal{O}(\{n_{pq}\})\, |\{n_{pq}\}\rangle\!\rangle. \tag{II.56}$$

This representation compensates for the multinomial factor present in the density matrices in Eq. (II.14) when calculating expectation values. The expansion coefficients $\mathcal{O}(\{n_{pq}\})$ are nonzero only for sets summing up to N. The expectation value of this operator is then determined by combining its supervector components with those of the density matrix:

$$\langle \mathcal{O} \rangle = \sum_{\{n_{pq}\}} \rho(\{n_{qp}\})\, \mathcal{O}(\{n_{pq}\}), \tag{II.57}$$

where the transposed set $\{n_{qp}\}$ defines a new set $\{m_{pq}\}$ such that $m_{pq} \equiv n_{qp}$.

The main task is to determine the supervector components $\mathcal{O}(\{n_{pq}\})$. While symmetric K-particle operators can be complemented to N-particle operators by inserting identity operators, this approach is cumbersome.

Instead, we derive K-particle operators as derivatives of a properly defined N-particle operator parameterized by M^2 variables $\{\lambda_{ij}\}$. This characteristic functional is given by:

$$\hat{\mathcal{F}}(\{\lambda_{ij}\}) = \prod_{\mu=1}^{N} \Big\{ \sum_{i,j=1}^{M} \lambda_{ij}\, \hat{\sigma}_{\mu,ij} \Big\}. \tag{II.58}$$

For a given set of variables $\{\lambda_{ij}\}$, this functional resembles the density matrix of uncorrelated particles in Eq. (II.15). However, the λ-parameters do not have a physical interpretation and are independent of each other.

Taking derivative of the functional (II.58) with respect to any λ-parameter selects the corresponding symmetrized combination of σ-operators. For example:

$$\frac{\partial \hat{\mathcal{F}}(\{\lambda_{ij}\})}{\partial \lambda_{pq}} = \sum_{\mu=1}^{N} \hat{\sigma}_{\mu,pq} \prod_{\substack{\nu=1 \\ \nu\neq\mu}}^{N} \Big\{ \sum_{i,j=1}^{M} \lambda_{ij}\, \hat{\sigma}_{\nu,ij} \Big\}.$$

Setting $\lambda_{ij} = \delta_{ij}$, the product of operators over $\nu \neq \mu$ simplifies to an identity operator. This yields the symmetric one-particle operator $\hat{J}_{pq}$:

$$\hat{J}_{pq} = \frac{\partial \hat{\mathcal{F}}(\{\lambda_{ij}\})}{\partial \lambda_{pq}}\bigg|_{\lambda_{ij}=\delta_{ij}}.$$

To construct a general K-particle operator, we differentiate the functional K times:

$$\hat{\mathcal{O}}^{(K)} = \sum_{\boldsymbol{p},\boldsymbol{q}} \mathcal{O}^{(K)}_{\boldsymbol{pq}} \frac{\partial^K \hat{\mathcal{F}}(\{\lambda_{ij}\})}{\partial \lambda_{p_1 q_1} \dots \partial \lambda_{p_K q_K}}\bigg|_{\lambda_{pq}=\delta_{pq}}, \tag{II.59}$$

where $\boldsymbol{p} = (p_1, \dots, p_K)$ and $\boldsymbol{q} = (q_1, \dots, q_K)$.

The key property of the functional is its similarity to density matrices. Using this analogy, we find the corresponding supervector representation $|\mathcal{F}(\{\lambda_{ij}\})\rangle\!\rangle$ as in Eq. (II.56):

$$|\mathcal{F}(\{\lambda_{ij}\})\rangle\!\rangle = \sum_{\{n_{ij}\}} \sqrt{\frac{N!}{\prod_{ij} n_{ij}!}}\, \mathcal{F}(\{\lambda_{ij}, n_{ij}\})\, |\{n_{ij}\}\rangle\!\rangle,$$

with the decomposition coefficients given by:

$$\mathcal{F}(\{\lambda_{ij}, n_{ij}\}) = \prod_{i,j=1}^{M} (\lambda_{ij})^{n_{ij}}.$$

This expression represents a product of all λ-coefficients, where the power of each λ_{ij} is determined by the occupation numbers n_{ij}.

Returning to Eq. (II.59), we replace the operators $\hat{\mathcal{O}}^{(K)}$ and $\hat{\mathcal{F}}(\{\lambda_{ij}\})$ with their supervector counterparts. The resulting expression can be seen as the definition of the supervector $|\mathcal{O}^{(K)}\rangle\!\rangle$, corresponding to the symmetric operator $\hat{\mathcal{O}}^{(K)}$:

$$|\mathcal{O}^{(K)}\rangle\!\rangle = \sum_{\boldsymbol{p},\boldsymbol{q}} \mathcal{O}^{(K)}_{\boldsymbol{pq}} \frac{\partial^K |\mathcal{F}(\{\lambda_{ij}\})\rangle\!\rangle}{\partial\lambda_{p_1q_1} \dots \partial\lambda_{p_Kq_K}}\bigg|_{\lambda_{ij}=\delta_{ij}}. \tag{II.60}$$

Then, the supervector components are found by applying the same differentiating operator to $\mathcal{F}(\{\lambda_{ij}, n_{ij}\})$:

$$\mathcal{O}^{(K)}(\{n_{ij}\}) = \sum_{\boldsymbol{p},\boldsymbol{q}} \mathcal{O}^{(K)}_{\boldsymbol{pq}} \frac{\partial^K \mathcal{F}(\{\lambda_{ij}, n_{ij}\})}{\partial\lambda_{p_1q_1} \dots \partial\lambda_{p_Kq_K}}\bigg|_{\lambda_{ij}=\delta_{ij}}. \tag{II.61}$$

This expression can be used to find the expectation value of the operator, following Eq. (II.57).

Two-Time Correlation Functions

The theory developed in this section can be used to compute a special class of averages, particularly two-time correlation functions of the following structure:

$$X(t,\tau) = \langle \hat{\mathcal{A}}^\dagger(t+\tau)\, \hat{\mathcal{B}}(t) \rangle = \mathrm{Tr}\left[\hat{\mathcal{A}}^\dagger\, \hat{U}(\tau)\, \hat{\mathcal{B}}\, \hat{\rho}(t)\right],$$

where $\hat{\mathcal{A}}$ and $\hat{\mathcal{B}}$ are operators associated with the system of particles, and $\hat{U}(\tau)$ is the evolution operator governed by the equation:

$$\frac{d\hat{U}(t)}{dt} = \mathcal{L}[\hat{U}(t)], \quad \hat{U}(0) = 1,$$

where the Liouvillian $\mathcal{L}[\dots]$ also governs the evolution of the density matrix.

Examining the two-time correlator, we interpret it as an inner product in the Liouville-Hilbert space. By properly inserting and rearranging the evolution operators, we can rewrite the correlator as follows:

$$X(t,\tau) = \langle\!\langle \mathcal{A}(\tau) | \hat{\mathcal{B}} | \rho(t) \rangle\!\rangle. \tag{II.62}$$

Here, the supervector $|\mathcal{A}(\tau)\rangle\!\rangle$, representing the operator $\hat{\mathcal{A}}$, evolves according to the adjoint master equation [128]:

$$\frac{d|\mathcal{A}(\tau)\rangle\!\rangle}{d\tau} = \hat{\mathcal{L}}^\dagger |\mathcal{A}(\tau)\rangle\!\rangle. \tag{II.63}$$

The solution to this equation represents a time-dependent object used to compute the specific correlation function. Notably, in the absence of dissipation, Eq. (II.63) reduces to the Heisenberg equation.

For two-level atoms, spectral line shapes are presented in Fig. II.2(d, e). The spectrum is obtained by averaging the Fourier transforms of the electric field. In the time domain, this average corresponds to a two-time correlation function. Specifically, for two-level atoms, the spectral line shape can be expressed as [119]:

$$S(\omega) \sim \mathrm{Re} \int_0^\infty dt \int_0^\infty d\tau\, X(t,\tau)\, e^{-i\omega\tau},$$

where $X(t,\tau)$ is the two-time correlation function, given by:

$$X(t,\tau) = \langle \hat{J}_{21}(t+\tau)\, \hat{J}_{12}(t) \rangle = \langle\!\langle J_{12}(\tau) | \hat{J}_{12} | \rho(t) \rangle\!\rangle.$$

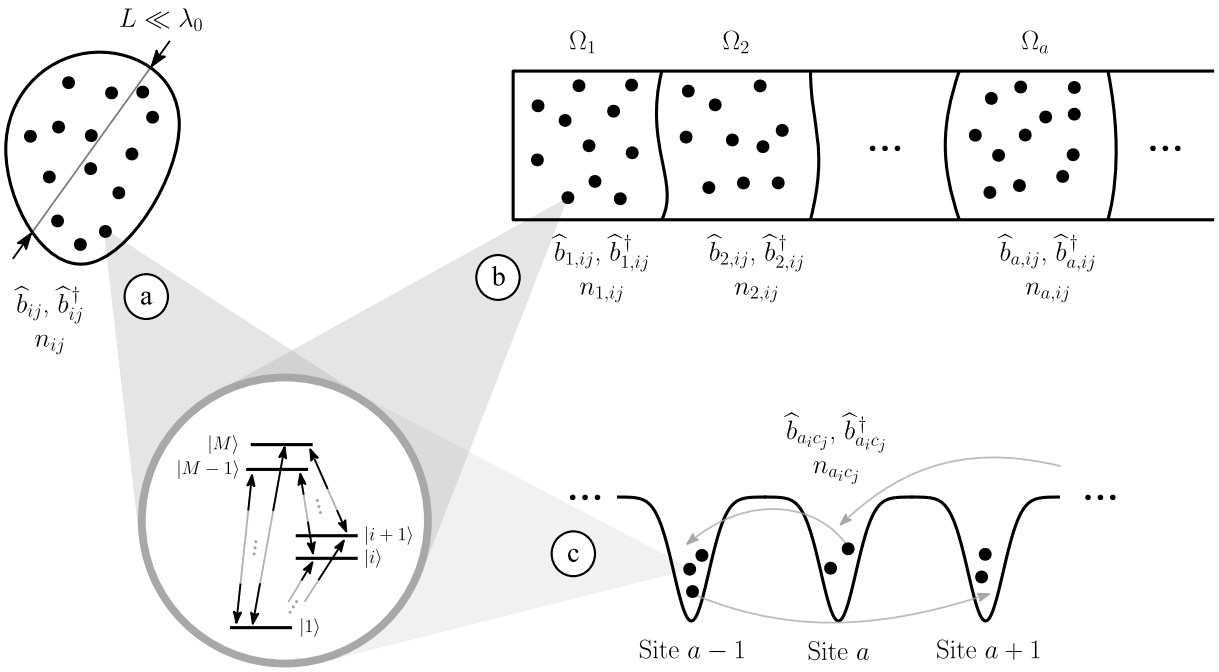

Figure II.13: Schematic representation of systems involving M-level emitters to which the developed formalism applies. (a) A compact system containing N particles confined to a region with a spatial size L, much smaller than any characteristic wavelength λ_0. (b) An extended, pencil-shaped medium subdivided into smaller subregions Ω_1, Ω_2, and so on, each with dimensions much smaller than the characteristic wavelength, enabling local quantization. (c) A Bose-Hubbard model with multiple lattice sites, where particles can hop between sites while potentially altering their internal states.

The supervector $|J_{12}(\tau)\rangle\rangle$ evolves over time according to the adjoint master equation (II.63), with the initial condition:

$$|J_{12}(0)\rangle\rangle = \sum_{\substack{n_{11},n_{22} \\ n_{11}+n_{22}=N-1}} \sqrt{\frac{N!}{n_{11}!\,n_{22}!}}\,|\{n_{11},1,0,n_{22}\}\rangle\rangle,$$

which is a direct consequence of expressions derived in this section.

4.3 Coarse-Grained Description and Bose-Hubbard Model

Up to this point, our focus has been on ensembles with global permutation symmetry, where particles are treated as indistinguishable (Fig. II.13 (a)). However, this framework can be extended to systems exhibiting local permutation symmetry, such as spatially extended systems.

In light-matter interactions, a pencil-shaped medium can be divided into smaller subregions, each with dimensions smaller than the characteristic emission wavelength. Within each subregion, particles are indistinguishable, and second quantization can be applied independently in each of them. A similar approach to quantization in Hilbert space was previously discussed for two-level systems (see Ref. [57]).

Consider a sample divided into small subregions, denoted as Ω_1, Ω_2, …, Ω_a,…, as illustrated in Fig. II.13 (b). By independently quantizing each subregion, we define local bosonic superoperators characterized by the commutation relations:

$$[\hat{b}_{a,ij},\, \hat{b}^\dagger_{c,st}] = \delta_{ac}\,\delta_{is}\,\delta_{jt}. \tag{II.64}$$

The subscripts a and c denote specific subregions Ω_a and Ω_c. This expression indicates that superoperators for different subregions commute with each other.

Local operators for the subregion Ω_a are defined by summing single-particle operators over all emitters confined within Ω_a. These local operators are bosonized as follows:

$$\sum_{\mu\in\Omega_a} \hat{\sigma}_{\mu,pq}\,\hat{\rho}\,\hat{\sigma}_{\mu,k\ell} \longleftrightarrow \hat{b}^\dagger_{a,p\ell}\,\hat{b}_{a,qk}\,|\rho\rangle\!\rangle. \tag{II.65}$$

Local occupation numbers $\{n_{a,pq}\}$ are introduced for each subregion Ω_a. The occupation-number basis is then parameterized by these local occupation numbers:

$$\hat{b}_{a,pq}\,|\{\ldots,n_{a,pq},\ldots\}\rangle\!\rangle = \sqrt{n_{a,pq}}\;|\{\ldots,n_{a,pq}-1,\ldots\}\rangle\!\rangle,$$
$$\hat{b}^\dagger_{a,pq}\,|\{\ldots,n_{a,pq},\ldots\}\rangle\!\rangle = \sqrt{n_{a,pq}+1}\;|\{\ldots,n_{a,pq}+1,\ldots\}\rangle\!\rangle.$$

We assume the number of emitters in Ω_a, denoted by N_a, remains constant. The total number of states in the occupation-number basis is then:

$$\prod_a \binom{N_a+M^2-1}{N_a} = \prod_a \frac{(N_a+M^2-1)!}{N_a!\,(M^2-1)!}. \tag{II.66}$$

When all particles are confined within a single subregion, the polynomial dependence from Eq. (II.12) is recovered. In the opposite case, where there are N subregions, each containing only a single particle ($N_a = 1$), the number of states grows exponentially as M^{2N}.

However, the scaling in Eq. (II.66) is too rapid for practical numerical studies of realistic systems. For instance, with just five subregions containing N two-level atoms, the number of basis vectors scales approximately as $N^{15}/6^5$.

The assumption of particle conservation within each subregion can be relaxed. The additional local index a can be used to distinguish different sites, as in the Bose-Hubbard model. In this model, N identical particles, each with M internal degrees of freedom, can localize at any of K sites. Particles may hop between these sites, changing their internal states, as illustrated in Fig. II.13 (c).

The notation $|a_i\rangle_\mu$ represents the μ-th emitter in the internal state $|i\rangle$, localized at the a-th site, with indices $i = 1,\ldots M$ and $a = 1,\ldots,K$. A particle hopping from site a to c and changing its internal state from $|i\rangle$ to $|j\rangle$ is described by the following transition operator:

$$|c_j\rangle_\mu\,\langle a_i|_\mu.$$

If inter-site hopping is forbidden, the previously described local superoperators suffice for modeling. When hopping is allowed, new bosonic superoperators $\hat{b}_{a_ic_j}$ and $\hat{b}^\dagger_{a_ic_j}$ must be introduced, satisfying the commutation relations:

$$[\hat{b}_{a_ic_j},\,\hat{b}^\dagger_{b_sd_t}] = \delta_{ab}\,\delta_{cd}\,\delta_{is}\,\delta_{jt},$$

with corresponding occupation numbers denoted by $\{n_{a_ic_j}\}$. The number of basis elements is then:

$$\binom{N+M^2K^2-1}{N} \sim \frac{N^{M^2K^2-1}}{(M^2K^2-1)!}.$$

For a single internal state ($M = 1$) and three sites ($K = 3$), the number of basis elements grows approximately as $N^8/8!$, significantly constraining the feasibility of a direct numerical solution.

Nevertheless, both frameworks from this section can be integrated with computational methods like tensor-network states [172, 173], or stochastic methods, as will be discussed in Chapter III (specifically, Sec. 3.5).

4.4 Partial Trace Operator

Our formalism has been primarily employed to derive a minimal set of equations governing the dynamics of emitters. However, its applicability extends further. Once a density matrix is determined, either analytically or numerically, its structure can be examined. For instance, if

the density matrix has a separable tensor product structure, as in Eq. (II.15), tracing out the degrees of freedom of any particle does not affect the state of the others.

This brings us to the concept of quantum entanglement, widely recognized for its applications in quantum information science [174]. Entanglement is well understood for distinguishable particles: when two entangled particles can be individually addressed in an experiment, a measurement upon one particle influences the state of the other. However, the concept of quantum entanglement becomes more contentious when applied to identical particles [175, 176]. Due to (anti)-symmetrization, the states of identical particles have inseparable structures, leading to their formal classification as entangled. Yet, because identical particles cannot be individually addressed, this interpretation of entanglement remains debated.

Some authors define the entanglement of identical operators as correlations that extend beyond those arising solely from (anti)-symmetrization [177]. A more practical approach seeks to project these correlations onto distinguishable degrees of freedom [178, 179]. The goal of this section is not to establish criteria for identifying entanglement but rather to propose a tool for analyzing the structure of a given density matrix.

The presence of correlations implies that measurements upon one particle affect the others. A theoretical method for probing these correlations is to take a partial trace over one or more particles. Since the particles are identical, the outcome is independent of which particles are traced out.

Taking a partial trace effectively reduces the number of particles in the system. To construct a linear operator $\hat{T}$ that excludes a particle from the density matrix, it must be proportional to annihilation superoperators. Supervectors $|i \neq j\rangle\!\rangle$ do not contribute to the trace, as their trace is zero. Consequently, the partial trace operator must be proportional to annihilation superoperators with matching indices, specifically $\hat{T} \sim \sum_i \hat{b}_{ii}$.

The partial trace must preserve both the norm and the probabilistic interpretation of the resulting density matrix. When the annihilation superoperator $\hat{b}_{ii}$ is applied, it introduces a factor of $\sqrt{n_{ii}}$. To give a probabilistic meaning to this factor, it should be divided by the square root of the total number of particles before taking the trace, yielding the square root of the probability of finding a particle in state $|ii\rangle\!\rangle$. These heuristic considerations lead to the definition of the operator:

$$\hat{T} = \frac{1}{\sqrt{\hat{N}+1}} \sum_{i=1}^{M} \hat{b}_{ii}. \tag{II.67}$$

Applying this operator K times traces out K particles from the state. This can be rigorously derived by explicitly computing the partial trace of a density matrix in the occupation-number basis, using the representation of basis vectors in Eq. (II.11).

For uncorrelated particles, as described in Eq. (II.15), let us denote the state by $\hat{\rho}_N$ to emphasize the number of particles. Then, applying the partial trace $K < N$ times results in the same state but with $N - K$ particles:

$$\hat{T}^K |\rho_N\rangle\!\rangle = |\rho_{N-K}\rangle\!\rangle.$$

An illustrative example of a non-trivial state with an inseparable structure is the Dicke state of two-level atoms, $|L_N\rangle\!\rangle$, where L out of N atoms are excited (Sec. 1.4). Tracing out $K < N$ particles from this state yields the following statistical mixture:

$$\hat{T}^K |L_N\rangle\!\rangle = \sum_{\ell=0}^{K} \frac{\binom{L}{\ell}\binom{N-L}{K-\ell}}{\binom{N}{K}} |(L-\ell)_{N-K}\rangle\!\rangle. \tag{II.68}$$

The same result was obtained in Ref. [180]. Notably, the coefficients in this sum resemble a hypergeometric distribution. If a discrete random variable x follows a hypergeometric distribution, the probability of $x = \ell$ is given by:

$$\binom{L}{\ell}\binom{N-L}{K-\ell} \Big/ \binom{N}{K}.$$

Here, N is the population size (number of particles), L is the number of "success" states in the population (number of excited atoms before tracing), K is the number of "draws" (number of excluded particles), and ℓ is the number of observed successes. These coefficients also appear in the bipartitions of Dicke states [181, 182] and serve as Schmidt decomposition coefficients.

To analyze the structure of a symmetric density matrix, one can follow a straightforward procedure. The purity of the quantum state is determined by the norm of the density matrix in the Liouville-Hilbert space:

$$\mathrm{Tr}\left[\hat{\rho}^{\,2}\right] = \langle\langle\rho|\rho\rangle\rangle.$$

If this norm equals one, the state is pure. By applying the partial trace operator, the reduced density matrix $\hat{T}|\rho\rangle\rangle$ is obtained. The norm of the reduced density matrix determines the purity of the resulting quantum state:

$$\langle\langle\rho|\hat{T}^\dagger\,\hat{T}|\rho\rangle\rangle.$$

If this value is less than one, it implies that tracing out a particle results in a statistical mixture, revealing an inseparable tensor structure in the original *pure* density matrix. For example, Dicke states produce statistical mixtures upon tracing out particles, as shown in Eq. (II.68). In contrast, for the density matrix of uncorrelated particles in Eq. (II.15), where ρ_{pq} represent a pure state, the resulting state always has a unit norm.

If the original density matrix is statistically mixed, identifying purely quantum correlations becomes problematic, making this criterion unreliable.

Let's consider the density matrices defined in Eq. (II.15) for general values of ρ_{pq}. Tracing out K particle results in the density matrix $|\rho_{N-K}\rangle\rangle$. The logarithm of the norm of this density matrix, divided by the number of remaining particles, is invariant with respect to the total number of particles:

$$\frac{\ln\left[\langle\langle\rho_{N-K}|\rho_{N-K}\rangle\rangle\right]}{N-K} = \sum_{i,j=1}^{M}\rho_{ij}\,\rho_{ji}.$$

This invariance allows for identifying such structures. However, the density matrices defined in Eq. (II.15) do not encompass all mixed states of uncorrelated particles, which may be generated by alternative mixing protocols, such as general diagonal symmetric states [183]. Depending on the specific context, the procedure may require further refinement.

5 Conclusion

In conclusion, we have developed the second-quantized representation of density matrices in Liouville space, as summarized in Sec. 1.8. This framework was applied in Sec. 2 to analyze collective emission in two- and three-level systems of identical emitters prepared in statistically mixed states or excited by incoherent pumping.

We investigated the effects of statistical mixing on collective emission, identified a class of dark many-body steady states, and characterized their properties. By deriving some analytical solutions, we established a relationship between the behavior of correlators and the symmetry properties of the states.

A numerical implementation of the formalism is detailed in Sec. 3, with potential extensions discussed in Sec. 4.

As for limitations, the polynomial scaling of the number of basis states still constrains the feasibility of a direct numerical implementation. Additionally, we encountered numerical instabilities, as illustrated in Fig. II.3. The formalism offers limited advantages when applied to spatially extended systems or Bose-Hubbard models.

A possible extension of the formalism may help overcome these limitations. By leveraging bosonic superoperators, we can define an analogue of the coherent-state basis and represent the density matrix in this basis. This approach enables a phase-space description of the dynamics, which can be efficiently sampled using stochastic differential equations. The next chapter explores this possibility in depth.

Chapter III

Stochastic Methodology for Superradiance

In Chapter II, we focused on medium-sized quantum systems with around 100 atoms. However, for larger systems (typically $N \gtrsim 10^3$), the polynomial growth in the number of basis elements becomes a significant limitation. Additionally, when using explicit methods to solve large systems of differential equations, we encounter numerical instabilities, as shown in Fig. II.3. Despite its efficacy, the method is limited to ensembles with $N \lesssim 150$ atoms.

Phase-space techniques have the potential to overcome this limitation. The quantum master equation can be converted into a Fokker-Planck equation for a positive P function [97, 99, 122]. This approach is well-suited for systems of bosons, where the density matrix is represented as a combination of the following projection operators in the coherent state basis [99]:

$$\hat{\Lambda}(\alpha, \alpha^\dagger) = \frac{|\alpha\rangle\langle\alpha^{\dagger *}|}{\langle\alpha^{\dagger *}|\alpha\rangle}, \tag{III.1}$$

and can be extended to two-level systems [98, 184–188] by introducing spin-coherent states [189–192]. Here, α and $\alpha^\dagger$ are independent complex variables, representing the eigenvalues of the annihilation operator, $\hat{a}|\alpha\rangle = \alpha|\alpha\rangle$.

The projection operators in Eq. (III.1) convert bosonic operators into c-numbers, leading to the following property:

$$\mathrm{Tr}\left[\hat{a}^\dagger\, \hat{a}\, \hat{\Lambda}(\alpha, \alpha^\dagger)\right] = \alpha^\dagger \alpha. \tag{III.2}$$

In other words, the coherent ket maps the annihilation operator $\hat{a}$ to the number α, and the coherent bra maps the creation operator $\hat{a}^\dagger$ to the number $\alpha^\dagger$. This holds for any normal-ordered combination of bosonic operators.

The density matrix can be expressed as the following superposition of the operators $\hat{\Lambda}$:

$$\hat{\rho}(t) = \int d^2\alpha \int d^2\alpha^\dagger\, P(\alpha, \alpha^\dagger, t)\, \hat{\Lambda}(\alpha, \alpha^\dagger), \tag{III.3}$$

where the integration runs over the entire complex plane for α and $\alpha^\dagger$. Notably, $\alpha^\dagger \not\equiv \alpha^*$; equating them yields the Glauber-Sudarshan representation [95, 96]. The expectation value of any normal-ordered combination of bosonic operators can then be calculated using integrals with the P function:

$$\mathrm{Tr}\left[\hat{a}^\dagger\, \hat{a}^\dagger \ldots \hat{a}\, \hat{\rho}(t)\right] = \frac{\int d^2\alpha \int d^2\alpha^\dagger\, \alpha^\dagger\, \alpha^\dagger \ldots \alpha\, P(\alpha, \alpha^\dagger, t)}{\int d^2\alpha \int d^2\alpha^\dagger\, P(\alpha, \alpha^\dagger, t)}.$$

This implies that the P function can be interpreted as a probability density function. Additionally, this formalism can be used to construct many-time correlators, as shown in Ref. [193].

We can derive a partial differential equation for the P function from the master equation for the density matrix. If the quantum master equation contains no terms with more than two

annihilation or creation operators, the resulting equation for the P function takes the form of a Fokker-Planck equation.

This approach is known as the positive P representation, where P is positive, and the corresponding Fokker-Planck equation has a positive semidefinite diffusion matrix [97, 103]. In this framework, averages obtained using the P function can be computed using a Monte Carlo approach by solving Itô stochastic differential equations for the dynamical variables.

In this chapter, we extend the positive P formalism to open quantum systems of N identical M-level emitters. Our formalism of second quantization in Chapter II reformulates the dynamics in terms of M^2 harmonic oscillators, represented by M^2 pairs of bosonic superoperators. Therefore, we can adapt the positive P formalism with minimal adjustments. The following sections provide a step-by-step derivation and detailed discussion of the method, with a summary in Sec. 1.8.

1 General Formalism

Our goal is to construct a representation in Liouville-Hilbert space analogous to Eq. (III.3). The projection operators in Eq. (III.1) consist of coherent-state bra and ket vectors. However, in Liouville-Hilbert space, only superkets exist, meaning that the corresponding "projection" superoperator must be represented as a supervector. After bosonization, we have M^2 annihilation superoperators $\hat{b}_{ij}$. We now aim to construct a coherent-state analogue for these superoperators.

For many-mode bosonic fields, each bosonic operator $\hat{a}_f$ is associated with a distinct eigenvalue α_f. Similarly, we assume that each bosonic superoperator $\hat{b}_{ij}$ is associated with a parameter β_{ij}, giving a total of M^2 independent parameters.

We denote the supervector analogue of the Λ-projection operator as $|\Lambda(\{\beta_{ij}\})\rangle\!\rangle$, where $\{\beta_{ij}\}$ represents the set of parameters introduced above. The following ansatz is proposed for the density matrix:

$$|\rho(t)\rangle\!\rangle = \int \prod_{i,j=1}^{M} (d^2\beta_{ij})\, P(\{\beta_{ij}\}, t)\, |\Lambda(\{\beta_{ij}\})\rangle\!\rangle, \tag{III.4}$$

where the integration runs over M^2 independent complex numbers β_{ij}.

The supervector $|\Lambda(\{\beta_{ij}\})\rangle\!\rangle$ should satisfy an analogous property to Eq. (III.2), where operators are translated into numbers. For emitters, the relevant operators include σ-operators and bosonic superoperators. For example, applying the collective operator $\hat{J}_{qp}$ from Eq. (II.6) to the supervector $|\Lambda(\{\beta_{ij}\})\rangle\!\rangle$ and bosonizing it according to Eq. (II.22) yields:

$$\mathrm{Tr}\left[\hat{J}_{qp}\, |\Lambda(\{\beta_{ij}\})\rangle\!\rangle\right] \equiv \mathrm{Tr}\left[\hat{b}^{\dagger}_{qq}\, \hat{b}_{pq}\, |\Lambda(\{\beta_{ij}\})\rangle\!\rangle\right]. \tag{III.5}$$

Our objective is to find Λ-supervectors such that the right-hand side simplifies to β_{pq}.

A supervector, created by applying a standard displacement operator to the vacuum superstate, does not satisfy the desired property, as discussed in Sec. 5.1. To achieve the desired outcome, the displacement operator must be slightly modified, yielding the following expression:

$$|\Lambda(\{\beta_{ij}\})\rangle\!\rangle = \exp\left[-\sum_{p=1}^{M} \beta_{pp} + \frac{1}{\sqrt{\hat{N}}} \sum_{p,q=1}^{M} \beta_{pq}\, \hat{b}^{\dagger}_{pq}\right] |\mathrm{vac}\rangle\!\rangle. \tag{III.6}$$

The first term in the exponent ensures that this supervector has a unit trace. This differs from the conventional displacement operator by the additional factor of $\hat{N}^{-1/2}$, where $\hat{N} = \sum_{i,j} \hat{b}^{\dagger}_{ij}\, \hat{b}_{ij}$ is the particle number operator. The properties of these supervectors are analyzed in Sec. 5.1.

The supervector in Eq. (III.6) does not directly map bosonic superoperators to numbers. Instead, it transforms the following combinations of these operators with $\hat{N}^{\pm 1/2}$:

$$\begin{aligned} \hat{b}_{pq} \sqrt{\hat{N}}\, |\Lambda(\{\beta_{ij}\})\rangle\!\rangle &= \beta_{pq}\, |\Lambda(\{\beta_{ij}\})\rangle\!\rangle, \\ \frac{1}{\sqrt{\hat{N}}}\, \hat{b}^{\dagger}_{pq}\, |\Lambda(\{\beta_{ij}\})\rangle\!\rangle &= \Big(\frac{\partial}{\partial \beta_{pq}} + \delta_{pq}\Big) |\Lambda(\{\beta_{ij}\})\rangle\!\rangle. \end{aligned}$$

The first line shows that β_{pq} directly corresponds to the annihilation superoperator $\hat{b}_{pq}$. The second line, after tracing, reduces to δ_{pq}, revealing that there are no separate phase-space variables for the creation superoperators. Typically, annihilation $\hat{a}$ and creation $\hat{a}^\dagger$ operators are associated with independent complex variables α and $\alpha^\dagger$, doubling the number of phase-space variables. However, in our supervector formulation, bosonic superoperators $\hat{b}_{pq}$ and $\hat{b}^\dagger_{pq}$ are represented solely by the numbers β_{pq}.[1]

Incorporating factors of $\hat{N}^{\pm 1/2}$ does not alter the quantum master equation, as long as the number of emitters is fixed. Additionally, any bosonized symmetric operator contains equal numbers of annihilation and creation superoperators, according to Eq. (II.24), thereby ensuring the conservation of the number of emitters. This allows the inclusion of factors $\hat{N}^{\pm 1/2}$ directly in bosonized expressions of symmetric operators. As a result, Eq. (III.5) simplifies to:

$$\mathrm{Tr}\left[\hat{J}_{qp}\,|\Lambda(\{\beta_{ij}\})\rangle\!\rangle\right] \equiv \mathrm{Tr}\Big[\frac{1}{\sqrt{\hat{N}}}\,\hat{b}^\dagger_{qq}\,\hat{b}_{pq}\,\sqrt{\hat{N}}\;|\Lambda(\{\beta_{ij}\})\rangle\!\rangle\Big] = \beta_{pq}. \tag{III.7}$$

The quantum master equation for the density matrix can be transformed into a partial differential equation for the function $P(\{\beta_{ij}\},t)$ by applying the following replacement rules:

$$\hat{b}_{pq}\,\sqrt{\hat{N}}\;|\rho(t)\rangle\!\rangle \longrightarrow \beta_{pq}\,P(\{\beta_{ij}\},t), \tag{III.8a}$$

$$\frac{1}{\sqrt{\hat{N}}}\,\hat{b}^\dagger_{pq}\,|\rho(t)\rangle\!\rangle \longrightarrow \Big(\delta_{pq} - \frac{\partial}{\partial\beta_{pq}}\Big)P(\{\beta_{ij}\},t). \tag{III.8b}$$

Before applying these rules, the associated Liouvillian must first be bosonized and expressed in normal order. When the Liouvillian includes terms with at most two creation or two annihilation superoperators, the equation for the P-function takes the form of a Fokker-Planck equation.

Using the ansatz for the density matrix in Eq. (III.4), we can relate quantum-mechanical expectation values to statistical averages computed with the P-function:

$$\sum_{\mu_1\neq\ldots\neq\mu_K}\mathrm{Tr}\left[\hat{\sigma}_{\mu_1,q_1p_1}\ldots\hat{\sigma}_{\mu_K,q_Kp_K}\,\hat{\rho}(t)\right] = \frac{\displaystyle\int\prod_{i,j=1}^{M}(d^2\beta_{ij})\,\beta_{p_1q_1}\,\ldots\,\beta_{p_Kq_K}\,P(\{\beta_{ij}\},t)}{\displaystyle\int\prod_{i,j=1}^{M}(d^2\beta_{ij})\,P(\{\beta_{ij}\},t)}, \tag{III.9}$$

where $K \leq N$. Note that the indices of the β-variables on the right-hand side are in reverse order relative to those of the σ-operators on the left-hand side. The interpretation of many-time correlators follows the general principles of the positive P formalism, as described in Ref. [193].

These results form the basis for further investigations. In the next section, we derive the Fokker-Planck equation corresponding to a model Liouvillian that includes terms quadratic and quartic in bosonic superoperators.

1.1 Fokker-Planck Equation

We now apply the principles from the previous section to a model Liouvillian and derive the corresponding Fokker-Planck equation. Our focus will be on a class of Liouvillians that include symmetric one-particle and two-particle operators. After bosonization, these Liouvillians comprise terms that are quadratic and quartic in bosonic superoperators. When expressed in normal order, the bosonized Liouvillian takes the form:

$$\hat{\mathcal{L}} = \sum_{p,q,r,s}\mathscr{L}^{rs}_{pq}\,\hat{b}^\dagger_{pq}\,\hat{b}_{rs} + \sum_{\substack{p,q,r,s\\p',q',r',s'}}\mathscr{L}^{rsr's'}_{pqp'q'}\,\hat{b}^\dagger_{pq}\,\hat{b}^\dagger_{p'q'}\,\hat{b}_{rs}\,\hat{b}_{r's'}.$$

[1] Mathematically, this arises from the structure of Liouville-Hilbert space, where both the bra and ket components of density matrices can be accessed through superoperators acting from the left. One could consider that the phase space is already extended as variables β_{ij} are indexed by pairs of indices.

The placement of the indices (upper and lower) is chosen for convenience and does not imply tensorial properties. The first term, which is quadratic, can describe the Lindblad operators in Eq. (II.26) or free oscillations. The quartic term represents two-particle interactions and vanishes when there is only one emitter. It is important to note that the bosonized Liouvillian no longer explicitly encodes the number of emitters; this information is specified solely through the initial conditions.

This Liouvillian defines the quantum master equation (II.25) for the density matrix. It should conserve probability, meaning that the density matrix should always have a unit trace. This leads to the following constraints on the Liouvillian coefficients:

$$\sum_p \mathscr{L}^{rs}_{pp} = 0, \qquad \sum_{p,q} \mathscr{L}^{rsr's'}_{ppqq} = 0.$$

We represent the density matrix as in Eq. (III.4) and apply the replacement rules from Eqs. (III.8) to transform the quantum master equation into a partial differential equation for the P function. This yields the following Fokker-Planck equation:

$$\frac{\partial P(\{\beta_{ij}\},t)}{\partial t} = -\sum_{p,q} \frac{\partial}{\partial \beta_{pq}} \Big[\{\mathscr{A}_{pq}(\{\beta_{ij}\}) + \sum_n \mathscr{D}_{pqnn}(\{\beta_{ij}\})\} P(\{\beta_{ij}\},t) \Big] + \frac{1}{2} \sum_{p,q,p',q'} \frac{\partial^2}{\partial \beta_{pq} \partial \beta_{p'q'}} \Big[\mathscr{D}_{pqp'q'}(\{\beta_{ij}\})\, P(\{\beta_{ij}\},t) \Big]. \quad \text{(III.10a)}$$

The first-order derivatives represent the *drift* terms, while the second-order derivatives correspond to the *diffusion* terms. The functions $\mathscr{A}_{pq}(\{\beta_{ij}\})$ define the linear components of the drift as:

$$\mathscr{A}_{pq}(\{\beta_{ij}\}) = \sum_{r,s} \mathscr{L}^{rs}_{pq}\, \beta_{rs}. \quad \text{(III.10b)}$$

This linear contribution originates from the quadratic term of the Liouvillian. The drift function also includes a quadratically nonlinear component, determined by the diffusion matrix elements. The diffusion matrix is given by:

$$\mathscr{D}_{pqp'q'}(\{\beta_{ij}\}) = \sum_{r,s,r',s'} (\mathscr{L}^{rsr's'}_{pqp'q'} + \mathscr{L}^{rsr's'}_{p'q'pq})\, \beta_{rs}\, \beta_{r's'}, \quad \text{(III.10c)}$$

which satisfies $\mathscr{D}_{pqp'q'}(\{\beta_{ij}\}) \equiv \mathscr{D}_{p'q'pq}(\{\beta_{ij}\})$. This matrix is determined by the quartic component of the Liouvillian.

1.2 Itô Stochastic Differential Equations

The P-function describes the statistical properties of phase-space variables. Averages computed using this function can be found using a Monte Carlo approach by generating stochastic trajectories in phase space [88, 122]. These trajectories are found as solutions to Itô stochastic differential equations for the dynamical variables. For the Fokker-Planck equation in Eq. (III.10a), the stochastic equations are:

$$\frac{d\beta_{pq}(t)}{dt} = \mathscr{A}_{pq}(\{\beta_{ij}(t)\}) + \sum_n \mathscr{D}_{pqnn}(\{\beta_{ij}(t)\}) + F_{pq}(\{\beta_{ij}(t)\},t). \quad \text{(III.11a)}$$

Here, the deterministic part stems from the drift terms in the Fokker-Planck equation. The terms $F_{pq}(\{\beta_{ij}\},t)$ represent stochastic processes, with zero means and correlation properties defined by the diffusion matrix in Eq. (III.10c):

$$\langle F_{pq}(\{\beta_{ij}\},t)\, F_{p'q'}(\{\beta_{ij}\},t')\rangle = \mathscr{D}_{pqp'q'}(\{\beta_{ij}\})\, \delta(t-t'). \quad \text{(III.11b)}$$

The right-hand side is quadratically nonlinear in $\{\beta_{ij}\}$. Depending on the structure of the tensor on the right-hand side of Eq. (III.10c), it can be decomposed into a sum of lower-order tensors as follows:

$$\mathscr{D}_{pqp'q'}(\{\beta_{ij}\}) = \sum_\alpha \Big\{ \sum_{r,s} \mathscr{B}^{(\alpha)}_{pqrs}\, \beta_{rs} \sum_{r',s'} \mathscr{B}^{(\alpha)}_{p'q'r's'}\, \beta_{r's'} \Big\}, \quad \text{(III.11c)}$$

where $\mathscr{B}^{(\alpha)}_{pqrs}$ are coefficients determined by the Liouvillian. This decomposition enables the representation of stochastic processes in terms of elementary noise terms:

$$F_{pq}(\{\beta_{ij}\},t) = \sum_{\alpha} \mathrm{S}_{\alpha}(t) \sum_{r,s} \mathscr{B}^{(\alpha)}_{pqrs}\, \beta_{rs}, \tag{III.11d}$$

where $\mathrm{S}_{\alpha}(t)$ are independent Gaussian white noise processes with zero means and delta-correlated second moments:

$$\langle \mathrm{S}_{\alpha}(t)\, \mathrm{S}_{\beta}(t') \rangle = \delta_{\alpha\beta}\, \delta(t-t').$$

When Eq. (III.11c) holds, the noise terms in Eq. (III.11d) exhibit the correlation properties in Eq. (III.11b). In this way, we formulate a noise representation that is linear in $\{\beta_{ij}\}$.

The decomposition presented in Eq. (III.11c) is not universally guaranteed, nor can we provide general expressions. However, in the specific context of our physical problems, this representation does apply. For the quantum master equation in Eq. (II.31), the coefficients of the quartic contributions are proportional to scalar products of dipole moments. These products can be decomposed into component-wise sums, yielding expressions similar to Eq. (III.11c). We expect the minimum number of noise terms $\mathrm{S}_{\alpha}(t)$ to be determined by the number of polarization components of the dipole moments.

Stochastic differential equations are solved by generating multiple realizations of the noise processes and initial conditions, followed by averaging the resulting trajectories. In theory, correct expectation values are obtained as the number of realizations approaches infinity. However, in practice, numerical implementation is limited to a finite number of realizations, raising convergence issues that we will address later.

The expectation value in Eq. (III.9) can now be calculated by directly averaging over the stochastic realizations:

$$\sum_{\mu_1 \neq \ldots \neq \mu_K} \mathrm{Tr}\left[\hat{\sigma}_{\mu_1,q_1p_1} \ldots \hat{\sigma}_{\mu_K,q_Kp_K}\, \hat{\rho}(t)\right] = \langle \beta_{p_1q_1}(t) \ldots \beta_{p_Kq_K}(t) \rangle, \tag{III.12}$$

where $K \leq N$. The statistical average on the right-hand side is understood as the following limit:

$$\frac{1}{N_{\mathrm{traj.}}} \sum_{n=1}^{N_{\mathrm{traj.}}} \beta^{(n)}_{p_1q_1}(t) \ldots \beta^{(n)}_{p_Kq_K}(t) \longrightarrow \langle \beta_{p_1q_1}(t) \ldots \beta_{p_Kq_K}(t) \rangle,$$

as the number of trajectories $N_{\mathrm{traj.}}$ tends to infinity. The superscript $^{(n)}$ distinguishes different stochastic realizations, and $\beta^{(n)}_{pq}(t)$ are solutions of the stochastic equations for a specific realization of the noise processes and initial conditions.

In principle, we can average combinations of stochastic variables even when their number exceeds the number of emitters, namely $K > N$. Although such averages lack physical meaning, they may still exhibit non-trivial dynamics and nonzero values, potentially distorting the physical expectation values. Indeed, we can derive a hierarchy of equations for the expectation values, similar to those in Eq. (I.27). The equation for the average of K stochastic variables typically depends on the averages of $K+1$ variables. When formulating the equation for an average of N variables, all expectation values involving $N+1$ variables should be set to zero.

However, the stochastic equations we derived contain no information about the number of emitters. This information is encoded solely in the initial conditions, as the ensemble is prepared in a state with a specific number of emitters. Accurately specifying the initial conditions is therefore crucial to exclude contributions from nonphysical expectation values.

1.3 Initial Conditions for Stochastic Variables

At $t = 0$, the statistical properties of the phase-space variables are characterized by the function $P(\{\beta_{ij}\}, 0)$, indicating that the initial conditions for the stochastic variables are generally non-deterministic. According to Eq. (III.12), the average of any combination of stochastic

variables corresponds to the expectation value of a specific symmetric operator, which can be bosonized via Eq. (II.24). Denoting the initial density matrix as $|\rho_0\rangle\!\rangle$, we write:

$$\langle \beta_{p_1q_1}(0) \ldots \beta_{p_Kq_K}(0) \rangle = \mathrm{Tr}\left[\hat{b}^\dagger_{q_1q_1} \ldots \hat{b}^\dagger_{q_Kq_K} \hat{b}_{p_1q_1} \ldots \hat{b}_{p_Kq_K} |\rho_0\rangle\!\rangle\right], \tag{III.13a}$$

where $K \leq N$. This average can be computed directly when the density matrix is represented in the occupation-number basis as in Eq. (II.14), with decomposition coefficients $\rho_0(\{n_{ij}\})$.[2] Assuming the particles are initially in the uncorrelated state described by Eq. (II.15), the average in Eq. (III.13a) becomes:

$$\langle \beta_{p_1q_1}(0) \ldots \beta_{p_Kq_K}(0) \rangle = \frac{N!}{(N-K)!} \rho_{p_1q_1} \ldots \rho_{p_Kq_K}, \tag{III.13b}$$

where $K \leq N$. Otherwise, when $K > N$, applying K annihilation superoperators to a state of N emitters destroys the state, resulting in zero.

The expression in Eq. (III.13b) defines statistical moments for the distribution $P(\{\beta_{ij}\}, 0)$, thereby establishing the initial statistics of the stochastic variables. Notably, all moments higher than N vanish. A similar expression for the initial conditions was derived in Ref. [194].

Following Ref. [194], we introduce a new statistical object, denoted as η, which possesses exactly N nonzero statistical moments determined by Eq. (III.13b). To incorporate the properties of this object into the stochastic variables, we apply the following change of variables:

$$\beta_{pq}(t) = N\beta'_{pq}(t)\eta. \tag{III.14}$$

To reproduce the averages at $t = 0$ in Eq. (III.13b), the statistical moments of η must be:

$$\langle \eta^K \rangle = \begin{cases} \dfrac{N!}{(N-K)!\,N^K}, & 0 \leq K \leq N, \\ 0, & K > N. \end{cases} \tag{III.15}$$

Here, the brackets $\langle \ldots \rangle$ denote an average over the distribution of η. Then, the left-hand side of Eq. (III.13b) becomes:

$$\langle \beta_{p_1q_1}(0) \ldots \beta_{p_Kq_K}(0) \rangle = N^K \langle \eta^K \rangle \, \beta'_{p_1q_1}(0) \ldots \beta'_{p_Kq_K}(0).$$

Due to properties of η, this expression nullifies when $K > N$. The primed variables at $t = 0$ are deterministic numbers, $\beta'_{pq}(0) = \rho_{pq}$, and the function $P(\{\beta_{ij}\}, 0)$, reformulated in terms of the primed variables β'_{ij}, is proportional to a product of delta functions:

$$P(\{\beta'_{ij}\}, 0) = \prod_{p,q} \delta(\beta'_{pq} - \rho_{pq}).$$

Thus, the initial distribution is now entirely represented by the η-object.

The connection between averages of unprimed and primed variables is given by:

$$\langle \beta_{p_1q_1}(t) \ldots \beta_{p_Kq_K}(t) \rangle_{\text{stoch.}+\eta} = N^K \langle \eta^K \, \beta'_{p_1q_1}(t) \ldots \beta'_{p_Kq_K}(t) \rangle_{\text{stoch.}+\eta}, \tag{III.16}$$

where the averaging is performed over both realizations of η and stochastic processes. The variables $\beta'_{ij}(t)$ still depend on η, which explicitly appears in their equations, particularly in

[2] The result is:

$$\langle \beta_{p_1q_1}(0) \ldots \beta_{p_Kq_K}(0) \rangle = \sum_{\substack{\{n_{ij}\} \\ n_{i\neq j} = k_{i\neq j}}} \rho_0(\{n_{ij}\}) \prod_{p,q=1}^{M} \frac{n_{pq}!}{(n_{pq} - k_{pq})!},$$

where $K \leq N$. Here, k_{pq} denotes the frequency of each pair of indices p, q in the combination of stochastic variables in Eq. (III.13a). For example, in $\langle \beta_{12}(0)\,\beta_{22}(0)\,\beta_{22}(0)\,\beta_{21}(0) \rangle$, the counts are $k_{11} = 0$, $k_{12} = 1$, $k_{21} = 1$, and $k_{22} = 2$. The summation on the right-hand side runs over all sets summing up to N, where the numbers with distinct indices $n_{p\neq q}$ coincide with the respective counts $k_{p\neq q}$, and the diagonal occupations satisfy $n_{pp} \geq k_{pp}$.

the nonlinear drift term. Averaging over η nullifies expectation values involving more than N variables.

In the limit of a large number of emitters, all statistical moments of the η-object approach one, making it effectively deterministic. Consequently, in such ensembles, the statistical properties of η can either be neglected or treated as a small correction. Thus, stochastic equations (III.11) remain unchanged.

Conversely, when $N = 1$, the quartic term in the Liouvillian vanishes, eliminating both diffusion and nonlinear drift components in the corresponding Fokker-Planck equation. The dynamics is then governed solely by equations derived from the quadratic component of the Liouvillian. Applying stochastic equations (III.11) in this case would introduce artifacts, as the noise terms become redundant.

In the general case, where N is not necessarily large, the η-object poses a challenge because it cannot be sampled like a conventional random variable. Although the initial conditions are deterministic, the equations for the variables $\beta'_{ij}(t)$ still depend on η. One possible solution is to introduce a hierarchy of stochastic variables for different orders of η up to N. However, this approach results in a linear increase in the number of variables with N, which limits the feasibility of numerical solutions.

An alternative approach involves modifying the P-function to introduce new stochastic variables independent of η. This modification allows for explicit averaging over η in Eq. (III.16), thereby eliminating its influence. This method will be explored in the next section.

1.4 Stochastic Variables for N Emitters

To summarize, directly implementing the η-object, which has only N nonzero statistical moments defined in Eq. (III.15), is challenging and demands additional computational effort. This highlights the need to derive stochastic equations for new stochastic variables that are entirely independent of η.

If stochastic equations (III.11) had no nonlinear drift components, one could simply divide both sides by η after the change of variables in Eq. (III.14), and then average over it in Eq. (III.16). The nonlinear drift components arise from the quartic term in the Liouvillian, which contributes through the Kronecker deltas in the replacement rule (III.8b). These Kronecker deltas, in turn, originate from the normalization factor $e^{-\sum_i \beta_{ii}}$ in the definition of the Λ-supervectors in Eq. (III.6).

If we extract this normalization factor from the Λ-supervector and incorporate it into the definition of the P-function, the replacement rule for creation superoperators in Eq. (III.8) would change. Specifically, each creation superoperator is replaced by a derivative with respect to the corresponding phase-space variable, without the Kronecker delta term. This modification affects only the drift functions, leaving the diffusion matrix unchanged. In this representation, there are no nonlinear drift components, thus allowing the equations to be divided by η.

In Sec. 5.2, we provide a detailed analysis of non-normalized Λ-supervectors. As noted above, the exclusion of the normalization factor can be interpreted as a redefinition of the probability density function. For instance, a similar transformation plays a pivotal role in the quantum-state diffusion formalism, where it shifts the noise terms—the so-called Girsanov transformation [83]. Furthermore, this transformation serves as a specific example of stochastic gauge freedom [100, 101].

In Sec. 5.3, we outline the steps required to eliminate the η-object in the "non-normalized" representation. The process begins with a change of variables as in Eq. (III.14), which removes η from both the equations and the initial conditions. This allows averaging over η in the expressions for expectation values. However, the resulting representation has several inconveniences, such as cumbersome expressions for averages. These issues are addressed in the same section by performing a second transformation of the P-function.[3]

As a result, we derive a new set of stochastic variables, $\rho_{pq}(t)$, which are entirely independent

[3] This idea of eliminating η was proposed by Stasis Chuchurka.

of η and satisfy the following Itô stochastic equations:

$$\frac{d\rho_{pq}(t)}{dt} = \mathscr{A}_{pq}(\{\rho_{ij}(t)\}) + (N-1)\sum_n \mathscr{D}_{pqnn}(\{\rho_{ij}(t)\}) + F_{pq}(\{\rho_{ij}(t)\},t) - \rho_{pq}(t)\sum_s F_{ss}(\{\rho_{ij}(t)\},t), \quad \text{(III.17a)}$$

where the stochastic processes $F(\{\rho_{ij}\},t)$ keep their original correlation properties from Eq. (III.11b) but are now parameterized by the new variables:

$$\langle F_{pq}(\{\rho_{ij}\},t)\, F_{p'q'}(\{\rho_{ij}\},t')\rangle = \mathscr{D}_{pqp'q'}(\{\rho_{ij}\})\,\delta(t-t'). \quad \text{(III.17b)}$$

Comparing these new equations with the original ones in Eqs. (III.11), several differences become apparent. First, the multiplier of the nonlinear term is now $(N-1)$, reflecting that it describes two-particle interactions, which vanish for a single particle. Second, there is an additional noise contribution represented by the last term, which is quadratically nonlinear in the stochastic variables.

The nonlinear noise contribution ensures that the sum of the "diagonal" stochastic variables equals one for each realization. Using equations (III.17a), we derive:

$$\frac{d}{dt}\Big[1-\sum_r \rho_{rr}(t)\Big] = -\Big[1-\sum_r \rho_{rr}(t)\Big]\sum_s F_{ss}(\{\rho_{ij}(t)\},t).$$

At $t=0$, the expression under the derivative is zero, namely $1-\sum_r \rho_{rr}(0)=0$, and this term appears as a multiplier on the right-hand side. In the Itô formalism, such a multiplier remains zero since the coefficients of the noise terms are evaluated at the preceding time step. Consequently, the stochastic variables are normalized at every time step, ensuring that $\sum_r \rho_{rr}(t)=1$ for each realization, effectively reducing the number of independent variables by one.

The relationship between statistical averages and quantum-mechanical expectation values is given by:

$$\langle \rho_{p_1q_1}(t)\,\ldots\,\rho_{p_Kq_K}(t)\rangle = \frac{(N-K)!}{N!}\sum_{\mu_1\neq\ldots\neq\mu_K} \mathrm{Tr}\left[\hat{\sigma}_{\mu_1,q_1p_1}\,\ldots\,\hat{\sigma}_{\mu_K,q_Kp_K}\,\hat{\rho}(t)\right], \quad \text{(III.17c)}$$

when $K \leq N$. Otherwise, the averages are nonphysical and have no influence on the dynamics.

At time $t=0$, stochastic variables $\rho_{pq}(t)$ are deterministic numbers ρ_{pq} originating from the initial density matrix in Eq. (II.15):

$$\rho_{pq}(0) = \rho_{pq}, \quad \text{(III.17d)}$$

requiring no additional statistical sampling or computational effort.

It is important to note, however, that for individual realizations, the variables $\rho_{pq}(t)$ do not form a physical density matrix. These variables are generally complex-valued and do not satisfy the Hermiticity condition before averaging, namely $\rho^*_{pq}(t) \not\equiv \rho_{qp}(t)$ for $t>0$ (but $\langle\rho^*_{pq}(t)\rangle \equiv \langle\rho_{qp}(t)\rangle$). They become meaningful only after averaging over a sufficiently large number of stochastic realizations. Given these properties, we refer to $\rho_{pq}(t)$ as a *stochastic density matrix*, emphasizing that physically meaningful results are obtained only after statistical averaging.

The same set of equations can be derived through an alternative approach. Starting with the density matrix in Eq. (II.15) and allowing the coefficients ρ_{ij} to evolve over time, one can obtain equations for these time-dependent variables directly from the quantum master equation. However, the resulting equations lack quantum correlations since all particles in state (II.15) are uncorrelated. We introduce noise terms specifically designed to restore the neglected quantum correlations, yielding the same set of stochastic differential equations [109, 195]. While this alternative approach requires fewer derivation steps, the formalism used in this dissertation has the advantage of being integrated into the positive P formalism, ensuring both a probabilistic interpretation and a consistent correspondence between quantum and statistical averages.

1.5 Stochastic Differential Equations for Light-Matter Interaction

The previous sections established a general theory for systems of N identical emitters. Here, we apply this framework to the Born-Markov master equation presented in Eq. (II.31). This equation is reformulated as a Fokker-Planck equation of the form in Eq. (III.10a), with the following diffusion matrix:

$$\mathscr{D}_{pqp'q'}(\{\beta_{ij}\}) = \frac{\gamma}{2}\sum_{r,r'=1}^{M}\Big\{\overline{\mathbf{d}}_{p<r}\,\beta_{rq}\cdot(\beta_{p'r'}\,\overline{\mathbf{d}}_{r'>q'} - \overline{\mathbf{d}}_{p'>r'}\,\beta_{r'q'}) + \beta_{pr}\,\overline{\mathbf{d}}_{r>q}\cdot(\overline{\mathbf{d}}_{p'<r'}\,\beta_{r'q'} - \beta_{p'r'}\,\overline{\mathbf{d}}_{r'<q'}) + \beta_{p'r'}\,\overline{\mathbf{d}}_{r'>q'}\cdot(\overline{\mathbf{d}}_{p<r}\,\beta_{rq} - \beta_{pr}\,\overline{\mathbf{d}}_{r<q}) + \overline{\mathbf{d}}_{p'<r'}\,\beta_{r'q'}\cdot(\beta_{pr}\,\overline{\mathbf{d}}_{r>q} - \overline{\mathbf{d}}_{p>r}\,\beta_{rq})\Big\}.$$

These matrix elements also make a nonlinear contribution to the drift. The linear component of the drift is given by:

$$\mathscr{A}_{pq}(\{\beta_{ij}\}) = -i\omega_{pq}\beta_{pq} + \frac{\gamma}{2}\sum_{r,s=1}^{M}\{2\beta_{rs}\,(\overline{\mathbf{d}}_{p<r}\cdot\overline{\mathbf{d}}_{s>q}) - (\overline{\mathbf{d}}_{p>r}\cdot\overline{\mathbf{d}}_{r<s})\,\beta_{sq} - \beta_{pr}\,(\overline{\mathbf{d}}_{r>s}\cdot\overline{\mathbf{d}}_{s<q})\}.$$

As before, the notation $p>q$ ($p<q$) in the subscripts of the dipole moments signifies that the associated summation runs over all indices p,q such that $p>q$ ($p<q$).

Following Sec. 1.4, we transform the variables $\beta_{pq}(t)$ to $\rho_{pq}(t)$, which satisfy the following Itô stochastic equations:

$$\begin{aligned}\frac{d\rho_{pq}(t)}{dt} &= -i\omega_{pq}\,\rho_{pq}(t)\\ &+\frac{\gamma}{2}\sum_{r,s=1}^{M}\{2\rho_{rs}(t)\,(\overline{\mathbf{d}}_{p<r}\cdot\overline{\mathbf{d}}_{s>q}) - (\overline{\mathbf{d}}_{p>r}\cdot\overline{\mathbf{d}}_{r<s})\,\rho_{sq}(t) - \rho_{pr}(t)\,(\overline{\mathbf{d}}_{r>s}\cdot\overline{\mathbf{d}}_{s<q})\}\\ &+\frac{\gamma(N-1)}{2}\,\boldsymbol{\mathcal{P}}^{(+)}(t)\cdot\sum_{r=1}^{M}\{\rho_{pr}(t)\,\overline{\mathbf{d}}_{r>q} - \overline{\mathbf{d}}_{p>r}\,\rho_{rq}(t)\}\\ &+\frac{\gamma(N-1)}{2}\,\boldsymbol{\mathcal{P}}^{(-)}(t)\cdot\sum_{r=1}^{M}\{\overline{\mathbf{d}}_{p<r}\,\rho_{rq}(t) - \rho_{pr}(t)\,\overline{\mathbf{d}}_{r<q}\}\\ &+F_{pq}(\{\rho_{ij}(t)\},t) - \rho_{pq}(t)\sum_{s=1}^{M}F_{ss}(\{\rho_{ij}(t)\},t).\end{aligned} \tag{III.18a}$$

Initially, the ensemble is in the state (II.15), where all particles are uncorrelated, and the initial conditions are $\rho_{pq}(0)=\rho_{pq}$. The polarization fields $\boldsymbol{\mathcal{P}}^{(\pm)}(t)$ are defined analogously to their quantum-mechanical counterparts in Eq. (II.29):

$$\boldsymbol{\mathcal{P}}^{(+)}(t) = \sum_{i,j=1}^{M}\overline{\mathbf{d}}_{i<j}\,\rho_{ji}(t), \qquad \boldsymbol{\mathcal{P}}^{(-)}(t) = \sum_{i,j=1}^{M}\overline{\mathbf{d}}_{i>j}\,\rho_{ji}(t).$$

All terms in Eq. (III.18a) except the last line correspond to the semiclassical Maxwell-Bloch equations. Quantum effects, such as spontaneous emission, are captured by the noise terms $F_{pq}(\{\rho_{ij}\},t)$, whose correlation properties are determined by the diffusion matrix of the Fokker-Planck equation.

The noise terms can be expressed via Gaussian white noise vectors, $\mathbf{f}(t)$, $\mathbf{f}^{\dagger}(t)$, $\mathbf{g}(t)$, and $\mathbf{g}^{\dagger}(t)$, as follows:

$$F_{pq}(\{\rho_{ij}\},t) = \sqrt{\frac{\gamma}{2}}\sum_{r=1}^{M}\Big\{(\overline{\mathbf{d}}_{p<r}\,\rho_{rq} - \rho_{pr}\,\overline{\mathbf{d}}_{r<q})\cdot\mathbf{f}(t) + \rho_{pr}\,\overline{\mathbf{d}}_{r>q}\cdot\mathbf{f}^{\dagger}(t) + (\rho_{pr}\,\overline{\mathbf{d}}_{r>q} - \overline{\mathbf{d}}_{p>r}\,\rho_{rq})\cdot\mathbf{g}(t) + \overline{\mathbf{d}}_{p<r}\,\rho_{rq}\cdot\mathbf{g}^{\dagger}(t)\Big\}. \tag{III.18b}$$

The components of the noise vectors have the following correlation properties:

$$\langle \mathrm{f}^{(\alpha)}(t)\, \mathrm{f}^{\dagger(\beta)}(t')\rangle = \langle \mathrm{g}^{(\alpha)}(t)\, \mathrm{g}^{\dagger(\beta)}(t')\rangle = \delta_{\alpha\beta}\, \delta(t-t'), \tag{III.18c}$$

and all other first- and second-order correlators are zero. The pairs $\mathbf{f}(t), \mathbf{f}^{\dagger}(t)$ and $\mathbf{g}(t), \mathbf{g}^{\dagger}(t)$ are statistically independent of each other.

The quadratically nonlinear noise term can be expressed via the polarization fields:

$$-\rho_{pq}(t) \sum_{s=1}^{M} F_{ss}(\{\rho_{ij}(t)\}, t) = -\rho_{pq}(t) \sqrt{\frac{\gamma}{2}} \{\boldsymbol{\mathcal{P}}^{(-)}(t) \cdot \mathbf{f}^{\dagger}(t) + \boldsymbol{\mathcal{P}}^{(+)}(t) \cdot \mathbf{g}^{\dagger}(t)\}. \tag{III.18d}$$

As previously demonstrated, the presence of these noise terms ensures that the trace of the stochastic density matrix equals one for each realization, namely $\sum_r \rho_{rr}(t) = 1$.

During numerical simulations, we may encounter unstable realizations that reach numerical infinity. Such divergences emerge because individual realizations of the stochastic density matrix violate the Hermiticity condition, $\rho_{pq}(t) \not\equiv \rho^{*}_{qp}(t)$. Additionally, the polarization fields are also not conjugates, $\left[\boldsymbol{\mathcal{P}}^{(+)}(t)\right]^{*} \not\equiv \boldsymbol{\mathcal{P}}^{(-)}(t)$.

If the initial density matrix is Hermitian, the solution to deterministic equations remains within the Bloch sphere. However, anti-Hermitian components introduced by noise can push the solution into a hyperboloid extending to infinity, leading to unbounded realizations. This can be easily confirmed by solving the deterministic equations with anti-Hermitian initial conditions. For two-level atoms, this condition is $\rho^{*}_{12}(0) = -\rho_{21}(0)$. Although the system starts in a Hermitian density matrix, stochastic differential equations do not preserve Hermiticity. Over time, the stochastic density matrix accumulates anti-Hermitian components through random fluctuations, which may ultimately lead to divergence. These issues are examined in greater detail in the next section, beginning with a simplified discussion focused on two-level emitters.

1.6 Equations for Two-Level Emitters

For two-level emitters, there is a single transition characterized by the transition dipole moments $\overline{\mathbf{d}}_{12}$ and $\overline{\mathbf{d}}_{21}$. For simplicity, we assume these dipole moments have a unit magnitude and are polarized along the x-axis. As a result, the x-components of the noise terms take part in the system's dynamics. These projections are denoted as $\mathrm{f}(t)$, $\mathrm{f}^{\dagger}(t)$, $\mathrm{g}(t)$, and $\mathrm{g}^{\dagger}(t)$.

Free oscillation terms are eliminated by absorbing them into the stochastic variables, which now represent the envelopes. The deterministic part of Eqs. (III.18a) becomes:

$$\frac{d\rho_{11}(t)}{dt} = \gamma\rho_{22}(t) + \gamma(N-1)\, \rho_{12}(t)\, \rho_{21}(t) + \ldots \tag{III.19a}$$

$$\frac{d\rho_{12}(t)}{dt} = -\frac{\gamma}{2}\, \rho_{12}(t) + \frac{\gamma(N-1)}{2} \rho_{12}(t)\, \left[\rho_{22}(t) - \rho_{11}(t)\right] + \ldots \tag{III.19b}$$

$$\frac{d\rho_{21}(t)}{dt} = -\frac{\gamma}{2}\, \rho_{21}(t) + \frac{\gamma(N-1)}{2} \rho_{21}(t)\, \left[\rho_{22}(t) - \rho_{11}(t)\right] + \ldots \tag{III.19c}$$

$$\frac{d\rho_{22}(t)}{dt} = -\gamma\rho_{22}(t) - \gamma(N-1)\, \rho_{12}(t)\, \rho_{21}(t) - \ldots \tag{III.19d}$$

Note that these equations coincide with the semiclassical equations derived in Eq. (I.29). The noise components of the equations are given by:

$$\frac{d\rho_{11}(t)}{dt} = \ldots + \sqrt{\gamma}\, \rho_{21}(t)\, \frac{\mathrm{f}(t) + \mathrm{g}^{\dagger}(t)}{\sqrt{2}} + \sqrt{\gamma}\, \rho_{12}(t)\, \frac{\mathrm{f}^{\dagger}(t) + \mathrm{g}(t)}{\sqrt{2}} - \sqrt{\gamma}\, \rho_{11}(t)\, \mathrm{h}(t), \tag{III.19e}$$

$$\frac{d\rho_{12}(t)}{dt} = \ldots + \sqrt{\gamma}\, \rho_{22}(t)\, \frac{\mathrm{f}(t) + \mathrm{g}^{\dagger}(t)}{\sqrt{2}} - \sqrt{\gamma}\, \rho_{11}(t)\, \frac{\mathrm{f}(t)}{\sqrt{2}} - \sqrt{\gamma}\, \rho_{12}(t)\, \mathrm{h}(t), \tag{III.19f}$$

$$\frac{d\rho_{21}(t)}{dt} = \ldots + \sqrt{\gamma}\, \rho_{22}(t)\, \frac{\mathrm{f}^{\dagger}(t) + \mathrm{g}(t)}{\sqrt{2}} - \sqrt{\gamma}\, \rho_{11}(t)\, \frac{\mathrm{g}(t)}{\sqrt{2}} - \sqrt{\gamma}\, \rho_{21}(t)\, \mathrm{h}(t), \tag{III.19g}$$

$$\frac{d\rho_{22}(t)}{dt} = \ldots - \sqrt{\gamma}\, \rho_{21}(t)\, \frac{\mathrm{f}(t)}{\sqrt{2}} - \sqrt{\gamma}\, \rho_{12}(t)\, \frac{\mathrm{g}(t)}{\sqrt{2}} - \sqrt{\gamma}\, \rho_{22}(t)\, \mathrm{h}(t). \tag{III.19h}$$

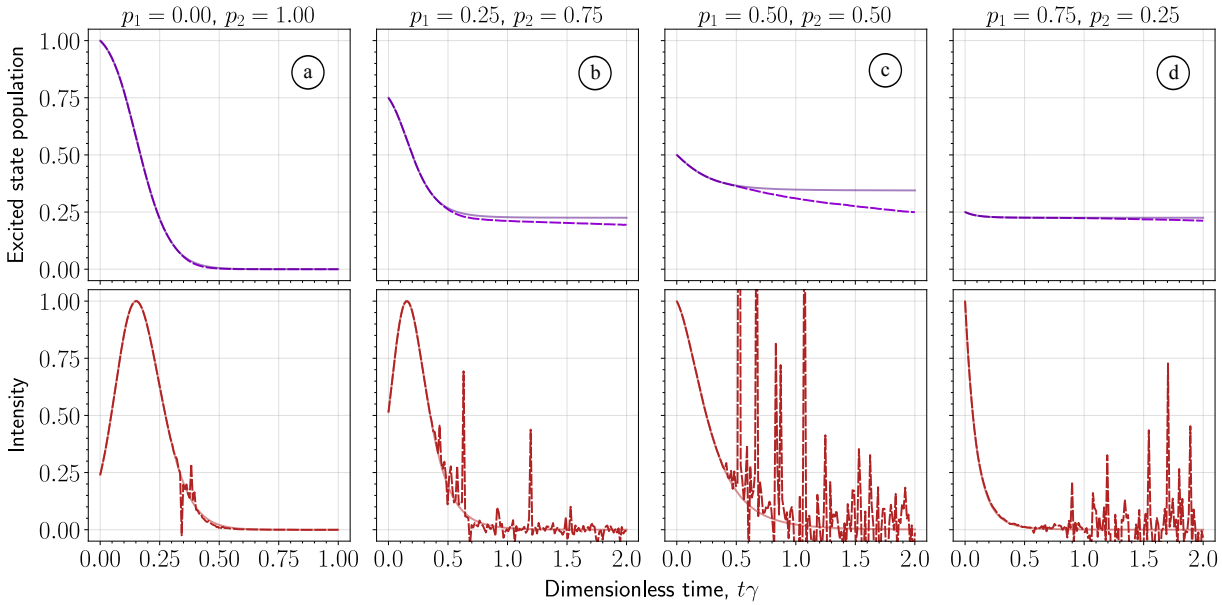

Figure III.1: The solution of stochastic equations (III.19) (dashed lines) compared with the exact solution (semi-transparent lines) for $N = 20$ identical two-level atoms. The initial non-diagonal density matrix elements are zero, $\rho_{12}(0) = \rho_{21}(0) = 0$, and the populations are $\rho_{11}(0) = p_1$ and $\rho_{22}(0) = p_2$. Intensities are normalized to the maximum of the exact solution. For each plot, we average over 10^5 stochastic realizations.

Here, the function $\mathrm{h}(t)$ denotes the following noise term:

$$\mathrm{h}(t) = \rho_{12}(t)\,\frac{\mathrm{f}^\dagger(t)}{\sqrt{2}} + \rho_{21}(t)\,\frac{\mathrm{g}^\dagger(t)}{\sqrt{2}}, \tag{III.19i}$$

which appears after the elimination of the η-object. This contribution ensures that $\rho_{11}(t) + \rho_{22}(t) = 1$ for each realization.

The functions $\mathrm{f}(t)$, $\mathrm{f}^\dagger(t)$, $\mathrm{g}(t)$, and $\mathrm{g}^\dagger(t)$ are independent Gaussian white noise processes with the following correlation properties:

$$\langle \mathrm{f}(t)\,\mathrm{f}^\dagger(t')\rangle = \langle \mathrm{g}(t)\,\mathrm{g}^\dagger(t')\rangle = \delta(t - t'), \tag{III.19j}$$

and all other first- and second-order correlators are zero. We can choose the noise terms to satisfy $\mathrm{g}^*(t) = \mathrm{g}^\dagger(t)$ and $\mathrm{f}^*(t) = \mathrm{f}^\dagger(t)$. Notably, the noise components of our stochastic equations differ significantly from the phenomenological equations in Eq. (I.32).

Numerical simulations of Eqs. (III.19) reveal that some trajectories are unstable, which distorts statistical averages. Figure (III.1) shows solutions for $N = 20$ two-level atoms with the initial conditions:

$$\rho_{11}(0) = p_1, \qquad \rho_{22}(0) = p_2,$$

and $\rho_{12}(0) = \rho_{21}(0) = 0$. In panel (a), where all atoms are initially excited ($p_2 = 1$), the average excited-state population nearly matches the exact solution. However, the intensity curve contains spikes that persist even after averaging—a sign of instabilities.

Panel (b), which has a positive initial population inversion but not fully excited atoms ($p_2 = 0.75$), shows more frequent intensity spikes, and the excited-state population deviates significantly from the exact solution. In panel (c), where both states are initially equally populated ($p_2 = 0.5$), the excited-state population deviates substantially, and the intensity curve appears predominantly noisy. Panel (d), with a negative initial population inversion ($p_2 = 0.25$), shows only minor deviations in the excited-state population, though the intensity curve still features noticeable spikes.

In the next section, we analyze the origin of these divergences and outline a regularization strategy for superradiance in compact systems, as published in Ref. [109].

1.7 Diverging Trajectories and Stochastic Gauges

Numerical analysis reveals that diverging trajectories are characterized by an anti-conjugate relationship between coherences, $\rho_{12}^*(t) \approx -\rho_{21}(t)$. This is possible because equations for $\rho_{12}(t)$ and $\rho_{21}(t)$ have independent noise terms. When coherences are anti-conjugates, the deterministic parts of Eqs. (III.19) may explode.

The analytical form of these diverging solutions can be derived by neglecting the noise terms and assuming large density matrix elements. Under this approximation, the spontaneous decay terms can be disregarded. The resulting equations yield the following singular solution:

$$\widetilde{\rho}_{22}(t) - \widetilde{\rho}_{11}(t) = \frac{2}{\gamma(N-1)} \frac{1}{t - t_{\text{sing.}}}, \tag{III.20a}$$

$$\widetilde{\rho}_{12}(t) = \frac{ie^{i\phi}}{\gamma(N-1)} \frac{1}{t - t_{\text{sing.}}}, \tag{III.20b}$$

$$\widetilde{\rho}_{21}(t) = \frac{ie^{-i\phi}}{\gamma(N-1)} \frac{1}{t - t_{\text{sing.}}}. \tag{III.20c}$$

Here, ϕ is an arbitrary real number, and $t_{\text{sing.}}$ depends on system parameters and may vary between realizations. The coherences satisfy the anti-conjugate condition, $\widetilde{\rho}_{12}^*(t) \equiv -\widetilde{\rho}_{21}(t)$.

Such stability issues in the positive P-representation are well-known across various systems [103]. Diverging solutions, also called movable singularities, cause spikes in averages, as shown in Fig. III.1. These instabilities motivated the development of stochastic gauges [100, 101].

The term "stochastic gauge" typically refers to transformations applied to the P-function or stochastic differential equations that preserve expectation values. Since the P-function is not uniquely defined, different distributions can yield the same expectation values. In fact, we used such transformations when eliminating the η-object in Sec. 5.3.

Another symmetry is connected to the representation of the noise terms, which is also not unique. The representation in Eq. (III.18b) is merely one possible ansatz that reproduces the correct correlation properties dictated by the diffusion matrix. Any representation that reproduces these correlation properties should yield identical expectation values.

While gauges theoretically do not affect expectation values, obtaining exact results requires an infinite number of trajectories, as indicated by Eq. (III.12). Numerical simulations are restricted to a finite number of trajectories. As a result, gauges can either accelerate convergence, slow it down, or even introduce new instabilities. In essence, specific gauges prioritize certain expected system behaviors, serving as an initial guess for each realization. If this guess is successful, significantly fewer trajectories are needed to reach convergence.

The next two subsections outline two types of gauges used to stabilize the equations (III.18a): the drift gauge and the diffusion gauge [100, 101]. Both gauges are designed to favor realizations where the stochastic density matrix is close to being Hermitian while reducing the accumulation of anti-Hermitian components.

Stochastic Drift Gauges

Drift gauges modify the deterministic components of stochastic equations by introducing an additional stochastic variable called the weight function, which assigns a weight to each realization [100, 101]. A brief explanation of this technique is provided in Sec. 5.4.

The weight function has an exponential form:

$$\Omega(t) = e^{C_0(t)},$$

where $C_0(t)$ is a new stochastic variable. The equation for $C_0(t)$ determines changes in the drift functions of the original equations: the drift of $\rho_{ij}(t)$ is subtracted with a correlator between noise terms for $\rho_{ij}(t)$ and $C_0(t)$.

The weight function $\Omega(t)$ appears in expressions for averages. Let $\rho_{ij}(t)$ be the solution to the modified equations, and $\rho'_{ij}(t)$ be the solution to the original equations. Their averages are

related by:

$$\langle \rho'_{p_1q_1}(t) \ldots \rho'_{p_Kq_K}(t) \rangle = \frac{\langle \rho_{p_1q_1}(t) \ldots \rho_{p_Kq_K}(t)\, \Omega(t) \rangle}{\langle \Omega(t) \rangle}. \tag{III.21}$$

The left-hand side connects to quantum-mechanical expectation values as in Eq. (III.17c). Importantly, the introduction of $\Omega(t)$ does not affect the initial conditions of the stochastic variables $\rho_{pq}(t)$, as the initial condition $C_0(0) = 0$ ensures that $\Omega(0) = 1$.

In Ref. [109], we propose a modification to the drift terms of Eqs. (III.18a) that prevents the unbounded growth of the deterministic components. Specifically, we alter the nonlinear drift terms by replacing the polarization fields as follows:

$$\boldsymbol{\mathcal{P}}^{(\pm)}(t) \longrightarrow \boldsymbol{\mathcal{P}}^{(\pm)}(t) - \theta(t)\, \frac{\boldsymbol{\mathcal{P}}^{(\pm)}(t) - \left[\boldsymbol{\mathcal{P}}^{(\mp)}(t)\right]^*}{2}. \tag{III.22}$$

Here, $\theta(t)$ acts as a switch function, taking only two values: 0 (gauge off) and 1 (gauge on).

When the drift gauge is applied, the polarization fields in the equations are transformed as:

$$\boldsymbol{\mathcal{P}}^{(\pm)}(t)\Big|_{\theta(t)=1} \longrightarrow \frac{\boldsymbol{\mathcal{P}}^{(\pm)}(t) + \left[\boldsymbol{\mathcal{P}}^{(\mp)}(t)\right]^*}{2},$$

ensuring that only the Hermitian components of $\boldsymbol{\mathcal{P}}^{(\pm)}$ contribute to the equations. Consequently, the emitters interact with a Hermitian electric field, preventing unbounded growth of the deterministic part. Indeed, for an anti-Hermitian stochastic density matrix, the gauged polarization fields vanish, precluding the emergence of diverging solutions of type (III.20).

It is important to emphasize that the drift gauge modifies only the drift functions, without altering the definition of the physical field or its intensity. The only change is the inclusion of the weight function in the averages, as described in Eq. (III.21).

To implement the modification from Eq. (III.22), $C_0(t)$ must satisfy the following equation:

$$\frac{dC_0(t)}{dt} = \theta(t)\,(N-1) \times \sqrt{\frac{\gamma}{2}} \left\{ \frac{\boldsymbol{\mathcal{P}}^{(-)}(t) - \left[\boldsymbol{\mathcal{P}}^{(+)}(t)\right]^*}{2} \cdot \mathbf{f}^\dagger(t) + \frac{\boldsymbol{\mathcal{P}}^{(+)}(t) - \left[\boldsymbol{\mathcal{P}}^{(-)}(t)\right]^*}{2} \cdot \mathbf{g}^\dagger(t) \right\}. \tag{III.23}$$

The factors multiplying noise terms on the right-hand side are the anti-Hermitian components of the polarization fields. When the polarization fields are Hermitian, the right-hand side is zero, implying that the weight function remains static and no gauge is applied. However, as soon as the anti-Hermitian part becomes nonzero, the weight function exhibits non-trivial dynamics, which in turn leads to modifications of the polarization fields within the equations for $\rho_{pq}(t)$.

The non-Hermitian components in Eq. (III.23) are scaled by $(N-1)$, potentially introducing instability as the number of emitters increases. These issues will be discussed in Sections 3.2 and 3.4, where we additionally analyze the conditions for safely neglecting $\Omega(t)$ without significant loss of accuracy.

Finally, we need to define the switch function $\theta(t)$. Continuous application of the gauge often destabilizes $\Omega(t)$ and distorts statistical averages (Sec. 3.4). Therefore, the drift gauge should be activated only when necessary. Unfortunately, there is no universal criterion. In this dissertation and in Ref. [109], the drift gauge is applied during field amplification, because it may potentially increase anti-Hermitian components. Thus, the switch function is defined as:

$$\theta(t) = \begin{cases} 1, & \text{any } \mathrm{Re}[\rho_{ee}(t) - \rho_{gg}(t)] \geq 0, \\ 0, & \text{otherwise}, \end{cases} \tag{III.24}$$

where e represents any excited state and g represents any ground state, such that $\overline{\mathbf{d}}_{eg} \neq 0$. In other words, the drift gauge is activated when there is a positive population inversion between lasing energy levels.

We additionally employ another type of gauge, which alters the noise representation and suppresses the accumulation of anti-Hermitian components. This is discussed in the following subsection.

Stochastic Diffusion Gauges

Returning to stochastic equations (III.18a), the stochastic processes $F_{pq}(\{\rho_{ij}\},t)$ are represented using elementary Gaussian white noise terms, as defined in Eq. (III.18b). This representation ensures that $F_{pq}(\{\rho_{ij}\},t)$ have correlation properties from Eq. (III.18c). As long as these correlations are preserved, the noise terms theoretically produce identical expectation values, independent of their specific representation [100, 101].

We consider the following transformations for the noise vector components:

$$\tilde{\mathrm{f}}^{(\alpha)}(t) = F_\alpha(t)\,\mathrm{f}^{(\alpha)}(t), \qquad \tilde{\mathrm{f}}^{\dagger(\alpha)}(t) = F_\alpha^{-1}(t)\,\mathrm{f}^{\dagger(\alpha)}(t), \tag{III.25a}$$

$$\tilde{\mathrm{g}}^{(\alpha)}(t) = G_\alpha(t)\,\mathrm{g}^{(\alpha)}(t), \qquad \tilde{\mathrm{g}}^{\dagger(\alpha)}(t) = G_\alpha^{-1}(t)\,\mathrm{g}^{\dagger(\alpha)}(t). \tag{III.25b}$$

The transformed noise terms, indicated with tildes, satisfy the same correlator in Eq. (III.18c) and, therefore, yield the same statistical averages. In general, the functions F_α and G_α also depend on the stochastic variables $\rho_{pq}(t)$.

Our aim is to define F_α and G_α such that the growth of the non-Hermitian components of the polarization fields is minimized. This is achieved by minimizing the average growth of the anti-Hermitian component in the stochastic polarization fields:

$$\left\langle \left| \boldsymbol{\mathcal{P}}^{(+)}(t) - [\boldsymbol{\mathcal{P}}^{(-)}(t)]^* \right|^2 \right\rangle.$$

This functional depends on F_α and G_α, with the density matrix elements treated as fixed parameters. The noise terms vanish due to averaging.

The optimal functions $F_\beta(t)$ and $G_\beta(t)$ should satisfy:

$$|F_\beta(t)|^4 = \frac{\sum_\alpha \left\{ \left| P^{(ee)}_{\alpha\beta}(t) - P^{(+)}_\alpha(t) P^{(-)}_\beta(t) \right|^2 + \left| P^{(ge)}_{\alpha\beta}(t) - P^{(-)}_\alpha(t) P^{(-)}_\beta(t) \right|^2 \right\}}{\sum_\alpha \left\{ \left| P^{(eg)}_{\beta\alpha}(t) - P^{(eg)}_{\alpha\beta}(t) \right|^2 + \left| P^{(ee)}_{\beta\alpha}(t) - P^{(gg)}_{\alpha\beta}(t) \right|^2 \right\}}, \tag{III.26a}$$

$$|G_\beta(t)|^4 = \frac{\sum_\alpha \left\{ \left| P^{(eg)}_{\beta\alpha}(t) - P^{(+)}_\alpha(t) P^{(+)}_\beta(t) \right|^2 + \left| P^{(ee)}_{\beta\alpha}(t) - P^{(-)}_\alpha(t) P^{(+)}_\beta(t) \right|^2 \right\}}{\sum_\alpha \left\{ \left| P^{(ge)}_{\alpha\beta}(t) - P^{(ge)}_{\beta\alpha}(t) \right|^2 + \left| P^{(ee)}_{\alpha\beta}(t) - P^{(gg)}_{\beta\alpha}(t) \right|^2 \right\}}. \tag{III.26b}$$

The form of F_β and G_β is obtained by taking the fourth root and ignoring phase factors. The auxiliary tensors $P^{(pq)}_{\alpha\beta}(t)$ are defined as follows:[4]

$$P^{(gg)}_{\alpha\beta}(t) = \sum_{i,j,j'=1}^{M} d^{(\alpha)}_{i>j}\,\rho_{jj'}(t)\,d^{(\beta)}_{j'<i}, \qquad P^{(ge)}_{\alpha\beta}(t) = \sum_{i,j,j'=1}^{M} d^{(\alpha)}_{i>j}\,\rho_{jj'}(t)\,d^{(\beta)}_{j'>i}, \tag{III.26c}$$

$$P^{(eg)}_{\alpha\beta}(t) = \sum_{i,j,j'=1}^{M} d^{(\alpha)}_{i<j}\,\rho_{jj'}(t)\,d^{(\beta)}_{j'<i}, \qquad P^{(ee)}_{\alpha\beta}(t) = \sum_{i,j,j'=1}^{M} d^{(\alpha)}_{i<j}\,\rho_{jj'}(t)\,d^{(\beta)}_{j'>i}. \tag{III.26d}$$

From this point, we distinguish between the **ungauged** and **gauged** stochastic equations. The ungauged equations correspond to the original form in Eq. (III.18a). The gauged stochastic equations incorporate modifications to the drift and noise terms as described in the last two subsections, and are solved alongside Eq. (III.23). The weight function is then used to compute statistical averages, as given by Eq. (III.21).

1.8 Summary

In summary, we employed the formalism developed in Chapter II to formulate a coherent-state representation of density matrices within the Liouville-Hilbert space. This formulation is

[4] In two-band level structures, where intraband transitions are forbidden, $P^{(eg)}_{\alpha\beta}(t)$ and $P^{(ge)}_{\alpha\beta}(t)$ are zero. For two-level emitters, tensors $P^{(gg)}_{\alpha\beta}(t)$ and $P^{(ee)}_{\alpha\beta}(t)$ coincide with $\rho_{11}(t)$ and $\rho_{22}(t)$, respectively.

based on the supervectors $|\Lambda(\{\beta_{ij}\})\rangle\!\rangle$, providing the following ansatz for the density matrix:

$$|\rho(t)\rangle\!\rangle = \int \prod_{i,j=1}^{M} (d^2\beta_{ij})\, P(\{\beta_{ij}\}, t)\, |\Lambda(\{\beta_{ij}\})\rangle\!\rangle,$$

where the integration runs over M^2 complex variables $\{\beta_{ij}\}$. The supervector $|\Lambda(\{\beta_{ij}\})\rangle\!\rangle$ defined as (Eq. (III.6))

$$|\Lambda(\{\beta_{ij}\})\rangle\!\rangle = \exp\Big[-\sum_{i=1}^{M} \beta_{ii} + \frac{1}{\sqrt{\hat{N}}} \sum_{i,j=1}^{M} \beta_{ij}\, \hat{b}_{ij}^{\dagger} \Big] |\mathrm{vac}\rangle\!\rangle,$$

serves as an analogue to coherent states in the Liouville-Hilbert space. The properties of these supervectors are discussed in detail in Sec. 5.1.

The quantum master equation for the density matrix can be reformulated as an equation for the distribution $P(\{\beta_{ij}\}, t)$ by applying the following replacement rules (Eq. (III.8)):

$$\begin{aligned} \hat{b}_{pq} \sqrt{\hat{N}}\, |\rho(t)\rangle\!\rangle &\longrightarrow \beta_{pq}\, P(\{\beta_{ij}\}, t), \\ \frac{1}{\sqrt{\hat{N}}}\, \hat{b}_{pq}^{\dagger}\, |\rho(t)\rangle\!\rangle &\longrightarrow \Big(\delta_{pq} - \frac{\partial}{\partial \beta_{pq}}\Big) P(\{\beta_{ij}\}, t). \end{aligned}$$

The factors involving $\hat{N}^{\pm 1/2}$ cannot be neglected, and do not introduce complications, provided the quantum master equation conserves the total number of emitters.

In Sec. 1.1, we derived the Fokker-Planck equation corresponding to a model Liouvillian incorporating one- and two-particle collective operators. Subsequently, in Sec. 1.2, we formulated the Itô stochastic equations for the variables $\beta_{pq}(t)$.

These stochastic variables exhibit non-trivial statistics, as expectation values involving more variables than the number of particles must vanish (Sec. 1.3). We address this in Sec. 1.4 by introducing normalized stochastic variables for N emitters, $\rho_{pq}(t)$. These variables already incorporate the desired statistical properties and require no additional statistical sampling.

In Sec. 1.5, we applied the derived framework to light-matter interactions, obtaining the corresponding set of Itô stochastic equations (Eqs. (III.18)). The specific case for two-level atoms is analyzed in Sec. 1.6. Notably, the deterministic terms in the equations align with the well-known semiclassical Maxwell-Bloch equations, while the noise terms capture quantum effects, thus reintroducing quantum fluctuations into the semiclassical dynamics.

However, the derived stochastic equations allow for solutions that diverge as $1/(t - t_{\mathrm{sing.}})$ (Sec. 1.7). These equations do not preserve the Hermiticity of the stochastic density matrix, meaning $\rho_{pq}^{*}(t) \not\equiv \rho_{qp}(t)$. Noise terms can cause the stochastic density matrix to become anti-Hermitian, leading to unbounded growth of the deterministic part of the equations.

In the same section, we discussed two types of stochastic gauges [100,101] designed to stabilize the equations [109]. One is the drift gauge, which modifies the deterministic terms by enforcing Hermiticity in the polarization fields (Eq. (III.22)), thereby preventing unbounded growth. This technique introduces a weight function, $\Omega(t)$ (see Eq. (III.23) and its discussion). The other is the diffusion gauge, which rescales noise terms following Eq. (III.25), ensuring that gauged noise terms favor Hermitian realizations of stochastic density matrices.

In the next section, we will numerically analyze the performance of gauged equations in examples from Chapter II. This allows us to directly compare the statistical averages with the exact solution. In Sec. 3, we will discuss the outcomes of this analysis, including any challenges encountered during the simulations.

Furthermore, in Sec. 2.5, we will demonstrate how to extend the formalism to systems interacting with quantized fields. In Sec. 3.5, we will explore its application to systems with non-identical particles or spatially distributed configurations. As a practical example, Sec. 3.6 includes plots illustrating lasing from the $K\alpha$ transition in neon [38].

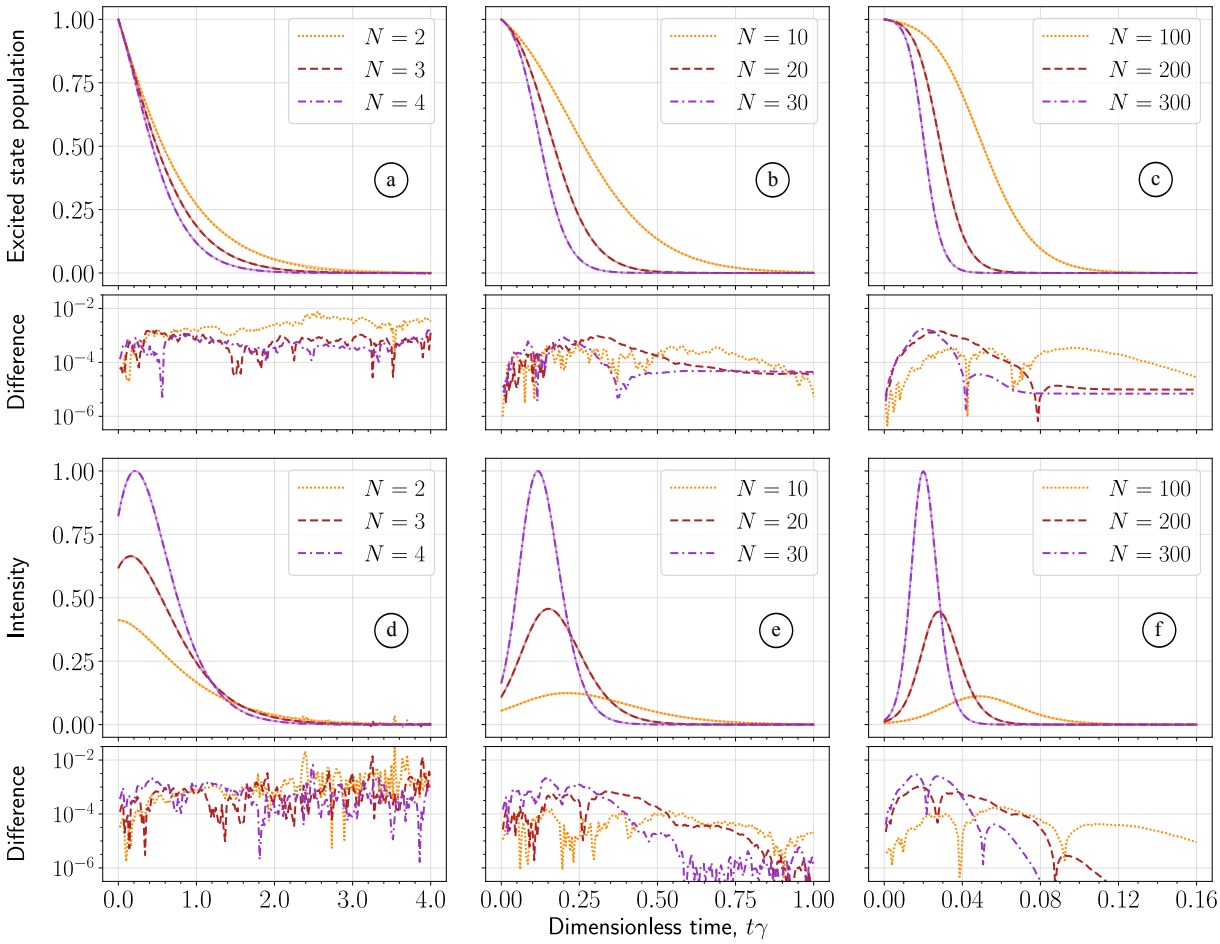

Figure III.2: Solutions of the gauged stochastic equations. Semi-transparent lines show the exact solutions, and opaque lines depict stochastic averages. The intensities in panels (d), (e), and (f) are normalized to the maximum of the exact solution in each respective panel. The subplots below each row display the absolute difference between the statistical averages and the quantum expectation values on a logarithmic scale. For each plot, 10^5 realizations were sampled. In panels (a) and (d), for $N = 2, 3, 4$, we excluded $22, 4, 3$ unstable trajectories, respectively.

2 Applications

In this section, we evaluate the performance of the developed formalism by applying it to examples with accessible exact solutions. By revisiting the models examined in Chapter II, we aim to assess the applicability and effectiveness of the derived stochastic equations. Unless stated otherwise, $\rho_{pq}(t)$ denotes a solution of the gauged stochastic equations.

Let us first establish the relationship between observables and statistical averages. Average populations of atomic levels are given by:

$$p_q(t) = \frac{1}{N}\sum_{\mu=1}^{N} \mathrm{Tr}\left[\hat{\sigma}_{\mu,qq}\,\hat{\rho}(t)\right] = \frac{\langle \rho_{qq}(t)\,\Omega(t)\rangle}{\langle \Omega(t)\rangle}.$$

In compact systems, field properties can be expressed through atomic variables. Except for an insignificant factor, the intensity of emission polarized along the $\mathbf{e}_\alpha$ axis is given by Eq. (II.30). Within the stochastic framework, the intensity is calculated as:

$$I_\alpha(t) = N\sum_{i,j,q=1}^{M} \overline{d}_{i<j}^{(\alpha)}\,\overline{d}_{q>i}^{(\alpha)}\,\frac{\langle \rho_{jq}(t)\,\Omega(t)\rangle}{\langle \Omega(t)\rangle} + N(N-1)\sum_{i,j,p,q=1}^{M} \overline{d}_{i<j}^{(\alpha)}\,\overline{d}_{q>p}^{(\alpha)}\,\frac{\langle \rho_{pq}(t)\,\rho_{ji}(t)\,\Omega(t)\rangle}{\langle \Omega(t)\rangle}. \quad \text{(III.27)}$$

The total intensity is the sum of all these components.

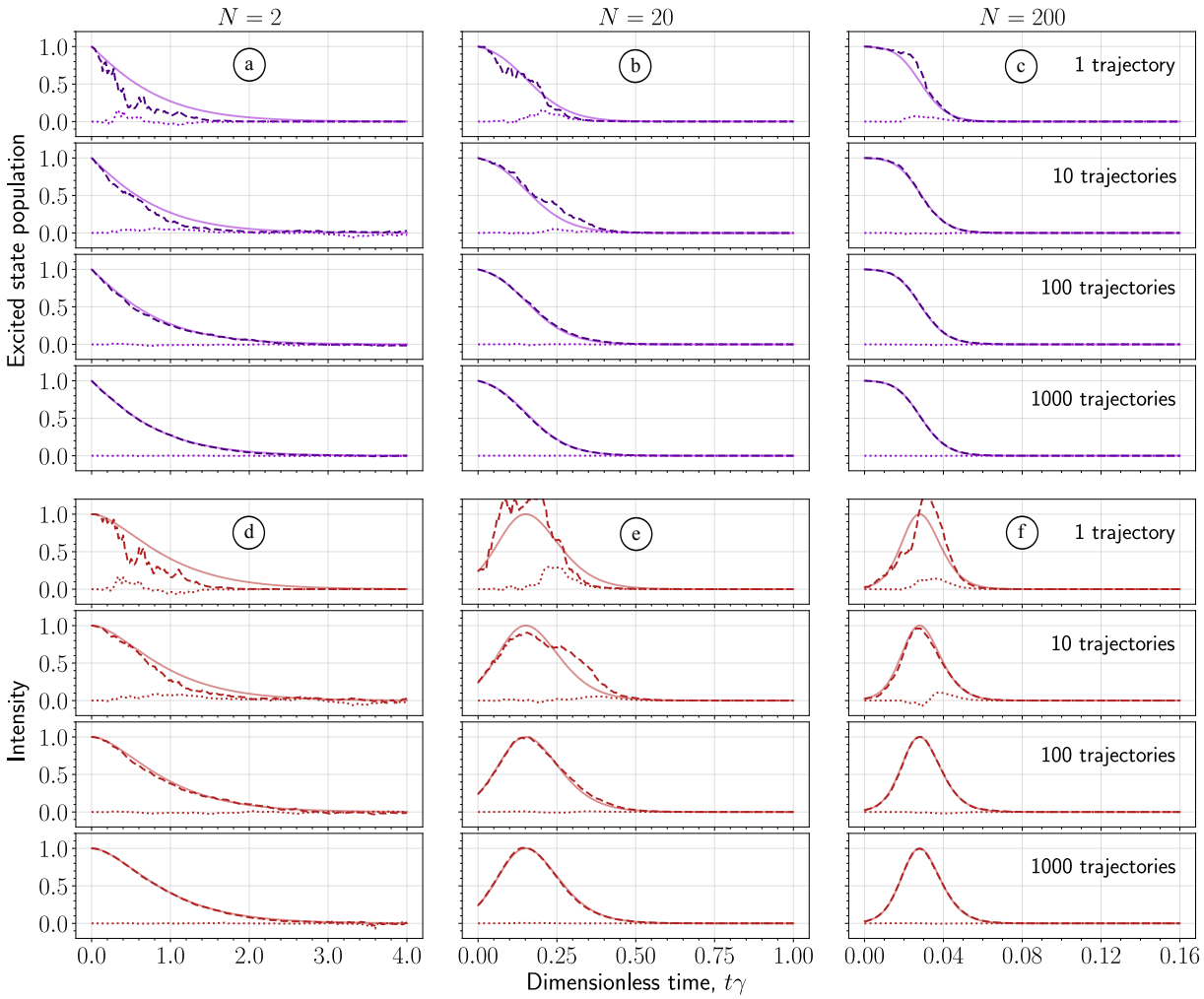

Figure III.3: Convergence of stochastic averages (dashed lines) to the exact solution (semi-transparent lines) for different numbers of atoms N and varying numbers of stochastic trajectories. Observables shown are the probability of finding an excited atom (a)-(c) and the intensity of the emitted field (d)-(f). Intensities are normalized to the maximum value of the exact solution. Dotted lines represent the imaginary parts of the corresponding quantities.

Details of the numerical implementation are provided in Sec. 4. We employ the `Tsit5` algorithm [155] combined with the Euler-Maruyama method for solving the equations, constraining the maximum step size to $T/10^4$, where T is the final time point of the simulation. Unstable realizations are excluded if they meet either of the following conditions: the weight function $\Omega(t) = e^{C_0(t)}$ exceeds e^5, or the absolute value of any stochastic density matrix element exceeds 100. The impact of excluding these trajectories is discussed in Sec. 3.2.

2.1 Cooperative Emission of Two-Level Atoms

As a first illustration, we revisit the example of identical two-level atoms collectively interacting with a bath of harmonic oscillators—a basic model of superradiance. As previously noted, the original stochastic equations (III.18a) exhibit divergent solutions, as shown in Fig. III.1. To regularize the equations, we employ the modifications detailed in Sec. 1.7.

For an initially fully excited ensemble, the phenomenon of superradiance is observed. Figure III.2 depicts the excited-state populations (a)-(c) and emission intensities (d)-(f) for varying atom numbers N. Each plot is supplemented by the absolute difference between stochastic averages and quantum-mechanical expectation values.

Discrepancies between stochastic and quantum expectation values remain below 1%. Panels (a) and (d) demonstrate that the differences are more pronounced for smaller N, likely due to

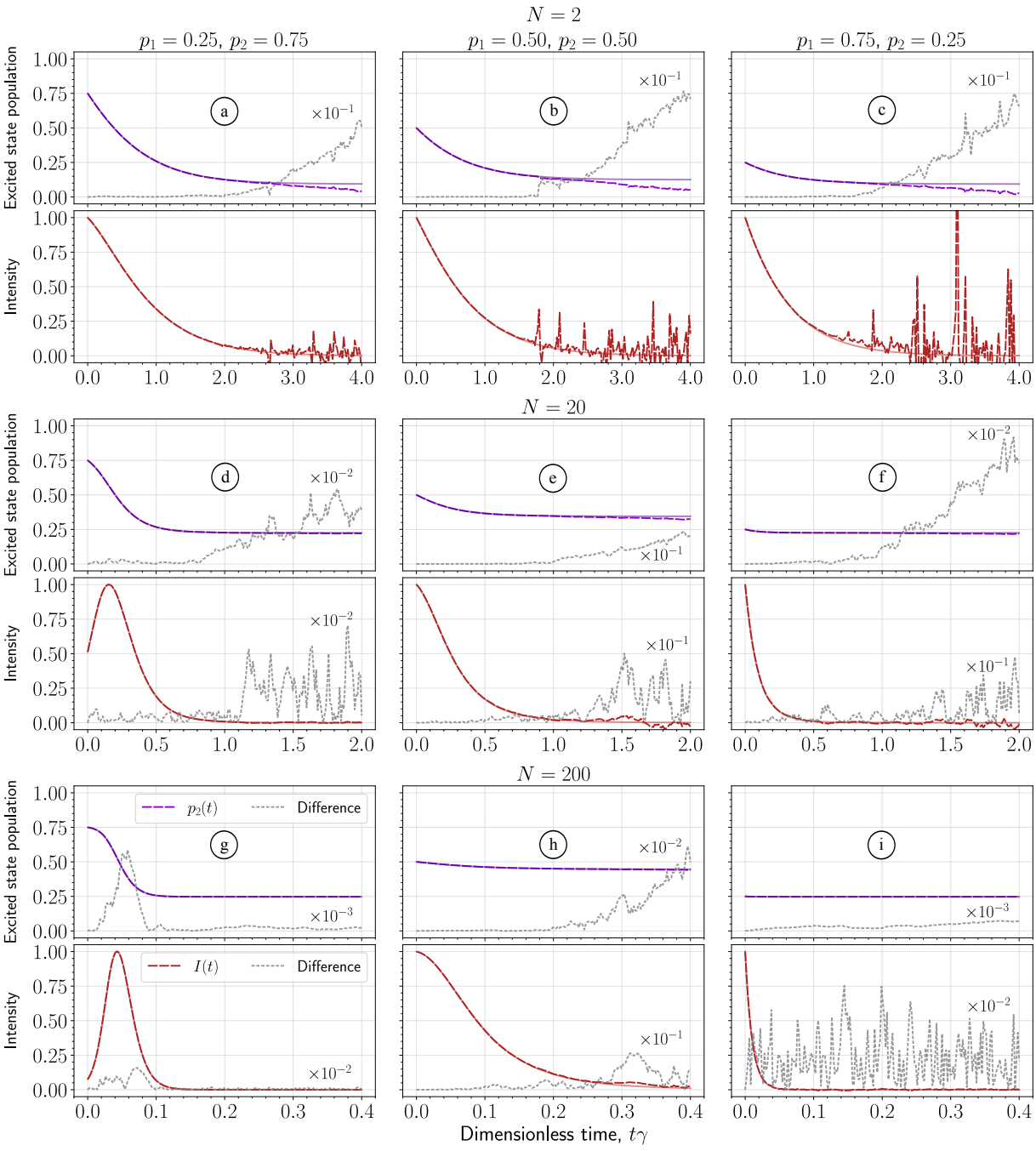

Figure III.4: The excited state population and emission intensity plotted for different numbers of atoms N and varying initial conditions. The semi-transparent lines show the exact solution, and the opaque lines depict the stochastic averages. The absolute differences between these values are indicated by gray dotted lines. Some differences are labeled with $\times 10^{-1}$, $\times 10^{-2}$, $\times 10^{-3}$ to indicate that the corresponding values should be multiplied by these factors. We sampled 10^5 trajectories, excluding the following numbers of unstable realizations: (a) 131; (b) 178; (c) 170; (d) 32; (e) 109; (f) 40; (g) 0; (h) 17; and (i) 0.

the nonlinear noise term, which can become comparable to the deterministic part for small N.

In Fig. III.2, we used 10^5 stochastic realizations for averaging. However, far fewer trajectories are typically needed to achieve convergence of selected observables. Figure III.3 illustrates the populations (a)-(c) and emission intensities (d)-(f) for varying numbers of stochastic realizations and atoms. For qualitative analysis, averaging over 10^2 trajectories is sufficient, while 10^3 provides relatively accurate averages. In addition to direct comparisons with exact solutions, we employ an additional convergence criterion: the imaginary parts of observables should vanish

after averaging. For individual trajectories, the imaginary parts are comparable in magnitude to the real parts, making single realizations physically meaningless. Statistical averages accurately represent observables only after averaging over a significant number of trajectories.

Subradiance

To study the influence of subradiant states, we assume initial conditions as given in Eq. (II.33). In terms of stochastic variables, these become:

$$\rho_{11}(0) = p_1, \qquad \rho_{22}(0) = p_2, \tag{III.28}$$

with zero coherences. Calculations from the previous chapter indicate that the ensemble reaches a steady state with a nonzero probability of finding an excited atom. In this steady state, the field intensity (III.27) is zero, leading to the following condition (for the ungauged variables):

$$\langle \rho_{22}^{(ss)} \rangle + (N-1) \langle \rho_{12}^{(ss)} \, \rho_{21}^{(ss)} \rangle = 0,$$

where (ss) stands for steady state. This implies that $\langle \rho_{12}^{(ss)} \, \rho_{21}^{(ss)} \rangle < 0$, which can only be satisfied if the coherences tend to be anti-Hermitian at the level of single stochastic realizations. This indicates that such realizations are statistically significant, and using gauges designed to minimize the influence of anti-Hermitian components may distort the resulting expectation values. However, as demonstrated in Fig. III.1, without gauges the solution is highly unstable.

Figure III.4 shows that subradiance is not fully captured by the gauged stochastic equations. For two atoms, shown in panels (a)-(c), the excited-state population does not converge to the correct curve, and the intensity is unstable. The situation improves with larger numbers of atoms. For $N = 20$, the case with $p_1 = 0.25$ ($p_2 = 0.75$) in panel (d) is well reproduced, without the spikes in intensities observed in Fig. III.1 (b). Furthermore, for $N = 200$, the curve corresponding to a negative population inversion $p_1 = 0.75$ ($p_2 = 0.25$) in panel (i) approaches the exact solution.

In contrast, the case where $p_1 = p_2 = 0.5$ consistently performs poorly, exhibiting larger deviations from the exact solutions and more unstable realizations, regardless of the number of atoms. The steady-state density matrix, described by Eq. (II.36a), depends on the parameter $(p_1\, p_2)$. When either population is close to 0 or 1, the state is closer to a pure state, with more population concentrated in the ground state. However, as $(p_1\, p_2)$ increases, a larger fraction of the population becomes trapped in the excited state. Higher values of this parameter result in stronger population trapping effects, amplifying the influence of subradiant states. This explains the problematic behavior observed for $p_1 = p_2 = 0.5$ across all atom numbers, as shown in Figs. III.4 (b), (e), and (h).

2.2 Incoherently Pumped Two-Level Emitters

In realistic scenarios, the excitation of the ensemble is not instantaneous. Instead, the system's initial state may be prepared through continuous incoherent pumping, as in x-ray lasing experiments [38, 161]. In such cases, a pump pulse ionizes atoms in their neutral state, initiating a lasing transition in the ionized atoms. Figure III.5 (a) provides a schematic of the level structure. The dynamics of this system was examined in the previous chapter, specifically in Sec. 2.2. Here, we assess the performance of the stochastic formalism under the same conditions.

The non-ionized state is represented by an additional stochastic variable, denoted as $\rho_{00}(t)$. This state is coupled to the excited state exclusively via incoherent pumping, as described in Eq. (II.37). The pumping process introduces an additional term to the equation for $\rho_{22}(t)$:

$$\frac{d\rho_{22}(t)}{dt} = \ldots + J_0(t)\, \rho_{00}(t),$$

while the evolution of the new variable $\rho_{00}(t)$ is governed by the following stochastic equation:

$$\frac{d\rho_{00}(t)}{dt} = -J_0(t)\, \rho_{00}(t) - \rho_{00}(t) \sqrt{\frac{\gamma}{2}} \{ \boldsymbol{\mathcal{P}}^{(-)}(t) \cdot \mathbf{f}^{\dagger}(t) + \boldsymbol{\mathcal{P}}^{(+)}(t) \cdot \mathbf{g}^{\dagger}(t) \}. \tag{III.29}$$

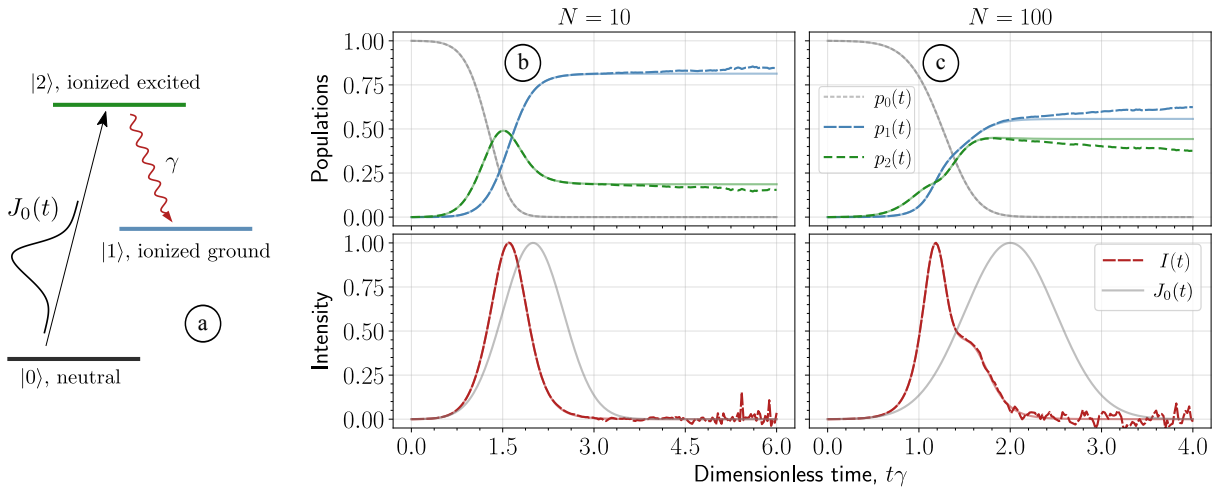

Figure III.5: Panel (a) illustrates the level structure of pumped two-level atoms. Panels (b) and (c) compare the statistical averages (opaque lines) with the exact solution (semi-transparent lines) for $N = 10$ and $N = 100$, respectively. Pump pulse has a Gaussian envelope: $J_0(t) = I_p \exp\left[-\frac{(t-t_0)^2}{2\tau^2}\right]/\sqrt{2\pi\tau^2}$, with parameters $I_p = 10$, $t_0 = 2.0/\gamma$, and $\tau = 0.5/\gamma$. We sampled 10^5 trajectories, excluding 199 unstable realizations in (b) and 3871 in (c).

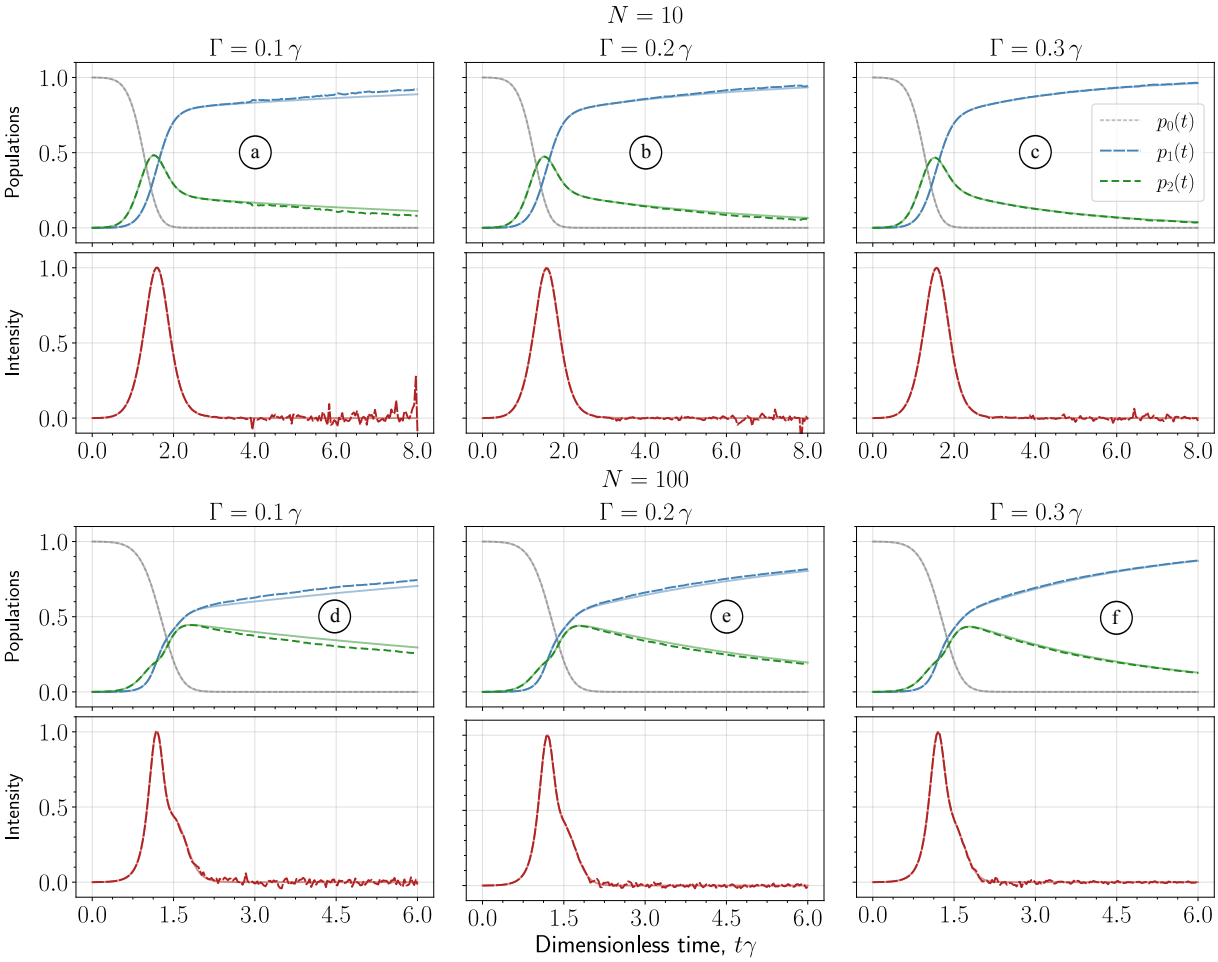

Figure III.6: Regularization of the system from Fig. III.5 for different values of Γ. Semi-transparent lines represent the exact solution, while opaque lines denote stochastic averages. We sampled 10^5 trajectories, neglecting (a) 268; (b) 119; (c) 59; (d) 2699; (e) 1061; and (f) 493 unstable realizations.

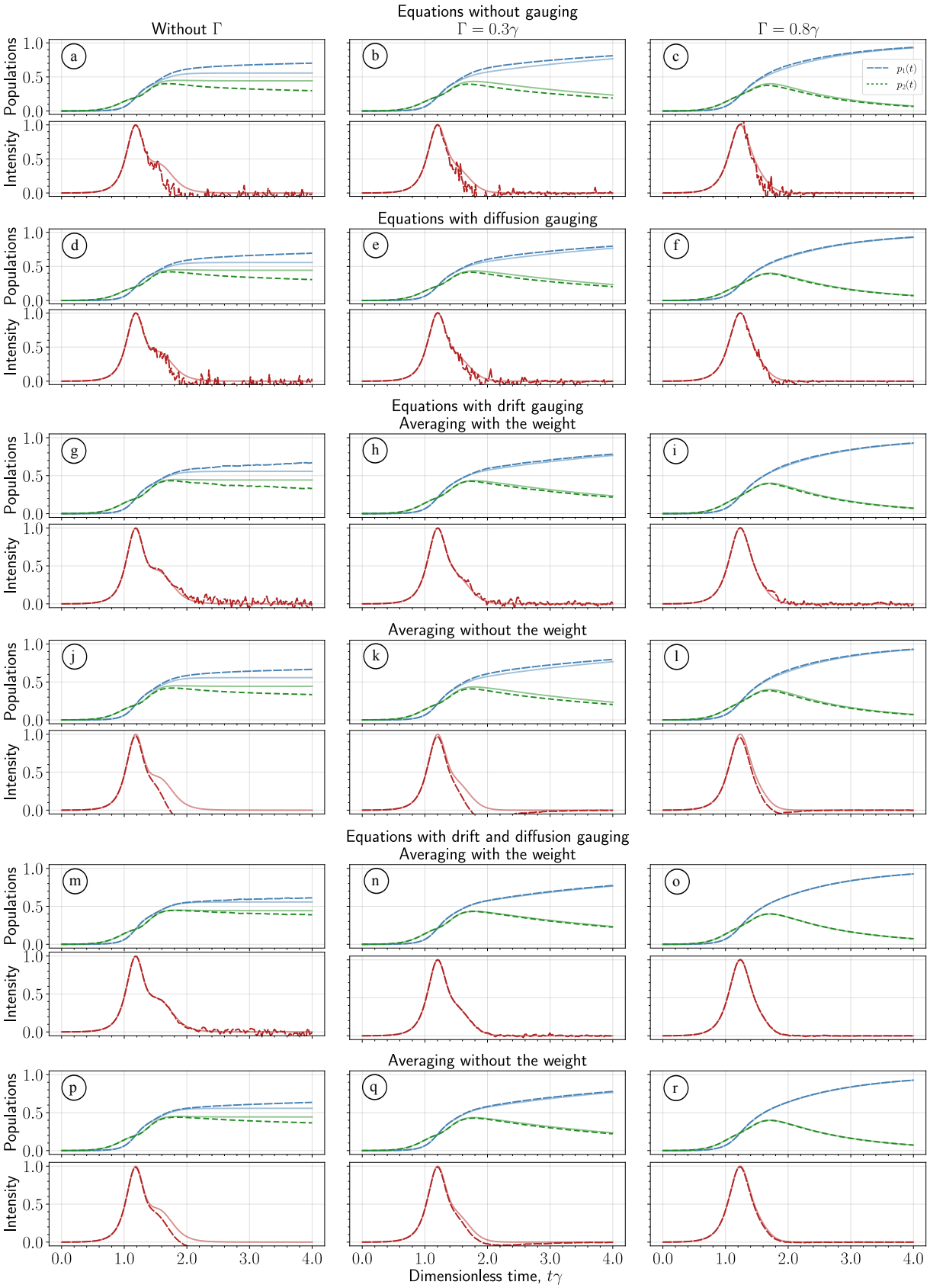

Figure III.7: $N = 100$ pumped two-level atoms. For each plot, we sampled 10^5 trajectories, and neglected the following numbers of unstable realizations. No gauges: (a) 438; (b) 207; and (c) 111. Only diffusion gauge: (d) 753; (e) 217; and (f) 57. Only drift gauge: with weight (g) 11 734; (h) 3812; (i) 907; and without weight (j) 2. Both gauges: (m) 3926; (n) 474; and (o) 22.

Here, $J_0(t)$ represents the temporal profile of the pump pulse, consistent with Eq. (II.37). We use the same Gaussian pump profile as specified in the caption of Fig. II.4.

The computed stochastic averages are shown in Figs. III.5 (b) and (c). In panel (b), for $N = 10$, we encounter the same issue with steady states as observed in Fig. III.4, where the final states are inaccurately captured. The populations fail to maintain constant values, deviating from the exact solution, while the intensities exhibit spikes at later times.

This issue persists in panel (c) for $N = 100$ atoms, with a significant increase in the number of unstable trajectories. We attribute these issues to the presence of subradiant states. Notably, the stationary population of the excited state is considerably higher for $N = 100$, reflecting a stronger population trapping effect.

Introducing additional dissipation channels can disrupt the formation of such steady states. In the previous chapter, we considered Auger-Meitner decay of the excited state. Here, we examine a different dissipation channel: incoherent decay to the ground state $2 \to 1$ at a rate Γ. This decay modifies the stochastic equations as follows:

$$\frac{d\rho_{11}(t)}{dt} = \ldots + \Gamma\rho_{22}(t), \qquad \frac{d\rho_{22}(t)}{dt} = \ldots - \Gamma\rho_{22}(t),$$
$$\frac{d\rho_{21}(t)}{dt} = \ldots - \frac{\Gamma}{2}\rho_{21}(t), \qquad \frac{d\rho_{12}(t)}{dt} = \ldots - \frac{\Gamma}{2}\rho_{12}(t).$$

Such losses may stem from isotropic spontaneous emission in directions where amplification is absent due to the sample's geometry.

Figure III.6 demonstrates the effect of dissipation on the discrepancies observed in Figs. III.5 (b, c). Increasing the dissipation rate Γ from 0.1γ to 0.3γ leads to noticeable improvements in convergence. Higher decay rates reduce the number of unstable realizations and improve the agreement between statistical averages and the exact solution. Our observations suggest that systems with a larger number of atoms may require higher dissipation rates for effective regularization. For studied parameters, dissipation at a rate comparable to spontaneous emission suffices to stabilize the system.

Comparing Solutions of Gauged and Ungauged Equations

We solve the equations using both types of gauges—drift and diffusion—and average the trajectories with a weight function. It is important to analyze how gauging impacts averaging by comparing results obtained without gauges, with only drift or diffusion gauges, and with and without the weight function. Figure III.7 presents this analysis for $N = 100$ incoherently pumped atoms across varying dissipation rates Γ.

Panels (a)-(c) depict solutions without any gauges. In panel (a), where $\Gamma = 0$, stochastic averages deviate significantly from the exact solution. Increasing the dissipation rate to $\Gamma = 0.3\gamma$ and $\Gamma = 0.8\gamma$ in panels (b) and (c), respectively, shows minimal improvement.

Panels (d)-(f) display results with only the diffusion gauge applied. Notably, in panel (f) ($\Gamma = 0.8\gamma$), the solution is closer to the exact solution compared to panel (c).

Panels (g)-(i) illustrate averages computed using only the drift gauge. In this case, the intensity curves align more closely with the exact solution than in previous scenarios. However, the weight function introduces instability, leading to a higher occurrence of unstable realizations. Panels (j)-(l) show averages where the weight function is omitted, yielding nonphysical intensities that often become negative.

Finally, panels (m)-(o) present results with both types of gauges applied. These demonstrate improved stability compared to using only the drift gauge, with fewer unstable trajectories. Panels (p)-(r) show averages computed without the weight function. Importantly, when dissipation is sufficiently strong, as in panel (r), neglecting the weight function has minimal effect, and the solution remains close to the exact result.

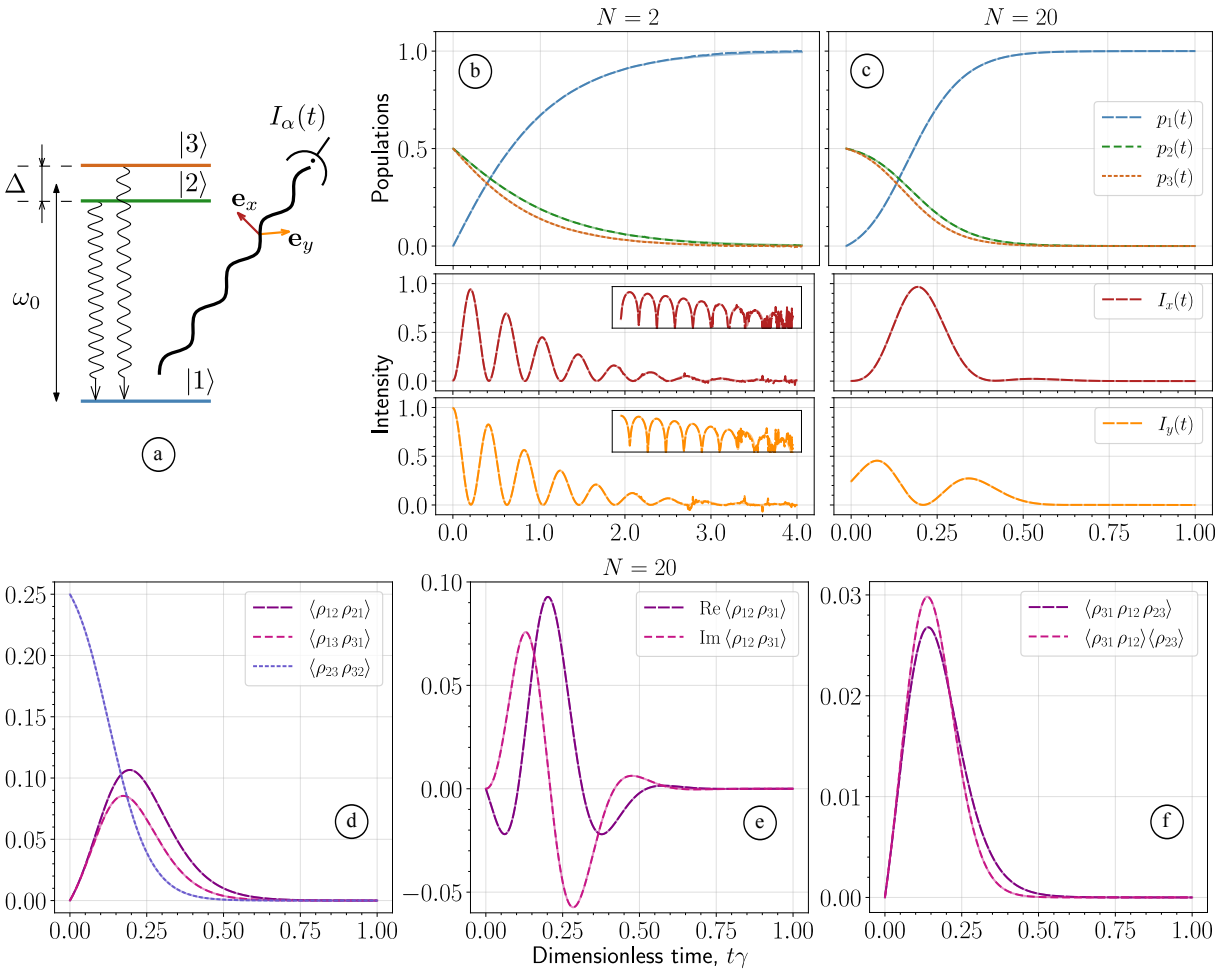

Figure III.8: Quantum beats in V systems, illustrated in panel (a), calculated for $N = 2$ (b) and $N = 20$ (c) atoms. In both cases, $\Delta = 15\gamma$. For the intensity curves in panel (b), the inset provides the same plots on a logarithmic scale. The intensities of different polarization components are normalized to the maximum total exact intensity. For $N = 20$, two- and three-particle correlators are shown in panels (d)-(f). Semi-transparent lines represent the exact solutions, while opaque lines indicate stochastic averages. We sampled 10^5 trajectories, neglecting 47 unstable realizations in panel (b).

2.3 Three-Level Systems: V-Type

To demonstrate that the stochastic formalism accurately captures multi-level effects, we analyze a V-type level configuration consisting of two excited states and a single ground state, as illustrated in Fig. III.8 (a). The energy gap between the excited states, Δ, is much smaller than the center frequency ($\Delta \ll \omega_0$). We assume orthogonal dipole moments for the transitions:

$$\overline{\mathbf{d}}_{31} = \frac{\overline{d}_{31}}{\sqrt{2}} \left(\mathbf{e}_x - i\mathbf{e}_y \right), \qquad \overline{\mathbf{d}}_{21} = \frac{\overline{d}_{21}}{\sqrt{2}} \left(\mathbf{e}_x + i\mathbf{e}_y \right),$$

with slightly different magnitudes, $|\overline{d}_{31}|^2 = 1$ and $|\overline{d}_{21}|^2 = 0.75$. Assuming that each emitter is prepared in a coherent superposition of excited states, as described in Eq. (II.39), quantum beats are observed, as shown in Fig. II.5. Within the stochastic framework, this state is represented by:

$$\rho_{22}(0) = \rho_{33}(0) = 0.5, \qquad \rho_{23}(0) = \rho_{32}(0) = -0.5,$$

and all other variables are zero.

As shown in Figs. III.8 (b) and (c), the stochastic equations accurately reproduce the quantum beats. For $N = 2$ in panel (b), intensity curves are also presented on a logarithmic

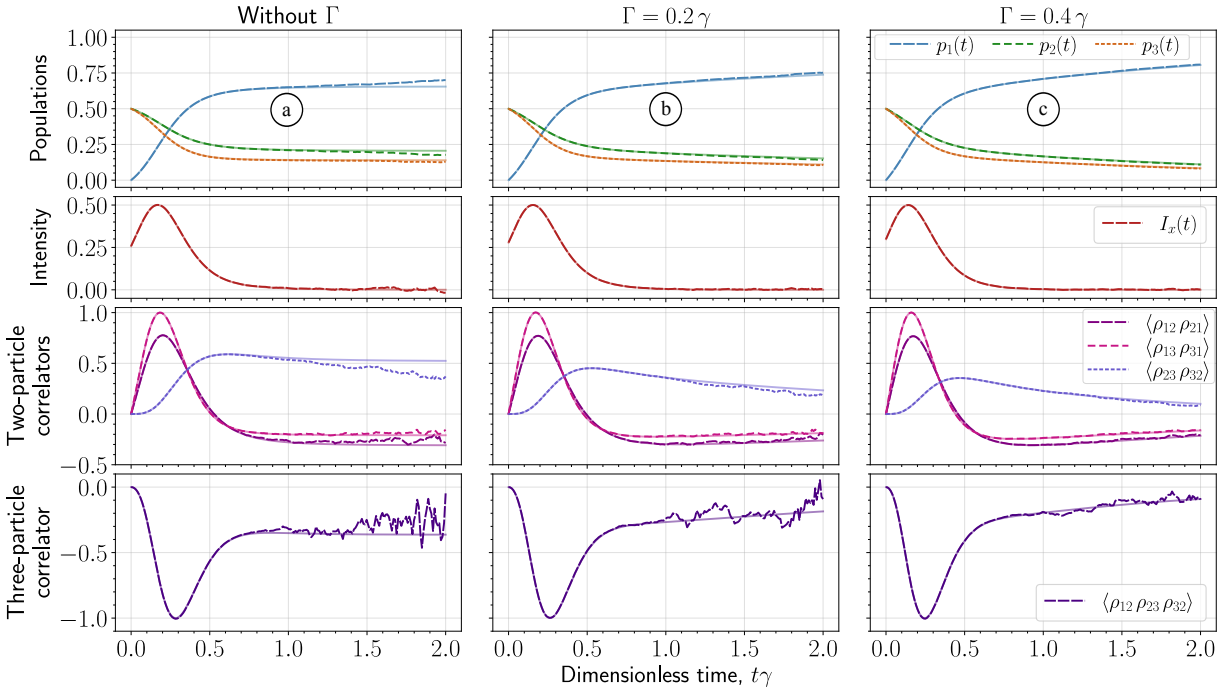

Figure III.9: Dynamics of $N = 20$ atoms with a V level structure and additional dissipation channels, as described in Eq. (III.31). Atoms start from the mixed state (III.30). The semi-transparent lines show the exact solution, and the opaque lines depict the stochastic averages. Intensities are normalized to the maximum total intensity. The two-particle correlators are normalized to the maximum of exact $\langle\rho_{13}\,\rho_{31}\rangle$; the three-particle correlators are normalized to the maximum. We neglected (a) 436; (b) 161; (c) 67 unstable realizations.

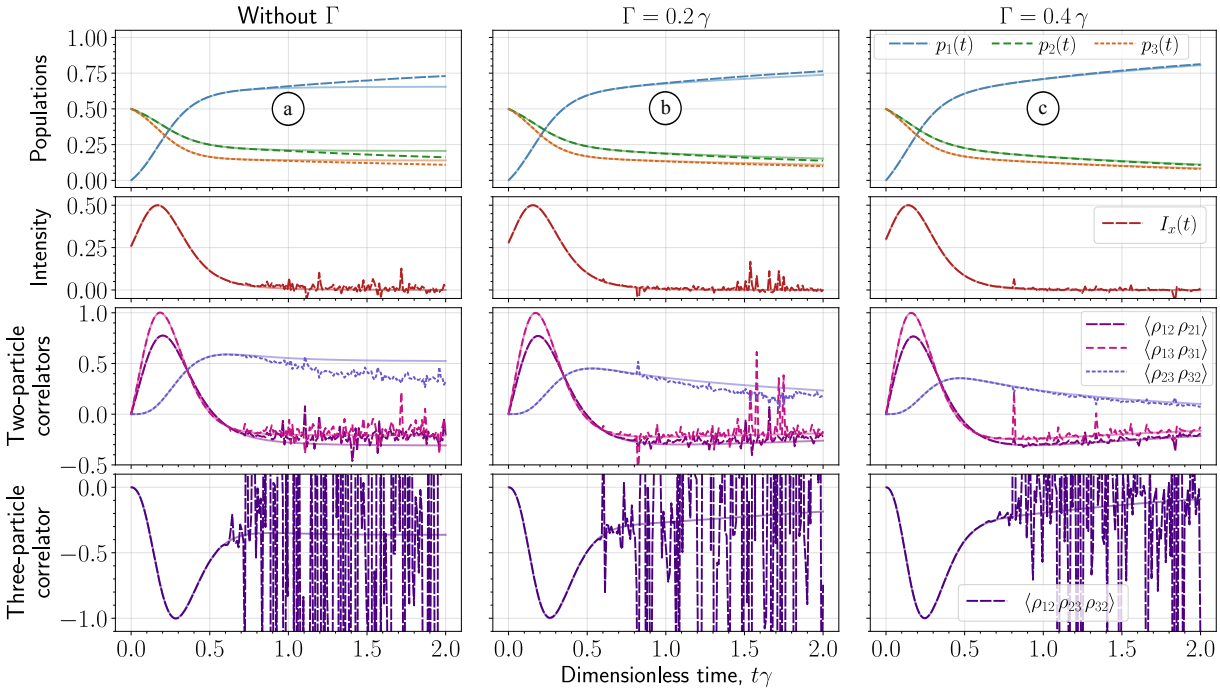

Figure III.10: Same as Fig. III.9, but for the ungauged stochastic equations. We neglected (a) 3; (b) 2; and (c) 1 unstable realizations.

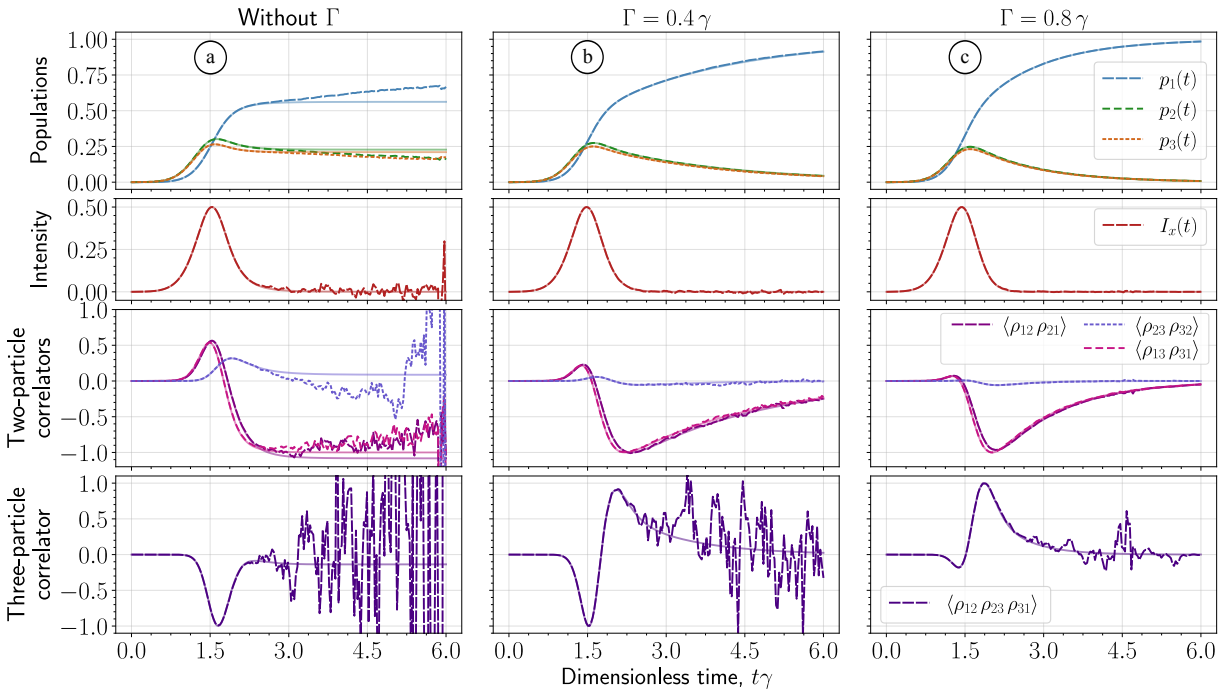

Figure III.11: Dynamics of $N = 20$ atoms with the V level structure and additional dissipation channels, as described in Eq. (III.31). Atoms are incoherently excited according to Eq. (III.32). Semi-transparent lines depict exact solutions, and the opaque lines depict stochastic averages. Intensities are normalized to the maximum total exact intensity. Two-particle correlators are normalized to the maximum absolute value of exact $\langle\rho_{13}\,\rho_{31}\rangle$; while three-particle correlators are normalized to their maximum. We neglected (a) 2500; (b) 106; and (c) 5 unstable realizations.

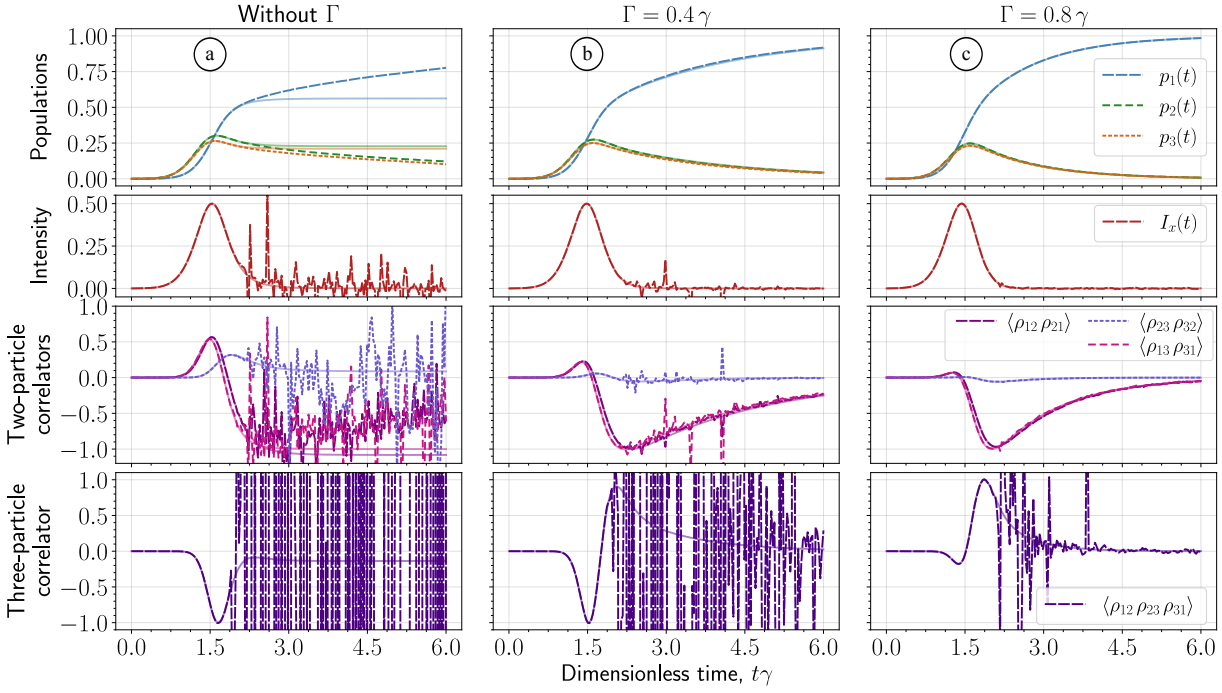

Figure III.12: Same as Fig. III.11, but for the ungauged stochastic equations. In panel (a), we neglected (a) 13 unstable realizations.

scale in the top-right inset. While low-amplitude oscillations are not fully captured, and small

spikes are observed, these spikes disappear for $N = 20$ in panel (c). Furthermore, the two-particle correlators shown in panels (d) and (e) and the three-particle correlator in panel (f) are accurately reproduced.

Mixed Initial State

We next consider a system starting from a statistically mixed state with no initial coherences. Unlike the previous example, where the observed quantum beats could also be predicted using a semiclassical approach, the dynamics here is initiated spontaneously, driven solely by noise terms.

We assume both excited states are equally populated, as described in Eq. (II.42). In terms of stochastic variables, this state is represented by:

$$\rho_{22}(0) = \rho_{33}(0) = 0.5, \tag{III.30}$$

and the rest of variables are zero. In this scenario, there are no quantum beats in the intensity, and the system evolves into a steady state.

The solution of the stochastic equations shown in Fig. III.9 (a) reveals convergence issues, with all averages deviating from the exact solution after approximately $\gamma t \approx 0.75$, when the system reaches a steady state. Since both polarization components evolve identically, we depict only the x-component, $I_x(t)$.

We regularize instabilities by introducing additional damping of excited states at a rate Γ:

$$\frac{d\rho_{11}(t)}{dt} = \ldots + \Gamma \sum_e \rho_{ee}(t) \tag{III.31a}$$

$$\frac{d\rho_{ee}(t)}{dt} = \ldots - \Gamma \rho_{ee}(t), \tag{III.31b}$$

where $e = 2, 3$. The coherences decay as follows:

$$\frac{d\rho_{1e}(t)}{dt} = \ldots - \frac{\Gamma}{2}\rho_{1e}(t), \tag{III.31c}$$

$$\frac{d\rho_{e1}(t)}{dt} = \ldots - \frac{\Gamma}{2}\rho_{e1}(t), \tag{III.31d}$$

$$\frac{d\rho_{e_1e_2}(t)}{dt} = \ldots - \Gamma \rho_{e_1e_2}(t). \tag{III.31e}$$

Setting $\Gamma = 0.2\gamma$ in Fig. III.9 (b) achieves a good agreement for both populations and intensities. However, the two- and three-particle correlators still do not converge. Increasing the rate to $\Gamma = 0.4\gamma$ in panel (c) brings them closer to the exact solution. For comparison, the same averages based on the ungauged equations are shown in Fig. III.10. Without gauging, two- and three-particle correlators are less stable and have many spikes.

Incoherent Pumping

To simulate the effect of non-instantaneous excitation through incoherent pumping, we assume that the atoms start from the additional state described by $\rho_{00}(t)$, as in Sec. 2.2. The atoms are then incoherently pumped to the excited states according to the Lindbladian in Eq. (II.44). The corresponding terms in the stochastic equations are:

$$\frac{d\rho_{ee}(t)}{dt} = \ldots + \frac{J_0(t)}{2}\rho_{00}(t), \qquad e = 2, 3, \tag{III.32}$$

while $\rho_{00}(t)$ satisfies Eq. (III.29). The pump profile $J_0(t)$ is the same Gaussian pulse as in Fig. III.5.

The simulations in Fig. III.11 (a) show more pronounced convergence issues than the scenario where atoms begin in a statistically mixed state. All averages exhibit instability and fail to

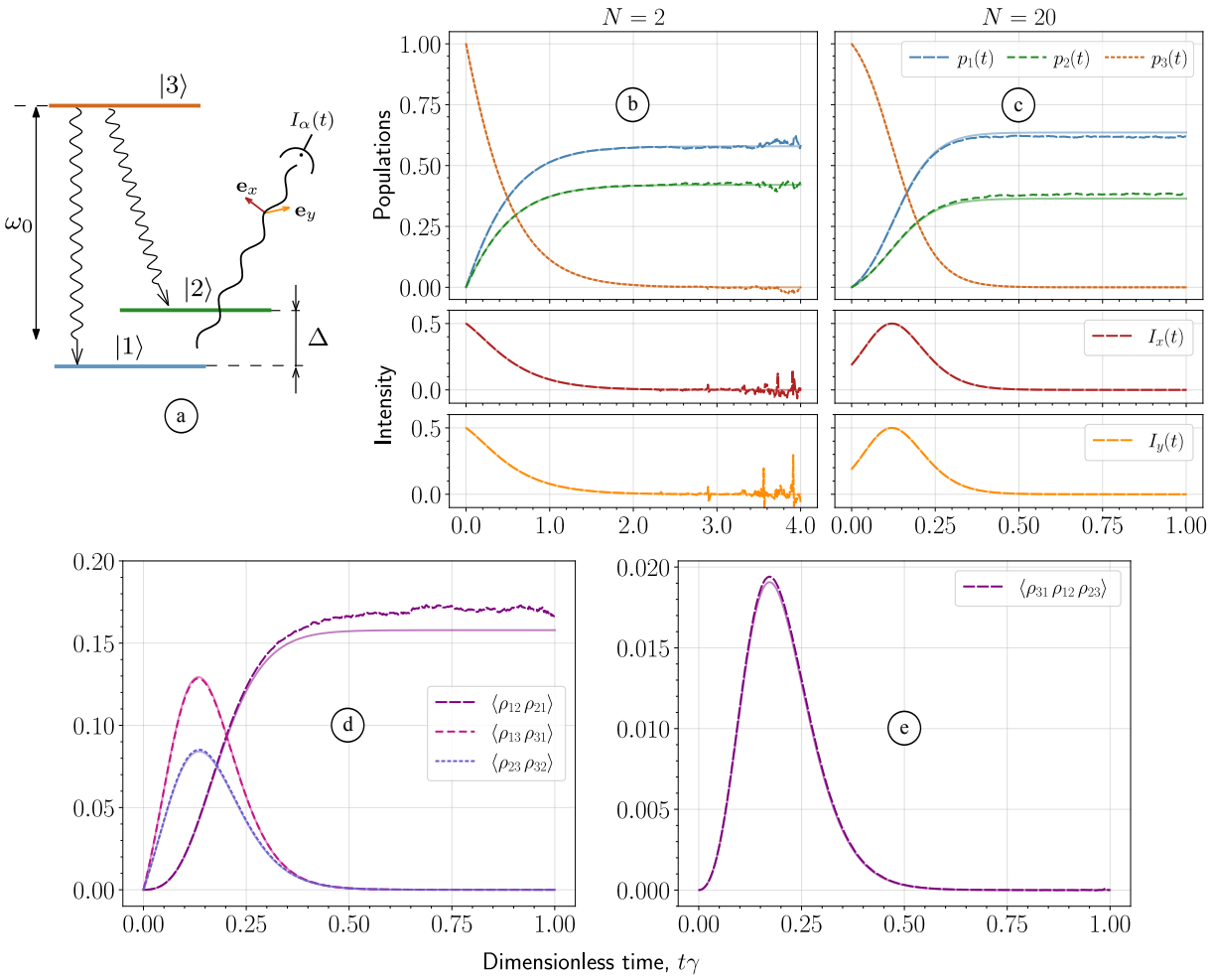

Figure III.13: Lasing from an ensemble of atoms with a Λ-level structure, illustrated in panel (a). The energy gap between ground states Δ is much smaller than the center frequency ω_0. Panels (b) and (c) depict the evolution of populations and intensity components for $N = 2$ and $N = 20$ atoms, respectively. Intensities are normalized to the maximum total exact intensity. Semi-transparent lines show the exact solution, while opaque lines depict stochastic averages. Panels (d) and (e) display two- and three-particle correlators. We sampled 10^5 trajectories, excluding (a) 470 and (b) 2325 unstable realizations.

converge as the system approaches a steady state. Since more population is trapped in the excited states compared to the case of an initially mixed state, we attribute the severity of discrepancies to a stronger influence of subradiant states.

Following Eqs. (III.31), we introduce additional nonradiative decay for the excited states. In Fig. III.11 (b), we set $\Gamma = 0.4\gamma$, which successfully stabilizes the populations, intensities, and two-particle correlators. However, the three-particle correlator remains highly unstable. Increasing the dissipation rate to $\Gamma = 0.8\gamma$ in panel (c) improves convergence, but the instability persists at later time moments. For comparison, the averages based on the ungauged equations are shown in Fig. III.12. Notably, the solutions are less stable without gauging, even for $\Gamma = 0.8\gamma$ in panel (c).

In summary, stabilizing higher-order correlators may require higher dissipation rates; with sufficiently strong damping, all observables can be accurately reproduced.

In the absence of initial coherences, the entire dynamics is initiated spontaneously and driven by noise terms. The fact that the three-particle correlator $\langle\rho_{31}\,\rho_{12}\,\rho_{23}\rangle$ remains close to the exact solution is important, as any factorization of this correlator would yield zero. This demonstrates that the formalism extends beyond semiclassical models and, when properly regularized, fully captures the quantum inherent in many-body correlations.

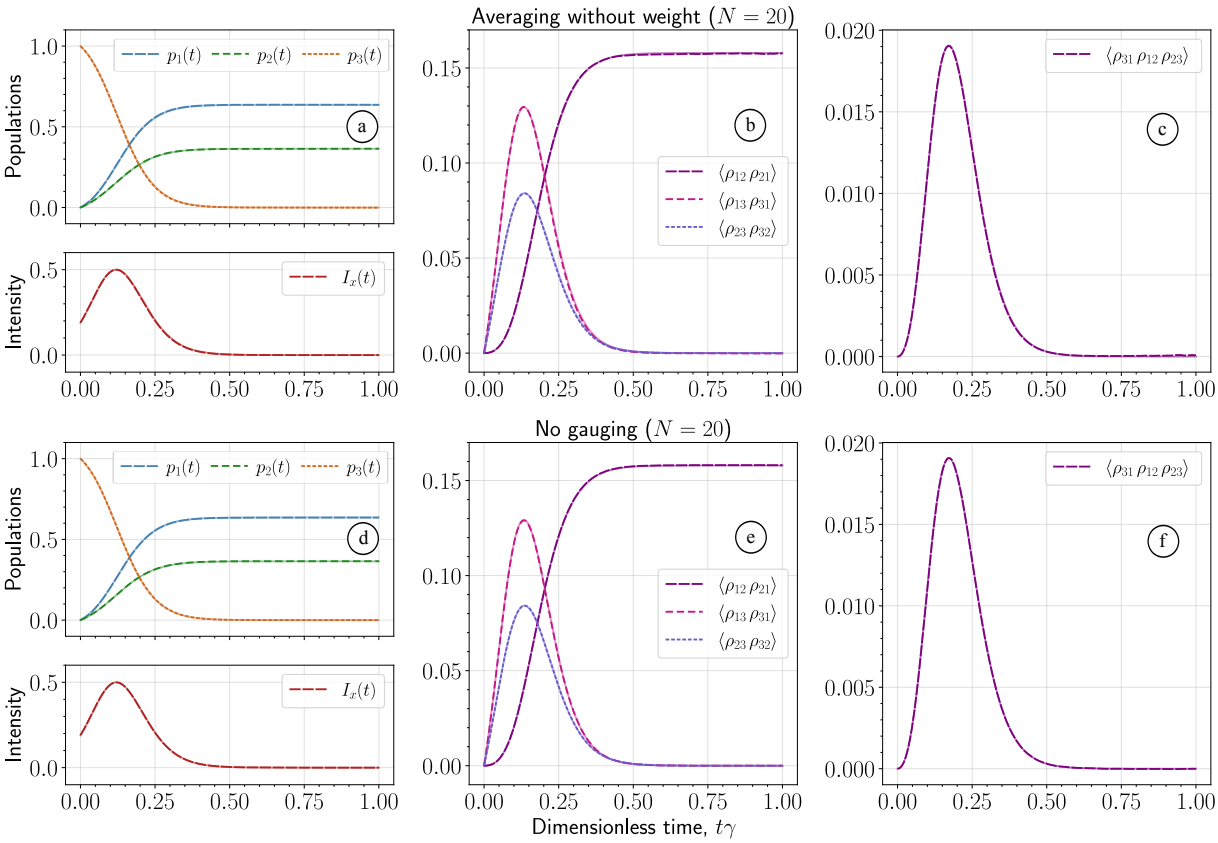

Figure III.14: Results for $N = 20$ from Fig. III.13 (c)-(e). Panels (a)-(c) show averages from the gauged stochastic equations without the weight function. Panels (d)-(f) depict averages from the ungauged stochastic equations.

2.4 Three-Level Systems: Λ-Type

Semiclassical models and stochastic electrodynamics can also predict quantum beats in V-systems [119]. However, certain models mistakenly predict quantum beats in Λ-systems [119, 196], which involve one excited state, $|3\rangle$, and two ground states, $|1\rangle$ and $|2\rangle$, as depicted in Fig. III.13 (a).

We analyze the Λ-configuration with orthogonal transition dipole moments, expressed as:

$$\overline{\mathbf{d}}_{31} = \frac{\overline{d}_{31}}{\sqrt{2}}(\mathbf{e}_x - i\mathbf{e}_y), \qquad \overline{\mathbf{d}}_{32} = \frac{\overline{d}_{32}}{\sqrt{2}}(\mathbf{e}_x + i\mathbf{e}_y).$$

The dipole moment magnitudes are slightly different, with $|\overline{d}_{31}|^2 = 1$ and $|\overline{d}_{32}|^2 = 0.75$. Transitions between the ground states are forbidden.

Our equations predict no intensity beats, consistent with quantum-mechanical expectations. Figure III.13 presents the populations and intensities for $N = 2$ (b) and $N = 20$ (c) atoms. Both polarization components of the emission have identical profiles, exhibiting no quantum beats. For $N = 2$ in panel (b), there are instabilities when the system relaxes to the ground states, where no dynamics should occur. These instabilities are attributed to nonlinear noise terms.

For $N = 20$ in panel (c), there is a noticeable systematic discrepancy in the populations. Panel (d) illustrates two-particle correlators, showing a significant deviation of the correlator involving ground states $\langle\rho_{12}\,\rho_{21}\rangle$ from the exact solution. Similarly, the three-particle correlator in panel (e) deviates slightly from the exact solution. This discrepancy arises from unnecessary gauging.

In the previous chapter, we established that the system's final state is a steady state described in Eq. (II.46). As the system evolves into this steady state, the resulting non-trivial dynamics may introduce fluctuations that amplify the anti-Hermitian components of $\rho_{pq}(t)$, destabilizing the weight function.

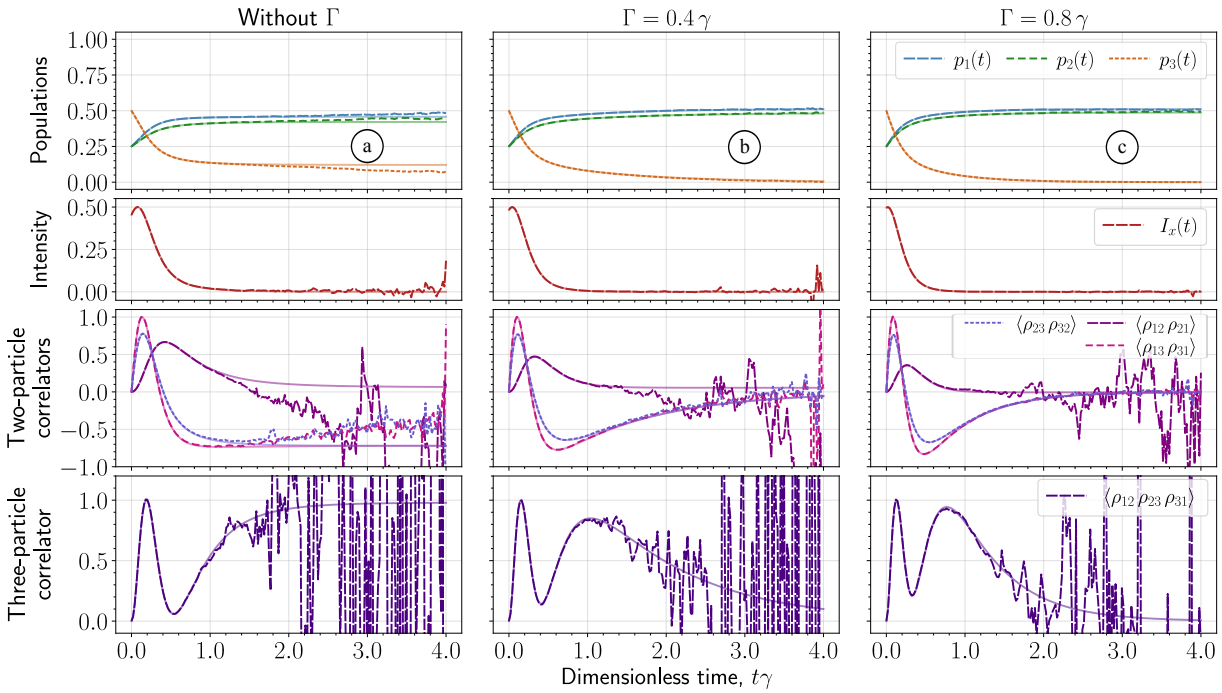

Figure III.15: Dynamics of $N = 20$ atoms with a Λ-level structure and additional dissipation channels (see Eqs. (III.34)). Atoms start from the mixed state in Eq. (III.33). Semi-transparent lines represent the exact solution, while opaque lines depict stochastic averages. Intensities are normalized to the maximum total exact intensity. Two-particle correlators are normalized to the maximum of $\langle\rho_{13}\rho_{31}\rangle$; three-particle correlators are normalized to the maximum. We excluded (a) 2503; (b) 965; (c) 756 unstable realizations.

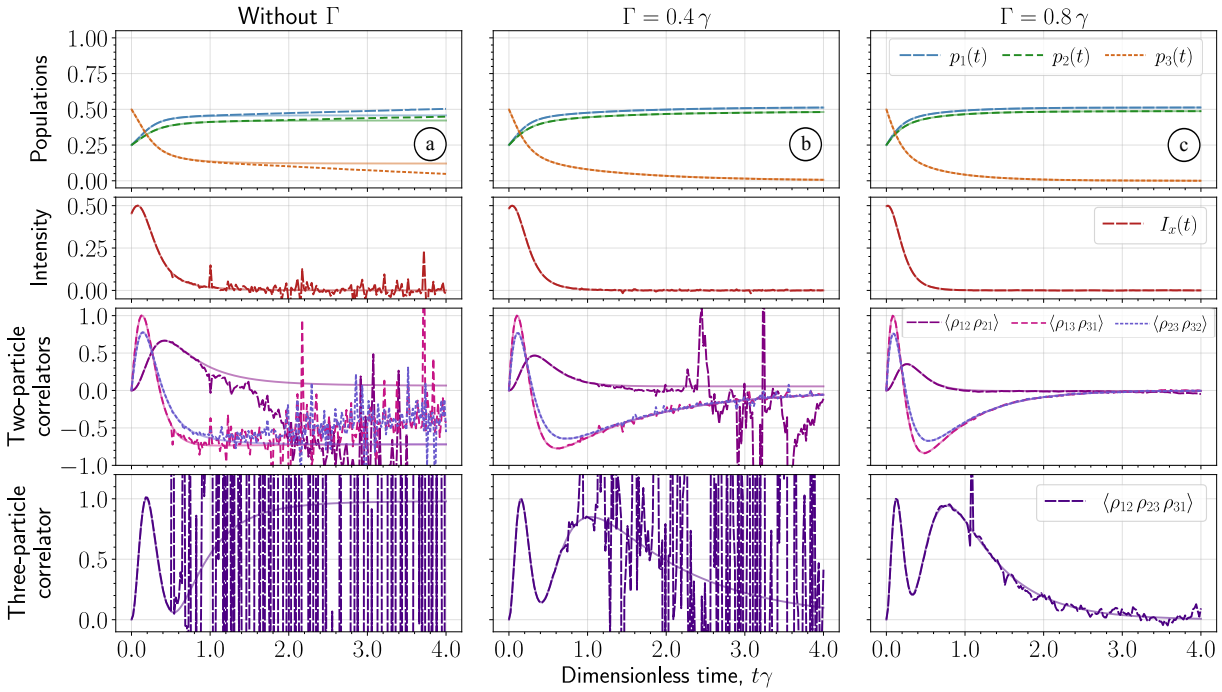

Figure III.16: Same as Fig. III.15, but for the ungauged stochastic equations. In panel (a), we excluded 6 unstable trajectories.

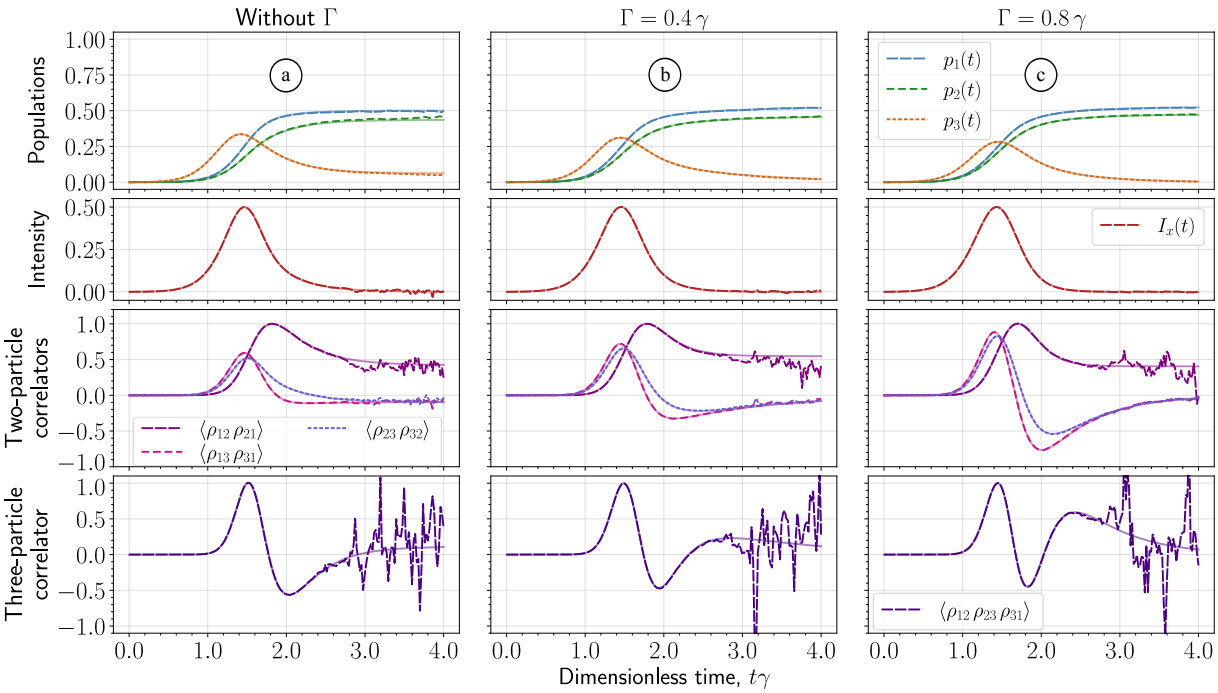

Figure III.17: Dynamics of $N = 20$ atoms with a Λ-level structure and additional dissipation channels (see Eqs. (III.34)). Atoms are incoherently excited according to Eq (III.35). Semi-transparent lines represent the exact solution, while opaque lines show stochastic averages. Intensities are normalized to the maximum total exact intensity. Two-particle correlators are normalized to the maximum of $\langle\rho_{12}\,\rho_{21}\rangle$; three-particle correlators are normalized to the maximum. We excluded (a) 1545; (b) 331; (c) 150 unstable realizations.

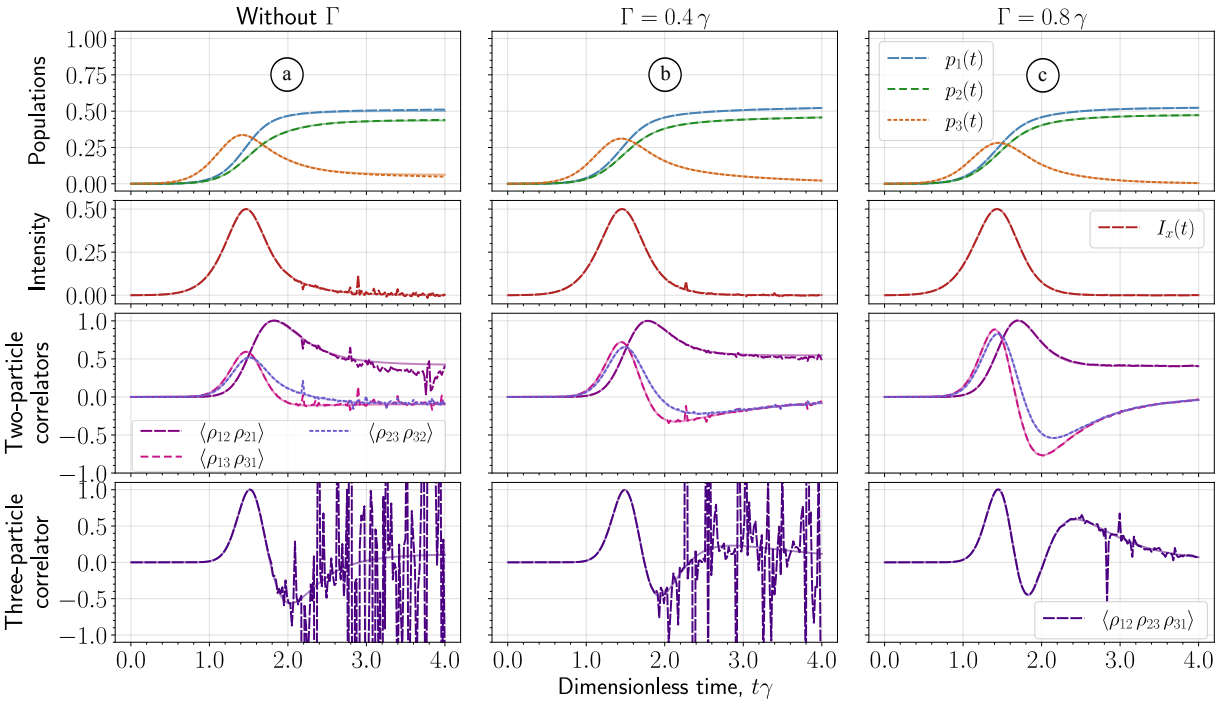

Figure III.18: Same as Fig. III.17, but for the ungauged stochastic equations. In panel (a), we excluded 4 unstable realizations.

To demonstrate that the weight function is a source of the observed instabilities, we present two sets of averages in Fig. III.14. The top row (a)-(c) shows averages derived from the gauged stochastic equations without the weight function, achieving a good agreement with the exact solution. The bottom row (d)-(f) displays results without any gauging applied, which also align closely with the exact solution.

Mixed Initial State

As in the previous section, we consider an ensemble prepared in a mixed state without coherences, where the initial level populations are:

$$\rho_{11}(0) = \rho_{22}(0) = 0.25, \qquad \rho_{33}(0) = 0.5, \tag{III.33a}$$

with all other matrix elements being zero. The solution reveals that the ensemble does not fully relax to the ground states but evolves into a steady state, with some population remaining in the excited state, as shown in Fig. III.15 (a). As the system reaches this steady state, populations deviate from the exact solution. Additionally, intensities exhibit small spikes, and two- and three-particle correlators are unstable.

To address these instabilities, we introduce additional damping of the excited state to the ground states ($3 \to 1, 2$) at a rate Γ:

$$\frac{d\rho_{gg}(t)}{dt} = \ldots + \Gamma\rho_{33}(t), \qquad \frac{d\rho_{33}(t)}{dt} = \ldots - 2\Gamma\rho_{33}(t), \tag{III.34a}$$

$$\frac{d\rho_{g3}(t)}{dt} = \ldots - \Gamma\rho_{g3}(t), \qquad \frac{d\rho_{3g}(t)}{dt} = \ldots - \Gamma\rho_{3g}(t), \tag{III.34b}$$

where $g = 1, 2$. Therefore, the excited state is depopulated at a rate of 2Γ. By setting $\Gamma = 0.4\gamma$ in Fig. III.15 (b), we achieve population dynamics consistent with the exact solution. Increasing Γ to 0.8γ in panel (c) stabilizes the intensity curve, though the three-particle correlator remains unstable. The two-particle correlator $\langle \rho_{12}\, \rho_{21} \rangle$ continues to show instability, similar to Fig. III.13 (d).

For comparison, we present averages from the ungauged equations in Fig. III.16. Notably, the solution for $\Gamma = 0.8\gamma$ in panel (c) is more stable than the gauged counterpart. In panels (a) and (b), the ungauged averages are generally less stable than those from the gauged equations.

Incoherent Pumping

The same instability issues arise when the ensemble is incoherently excited. In this case, the atoms start from an additional level, described by $\rho_{00}(t)$, and are incoherently pumped to the excited state following the Lindbladian in Eq. (II.48). This pumping introduces an additional term in the equations:

$$\frac{d\rho_{33}(t)}{dt} = \ldots + J_0(t)\, \rho_{00}(t), \tag{III.35}$$

where $\rho_{00}(t)$ evolves according to Eq. (III.29). We assume the same Gaussian pump profile $J_0(t)$ as in Fig. III.5. The simulation results are shown in Fig. III.17.

Panel (a) illustrates the case without additional damping. As the system reaches the steady state, populations deviate slightly from the exact solution. Furthermore, the correlator $\langle \rho_{12}\, \rho_{21} \rangle$ and the three-particle correlator exhibit instability.

By increasing the dissipation rate, as shown in panels (b) and (c), the agreement between the populations and intensities and the exact solution improves. However, the correlator $\langle \rho_{12}\, \rho_{21} \rangle$ and the three-particle correlator remain problematic.

In Fig. III.18, we present averages obtained from the ungauged stochastic equations. Panels (a) and (b) display less stability compared to the gauged equations. However, the case with stronger dissipation in panel (c) shows improved stability, with the exception of the three-particle correlator. This suggests that the gauging approach could be further refined and implies that the issues observed in Fig. III.17 (c) may be due to the unnecessary application of gauges.

To summarize, Λ systems exhibit more instability-related issues compared to two-level and V-systems. A possible explanation is that the ensemble evolves into a steady state, even with additional dissipation, characterized by:

$$\langle \rho_{12}^{(ss)}\, \rho_{21}^{(ss)} \rangle \neq 0, \tag{III.36}$$

where ss indicates the steady state. This non-trivial dynamics can result in slow convergence for certain correlators, as seen in the numerical examples. The coherences between the ground states, $\rho_{g_1 \neq g_2}(t)$, are not directly damped. Effective regularization might require either stronger decoherence to suppress the buildup of the steady state, or the introduction of an additional dissipation channel for the variables $\rho_{g_1 \neq g_2}(t)$.

2.5 Interaction with a Quantized Field

As demonstrated in the previous examples, the effectiveness of the formalism is constrained by convergence issues. In this section, we examine a particularly challenging case—the interaction between emitters and a limited number of quantized field modes, known as the spin-boson interaction [186]. Specifically, we derive the stochastic equations governing this model.

The field modes are represented by bosonic operators $\{\hat{a}_f, \hat{a}_f^\dagger\}$, with the P-function dependent on the corresponding variables $\{\alpha_f, \alpha_f^\dagger\}$. The ansatz for the density matrix must incorporate contributions from both photons (see Eq. (III.3)) and emitters (see Eq. (III.4)). This is achieved by forming the tensor product of these basis elements, expressed formally as:

$$\prod_f \hat{\Lambda}_f(\alpha_f, \alpha_f^\dagger) \otimes |\Lambda(\{\beta_{ij}\})\rangle\!\rangle.$$

Here, $\hat{\Lambda}_f$ denotes the projector from Eq. (III.3), acting within the subspace of the f-th field mode. The density matrix is expressed in this basis, with the P-function depending on all parameters $\{\alpha_f, \alpha_f^\dagger, \beta_{ij}\}$.

Starting from the general Hamiltonian described in Eqs. (I.21)-(I.22), which models a system of emitters interacting with the electromagnetic field, we simplify by omitting the phase factors $e^{i\mathbf{k}\cdot\mathbf{r}_\mu}$. This simplification assumes the atomic ensemble is compact.

Subsequently, we perform second quantization, reformulating the master equation solely in terms of bosonic superoperators. After applying normal ordering and using the replacement rules in Eq. (III.8), we obtain the following equation for the P-function:[5]

$$\begin{aligned}
\frac{\partial P}{\partial t} = &-\sum_{p,q=1}^{M} \frac{\partial}{\partial \beta_{pq}} \Big\{ -i\omega_{pq}\, \beta_{pq} - \frac{i}{\hbar} \sum_{\mathbf{k},\lambda} (\boldsymbol{\mathcal{E}}_{\mathbf{k},\lambda}\, \alpha_{\mathbf{k},\lambda} + \boldsymbol{\mathcal{E}}^*_{\mathbf{k},\lambda}\, \alpha^\dagger_{\mathbf{k},\lambda}) \cdot \sum_{r=1}^{M} (\beta_{pr}\, \mathbf{d}_{rq} - \mathbf{d}_{pr}\, \beta_{rq}) \Big\}\, P \\
&- \sum_{\mathbf{k},\lambda} \frac{\partial}{\partial \alpha_{\mathbf{k},\lambda}} \Big\{ -i\nu_{\mathbf{k}}\, \alpha_{\mathbf{k},\lambda} + \frac{i\boldsymbol{\mathcal{E}}^*_{\mathbf{k},\lambda}}{\hbar} \cdot \sum_{i,j=1}^{M} \mathbf{d}_{ji}\, \beta_{ij} \Big\}\, P - \sum_{\mathbf{k},\lambda} \frac{\partial}{\partial \alpha^\dagger_{\mathbf{k},\lambda}} \Big\{ i\nu_{\mathbf{k}}\, \alpha^\dagger_{\mathbf{k},\lambda} - \frac{i\boldsymbol{\mathcal{E}}_{\mathbf{k},\lambda}}{\hbar} \cdot \sum_{i,j=1}^{M} \mathbf{d}_{ji}\, \beta_{ij} \Big\}\, P \\
&+ \sum_{p,q=1}^{M} \sum_{\mathbf{k},\lambda} \frac{\partial}{\partial \beta_{pq}} \Big\{ \frac{\partial}{\partial \alpha_{\mathbf{k},\lambda}} \frac{i\boldsymbol{\mathcal{E}}^*_{\mathbf{k},\lambda}}{\hbar} \cdot \sum_{r=1}^{M} \mathbf{d}_{pr}\, \beta_{rq} - \frac{\partial}{\partial \alpha^\dagger_{\mathbf{k},\lambda}} \frac{i\boldsymbol{\mathcal{E}}_{\mathbf{k},\lambda}}{\hbar} \cdot \sum_{r=1}^{M} \beta_{pr}\, \mathbf{d}_{rq} \Big\} P,
\end{aligned}$$

where $P = P(\{\alpha_{\mathbf{k},\lambda}, \alpha^\dagger_{\mathbf{k},\lambda}, \beta_{ij}\}, t)$, and $\boldsymbol{\mathcal{E}}_{\mathbf{k},\lambda} = i\sqrt{2\pi\hbar\nu_{\mathbf{k}}/V}\, \mathbf{e}_{\mathbf{k},\lambda}\, e^{i\mathbf{k}\cdot\mathbf{r}}$.

The associated stochastic variables $\beta_{pq}(t)$ have non-trivial statistics at $t = 0$, characterized by the η-object in Eq. (III.15). The initial state of the field can be represented as a superposition of coherent states.

Removing the η-object from the Fokker-Planck equation is not straightforward due to the field drift term, which depends on atomic variables. This term arises from the normalization

[5] For the field variables, we use the following replacement rules:

$$\hat{a}_{\mathbf{k},\lambda}\, \hat{\rho} \longrightarrow \alpha_{\mathbf{k},\lambda}\, P, \qquad \hat{a}^\dagger_{\mathbf{k},\lambda}\, \hat{\rho} \longrightarrow \big(\alpha^\dagger_{\mathbf{k},\lambda} - \frac{\partial}{\partial \alpha_{\mathbf{k},\lambda}}\big) P, \qquad \hat{\rho}\, \hat{a}^\dagger_{\mathbf{k},\lambda} \longrightarrow \alpha^\dagger_{\mathbf{k},\lambda}\, P, \qquad \hat{\rho}\, \hat{a}_{\mathbf{k},\lambda} \longrightarrow \big(\alpha_{\mathbf{k},\lambda} - \frac{\partial}{\partial \alpha^\dagger_{\mathbf{k},\lambda}}\big) P.$$

factor $e^{-\sum_i \beta_{ii}}$ in Eq. (III.6). By following the steps in Sec. 5.3, we employ a non-normalized representation to eliminate the η-object. As a result, we obtain normalized stochastic variables for N emitters, $\rho_{pq}(t)$, which satisfy the following stochastic equations:

$$\begin{aligned}\frac{d\rho_{pq}(t)}{dt} &= -i\omega_{pq}\,\rho_{pq}(t) - \frac{i}{\hbar}\boldsymbol{\mathcal{E}}(t)\cdot\sum_{r=1}^{M}\{\rho_{pr}(t)\,\mathbf{d}_{rq} - \mathbf{d}_{pr}\,\rho_{rq}(t)\} \\ &+\sum_{r=1}^{M}\rho_{pr}(t)\,\mathbf{d}_{rq}\cdot\mathbf{f}^{\dagger}(t) + \sum_{r=1}^{M}\mathbf{d}_{pr}\,\rho_{rq}(t)\cdot\mathbf{g}^{\dagger}(t) - \rho_{pq}(t)\sum_{i,j=1}^{M}\mathbf{d}_{ji}\,\rho_{ij}(t)\cdot\{\mathbf{f}^{\dagger}(t)+\mathbf{g}^{\dagger}(t)\}.\end{aligned} \tag{III.37a}$$

The last term is a stochastic process with a quadratic nonlinearity, which ensures that the normalization condition $\sum_s \rho_{ss}(t) = 1$ is maintained. The stochastic analogue of the electric field is given by:

$$\boldsymbol{\mathcal{E}}(t) = \sum_{\mathbf{k},\lambda}\{\boldsymbol{\mathcal{E}}_{\mathbf{k},\lambda}\,\alpha_{\mathbf{k},\lambda}(t) + \boldsymbol{\mathcal{E}}^{*}_{\mathbf{k},\lambda}\,\alpha^{\dagger}_{\mathbf{k},\lambda}(t)\}.$$

The field variables $\alpha_{\mathbf{k},\lambda}(t)$ and $\alpha^{\dagger}_{\mathbf{k},\lambda}(t)$ satisfy stochastic equations resembling the classical equations in Eq. (I.13), but with added noise terms:

$$\frac{d\alpha_{\mathbf{k},\lambda}(t)}{dt} = -i\nu_{\mathbf{k}}\,\alpha_{\mathbf{k},\lambda}(t) + \frac{i\boldsymbol{\mathcal{E}}^{*}_{\mathbf{k},\lambda}}{\hbar}\cdot\{N\sum_{i,j=1}^{M}\mathbf{d}_{ji}\,\rho_{ij}(t) + \mathbf{g}(t)\}, \tag{III.37b}$$

$$\frac{d\alpha^{\dagger}_{\mathbf{k},\lambda}(t)}{dt} = i\nu_{\mathbf{k}}\,\alpha^{\dagger}_{\mathbf{k},\lambda}(t) - \frac{i\boldsymbol{\mathcal{E}}_{\mathbf{k},\lambda}}{\hbar}\cdot\{N\sum_{i,j=1}^{M}\mathbf{d}_{ji}\,\rho_{ij}(t) + \mathbf{f}(t)\}. \tag{III.37c}$$

The noise terms $\mathbf{f}(t)$, $\mathbf{f}^{\dagger}(t)$, $\mathbf{g}(t)$, and $\mathbf{g}^{\dagger}(t)$ are three-dimensional vectors of independent Gaussian white noise processes. The only non-trivial correlation properties are:

$$\langle \mathrm{f}^{(\alpha)}(t)\,\mathrm{f}^{\dagger(\beta)}(t')\rangle = \langle \mathrm{g}^{(\alpha)}(t)\,\mathrm{g}^{\dagger(\beta)}(t')\rangle = \delta_{\alpha\beta}\,\delta(t-t'), \tag{III.37d}$$

and all other first- and second-order correlators are zero. The pairs $\mathbf{f}(t), \mathbf{f}^{\dagger}(t)$ and $\mathbf{g}(t), \mathbf{g}^{\dagger}(t)$ are statistically independent of each other.

Finally, the relationship between stochastic averages and quantum-mechanical expectation values is given by:

$$\begin{aligned}&\langle \alpha^{\dagger}_{\mathbf{k}_1,\lambda_1}(t)\,\alpha^{\dagger}_{\mathbf{k}_2,\lambda_2}(t)\ldots\alpha_{\mathbf{k}_3,\lambda_3}(t)\ldots\rho_{p_1q_1}(t)\ldots\rho_{p_Kq_K}(t)\rangle \\ &\qquad = \frac{(N-K)!}{N!}\,\mathrm{Tr}\,[\hat{a}^{\dagger}_{\mathbf{k}_1,\lambda_1}\,\hat{a}^{\dagger}_{\mathbf{k}_2,\lambda_2}\ldots\hat{a}_{\mathbf{k}_3,\lambda_3}\ldots\sum_{\mu_1\neq\ldots\neq\mu_K}\hat{\sigma}_{\mu_1,q_1p_1}\ldots\hat{\sigma}_{\mu_K,q_Kp_K}\,\hat{\rho}(t)],\end{aligned} \tag{III.37e}$$

for $K \leq N$. Here, the bosonic operators are arranged in normal order.

The total number of stochastic variables equals twice the number of field modes plus M^2 atomic variables. At most, six independent complex-valued noise terms must be sampled. Although this formalism offers potential computational advantages over traditional quantum-mechanical methods, its applicability is limited by diverging trajectories.

In the next subsection, we investigate the interaction between two-level emitters and a single-mode quantized field.

Tavis-Cummings Model

As an illustration, we consider a compact system of two-level atoms interacting with a single-mode field resonant with the atomic transition. Neglecting counter-rotating terms, the resulting equations describe the Tavis-Cummings model, governed by the effective interaction Hamiltonian in Eq. (II.50). The cavity mode is assumed to have a single polarization. Only the projections of the noise terms onto this polarization axis contribute to the dynamics. These projections are denoted as $\mathrm{f}(t)$, $\mathrm{f}^{\dagger}(t)$, $\mathrm{g}(t)$, and $\mathrm{g}^{\dagger}(t)$.

After eliminating the free-oscillating components, we obtain the following equations for the stochastic density matrix:

$$\frac{d\rho_{11}(\tau)}{d\tau} = i\alpha(\tau)\,\rho_{12}(\tau) - i\alpha^{\dagger}(\tau)\,\rho_{21}(\tau) + \rho_{12}(\tau)\,\mathrm{f}^{\dagger}(\tau) + \rho_{21}(\tau)\,\mathrm{g}^{\dagger}(\tau) - \rho_{11}(\tau)\,\mathrm{h}(\tau), \tag{III.38a}$$

$$\frac{d\rho_{12}(\tau)}{d\tau} = -i\alpha^{\dagger}(\tau)\,[\rho_{22}(\tau) - \rho_{11}(\tau)] + \rho_{22}(\tau)\,\mathrm{g}^{\dagger}(\tau) - \rho_{12}(\tau)\,\mathrm{h}(\tau), \tag{III.38b}$$

$$\frac{d\rho_{21}(\tau)}{d\tau} = i\alpha(\tau)\,[\rho_{22}(\tau) - \rho_{11}(\tau)] + \rho_{22}(\tau)\,\mathrm{f}^{\dagger}(\tau) - \rho_{21}(\tau)\,\mathrm{h}(\tau), \tag{III.38c}$$

$$\frac{d\rho_{22}(\tau)}{d\tau} = -i\alpha(\tau)\,\rho_{12}(\tau) + i\alpha^{\dagger}(\tau)\,\rho_{21}(\tau) - \rho_{22}(\tau)\,\mathrm{h}(\tau), \tag{III.38d}$$

where $\tau = tg$ is the dimensionless time, g is the Rabi frequency from the Hamiltonian in Eq. (II.50), and $\mathrm{h}(\tau)$ denotes the noise process given by:

$$\mathrm{h}(\tau) = \rho_{12}(\tau)\,\mathrm{f}^{\dagger}(\tau) + \rho_{21}(\tau)\,\mathrm{g}^{\dagger}(\tau).$$

This noise appears after the elimination of the η-object.

The electromagnetic field is characterized by two variables, $\alpha(\tau)$ and $\alpha^{\dagger}(\tau)$, which evolve according to the stochastic equations:

$$\frac{d\alpha(\tau)}{d\tau} = -iN\rho_{21}(\tau) - i\mathrm{g}(\tau), \qquad \frac{d\alpha^{\dagger}(\tau)}{d\tau} = iN\rho_{12}(\tau) + i\mathrm{f}(\tau). \tag{III.38e}$$

The noise terms in these equations have the following correlation properties:

$$\langle \mathrm{f}(\tau)\,\mathrm{f}^{\dagger}(\tau')\rangle = \langle \mathrm{g}(\tau)\,\mathrm{g}^{\dagger}(\tau')\rangle = \delta(\tau - \tau'),$$

with all other first- and second-order correlators being zero.

A numerical implementation of these equations reveals that a significant portion of sampled trajectories diverges as the system evolves toward a quasi-stationary state. Unfortunately, we were unable to identify an effective gauge to stabilize the equations [197]. This dissertation focuses exclusively on the ungauged stochastic equations, without employing any stabilization gauges.

Figure III.19 illustrates three distinct regimes of the Tavis-Cummings model with $N = 50$ atoms, initially prepared in the ground state, and the field starting in a coherent state with the mean photon number $\langle n_{\mathrm{ph.}}\rangle$. In this figure, we exclude trajectories when they reach numerical infinity.

Panel (a) illustrates a case where the initial mean photon number is much smaller than the number of atoms, $\langle n_{\mathrm{ph.}}\rangle = 5$. The stochastic equations accurately reproduce the first few Rabi oscillations. However, as the simulation progresses, unstable trajectories emerge. The upper plot shows an exponential decrease in the number of trajectories: out of the initial 10^5 realizations, only about 64% remain stable at the final time point. The population inversion exhibits numerous spikes, while the mean photon number in the lower plot deviates significantly from the exact solution.

Panel (b) considers a case where the initial mean photon number matches the number of atoms, $\langle n_{\mathrm{ph.}}\rangle = 50$. By the end of the simulation, only 27% of the sampled trajectories remain stable, again showing exponential decrease. The population inversion is highly unstable, and the mean photon number significantly diverges from the exact solution.

Panel (c) depicts the regime where the initial mean photon number exceeds the number of atoms, $\langle n_{\mathrm{ph.}}\rangle = 500$. Here, 44% of trajectories remain stable by the end of simulation.

In all regimes, as the system approaches the collapse, the number of stable trajectories decreases exponentially, resulting in a clear deviation of the Rabi oscillations from the exact solution. Computation for later time points reveals that stochastic equations fail to reproduce the revival effect.

In Figure III.20, the same averages are shown, with realizations excluded when the absolute value of any stochastic variable exceeds 10^3. This figure illustrates that while omitting unstable realizations smooths the curves visually, it does not enhance the accuracy of the results.

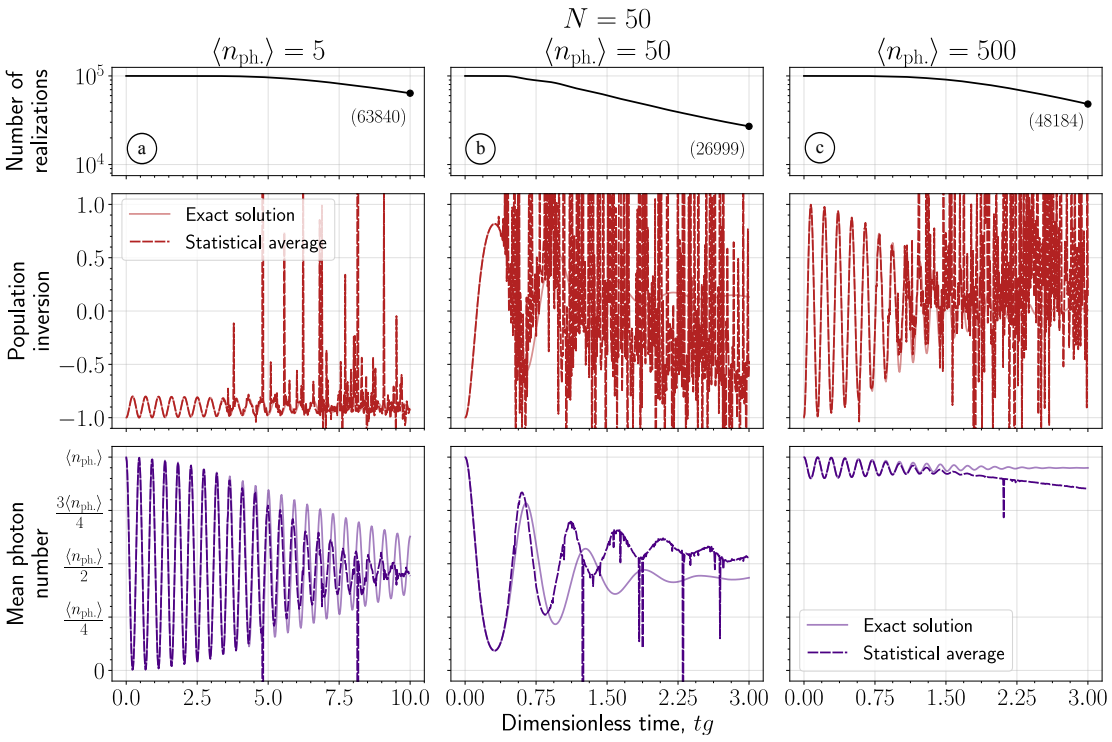

Figure III.19: Tavis-Cummings model with $N = 50$ atoms. Field is initially in a coherent state with a mean photon number $\langle n_{\mathrm{ph.}} \rangle$. Atoms start from the ground state. Semi-transparent lines show the exact solution, and opaque lines depict stochastic averages. Unstable realizations are omitted when any stochastic variable reaches numerical infinity. The top row shows the number of realizations (on a logarithmic scale) used for averaging; the middle row shows the average population inversion $\langle [\rho_{22}(\tau) - \rho_{11}(\tau)] \rangle$; and the bottom row shows the mean photon number $\langle \alpha^{\dagger}(\tau)\, \alpha(\tau) \rangle$.

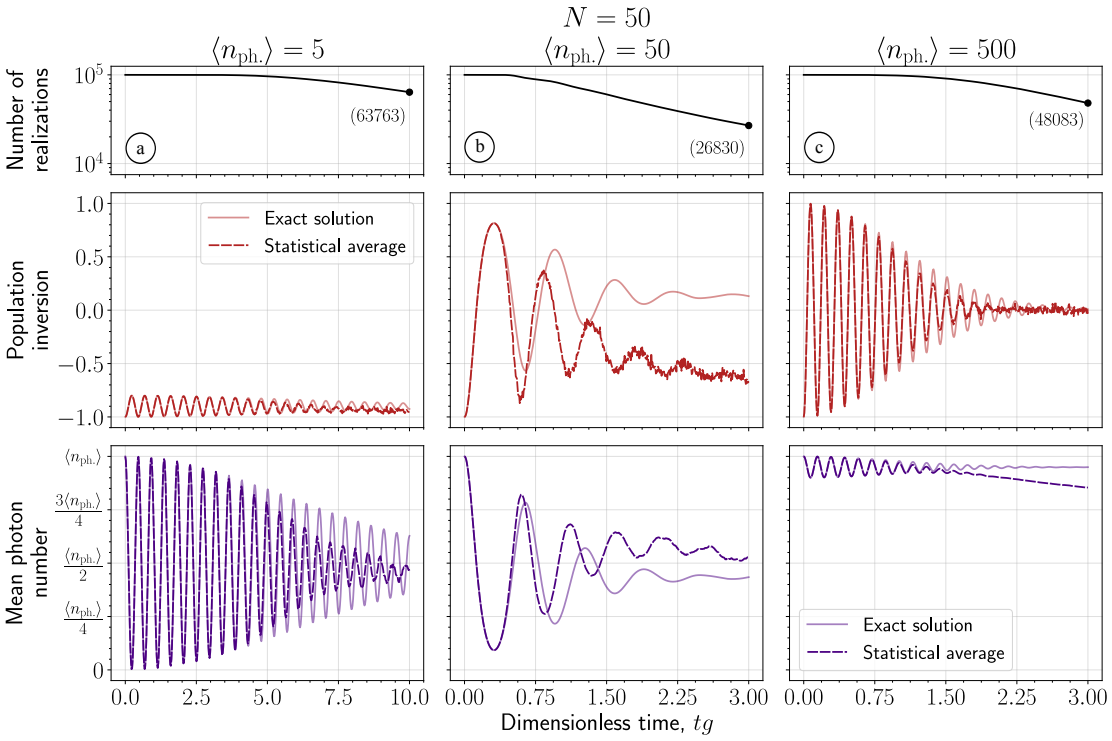

Figure III.20: Same as Fig. III.20, but realizations are omitted when the absolute value of any stochastic variable exceeds 10^3.

Numerical investigations reveal that unstable realizations are characterized by the anti-Hermiticity of both the field variables and the stochastic density matrix. Any gauge that we tried led to an extremely unstable weight function that had to be discarded. We also experimented with modifying the drift functions to enforce Hermiticity, as was done in the superradiance problem. While this modification stabilized the solutions, the resulting averages deviated significantly from the exact solution, even without the weight function.

Diverging Solutions

As in the case of superradiance, it is possible to derive an analytical expression for diverging solutions. Previously, we explicitly obtained such solutions for two-level emitters in Eq. (III.20). Similarly, by neglecting the noise terms in Eqs. (III.38) and seeking unstable solutions of the form $1/(\tau - \tau_{\text{sing.}})^k$, we find that the field variables can be expressed as follows:

$$\widetilde{\alpha}(\tau) = \frac{e^{i\phi}}{\tau - \tau_{\text{sing.}}}, \tag{III.39a}$$

and $\widetilde{\alpha}^\dagger(\tau) = -\widetilde{\alpha}^*(\tau)$. Here, ϕ is an arbitrary real number, and $\tau_{\text{sing.}}$ is a singularity point that depends on the system's parameters and initial conditions. The corresponding stochastic density matrix is given by:

$$\widetilde{\rho}_{12}(\tau) = -\frac{i}{N}\frac{e^{-i\phi}}{(\tau - \tau_{\text{sing.}})^2}, \qquad \widetilde{\rho}_{22}(\tau) - \widetilde{\rho}_{11}(\tau) = \frac{2}{N}\frac{1}{(\tau - \tau_{\text{sing.}})^2}, \tag{III.39b}$$

satisfying $\widetilde{\rho}_{21}(\tau) = -\widetilde{\rho}^*_{12}(\tau)$. Thus, all stochastic variables are anti-Hermitian. As noted previously, within the context of the positive P representation, diverging solutions are known as movable singularities [100, 101]. We attribute at least some of the unstable trajectories observed in Fig. III.20 to these diverging solutions.

However, not all unstable trajectories can be explained by the solutions in Eq. (III.39), as another type of instability exists within the system. The nature of this instability will become clearer when we analyze the Jaynes-Cummings model, which does not exhibit solutions with poles.

Jaynes-Cummings Model

The Jaynes-Cummings model is a specific case of the Tavis-Cummings model involving a single two-level atom.

When $N = 1$, the η-object can be directly eliminated from the original equations for $\beta_{pq}(t)$. These variables are linear in η, while the field variables do not depend on it. Consequently, the deterministic parts of the field equations vanish, leading to the following equations:

$$\frac{d\alpha(\tau)}{d\tau} = -i\mathrm{g}(\tau), \qquad \frac{d\alpha^\dagger(\tau)}{d\tau} = i\mathrm{f}(\tau).$$

The equations for the stochastic density matrix are as follows:

$$\begin{aligned}
\frac{d\rho_{11}(\tau)}{d\tau} &= i\alpha(\tau)\,\rho_{12}(\tau) - i\alpha^\dagger(\tau)\,\rho_{21}(\tau) + \rho_{12}(\tau)\,\mathrm{f}^\dagger(\tau) + \rho_{21}(\tau)\,\mathrm{g}^\dagger(\tau),\\
\frac{d\rho_{12}(\tau)}{d\tau} &= -i\alpha^\dagger(\tau)\,[\rho_{22}(\tau) - \rho_{11}(\tau)] + \rho_{22}(\tau)\,\mathrm{g}^\dagger(\tau),\\
\frac{d\rho_{21}(\tau)}{d\tau} &= i\alpha(\tau)\,[\rho_{22}(\tau) - \rho_{11}(\tau)] + \rho_{22}(\tau)\,\mathrm{f}^\dagger(\tau),\\
\frac{d\rho_{22}(\tau)}{d\tau} &= -i\alpha(\tau)\,\rho_{12}(\tau) + i\alpha^\dagger(\tau)\,\rho_{21}(\tau).
\end{aligned}$$

As observed, no additional noise terms appear in these equations. Therefore, the trace of the stochastic density matrix is not preserved for individual realizations.

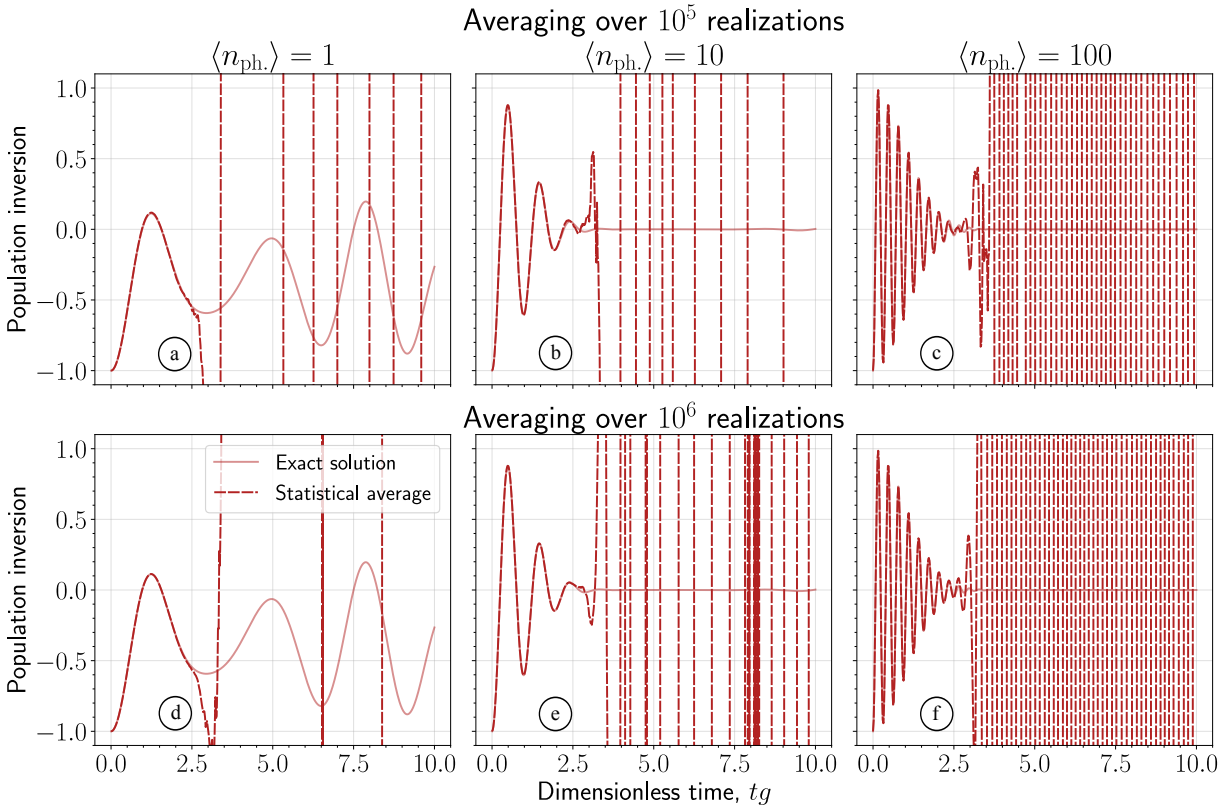

Figure III.21: Results of modeling the Jaynes-Cummings model using stochastic equations (solid lines) are compared with the exact solution (semi-transparent lines). The field is prepared in a coherent state with a mean photon number $\langle n_{\text{ph.}} \rangle$. Atoms start from the ground state. The top row shows the population inversion $\langle [\rho_{22}(\tau) - \rho_{11}(\tau)] \rangle$ averaged over 10^5 realizations, the bottom row—over 10^6 realizations.

In the Jaynes-Cummings model, there is no drift term for the field variables. The interaction between the field and the atom occurs exclusively through the noise terms. As a result, the deterministic equations do not permit diverging solutions of the form given in Eq. (III.39).

In Fig. III.21, we present the solutions of the equations for various initial mean photon numbers. In all cases, no diverging trajectories were encountered. However, the solutions still oscillate rapidly, exhibiting exponentially increasing amplitudes. Increasing the number of trajectories from 10^5 (a)-(c) to 10^6 (d)-(f) does not improve the situation.

While no diverging trajectories were observed, the solutions still exhibit instability in the form of rapid oscillations with frequent sign changes. This instability arises from a violation of the conjugation between the field variables. To better understand this behavior, we simplify the equations by neglecting noise terms and assuming the field variables to be constant and nonzero: $\alpha(t) \approx \alpha$ and $\alpha^\dagger(t) \approx \alpha^\dagger$. Under these approximations, we can solve the resulting deterministic equations analytically:

$$\widetilde{\rho}_{12}(\tau) = -i\sqrt{\frac{\alpha^\dagger}{\alpha}}\,\frac{p_2 - p_1}{2}\sin(2\sqrt{\alpha^\dagger\alpha}\,\tau),$$
$$\widetilde{\rho}_{21}(\tau) = i\sqrt{\frac{\alpha}{\alpha^\dagger}}\,\frac{p_2 - p_1}{2}\sin(2\sqrt{\alpha^\dagger\alpha}\,\tau),$$
$$\widetilde{\rho}_{22}(\tau) - \widetilde{\rho}_{11}(\tau) = (p_2 - p_1)\cos(2\sqrt{\alpha^\dagger\alpha}\,\tau),$$

where p_1 and p_2 represent the initial populations of the ground and excited states, respectively.

We assume that the field variables slightly deviate from the conjugation relation, specifically $\alpha^\dagger\alpha = |A|^2/4\; e^{2i\phi}$, where ϕ is a small real parameter. This allows us to expand the exponential in a Taylor series as $e^{i\phi} \approx 1 + i\phi$. Consequently, the trigonometric functions in the solutions can

be approximated as follows:

$$\sin(2\sqrt{\alpha^\dagger\alpha}\,\tau) \approx \frac{e^{-\phi|A|\tau}}{2i}\,e^{i|A|\tau} - \frac{e^{\phi|A|\tau}}{2i}\,e^{-i|A|\tau},$$
$$\cos(2\sqrt{\alpha^\dagger\alpha}\,\tau) \approx \frac{e^{-\phi|A|\tau}}{2}\,e^{i|A|\tau} + \frac{e^{\phi|A|\tau}}{2}\,e^{-i|A|\tau}.$$

Depending on the sign of ϕ, one term in these expressions oscillates rapidly with exponentially increasing amplitude as τ approaches infinity. This behavior can explain the rapid oscillations observed in Fig. III.21.

Although the phase mismatch ϕ averages to zero, its value is random in individual realizations. Even a slight deviation from the conjugation between the field variables can lead to the observed oscillations. Averaging out these oscillations requires an exponentially large number of trajectories, theoretically approaching infinity. As demonstrated in Fig. III.21, increasing the number of trajectories by an order of magnitude does not significantly improve convergence.

This highlights that stabilizing the Tavis-Cummings model is particularly challenging, as it involves two distinct types of instabilities that, unfortunately, we were unable to resolve [197]. Nevertheless, the formalism may still prove valuable when applied to the Tavis-Cummings model with strong dissipation.

Dissipative Tavis-Cummings Model

When modeling superradiance, we introduced additional damping of the excited states to stabilize trajectories. In cavities, dissipation can be accounted for either by damping the stochastic density matrix or by introducing photon leakage at a rate κ.

Cavity losses can be modeled using the following Lindblad operator:

$$\mathcal{L}_{\text{loss.}}[\hat{\rho}(t)] = \frac{\kappa}{2}\{2\hat{a}\hat{\rho}(t)\hat{a}^\dagger - \hat{a}^\dagger\hat{a}\hat{\rho}(t) - \hat{\rho}(t)\hat{a}^\dagger\hat{a}\}.$$

In terms of the stochastic variables, this Lindbladian introduces additional drift terms to the field variables:

$$\frac{d\alpha(t)}{dt} = \ldots - \frac{\kappa}{2}\alpha(t), \qquad \frac{d\alpha^\dagger(t)}{dt} = \ldots - \frac{\kappa}{2}\alpha^\dagger(t).$$

Numerical analysis suggests that strong dissipation, on the order of a few Rabi frequencies g, is necessary for regularization. However, under such conditions, the noise terms may become negligible, especially when the system's dynamics is primarily driven by the deterministic part.

To ensure the noise terms are significant, we assume the field is initially in the vacuum state with all atoms excited. In this case, the entire dynamics is triggered by the noise terms, which describe the emission of the first photons.

The simulation results are shown in Figs. III.22 (a)-(c) for different cavity loss rates. Setting κ to the Rabi frequency g in panel (a) does not improve convergence. Doubling the rate in panel (b) also fails to enhance stability. However, in the strong-dissipation regime, $\kappa = 4g$, the selected observables closely match the exact solution, with only a slight deviation observed around the second Rabi oscillation.

Another way to introduce dissipation is by including the nonradiative decay of atoms:

$$\frac{d\rho_{11}(t)}{dt} = \ldots + \gamma\rho_{22}(t), \qquad \frac{d\rho_{12}(t)}{dt} = \ldots - \frac{\gamma}{2}\rho_{12}(t),$$
$$\frac{d\rho_{21}(t)}{dt} = \ldots - \frac{\gamma}{2}\rho_{21}(t), \qquad \frac{d\rho_{22}(t)}{dt} = \ldots - \gamma\rho_{22}(t).$$

For effective regularization, γ should also be on the order of a few Rabi frequencies. Figures III.22 (d) and (e) illustrate the differences between stochastic averages and the exact solution for various values of κ and γ. As the total dissipation rate $\kappa+\gamma$ increases, this difference gradually decreases, reaching acceptable values around $4g$. This suggests that the current formalism is unable to fully describe the strong-coupling regime.

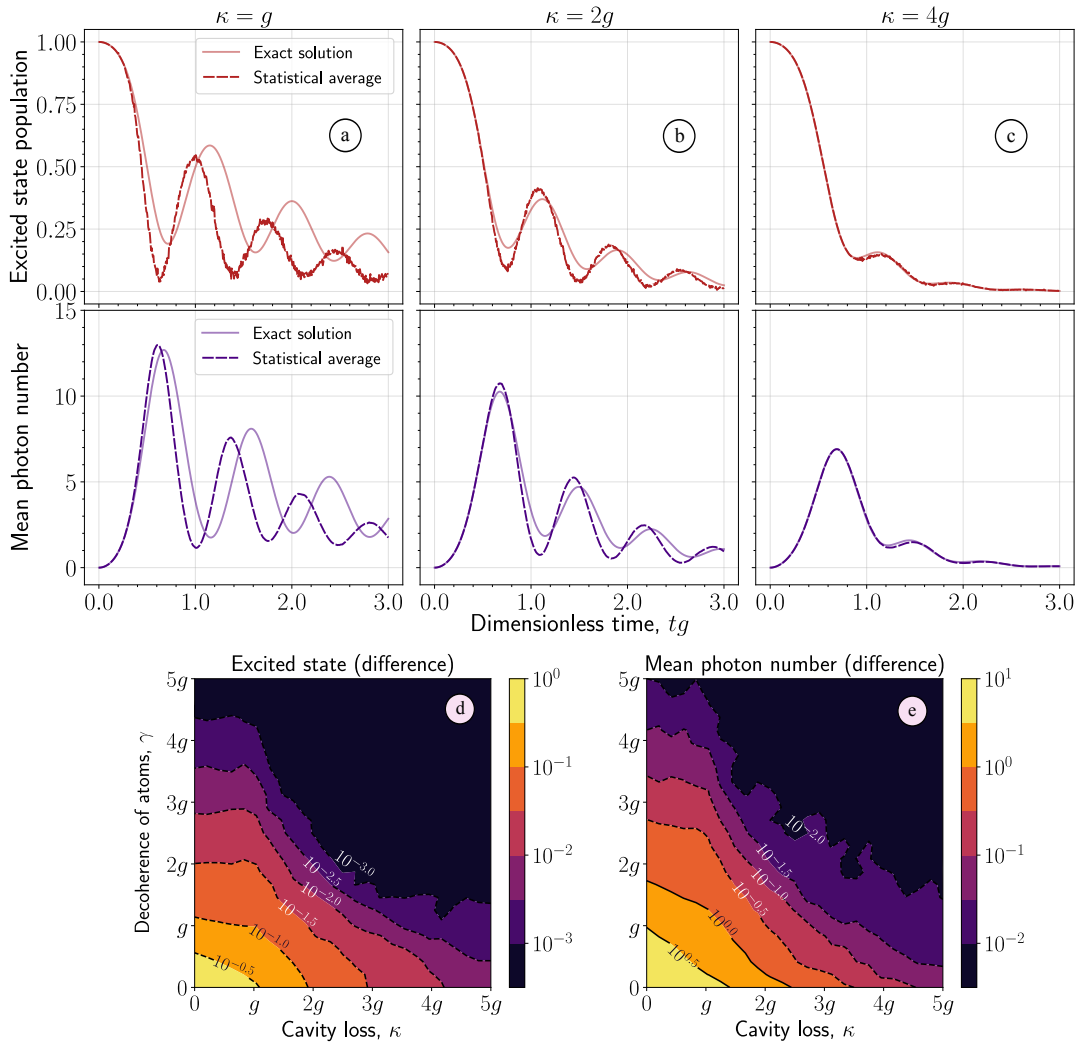

Figure III.22: Dissipative Tavis-Cummings model with $N = 20$ atoms. Panels (a)-(c) show the excited state population and mean photon number for varying cavity loss rates κ. We sampled 10^5 realizations, with (a) 61%; (b) 87%; and (c) 99% remaining until the end of the computation. The bottom panels (d) and (e) display the maximum differences in the excited state population and the mean photon number between the exact solution and statistical averages, across a range of cavity loss rates κ and decoherence rates γ. Additionally, when $\kappa > g$, we regularize the equations by dividing $\mathrm{g}^\dagger(t), \mathrm{f}^\dagger(t)$ by $\sqrt{\kappa}$, and multiplying $\mathrm{g}(t), \mathrm{f}(t)$ by $\sqrt{\kappa}$.

3 Discussion

In this section, we analyze the results of our numerical studies. Section 3.1 compares the computational effort required to solve the stochastic differential equations with that of a quantum-mechanical treatment. Another important question is the emergence of different types of instabilities. In all numerical examples, unstable realizations—characterized by large values of the stochastic density matrix or the weight function—are excluded. The implications of omitting these trajectories are discussed in Sections 3.2 and 3.3. Section 3.4 focuses on the weight function, formulating conditions under which it can be disregarded.

The conditions for disregarding the weight function are crucial, as they enable the description of realistic systems. In Sec. 3.5, we demonstrate the derivation of stochastic equations for non-identical particles and extend the approach to continuous variables. By transitioning to these variables, we can analyze spatially distributed systems and account for field propagation effects. In Sec. 3.6, we apply our stochastic formalism to one-dimensional treatment of $K\alpha$ lasing in neon. Finally, in Sec. 3.7, we conclude by formulating the applicability limits of our methodology.

System	Section	Figure	Master equation complexity	Number of emitters N	Master equation integration time, ms	Single trajectory integration time, ms
Two-level systems	2.1	IV.4 (d)	$\sim N^2/2!$	20	34	15 ± 2
		IV.4 (g)		200	3 600	15 ± 2
Pumped two-level systems	2.2	IV.6 (c)	$\sim N^3/3!$	10	56	16 ± 1
		IV.6 (f)		100	115 000	16 ± 2
V systems	2.3	IV.8 (b)	$\sim N^6/6!$	2	5	27 ± 2
		IV.8 (c)		20	53 000	27 ± 1
Λ systems	2.4	IV.13 (b)	$\sim N^6/6!$	2	4	27 ± 1
		IV.13 (c)		20	35 000	27 ± 1
Pumped V systems	2.3	IV.11 (c)*	$\sim N^7/7!$	2	7	28 ± 1
		IV.11 (c)		20	178 000	28 ± 2
Pumped Λ systems	2.4	IV.17 (c)*	$\sim N^7/7!$	2	6	28 ± 2
		IV.17 (c)		20	203 000	28 ± 2

Table III.1: Comparison of computational effort between stochastic and quantum-mechanical methods. The computational time for solving the master equation is averaged over 10 runs. The time to integrate a single stochastic trajectory is estimated from more than 100 realizations. An asterisk (*) preceding a figure number in the third column indicates that simulations were performed under identical conditions but with a different number of atoms.

3.1 Computational Effort

We compared the computational time required to solve stochastic equations with that needed for solving the quantum master equation using the method from Chapter II. Table III.1 shows that the average time required to integrate a single stochastic trajectory does not significantly vary across different models and is independent of N. In contrast, the complexity of solving the quantum master equation scales polynomially with N. Thus, the effectiveness of the stochastic method depends on the number of trajectories required for convergence.

Figure III.3 demonstrates convergence for two-level atoms, indicating that approximately 10^3 trajectories are necessary to achieve accurate averages. However, as N increases, the number of trajectories needed for convergence may rise due to instabilities, which are discussed in subsequent sections. A similar convergence analysis was conducted for pumped V and Λ systems. Figure III.23 presents the results for pumped V systems, while Fig. III.24 depicts pumped Λ systems. In both cases, good agreement is achieved with approximately 10^3 trajectories. Since exact solutions are unavailable for $N = 200$, statistical averages were compared to those from 10^5 trajectories.

For the Tavis-Cummings model, solving the quantum master equation for $N = 50$, as shown in Fig. III.22 (c), takes roughly two minutes. By comparison, integrating a single stochastic trajectory takes only about two milliseconds. Notably, generating plots for $N = 100$ incoherently pumped two-level atoms with Auger-Meitner decay, as in Fig. II.4 (c), requires several hours due to the number of equations approaching 2×10^6. By comparison, a single trajectory requires only 16 milliseconds to integrate, with convergence achieved after averaging 10^3-10^4 realizations.

In all cases, parallelized computation of approximately 10^3-10^4 trajectories significantly outperforms solving the quantum master equation for larger N. Convergence, however, depends on the presence of instabilities, which we begin discussing in the next section.

3.2 Instabilities: small N

Instabilities were consistently observed for systems with a small number of particles. These instabilities stem from the nonlinear noise term introduced after eliminating the η-object. For

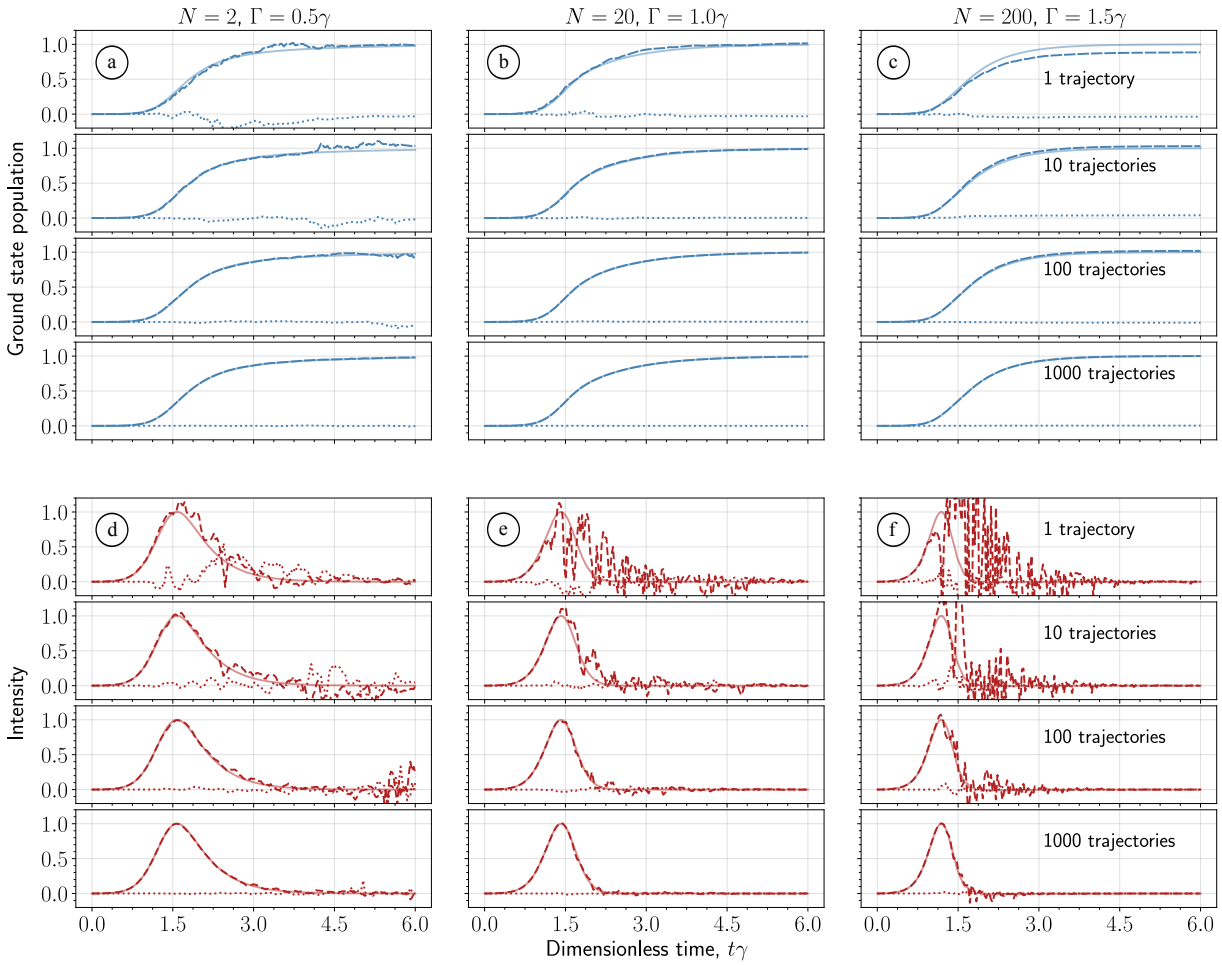

Figure III.23: Convergence of expectation values for pumped V systems, using the same parameters as in Fig. III.11, for different values of N and Γ. For $N = 2$ and $N = 20$, the results are compared with the exact solution (semi-transparent lines). For $N = 200$, the comparison is made using the average computed from 10^5 trajectories (semi-transparent lines). Dotted lines correspond to the imaginary parts of the respective averages.

reference, this term is denoted as $\mathrm{h}(t)$ in Eqs. (III.19). Due to its nonlinearity, this term can amplify any fluctuation in the noise processes, leading to unstable behavior. Such instabilities are evident in Fig. III.2 (d), Fig. III.8 (b), and Fig. III.13 (b). A potential solution to mitigate this issue is monitoring the dynamics of the nonlinear noise term and imposing a threshold to limit its growth. For simplicity, this dissertation adopts a more pragmatic approach: any realization in which any element of the stochastic density matrix exceeds 100 is excluded.

3.3 Instabilities: weight function

For systems with larger N, the primary source of instabilities becomes the weight function. Although the drift gauge effectively prevents diverging solutions of the form $1/(t - t_{\text{sing.}})$, anti-Hermitian components still contribute to the weight function equation via Eq. (III.23). These components are multiplied by $(N - 1)$ and subsequently exponentiated to compute the weight function, $\Omega(t) = e^{C_0(t)}$. As a result, even minor fluctuations can cause a rapid increase in the weight function. This issue is particularly pronounced in steady states, which are often characterized by anti-Hermitian realizations where $\langle \rho_{i\neq j}^{(ss)}\, \rho_{j\neq i}^{(ss)} \rangle < 0$. In all simulations, trajectories where the weight function exceeded e^5 were excluded.

Figure III.25 shows the percentage of unstable realizations—those where the weight function exceeds e^5 or any density matrix element exceeds 100—out of a total of 10^5 realizations. Panels (a)-(c) present results for different systems: (a) pumped two-level systems, (b) pumped V

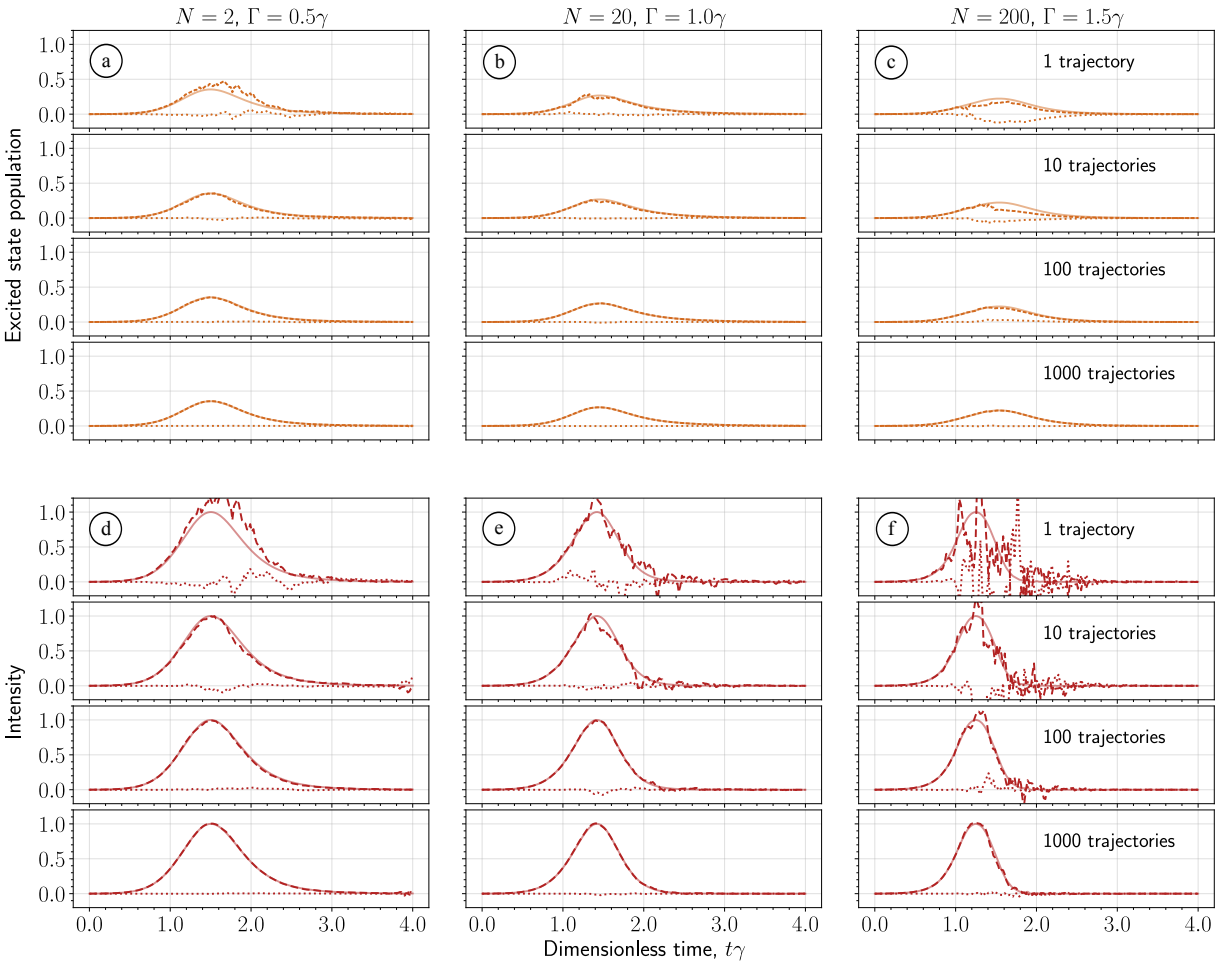

Figure III.24: Same as Fig. III.23, but for the pumped Λ systems, using the same parameters as in Fig. III.17.

systems, and (c) pumped Λ systems, each analyzed for various dissipation rates. The observed trends are similar across all systems: for each value of Γ, the number of unstable trajectories remains relatively low up to a critical N, after which it rises sharply. Higher dissipation rates, however, significantly reduce the number of unstable realizations. Our analysis reveals that a lower percentage of unstable trajectories correlates with more accurate results.

It is important to compare the effects of excluding unstable realizations from the **ungauged** equations with those of removing trajectories with unstable weights from the **gauged** equations. Excluding unstable realizations from the ungauged equations can lead to incorrect and non-physical results.

Figure III.26 provides this comparison. Panels (a) to (e) focus on incoherently pumped two-level systems from Fig. III.6 (f) with $N = 100$. In panel (a), averages from the gauged equations without excluding unstable realizations closely match the exact solution until instabilities arise. By removing just 0.5% of trajectories with unstable weights, panel (b) displays smooth curves that align well with the exact solution.

For the ungauged equations, panel (c) shows averages without excluding diverging realizations. These results deviate significantly from the exact solution, with the intensity curve appearing more unstable than in panel (a). Despite all density matrix elements remaining below 100, removing a few unstable realizations (where elements exceed 10), as shown in panel (d), does not improve accuracy. Further filtering (removing elements exceeding 1) in panel (e) yields a completely incorrect intensity profile.

Panels (f) to (j) explore a system with $N = 1000$ atoms and a dissipation rate $\Gamma = 0.8\gamma$. Although the exact solution is unavailable, we can still compare the averages obtained from the gauged and ungauged equations.

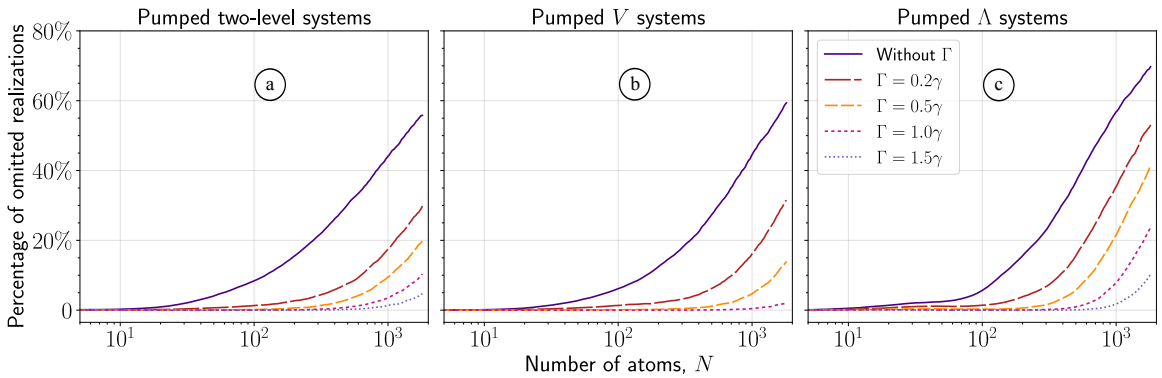

Figure III.25: Number of unstable realizations, where the weight function exceeds e^5 or density matrix elements exceed 100 in absolute value, for various systems and various dissipation rates: (a) pumped two-level systems (Fig. III.6); (b) pumped V systems (Fig. III.11); (c) pumped Λ systems (Fig. III.17).

Panel (f) shows the averages from the gauged equations without excluding any realizations. In this panel, noticeable spikes appear in both intensity and populations. By excluding 1.75% of the trajectories with unstable weights, panel (g) shows smoother and more physically meaningful results.

Panel (h) presents averages from the ungauged equations. While the population curves appear smoother than in panel (f), they differ significantly from those in panel (g), with a larger gap between excited and ground state populations. The intensity curve is unstable, despite no density matrix element exceeding 100. In panel (i), excluding a few diverging realizations (where density matrix elements exceed 10) has little effect on the population curves and does not visibly stabilize the intensity. Panel (j) demonstrates that further filtering (removing elements exceeding 1) introduces non-physical negative intensities.

In conclusion, removing trajectories with unstable weights from the gauged equations yields more accurate and physically meaningful results compared to excluding diverging trajectories from the ungauged equations. This highlights the advantages of using gauges, despite the instability of the weight function. In certain cases, the weight function can be disregarded entirely, a topic we will address in the next section.

3.4 Importance of Gauging and Weight Function

Let us revisit Figure III.7, which examines $N = 100$ incoherently pumped two-level atoms. Panels (a) to (c) display averages computed without gauges, revealing instability and deviations from the exact solution. In contrast, averages from the gauged equations in panels (n) to (o) are accurate. Notably, panel (r) shows that even without the weight function in averaging, gauged equations closely match the exact solution.

For V systems, comparisons between Figures III.9 (with gauges) and III.10 (without gauges), as well as Figures III.11 (with gauges) and III.12 (without gauges), indicate that applying gauges significantly enhances stability and convergence. Additional simulations reveal that the weight can be omitted for $\Gamma = 0.8\gamma$ without notably altering averages.

In Λ systems, however, gauging introduces complexity. Comparing Figures III.13 and III.14 shows that gauging may reduce the accuracy of certain averages. Moreover, Figures III.15 (with gauges) and III.16 (without gauges), alongside III.17 (with gauges) and III.18 (without gauges), suggest that if dissipation is sufficiently strong, gauging becomes unnecessary and even impedes convergence. Neglecting the weight function does not improve the accuracy. These observations suggest that the current gauging criterion, defined by Eq. (III.24), leads to unnecessary gauging and should be optimized, if feasible.

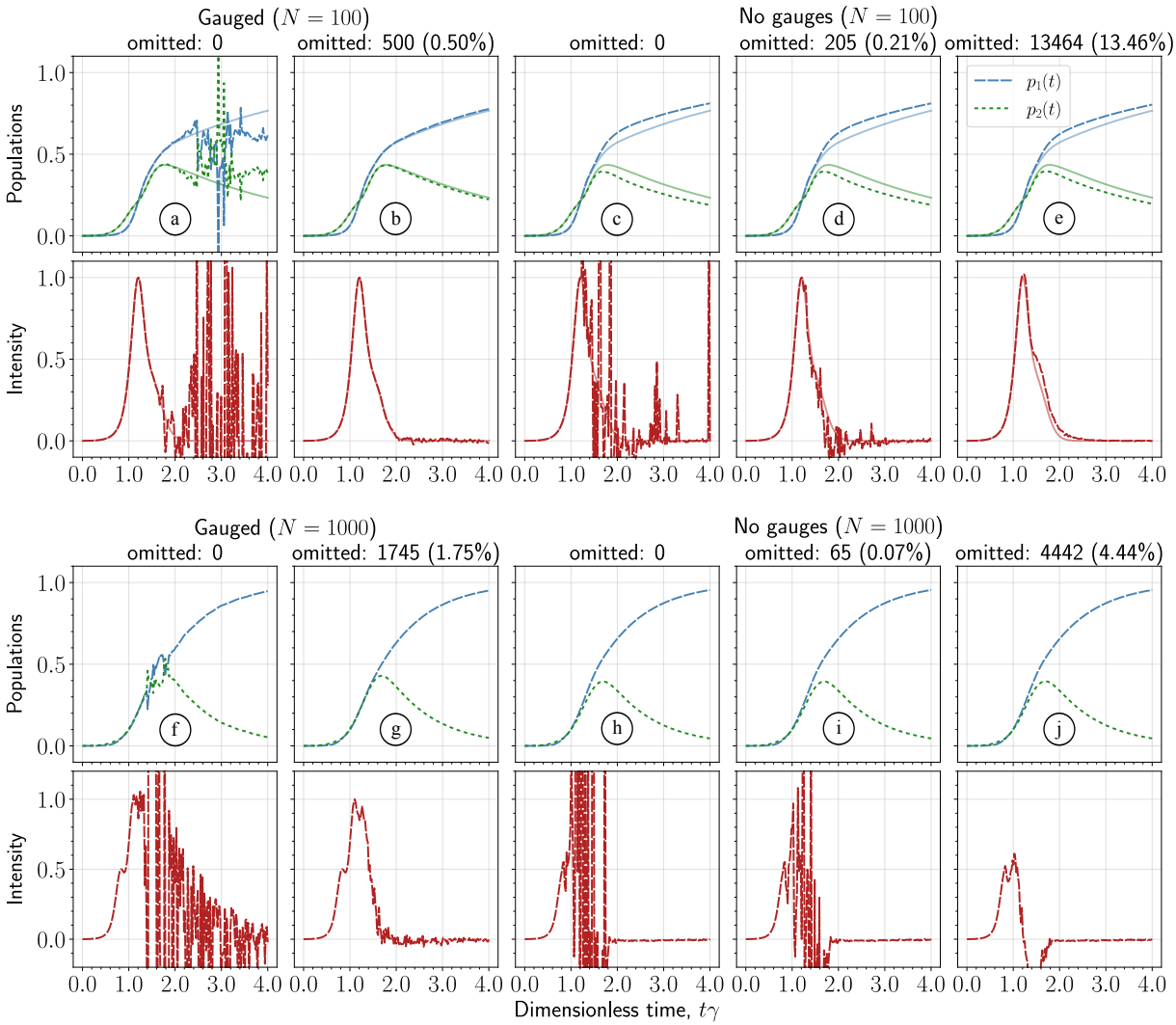

Figure III.26: Dynamics of $N = 100$ incoherently pumped two-level atoms, with a nonradiative decay rate $\Gamma = 0.3\gamma$ (a)-(e); and $N = 1000$ atoms with $\Gamma = 0.8\gamma$ (f)-(j). The pumping envelope is the same as in Fig. III.5. The dashed lines depict stochastic averages. In panels (a)-(e), the exact solution is shown by the semi-transparent line. For panels (f)-(j), the exact solution is not available.

Neglecting Weight Function

Let's explore conditions under which the importance of the weight function diminishes. Empirical evidence suggests three prerequisites for safely neglecting the weight function: (1) application of the diffusion gauge, (2) non-constant application of the drift gauge, and (3) sufficiently strong dissipation to suppress steady-state formation. Our results indicate that the dissipation rate should be comparable to the spontaneous decay rate. The number of unstable realizations reflects the steady state's prominence.

When the drift gauge is applied constantly, the weight function remains significant at all times, increasing the likelihood of unstable realizations. Figure III.27 analyzes the dynamics of $N = 100$ incoherently pumped two-level systems with $\Gamma = 0.8\,\gamma$. The gray-shaded regions in panels (a) to (d) denote the probability of applying the drift gauge. In panels (a) and (c), the gauging criterion follows Eq. (III.24), and the gray-shaded area represents the mean value of $\langle\theta(t)\rangle$. In panels (b) and (d), the drift gauge is applied constantly, meaning the probability is always one. Panel (e) illustrates the averages without applying any gauges.

Panel (a) of Fig. III.27 demonstrates excellent agreement with the exact solution, with only a few unstable realizations omitted. These averages are computed with the weight function, and the drift gauge is applied according to Eq. (III.24). Panel (c) displays the averages calculated

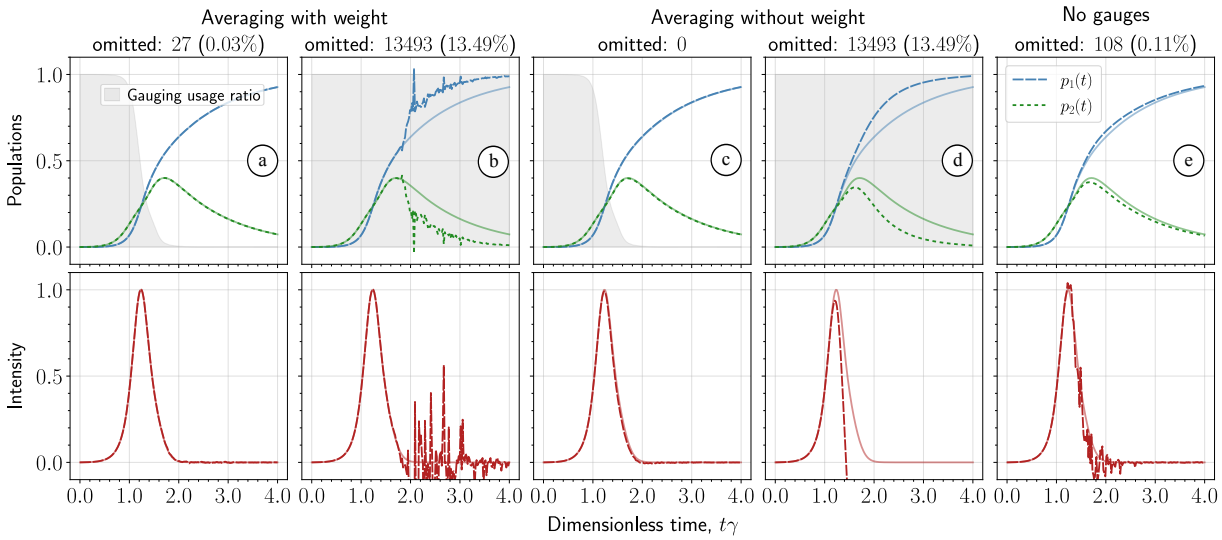

Figure III.27: Dynamics of $N = 100$ incoherently pumped two-level atoms with a nonradiative decay rate of $\Gamma = 0.8\gamma$. Semi-transparent lines show the exact solution, and opaque lines depict stochastic averages. In panels (a) and (c), the drift gauge is applied only when the population inversion is positive, whereas in panels (b) and (d) it is applied constantly. Panel (e) shows averages from the ungauged equations. Gray-filled areas show the gauging frequency.

without the weight function. Neglecting the weight function has minors effect on intensity, which vanish at higher dissipation rates. In contrast, the ungauged equations yield incorrect averages, as seen in panel (e).

When the drift gauge is applied constantly, there are significantly more unstable realizations, as evidenced in panel (b) of Fig. III.27. In this panel, trajectories are excluded if any density matrix element exceeds 100. The weight function, being highly unstable, is not used as a basis for omission: for 90% of realizations, it surpasses e^{10}. The populations deviate significantly from the exact solution, and the intensity has many spikes. Neglecting the weight function in panel (d) offers no improvement, as the intensity drops below zero.

This section highlights that, while the weight function can induce instability, it can be regularized by selectively omitting certain trajectories, unlike ungauged equations. Furthermore, in many cases, the weight function can be disregarded. Selective gauge application without the weight function has been utilized in Ref. [195], which explored x-ray superfluorescence under the paraxial approximation by solving three-dimensional coupled Maxwell-Bloch equations for continuous variables.

3.5 Stochastic Maxwell-Bloch Equations

The numerical examples discussed so far have focused on cooperative emission in small systems, where all particles interact cooperatively, and propagation effects are neglected. However, stochastic equations (III.37) can be extended to spatially distributed systems, where the propagation effects are crucial. This extension allows for the derivation of stochastic Maxwell-Bloch equations, describing both the atomic medium's evolution and the radiation's propagation.

We consider systems described by the Hamiltonian in Eq. (I.21), where $\mathbf{r}_\mu$ denotes the position of the μ-th emitter. In general, the ensemble cannot be treated as compact. Thus, as a first step, we adopt the local quantization strategy from Sec. 4.3 of Chapter II. In this approach, the sample is divided into subregions Ω_1, Ω_2, ..., each small enough to treat the particles within as identical (Fig. II.13 (b)). We then perform second quantization independently for each subregion, introducing a set of local bosonic superoperators, $\hat{b}_{a,ij}$ and $\hat{b}^\dagger_{a,ij}$.

Using these local bosonic superoperators, we construct the generalized Λ-supervector for distributed systems. Previously, the entire ensemble was described by phase-space variables $\{\beta_{ij}\}$. In distributed systems, phase-space variables gain an additional index to distinguish them,

$\{\beta_{a,ij}\}$. The generalized Λ-supervector is then constructed as a product of the supervectors in Eq. (III.6) for all subregions:

$$|\Lambda(\{\beta_{a,ij}\})\rangle\!\rangle = \prod_a \exp\Big(-\sum_{i=1}^{M} \beta_{a,ii} + \hat{N}_a^{-1/2} \sum_{i,j=1}^{M} \beta_{a,ij}\, \hat{b}^\dagger_{a,ij} \Big) |\mathrm{vac}\rangle\!\rangle, \tag{III.40}$$

where $\hat{N}_a = \sum_{i,j} \hat{b}^\dagger_{a,ij}\, \hat{b}_{a,ij}$ is the particle number operator for subregion Ω_a. This supervector has a unit trace and possesses the following property:

$$\mathrm{Tr}\Big[\sum_{\mu_1\in\Omega_1} \hat{\sigma}_{\mu_1,q_1p_1} \sum_{\mu_2\in\Omega_2} \hat{\sigma}_{\mu_2,q_2p_2} \ldots |\Lambda(\{\beta_{a,ij}\})\rangle\!\rangle \Big] = \beta_{1,p_1q_1}\, \beta_{2,p_2q_2}\, \ldots$$

The density matrix is represented using these supervectors, similar to the ansatz in Eq. (III.4). The associated P-distribution takes all phase-space variables $\{\beta_{a,ij}\}$ as arguments. The field variables are included as outlined in Sec. 2.5 of this chapter.

Following the methodology for deriving equations for identical particles in Eqs. (III.18a) and (III.37), we obtain equations for the stochastic variables $\rho_{a,pq}(t)$, describing particles in subregion Ω_a:

$$\frac{d\rho_{a,pq}(t)}{dt} = -i\omega_{pq}\, \rho_{a,pq}(t) - \frac{i}{\hbar} \boldsymbol{\mathcal{E}}(\mathbf{r}_a, t) \cdot \sum_{r=1}^{M} \{\rho_{a,pr}(t)\, \mathbf{d}_{rq} - \mathbf{d}_{pr}\, \rho_{a,rq}(t)\}$$
$$+ \sum_{r=1}^{M} \rho_{a,pr}(t)\, \mathbf{d}_{rq} \cdot \mathbf{f}^\dagger_a(t) + \sum_{r=1}^{M} \mathbf{d}_{pr}\, \rho_{a,rq}(t) \cdot \mathbf{g}^\dagger_a(t) - \rho_{a,pq}(t) \sum_{i,j=1}^{M} \mathbf{d}_{ji}\, \rho_{a,ij}(t) \cdot \{\mathbf{f}^\dagger_a(t) + \mathbf{g}^\dagger_a(t)\}.$$

Applying the rotating-wave approximation eliminates counter-rotating terms, restricting the dipole moment indices and retaining only terms with either positive or negative-frequency field components, as in Eqs. (III.18). The last term guarantees that the stochastic density matrix remains normalized for each realization, $\sum_i \rho_{a,ii}(t) = 1$. The vector $\mathbf{r}_a$ is the radius vector pointing to the center of subregion Ω_a.

The stochastic counterpart of the electric field, $\boldsymbol{\mathcal{E}}(\mathbf{r}, t)$, is defined as follows:

$$\boldsymbol{\mathcal{E}}(\mathbf{r}, t) = i\sqrt{\frac{2\pi\hbar}{V}} \sum_{\mathbf{k},\lambda} \sqrt{\nu_\mathbf{k}} \{\mathbf{e}_{\mathbf{k},\lambda}\, \alpha_{\mathbf{k},\lambda}(t)\, e^{i\mathbf{k}\cdot\mathbf{r}} - \mathbf{e}^*_{\mathbf{k},\lambda}\, \alpha^\dagger_{\mathbf{k},\lambda}(t)\, e^{-i\mathbf{k}\cdot\mathbf{r}}\},$$

which resembles the electric field operator in Eq. (I.18a). In the equations above, $\boldsymbol{\mathcal{E}}(\mathbf{r}_a, t)$ represents the field at Ω_a created by all subregions, including Ω_a itself. Addressing self-action typically requires the Weisskopf-Wigner approach, which introduces incoherent terms in $\rho_{a,pq}(t)$ that account for decoherence [195, 198].

The field stochastic variables $\alpha_{\mathbf{k},\lambda}(t)$ and $\alpha^\dagger_{\mathbf{k},\lambda}(t)$ satisfy the following stochastic equations, which resemble classical equations (I.13):

$$\frac{d\alpha_{\mathbf{k},\lambda}(t)}{dt} = -i\nu_\mathbf{k}\alpha_{\mathbf{k},\lambda}(t) + \sqrt{\frac{2\pi\nu_\mathbf{k}}{\hbar V}}\, \mathbf{e}^*_{\mathbf{k},\lambda} \cdot \sum_a \{N_a \sum_{p,q=1}^{M} \mathbf{d}_{qp}\, \rho_{a,pq}(t) + \mathbf{g}_a(t)\}\, e^{-i\mathbf{k}\cdot\mathbf{r}_a},$$
$$\frac{d\alpha^\dagger_{\mathbf{k},\lambda}(t)}{dt} = i\nu_\mathbf{k}\alpha^\dagger_{\mathbf{k},\lambda}(t) + \sqrt{\frac{2\pi\nu_\mathbf{k}}{\hbar V}}\, \mathbf{e}_{\mathbf{k},\lambda} \cdot \sum_a \{N_a \sum_{p,q=1}^{M} \mathbf{d}_{qp}\, \rho_{a,pq}(t) + \mathbf{f}_a(t)\}\, e^{i\mathbf{k}\cdot\mathbf{r}_a}.$$

These equations include the noise terms $\mathbf{f}_a(t)$ and $\mathbf{g}_a(t)$, which couple to $\mathbf{f}^\dagger_a(t)$ and $\mathbf{g}^\dagger_a(t)$ in the atomic equation through the correlation properties:

$$\langle \mathrm{f}^{(\alpha)}_a(t)\, \mathrm{f}^{\dagger(\beta)}_b(t')\rangle = \langle \mathrm{g}^{(\alpha)}_a(t)\, \mathrm{g}^{\dagger(\beta)}_b(t')\rangle = \delta_{ab}\, \delta_{\alpha\beta}\, \delta(t-t'), \tag{III.41}$$

and all other first- and second-order correlators are zero. Such correlations indicate that the noise terms from different subregions are statistically independent. The number of independent noise terms grows linearly with the number of subregions.

Continuous Variables

To describe a continuous medium of emitters (e.g., a gaseous medium), we assume that the volume of each subregion approaches zero, while their number tends to infinity. In this limit, the discrete parameters $\mathbf{r}_a$ transition to a continuous variable $\mathbf{r}$. The collective variable $\rho_{a,pq}(t)$, representing N_a particles within subregion Ω_a, transforms directly into the continuous stochastic variable $\rho_{pq}(\mathbf{r},t)$, which characterizes particles in the vicinity of $\mathbf{r}$.

For the field equations, this limit primarily affects the summation over a. Consider the deterministic part of the summation:

$$\sum_a N_a \rho_{a,pq}(t)\, e^{\pm i\mathbf{k}\cdot\mathbf{r}_a} = \sum_a \Delta V_a \frac{N_a}{\Delta V_a} \rho_{a,pq}(t)\, e^{\pm i\mathbf{k}\cdot\mathbf{r}_a},$$

where ΔV_a is the volume of subregion Ω_a. As $\Delta V_a \to 0$ and $N_a \to 0$, while the number of subregions approaches infinity, the summation becomes an integral, and $N_a/\Delta V_a$ converges to the concentration of emitters $n(\mathbf{r})$:

$$\sum_a \Delta V_a \frac{N_a}{\Delta V_a} \rho_{a,pq}(t)\, e^{\pm i\mathbf{k}\cdot\mathbf{r}_a} \longrightarrow \int d\mathbf{r}\, n(\mathbf{r})\, \rho_{pq}(\mathbf{r},t)\, e^{\pm i\mathbf{k}\cdot\mathbf{r}}.$$

For the noise terms, an uncompensated factor of ΔV_a remains, as there is no particle number to absorb it. However, this factor can be incorporated into the correlation properties of the noise terms, leading to a modification of Eq. (III.41) as follows:

$$\langle \mathrm{f}_a^{(\alpha)}(t)\, \mathrm{f}_b^{\dagger(\beta)}(t')\rangle = \langle \mathrm{g}_a^{(\alpha)}(t)\, \mathrm{g}_b^{\dagger(\beta)}(t')\rangle = \delta_{\alpha\beta} \frac{\delta_{ab}}{\Delta V_a}\, \delta(t-t').$$

As $\Delta V_a \to 0$, the noise terms become continuous functions of $\mathbf{r}$, and the factor $\delta_{ab}/\Delta V_a$ converges to a spatial delta function:

$$\langle \mathrm{f}^{(\alpha)}(\mathbf{r},t)\, \mathrm{f}^{\dagger(\beta)}(\mathbf{r}',t')\rangle = \langle \mathrm{g}^{(\alpha)}(\mathbf{r},t)\, \mathrm{g}^{\dagger(\beta)}(\mathbf{r}',t')\rangle = \delta_{\alpha\beta}\, \delta(\mathbf{r}-\mathbf{r}')\, \delta(t-t'). \tag{III.42}$$

Thus, summations over a transition into integrals over $d\mathbf{r}$ with continuous noise terms, completing the shift to continuous variables.

Notably, equations for $\alpha_{\mathbf{k},\lambda}(t)$ and $\alpha^\dagger_{\mathbf{k},\lambda}(t)$ naturally lead to Maxwell's equations for the stochastic electric and magnetic fields, where continuous noise terms define stochastic polarization and magnetization fields. Together with the equations for the stochastic density matrix, these form a coupled set of stochastic Maxwell-Bloch equations. These aspects are discussed in detail in Refs. [195, 198]. Ref. [195] describes the general equations and their specific application to the paraxial geometry, while Ref. [198] additionally explores the transition to a one-dimensional treatment. Both approaches introduce the retarded time framework, which involves subtleties not covered in this dissertation.

The next section demonstrates an application of the formulated framework to collective emission in neon gas.

3.6 X-Ray Lasing in Neon

In this subsection, we present the equations governing lasing from the $K\alpha$ transition in neon, using parameters similar to those experimentally realized in Ref. [38]. In that study, x-ray amplified emission from neon gas was observed following photoionization by an XFEL pulse tuned to a photon energy of 960 eV. The photoionization cross section of the $1s$ shell is $\sigma_2 = 0.3$ Mb, while that of the $2p$ shell is much smaller, $\sigma_1 = 0.0084$ Mb. A vacancy created in the $1s$ shell can be filled by an electron from the $2p$ shell, accompanied by the emission of a photon with an energy of 849 eV.

The effective timescale of spontaneous emission is $\tau_{\mathrm{sp.}} = 320$ fs. Alternatively, the system may relax via the Auger-Meitner effect, leading to the autoionization of a second electron. This

competing process occurs on a much faster timescale, $\tau_{\text{Auger}} = 2.4$ fs. A sketch of the energy level structure is shown in Fig. III.28 (a).

The neon gas is contained in an 18 mm-long cell, with a concentration of $n = 1.6 \times 10^{19}$ cm^{-3}. The pump cross-section has a radius of approximately 2 µm (FWHM), creating an active medium with about $N \sim 3 \times 10^{12}$ atoms. This setup has a pencil-shaped geometry characterized by a Fresnel number of $F \sim 0.5$.

In our analysis, we neglect plasma and recombination effects and focus on the effective two-level scheme shown in Fig. III.28 (a). Given the large number of atoms in the active medium, we disregard the statistical properties of the η-object in Eq. (III.15), meaning our equations will not include a nonlinear noise term.

Additionally, we restrict our analysis to a one-dimensional treatment, focusing only on the field component that propagates parallel to the axis of the sample. Since population inversion is generated by the pump, which travels together with the emission, only the mode along the sample experiences significant amplification, allowing us to neglect the back-propagating waves.

Self-Consistent Set of Equations

The field is characterized by a single carrier frequency corresponding to 849 eV and a single polarization axis. Consequently, only the projections of the noise terms along this axis contribute to the dynamics. These noise terms are denoted by $\mathrm{f}(z,t)$, $\mathrm{f}^\dagger(z,t)$, $\mathrm{g}(z,t)$, and $\mathrm{g}^\dagger(z,t)$. Additionally, we decompose the stochastic electric field into its positive and negative frequency components:

$$\mathcal{E}(z,t) = \mathcal{E}^{(+)}(z,t)\, e^{-i\omega_0(t-z/c)} + \mathcal{E}^{(-)}(z,t)\, e^{i\omega_0(t-z/c)},$$

where z denotes the coordinate along the sample.

For simplicity, we assume that the transition dipole moments d_{12} and d_{21} are real-valued and equal d_0. It is convenient to describe the field in terms of the Rabi frequencies in the retarded time framework:

$$\Omega^{(\pm)}(z,\tau) = \frac{d_0}{\hbar}\mathcal{E}^{(\pm)}(z,\tau + z/c),$$

where $\tau = t - z/c$ is the retarded time. The propagation of the emission can be described by the following equations [195, 198]:

$$\frac{\partial\Omega^{(+)}(z,\tau)}{\partial z} = \frac{3i\lambda_0^2\gamma}{8\pi}\left[n\rho_{21}(z,\tau) + \mathrm{g}(z,\tau)\right], \tag{III.43a}$$

$$\frac{\partial\Omega^{(-)}(z,\tau)}{\partial z} = -\frac{3i\lambda_0^2\gamma}{8\pi}\left[n\rho_{12}(z,\tau) + \mathrm{f}(z,\tau)\right]. \tag{III.43b}$$

Here, $\lambda_0 = 1.46$ nm is the carrier wavelength, and $\gamma = 1/\tau_{\text{sp.}}$ is spontaneous decay rate. The numerical coefficient in front of the brackets relates to the emission solid angle $\Delta o = 3\lambda_0^2/(8\pi S^\perp)$, where $S^\perp$ is the sample's cross-sectional area. For the given parameters, $\Delta o \sim 10^{-8}$.

The x-ray pump pulse is modeled as a photon flux, denoted by $J_0(z,\tau)$. At the entrance of the sample ($z = 0$), the pulse has a Gaussian temporal profile described by:

$$J_0(0,\tau) = \frac{N_p}{\sqrt{2\pi\Delta\tau^2}}\exp\Big[-\frac{(\tau-\tau_0)^2}{2\Delta\tau^2}\Big],$$

where $\Delta\tau = 40/\sqrt{8\ln 2}$ fs is the pulse duration, and the pulse is centered at $\tau_0 = 50$ fs. The pulse energy is 0.24 mJ, corresponding to $N_p = 1.56 \times 10^{12}$ photons. The attenuation of the pump pulse as it propagates through the medium is described by:

$$\frac{\partial J_0(z,\tau)}{\partial z} = -n(\sigma_1+\sigma_2)\,\rho_{00}(z,\tau)\,J_0(z,\tau),$$

where $\rho_{00}(z,\tau)$ represents the population of the neutral ground state. The neutral ground state is depleted by the photon flux according to:

$$\frac{\partial\rho_{00}(z,\tau)}{\partial\tau} = -(\sigma_1+\sigma_2)\,\rho_{00}(z,\tau)\,J_0(z,\tau).$$

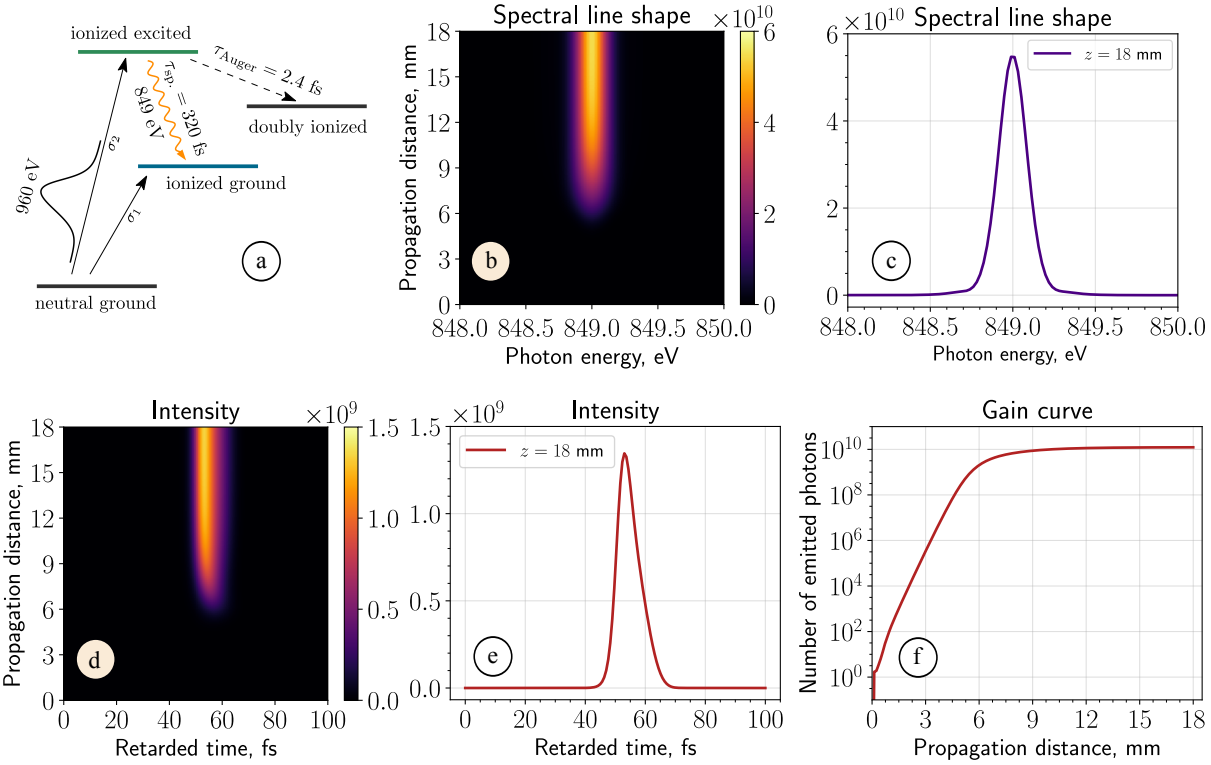

Figure III.28: X-ray lasing from the $K\alpha$ transition in neon, with the effective level structure depicted in panel (a). Panels (b) and (c) illustrate the evolution of the spectral line shape, with the integral over photon energies giving the total number of emitted photons. Panels (d) and (e) display the emission intensity, with the integral over time giving the total number of emitted photons. Panel (f) shows the gain curve, representing $\int d\tau\, I(z,\tau)$, on a logarithmic scale. The presented plots are based on 10^4 realizations, sampled within a few minutes.

These equations do not contain any stochastic components. If we had accounted for the η-object, the equation for $\rho_{00}(z,t)$ would have gained a nonlinear noise term, as in Eq. (III.29).

The equations for the stochastic density matrix can be conveniently divided into three distinct group of terms. The first group describes the rate equations:

$$\begin{aligned}
\frac{\partial \rho_{11}(z,\tau)}{\partial \tau} &= \gamma \rho_{22}(z,\tau) + \sigma_1 \rho_{00}(z,\tau)\, J_0(z,\tau) - \dots \\
\frac{\partial \rho_{12}(z,\tau)}{\partial \tau} &= -\frac{(\gamma+\Gamma)}{2}\, \rho_{12}(z,\tau) + \dots \\
\frac{\partial \rho_{21}(z,\tau)}{\partial \tau} &= -\frac{(\gamma+\Gamma)}{2}\, \rho_{21}(z,\tau) - \dots \\
\frac{\partial \rho_{22}(z,\tau)}{\partial \tau} &= -(\gamma+\Gamma)\, \rho_{22}(z,\tau) + \sigma_2 \rho_{00}(z,\tau)\, J_0(z,\tau) + \dots
\end{aligned}$$

where $\Gamma = 1/\tau_{\text{Auger}}$ is the characteristic decay rate due to the Auger-Meitner effect, and γ is spontaneous decay rate. These equations also account for population increase via photoionization.

The next group of terms describes the interaction with the fields $\Omega^{(\pm)}(z,\tau)$:

$$\begin{aligned}
\frac{\partial \rho_{11}(z,\tau)}{\partial \tau} &= \dots - i\Omega^{(+)}(z,\tau)\, \rho_{12}(z,\tau) + i\Omega^{(-)}(z,\tau)\, \rho_{21}(z,\tau) + \dots \\
\frac{\partial \rho_{12}(z,\tau)}{\partial \tau} &= \dots + i\Omega^{(-)}(z,\tau)\, [\rho_{22}(z,\tau) - \rho_{11}(z,\tau)] + \dots \\
\frac{\partial \rho_{21}(z,\tau)}{\partial \tau} &= \dots - i\Omega^{(+)}(z,\tau)\, [\rho_{22}(z,\tau) - \rho_{11}(z,\tau)] + \dots \\
\frac{\partial \rho_{22}(z,\tau)}{\partial \tau} &= \dots + i\Omega^{(+)}(z,\tau)\, \rho_{12}(z,\tau) - i\Omega^{(-)}(z,\tau)\, \rho_{21}(z,\tau).
\end{aligned}$$

This part has the structure of the semiclassical Bloch equations [9,65]. In the absence of noise terms, the dynamics is purely semiclassical, meaning there is no evolution without external driving or nonzero initial dipole moment. However, including the following noise terms—coupled with the field equations—adds the effect of spontaneous emission into the system:

$$\begin{aligned}\frac{\partial\rho_{11}(z,\tau)}{\partial\tau} &= \ldots + \rho_{12}(z,\tau)\,\mathrm{f}^{\dagger}(z,\tau) + \rho_{21}(z,\tau)\,\mathrm{g}^{\dagger}(z,\tau).\\ \frac{\partial\rho_{12}(z,\tau)}{\partial\tau} &= \ldots + \rho_{22}(z,\tau)\,\mathrm{g}^{\dagger}(z,\tau),\\ \frac{\partial\rho_{21}(z,\tau)}{\partial\tau} &= \ldots + \rho_{22}(z,\tau)\,\mathrm{f}^{\dagger}(z,\tau).\end{aligned}$$

The equation for $\rho_{22}(z,\tau)$ contains no stochastic terms. These noise terms couple to the field equations through the relations:

$$\langle \mathrm{f}^{\dagger}(z,\tau)\,\mathrm{f}(z',\tau')\rangle = \langle \mathrm{g}^{\dagger}(z,\tau)\,\mathrm{g}(z',\tau')\rangle = \delta(z-z')\,\delta(\tau-\tau'),$$

and all other first- and second-order correlators are zero. We adopt a representation where $\mathrm{f}^{\dagger}(z,\tau) = \mathrm{f}^{*}(z,\tau)$ and $\mathrm{g}^{\dagger}(z,\tau) = \mathrm{g}^{*}(z,\tau)$.

Finally, the doubly ionized state, represented by $\rho_{33}(z,\tau)$, is governed by:

$$\frac{\partial\rho_{33}(z,\tau)}{\partial\tau} = \Gamma\rho_{22}(z,\tau).$$

Stochastic Gauges

To prevent the unbounded growth of the deterministic component of the atomic equations, we apply the drift gauge as described in Eq. (III.22). Specifically, we ensure the coherences on the right-hand side of the field equations (III.43) remain Hermitian:

$$\begin{aligned}\rho_{12}(z,\tau) &\to \rho_{12}(z,\tau) - \theta(t)\,\frac{\rho_{12}(z,\tau) - \rho_{21}^{*}(z,\tau)}{2},\\ \rho_{21}(z,\tau) &\to \rho_{21}(z,\tau) - \theta(t)\,\frac{\rho_{21}(z,\tau) - \rho_{12}^{*}(z,\tau)}{2},\end{aligned}$$

where $\theta(t)$ is defined in Eq. (III.24). Due to the large number of particles, the weight function becomes highly unstable in each realization and must therefore be disregarded. As discussed in Sec. 3.4, this simplification is valid when the influence of dark states is negligible. In distributed systems, such dark states do not exist, since the emitted field propagates through the sample without allowing particles to interact with their own emission.

To reduce errors introduced by neglecting the weight function, we apply the diffusion gauge, as described in Eq. (III.25). Here, the gauging functions can be chosen to coincide, $F(z,\tau) \equiv G(z,\tau)$, and are defined as follows:

$$F(z,\tau) = \sqrt{\frac{8\pi}{3\lambda_0^2\gamma}\,\frac{|\rho_{22}(z,\tau)|}{|\rho_{22}(z,\tau) - \rho_{11}(z,\tau)|}}\,.$$

We refer to the equations incorporating the drift gauge and noise terms scaled as described above as the gauged equations.

Results

The solution to the gauged equations without a weight function is shown in Fig. III.28. Panel (a) illustrates the evolution of the spectral line shape as the radiation propagates through the sample, while panel (c) shows the spectral profile at the sample's exit. The line width is approximately 0.21 eV, in satisfactory agreement with the upper state's lifetime.

Panel (d) demonstrates the evolution of emission intensity, with its time integral yielding the number of emitted photons. The characteristic emission profile at the sample's end is shown

in panel (e), with a full width at half maximum (FWHM) of 8 fs. The total number of emitted photons is approximately 1.23×10^{10}. Comparing this to the photon count in the pump pulse (1.56×10^{12}) gives a conversion efficiency of about 1%.

The pumping induces a maximum population inversion of $\Delta P = 0.048$. Consequently, the gain length, which characterizes the field amplification [198], is given by

$$L_g = \frac{8\pi}{3}\frac{\Gamma}{\gamma}(\Delta P n \lambda_0^2),^{-1}$$

and is approximately 0.7 mm for the given parameters. We will use this parameter to characterize the gain curve, which is defined as the number of emitted photons as a function of propagation distance. Mathematically, it is found as a time integral of the emission intensity, $\int d\tau\, I(z,\tau)$. The gain curve, shown in panel (f) on a logarithmic scale, indicates that the exponential gain region extends to approximately $z = 7$ mm, or $10\,L_g$. After that, amplification slows and reaches saturation around $z = 9$ mm ($12.9\,L_g$), as the pump pulse becomes significantly attenuated, preventing further generation of population inversion.

In our numerical analysis, we omitted the weight function and the nonlinear noise term. As demonstrated in Ref. [198], the model for noise terms significantly impacts the initial stage of the process, during which spontaneous photons are produced. For instance, the applied simplifications may lead to an underestimation of the number of spontaneous photons. This, in turn, influences the point at which the field reaches saturation and the subsequent Rabi oscillations, assuming the field is sufficiently intense to induce them. Nevertheless, the overall qualitative behavior remains largely unchanged.

3.7 Conclusion

In conclusion, we have comprehensively analyzed the derived framework across various systems. Our numerical analysis demonstrates good agreement with exact solutions in cases where the influence of dark many-body states—identified and discussed in Chapter II—is minimal. These dark states arise only in compact systems, where they are characterized by non-vanishing correlations between particles. Within the stochastic framework, such correlations may destabilize stochastic trajectories. We found that introducing regularization via stochastic gauges and additional nonradiative dissipation channels effectively stabilizes trajectories, provided the dissipation rates are comparable to the spontaneous decay rate. The computational advantages over the method in Chapter II are discussed in Sec. 3.1. The stochastic framework is significantly faster, with a computational complexity comparable to that of a semiclassical problem, requiring statistical sampling of approximately 10^3-10^4 trajectories to achieve convergence.

We emphasized the critical role of stochastic gauges in regularizing the equations. Although the weight function can introduce instability (Sec. 3.2), post-selecting realizations and discarding those with unstable weights yielded accurate results. Furthermore, we identified specific conditions under which the weight function can be omitted (Sec. 3.4): sufficiently strong dissipation, infrequent application of the drift gauge according to Eq. (III.24), and the use of the diffusion gauge, as outlined in Eq. (III.25). This approach was later applied to treat a realistic system in Sec. 3.6.

We also examined the non-Markovian dynamics of systems of emitters interacting with quantized fields (Sec. 2.5). Unfortunately, we could not stabilize the equations for the Tavis-Cummings model in the strong-coupling regime.

The application of the framework to non-identical particles and extended systems using continuous variables was addressed in Sec. 3.5. In Sec. 3.6 we presented results for the one-dimensional treatment of lasing in neon. However, in this study, we neglected the weight function and nonlinear noise terms in order to stabilize trajectories, which introduced distortions in the predictions. For a refined stochastic theory free from divergences, we refer readers to Ref. [198], which treats noise terms as small perturbations to dynamics dominated by dissipation and stimulated emission. This extension lies beyond the scope of this dissertation and will not be discussed further.

4 Numerical Implementation

In this section, we discuss the numerical solution of stochastic differential equations and provide a code example implemented in `Julia v1.8.5`. Readers who are not interested in the numerical aspects may proceed to Sec. 5.

4.1 Stochastic Differential Equations on a Grid

Let us discuss the interpretation of stochastic differential equations on a grid, using the simple example of a particle moving in a gas. We observe the particle at regular time intervals, with step size Δt. As the particle moves through the gas, collisions with gas molecules cause random fluctuations in its velocity. These fluctuations are modeled as Gaussian random variables.

It is well-established that the stochastic contribution scales as $\sqrt{\Delta t}$. However, let's first consider the scenario where the stochastic component contributes at the same order as the deterministic component, specifically on the order of Δt. The change in the particle's position between times t_k and t_{k-1} can be estimated as:

$$\mathbf{x}(t_k) - \mathbf{x}(t_{k-1}) = (\boldsymbol{\mathscr{V}} + \sqrt{2\mathscr{D}}\,\mathbf{S}_k)\Delta t, \tag{III.44}$$

where $\mathbf{x}(t)$ is the particle's position, $\mathscr{D}$ is the diffusion coefficient, and $\boldsymbol{\mathscr{V}}$ is the drift velocity in the absence of collisions. The vector of random variables $\mathbf{S}_k$ consists of three components, each following a standard normal distribution:

$$\langle \mathrm{S}_k^{(\alpha)} \rangle = 0,$$
$$\langle \mathrm{S}_k^{(\alpha)}\, \mathrm{S}_{k'}^{(\alpha')} \rangle = \delta_{kk'}\, \delta_{\alpha\alpha'},$$

where α, α' represent spatial axes (x, y, z), and k, k' distinguish time points. Expanding Eq. (III.44) iteratively from $\mathbf{x}(0)$ gives:

$$\mathbf{x}(t_k) = \mathbf{x}(0) + \{k\boldsymbol{\mathscr{V}} + \sqrt{2\mathscr{D}}\,(\mathbf{S}_1 + \mathbf{S}_2 + \ldots + \mathbf{S}_k)\}\Delta t.$$

Since the sum of k independent normally distributed random variables is also normally distributed, with a variance scaled by k, we introduce a new random variable $\mathbf{S}$, whose components are independent standard Gaussian random variables, with $\langle \mathrm{S} \rangle = 0$ and $\langle \mathrm{S}_k\, \mathrm{S}_{k'} \rangle = \delta_{kk'}$. This allows us to rewrite the expression for $\mathbf{x}(t_k)$ as:

$$\mathbf{x}(t_k) = \mathbf{x}(0) + \left(\boldsymbol{\mathscr{V}} + \sqrt{\frac{2\mathscr{D}}{k}}\,\mathbf{S}\right) k\Delta t.$$

As we take the limit $\Delta t \to 0$ and $k \to \infty$, while keeping their product constant such that $k\Delta t \equiv t$, the stochastic contribution vanishes and the solution becomes purely deterministic:

$$\mathbf{x}(t) = \mathbf{x}(0) + \boldsymbol{\mathscr{V}} t.$$

This implies that the interpretation of the stochastic differential equations in Eq. (III.44) fails to capture any stochastic behavior. Consequently, the assumption that stochastic fluctuations contribute at the same order as the deterministic part (on the order of Δt) is incorrect [199].

The presence of the factor $\sqrt{k}$ in the stochastic term suggests that its contribution should be on the order of $\sqrt{\Delta t}$, ensuring that the effect of stochastic fluctuations does not vanish as $\Delta t \to 0$. This adjustment modifies the scheme proposed in Eq. (III.44) as follows:

$$\mathbf{x}(t_k) - \mathbf{x}(t_{k-1}) = \boldsymbol{\mathscr{V}}\Delta t + \mathbf{S}_k\sqrt{2\mathscr{D}\,\Delta t}\,. \tag{III.45}$$

Then, the approximate solution for time t_k becomes:

$$\mathbf{x}(t_k) = \mathbf{x}(0) + \boldsymbol{\mathscr{V}}\, k\Delta t + \mathbf{S}\sqrt{2\mathscr{D}\, k\Delta t}\,,$$

where $\mathbf{S}$ is a vector of standard normal Gaussian random variables. In the limit as $\Delta t \to 0$, $k \to \infty$, and $k\Delta t \equiv t$, we find:

$$\mathbf{x}(t) = \mathbf{x}(0) + \boldsymbol{\mathscr{V}} t + \mathbf{S}\sqrt{2\mathscr{D}t}\,.$$

After averaging this solution, the noise contribution vanishes, and the particle moves with a constant velocity $\boldsymbol{\mathscr{V}}$ on average. The mean square displacement, however, includes an additional term:

$$\left\langle \left[\mathbf{x}(t) - \mathbf{x}(0)\right]^2 \right\rangle = \boldsymbol{\mathscr{V}}^2\, t^2 + 6\mathscr{D}t.$$

In the absence of drift, when $\boldsymbol{\mathscr{V}} = 0$, we recover the well-known result from random-walk theory: the mean square displacement grows linearly with time.

This analysis uses simplified stochastic differential equations with additive noise, where both drift and diffusion are independent of stochastic variables. When modeling light-matter interactions, the situation becomes more complex: drift terms depend on stochastic variables, and noise terms are multiplicative (Eqs. (III.18a)).

Consider the stochastic variables $x_1(t)$, $x_2(t)$, ... governed by the following set of stochastic differential equations [200]:

$$dx_p(t) = \mathscr{A}_p(\{x_i(t)\})\, dt + \sum_\alpha \mathscr{B}_p^{(\alpha)}(\{x_i(t)\})\, \delta W^{(\alpha)}(t), \tag{III.46}$$

where $W^{(\alpha)}(t)$ are independent Wiener processes. The increments of these Wiener processes can be formally written as:

$$\delta W^{(\alpha)}(t) = W^{(\alpha)}(t + dt) - W^{(\alpha)}(t) = \mathrm{S}^{(\alpha)}\sqrt{dt}\,.$$

Here, $\mathrm{S}^{(\alpha)}$ are independent random variables following standard normal Gaussian distribution, $\langle \mathrm{S}^{(\alpha)} \rangle = 0$ and $\langle \mathrm{S}^{(\alpha)}\, \mathrm{S}^{(\beta)} \rangle = \delta_{\alpha\beta}$. When numerically solving these equations on a grid, these random variables are independently sampled at each time step. The factor $\sqrt{dt}$ formally reflects that the variance of each Wiener process increment is proportional to dt.

There are important nuances regarding the fact that the result of integrating Eqs. (III.46) depends on the time points at which the function $\mathscr{B}_p^{(\alpha)}(\{x_i(t)\})$ is evaluated [199,201]. Throughout this dissertation, we adopt the Itô interpretation, where the functions multiplying the noise terms are evaluated at the preceding time step.

4.2 Algorithm for Solving Stochastic Differential Equations

The leading contribution to discretized equations comes from noise terms, proportional to $\sqrt{\Delta t}$. The deterministic component can be integrated separately from the noise terms using higher-order methods. This separation does not affect the solution, as the numerical scheme still converges to the same set of equations in the limit as $\Delta t \to 0$.

Let $\{x_i(t_k)\}$ denote the solution at time $t = t_k$. We propose the following algorithm to advance the solution to time t_{k+1}, with a step $t_{k+1} - t_k = \Delta t$:

1. First, we integrate only the deterministic part of the equations:

   $$dx_p(t) = \mathscr{A}_p(\{x_i(t)\})dt.$$

   As a result, we obtain the updated values $\{\widetilde{x}_i(t_{k+1})\}$. These intermediate values do not approximate the solution to the stochastic differential equations, as they lack the necessary stochastic components.

2. We sample the variables $\mathrm{S}_{k+1}^{(\alpha)}$ and add the stochastic increments to $\{\widetilde{x}_i(t_{k+1})\}$ in Itô sense, which results in the updated values $\{x_i(t_{k+1})\}$:

   $$x_p(t_{k+1}) = \widetilde{x}_p(t_{k+1}) + \sum_\alpha \mathscr{B}_p^{(\alpha)}(\{x_i(t_k)\})\, \mathrm{S}_{k+1}^{(\alpha)}\sqrt{\Delta t}\,.$$

   The values $\{x_i(t_{k+1})\}$ are then used to advance the solution to the next time step.

Although a higher-order method can be used to integrate the deterministic part, it does not increase the overall order of the scheme, which remains dominated by the stochastic term and is still $O(\sqrt{\Delta t})$. However, employing a higher-order method for the deterministic component helps reduce accumulated errors specific to that part of the calculation.

The first step of this algorithm can be implemented using the `DifferentialEquations` library [155]. For the second step, the `DiffEqCallbacks` library is particularly useful. The `FunctionCallingCallback` feature allows users to define a function that executes at the end of each integration step. Through this interface, the deterministic part can be solved using any appropriate method, and at the end of each step, the callback function is invoked to add the stochastic components to the solution.

We present the numerical implementation of solving stochastic equations (III.18), with the drift term modified according to Eq. (III.22), and the noise terms rescaled as in Eq. (III.25). These equations are solved in conjunction with the equation for the variable $C_0(t)$, given in Eq. (III.23).

4.3 Parameters

First, we need to initialize all input data and store it in the object called `parameters`. This includes defining parameters such as dipole moments $\overline{\mathbf{d}}_{ij}$, transition frequencies ω_{ij}, initial density matrix, and decay rates. The following code snippet demonstrates how to set up the parameters used for the calculations in Fig. III.13 (c), where we illustrate the evolution of $N = 20$ atoms with Λ-type level configuration:

```
using Parameters
function generate_parameters()
    N  = 20           # number of atoms
    M  = 3            # number of states
    nᵅ = 2            # number of involved polarizations
    d  = zeros(ComplexF64,M,M,nᵅ) # dipole moments
    ω  = zeros(Float64,M,M)       # transition frequencies

    # Constructing the Λ system
    ground  = (1,2)  # manifold of ground states
    excited = (3)    # manifold of excited states
    ω₀      = 0.0    # center frequency, eliminated in RWA
    Δ       = 15     # frequency gap between lower states, in units of γ
    ω[2,1] = Δ
    ω[3,1] = ω₀+Δ/2
    ω[3,2] = ω₀-Δ/2
    @. d[3,1,:] = [1,-im]/√(2);
    @. d[3,2,:] = [1, im]/√(2)*√(0.75);
    for g in ground, e in excited
        ω[g,e] = -ω[e,g]
        @. d[g,e,:] = conj(d[e,g,:])
    end
    # initializing the initial density matrix
    p₁ = 0.0 # initial population of the state |1⟩
    p₂ = 0.0 # initial population of the state |2⟩
    p₃ = 1.0 # initial population of the state |3⟩
    ρ₀ = zeros(ComplexF64,M,M)
    ρ₀[1,1] += p₁
    ρ₀[2,2] += p₂
    ρ₀[3,3] += p₃
    parameters_draft = (; N, M, nᵅ, ground, excited, ω, d, ρ₀)
    # filling the decay matrix
    γ = zeros(ComplexF64,M,M,M,M)
    fill_rate_matrix!(γ, parameters_draft)

    # time grid parameters
    T     = 1       # final time point
    Nᵗ    = 200     # number of points to save
    gridᵗ = range(0.0, T, Nᵗ)
    Δtᵐᵃˣ = T/10000 # maximum allowed time step
    parameters_draft = (; parameters_draft..., γ, T, Nᵗ, gridᵗ, Δtᵐᵃˣ)
    return parameters_draft
end
```

Within this function, we call `fill_rate_matrix!`, which calculates the coefficients for the incoherent part of the stochastic equations, corresponding to the second line in Eq. (III.18a):

$$\frac{d\rho_{pq}(t)}{dt} = \ldots + \frac{\gamma}{2}\sum_{r,s=1}^{M}\left\{2\rho_{rs}(t)\left(\overline{\mathbf{d}}_{p<r}\cdot\overline{\mathbf{d}}_{s>q}\right) - \left(\overline{\mathbf{d}}_{p>r}\cdot\overline{\mathbf{d}}_{r<s}\right)\rho_{sq}(t) - \rho_{pr}(t)\left(\overline{\mathbf{d}}_{r>s}\cdot\overline{\mathbf{d}}_{s<q}\right)\right\} + \ldots$$

This contribution can be represented as $\sum_{r,s}\gamma_{pqrs}\,\rho_{rs}(t)$. The `fill_rate_matrix!` function stores the coefficients γ_{pqrs} in the matrix Υ:

```
function fill_rate_matrix!(Υ, parameters)
    @unpack M, nᵅ, d = parameters
    @. Υ = 0.0
    @inbounds for p in 1:M, q in 1:M, r in 1:M, s in 1:M
        if s>q && p<r
            for α in 1:nᵅ
                Υ[p,q,r,s] += d[s,q,α]*d[p,r,α]
            end
        end
        if p>r && r<s
            for α in 1:nᵅ
                Υ[p,q,s,q] -= d[p,r,α]*d[r,s,α]/2
            end
        end
        if r>s && s<q
            for α in 1:nᵅ
                Υ[p,q,p,r] -= d[r,s,α]*d[s,q,α]/2
            end
        end
    end
end
```

The function `fill_rate_matrix!` executes in approximately 235 nanoseconds without any additional memory allocations. It can be also adapted to incorporate nonradiative decay rates. The parameters are generated by the following line:

```
    parameters = generate_parameters();
```

Next, we need to define a function that generates initial conditions for both the stochastic density matrix $\rho_{pq}(t)$ and the variable $C_0(t)$, which determines the weight function as $\Omega(t) = e^{C_0(t)}$. Initial density matrix is represented by `parameters.ρ₀`, while $C_0(0) = 0$. The following function generates `ArrayPartition` of the initial objects based on the given parameters:

```
using RecursiveArrayTools

function initial_conditions(parameters)
    @unpack M, ρ₀ = parameters
    ρⁱⁿ   = zeros(ComplexF64,M,M)
    ρⁱⁿ .+= ρ₀
    C₀    = zeros(ComplexF64,1)
    return ArrayPartition(reshape(ρⁱⁿ, M^2), C₀)
end
```

This function executes in approximately 132 nanoseconds and uses 368 bytes of memory, with most of the space occupied by the generated object. We explicitly vectorize the density matrix with `reshape(ρⁱⁿ, M^2)` to ensure that all variables have the same data type, which is important for performance of `DifferentialEquations.jl`.

4.4 Drift Function

In this section, we discuss the implementation of the function responsible for generating the drift components of the stochastic equations (III.18a) with the modification as in Eq. (III.22).

We begin by defining a structure that stores containers for repeated use in calculations:

```
mutable struct Drift
    nᵅ :: Int64
    P⁺ :: Array{ComplexF64,1}
    P⁻ :: Array{ComplexF64,1}
    θ  :: Bool
    function Drift(parameters)
        @unpack nᵅ = parameters
        self    = new()
        self.nᵅ = nᵅ
        self.P⁺ = zeros(ComplexF64,nᵅ)
        self.P⁻ = zeros(ComplexF64,nᵅ)
        self.θ  = false
        return self
    end
end
```

The structure contains several fields:

1. `nᵅ` represents the number of polarizations used in generating the structure.
2. `P⁺` and `P⁻` are vectors used for storing the gauged polarization fields (Eq. (III.22)).
3. `θ` is a boolean variable, playing the role of $\theta(t)$ in Eq. (III.24).

Next, we define a function associated with this structure that has access to all its fields, and calculates the drift of the gauged equations:

```
function (self::Drift)(dx, x, parameters, time)
    @unpack nᵅ, P⁺, P⁻, θ = self
    @unpack N, M, d, ω, ground, excited, γ = parameters
    ρ   = reshape(view( x.x[1],:),M,M) # pointer to stochastic density matrix
    dρ  = reshape(view(dx.x[1],:),M,M) # pointer to its derivative
    dC₀ = view(dx.x[2],:) # pointer to derivative of C₀
    @. dC₀ = 0.0          # weight has no drift

    @inbounds for α in 1:nᵅ  # calculating gauged polarizations times (N-1)/2
        P⁺[α] = 0.0; P⁻[α] = 0.0
        for g in ground, e in excited
            P⁺[α] += 0.5*(N-1)*d[g,e,α]*(ρ[e,g]-0.5*θ*(ρ[e,g]-conj(ρ[g,e])))
            P⁻[α] += 0.5*(N-1)*d[e,g,α]*(ρ[g,e]-0.5*θ*(ρ[g,e]-conj(ρ[e,g])))
        end
    end

    @inbounds for p in 1:M, q in 1:M # generating unitary part of equations
        dρ[p,q] = -im*ω[p,q]*ρ[p,q]
        for r in 1:M
            if p>r
                for α in 1:nᵅ
                    dρ[p,q] -= P⁺[α]*d[p,r,α]*ρ[r,q]
                end
            elseif p<r
                for α in 1:nᵅ
                    dρ[p,q] += P⁻[α]*d[p,r,α]*ρ[r,q]
                end
            end
            if r>q
                for α in 1:nᵅ
                    dρ[p,q] += P⁺[α]*ρ[p,r]*d[r,q,α]
                end
            elseif r<q
                for α in 1:nᵅ
                    dρ[p,q] -= P⁻[α]*ρ[p,r]*d[r,q,α]
                end
            end
         end
    end
    @einsum dρ[p,q] += γ[p,q,r,s]*ρ[r,s] # incoherent part of equations
    return nothing
end
```

This drift function is generated by running:

```
drift! = Drift(parameters)
```

When applied to the initial conditions, this function executes in 245 nanoseconds without allocating any additional memory.

4.5 Noise Function

The next step is implementing a function that adds the stochastic components. Similar to how we handled the drift function, we first define a structure to allocate all the necessary arrays for the calculations:

```
mutable struct Noise
    nᵅ  :: Int64
    f   :: Array{ComplexF64,1}
    g   :: Array{ComplexF64,1}
    f⁺  :: Array{ComplexF64,1}
    g⁺  :: Array{ComplexF64,1}
    F   :: Array{Float64,1}
    G   :: Array{Float64,1}
    Pᵉᵉ :: Matrix{ComplexF64}
    Pᵍᵍ :: Matrix{ComplexF64}
    function Noise(parameters)
        @unpack nᵅ = parameters
        self    = new()
        self.nᵅ = nᵅ
        self.f  = zeros(ComplexF64,nᵅ)
        self.g  = zeros(ComplexF64,nᵅ)
        self.f⁺ = zeros(ComplexF64,nᵅ)
        self.g⁺ = zeros(ComplexF64,nᵅ)
        self.F  = ones(Float64,nᵅ)
        self.G  = ones(Float64,nᵅ)
        self.Pᵉᵉ = zeros(ComplexF64,nᵅ,nᵅ)
        self.Pᵍᵍ = zeros(ComplexF64,nᵅ,nᵅ)
        return self
    end
end
```

The fields in this structure serve the following purposes:

1. `nᵅ` is the number of polarizations used in generating the structure.
2. `f`, `f⁺`, `g`, and `g⁺` are containers for the elementary noise terms $\mathbf{f}$, $\mathbf{f}^\dagger$, $\mathbf{g}$, and $\mathbf{g}^\dagger$.
3. `F`, `G`, `Pᵍᵍ`, and `Pᵉᵉ` are containers for the diffusion gauge functions F_α, G_α, $P^{(gg)}_{\alpha\beta}$, and $P^{(ee)}_{\alpha\beta}$ defined in Eqs. (III.26).

In our numerical implementation, the noise terms $\mathbf{f}(t)$, $\mathbf{f}^\dagger(t)$, $\mathbf{g}(t)$, and $\mathbf{g}^\dagger(t)$, which satisfy the correlation properties in Eq. (III.18c), are sampled as follows:

$$\mathrm{f}^{(\alpha)}(t) = \frac{\mathrm{S}_1^{(\alpha)}(t) + i\mathrm{S}_2^{(\alpha)}(t)}{\sqrt{2}}, \qquad \mathrm{f}^{\dagger(\alpha)}(t) = \frac{\mathrm{S}_1^{(\alpha)}(t) - i\mathrm{S}_2^{(\alpha)}(t)}{\sqrt{2}},$$
$$\mathrm{g}^{(\alpha)}(t) = \frac{\mathrm{S}_3^{(\alpha)}(t) + i\mathrm{S}_4^{(\alpha)}(t)}{\sqrt{2}}, \qquad \mathrm{g}^{\dagger(\alpha)}(t) = \frac{\mathrm{S}_3^{(\alpha)}(t) - i\mathrm{S}_4^{(\alpha)}(t)}{\sqrt{2}}.$$

Here, the variables $\mathrm{S}_a^{(\alpha)}(t)$ are independent, real-valued standard Gaussian random variables with the following correlation properties:

$$\langle \mathrm{S}_a^{(\alpha)}(t) \rangle = 0, \qquad \langle \mathrm{S}_a^{(\alpha)}(t)\, \mathrm{S}_b^{(\beta)}(t') \rangle = \delta_{ab}\, \delta_{\alpha\beta}\, \delta(t - t').$$

It is straightforward to verify that these definitions ensure that the noise terms satisfy the correlation properties in Eq. (III.18c). Notably, in this representation, we have $\mathbf{f}^*(t) = \mathbf{f}^\dagger(t)$ and $\mathbf{g}^*(t) = \mathbf{g}^\dagger(t)$.

These noise terms must be rescaled in accordance with Eqs. (III.25) and (III.26). We implement the following function to compute F_α and G_α at the current time step based on the stochastic density matrix ρ from the previous step:

```
function get_diffusion_functions!(containers, ρ, parameters)
    F, G, P⁺, P⁻, Pᵍᵍ, Pᵉᵉ = containers
    @unpack nᵅ, d, excited, ground = parameters
    @inbounds for α in 1:nᵅ
        P⁺[α] = 0.0; P⁻[α] = 0.0; @. Pᵍᵍ[α,:] = 0.0; @. Pᵉᵉ[α,:] = 0.0
        for g in ground, e in excited
            P⁺[α] += d[g,e,α]*ρ[e,g]
            P⁻[α] += d[e,g,α]*ρ[g,e]
        end
        for β in 1:nᵅ
            for g in ground, e in excited
                for g′ in ground
                    Pᵍᵍ[α,β] += d[e,g,α]*ρ[g,g′]*d[g′,e,β]
                end
                for e′ in excited
                    Pᵉᵉ[α,β] += d[g,e,α]*ρ[e,e′]*d[e′,g,β]
                end
            end
        end
    end
    @einsum F[β]  = abs(Pᵉᵉ[α,β]-P⁺[α]*P⁻[β])^2
    @einsum F[β] += abs(P⁻[α]*P⁻[β])^2
    @einsum F[β] /= abs(Pᵉᵉ[β,α]-Pᵍᵍ[α,β])^2
    @. F = √(√(F))
    @einsum G[β]  = abs(Pᵉᵉ[β,α]-P⁺[β]*P⁻[α])^2
    @einsum G[β] += abs(P⁺[α]*P⁺[β])^2
    @einsum G[β] /= abs(Pᵉᵉ[α,β]-Pᵍᵍ[β,α])^2
    @. G = √(√(G))
    val = 0.0
    @inbounds for α in 1:nᵅ
        val += abs(F[α])+abs(G[α])+1/abs(F[α])+1/abs(G[α])
    end
    return val
end
```

This function returns `val`, which is the sum of the absolute values of all components of the gauging functions and their inverses. If `val` is `NaN` or exceeds 10^5, all noise terms will be nullified. However, based on our experience, this condition has never occurred.

After calculating these functions, we rescale the noise terms according to Eq. (III.25) to obtain the gauged noise terms, denoted with tildes, which then enter the noise part of Eqs. (III.18) and (III.23). Note that in the noise representation in Eq. (III.18b), each noise term is divided by a factor of $\sqrt{2}$. To reduce the number of operators in our code, we incorporate this factor directly into the definitions of the noise terms. Consequently, the objects `f`, `f⁺`, `g`, and `g⁺` actually correspond to $\tilde{\mathbf{f}}(t)/\sqrt{2}$, $\tilde{\mathbf{f}}^\dagger(t)/\sqrt{2}$, $\tilde{\mathbf{g}}(t)/\sqrt{2}$, and $\tilde{\mathbf{g}}^\dagger(t)/\sqrt{2}$.

Below, we will define the function associated with the `Noise` structure, which adds stochastic components to the solution. This function takes three arguments: solution at the current point `u`, time `t`, and `integrator`. The properties of the `integrator` object can be found in the `DifferentialEquations.jl` library documentation.

The function begins by calculating the diffusion gauging functions and sampling the gauged noise terms. After that, the solution at the current step is updated with the stochastic components. Importantly, all coefficients multiplying the noise terms are computed at the previous time step, following Itô interpretation. Finally, the function generates the equation for the variable $C_0(t)$ (Eq. (III.23)) and verifies whether the drift needs to be gauged at the next step, according to the criterion in Eq. (III.24). The implementation of this noise function is shown below:

```
function (self::Noise)(u, t, integrator)
    @unpack N, M, d, excited, ground = integrator.p
    @unpack nᵅ, f, g, f⁺, g⁺, F, G, Pᵉᵉ, Pᵍᵍ = self
    @unpack P⁺, P⁻ = integrator.f.f # accessing containers of the drift
    ρ̃ = reshape(view(integrator.uprev.x[1],:),M,M) # ρ from the previous step

    val = get_diffusion_functions!((F, G, P⁺, P⁻, Pᵍᵍ, Pᵉᵉ), ρ̃, integrator.p)
    if val > 1e5 || isnan(val)
        return nothing
    end

    Δt = integrator.t-integrator.tprev
    @inbounds for α in 1:nᵅ
        f[α]  = (randn()+im*randn())/2*√(Δt)*F[α]
        g[α]  = (randn()+im*randn())/2*√(Δt)*G[α]
        f⁺[α] = conj(f[α])/F[α]^2; g⁺[α] = conj(g[α])/G[α]^2
    end

    ρ = reshape(view(integrator.u.x[1],:),M,M) # ρ from the current step
    @inbounds for p in 1:M, q in 1:M
        for r in 1:M
            if r>p
                for α in 1:nᵅ
                    ρ[p,q] += d[p,r,α]*ρ̃[r,q]*(f[α]+g⁺[α])
                end
            elseif r<p
                for α in 1:nᵅ
                    ρ[p,q] -= d[p,r,α]*ρ̃[r,q]*g[α]
                end
            end
            if r>q
                for α in 1:nᵅ
                    ρ[p,q] += ρ̃[p,r]*d[r,q,α]*(g[α]+f⁺[α])
                end
            elseif r<q
                for α in 1:nᵅ
                    ρ[p,q] -= ρ̃[p,r]*d[r,q,α]*f[α]
                end
            end
        end
    end
    h = 0.0
    for α in 1:nᵅ
        h += P⁻[α]*f⁺[α]+P⁺[α]*g⁺[α]
    end
    @. ρ -= ρ̃*h

    # generating equation for C₀
    @unpack θ = integrator.f.f
    if θ
        C₀  = view(integrator.u.x[2],:)
        ΔC₀ = 0.0
        @inbounds for α in 1:nᵅ
            ΔC₀ += (P⁻[α]-conj(P⁺[α]))*f⁺[α]+(P⁺[α]-conj(P⁻[α]))*g⁺[α]
        end
        @. C₀ += 0.5*(N-1)*ΔC₀
    end

    # verifying if the drift gauge is required for the next step
    θ = false
    @inbounds for g in ground, e in excited
        θ = θ || (real(ρ[e,e]-ρ[g,g])>0.0)
    end
    integrator.f.f.θ = θ
    return nothing
end
```

The noise function is generated by running:

```
    noise! = Noise(parameters);
```

The performance of this function estimates as 388 nanoseconds.

4.6 Single Trajectory Integration

Finally, we define the function used for integrating multiple stochastic realizations:

```
function integrate_trajectory(prob, noise_cb, trajectory_number)
    @unpack Δtᵐᵃˣ, gridᵗ = prob.p
    output = []
    for _ in 1:trajectory_number
        data = solve(prob, Tsit5(), adaptive=true, dtmax=Δtᵐᵃˣ, saveat=gridᵗ,
     callback=noise_cb)
        push!(output, data.u)
    end
    return output
end
```

This function is called in the following snippet:

```
using OrdinaryDiffEq, Einsum, DiffEqCallbacks

@unpack T = parameters;
u0       = initial_conditions(parameters);
tspan    = (0,T)
prob     = ODEProblem(drift!, u0, tspan, parameters);
noise_cb = FunctionCallingCallback(noise!);

trajectory_number = 1;
output = integrate_trajectory(prob, noise_cb, trajectory_number);
```

The object `output` is a list containing data for all trajectories, which should be processed further by averaging the selected observables. Since working with stochastic variables is intuitive—unlike the complexity of our second-quantization formalism from Chapter II—we do not include the details of this processing step, as it is relatively straightforward.

The performance of the presented code is summarized in Table III.1 and discussed in Sec. 3.1 for all models considered in Sec. 2.

5 Supplementary Sections

This appendix provides technical calculations and detailed discussions supplementing the main text. In Sec. 5.1, we explore the properties of the Λ-supervectors introduced in Eq. (III.6). The following section, Sec. 5.2, analyzes a representation where the normalization coefficient of the Λ-supervector is absorbed into the P-function. In Sec. 5.3, we use this representation to eliminate the η-object defined in Eq. (III.15) from the equations. Finally, Sec. 5.4 examines aspects of stochastic drift gauges, which were used in Sec. 1.7.

Readers uninterested in these supplementary discussions may proceed directly to the final chapter, "Conclusion and Outlook," in Chapter IV.

5.1 Properties of the Λ-Supervectors

At the beginning of this chapter, we introduced the P-representation for supervectors, defining the supervector $|\Lambda(\{\beta_{ij}\})\rangle\!\rangle$ in Eq. (III.6) as the basis for this representation. In this section, we study their properties in more detail.

Let's expand the exponential as a Taylor series and derive the representation of the Λ supervector in the occupation-number basis:

$$|\Lambda(\{\beta_{ij}\})\rangle\!\rangle = e^{-\sum_i \beta_{ii}} \sum_{N=0}^{\infty} \sum_{\substack{\{n_{ij}\} \\ \sum_{i,j} n_{ij}=N}} \sqrt{\frac{\prod_{i,j} n_{ij}!}{N!}} \left[\prod_{i,j=1}^{M} \frac{(\beta_{ij})^{n_{ij}}}{n_{ij}!} \right] |\{n_{ij}\}\rangle\!\rangle.$$

This supervector represents a statistical mixture of states with all possible particle numbers, including the vacuum superstate. Each term in the summation over N represents a state of N uncorrelated particles, as in Eq. (II.16). Coefficients $\{\beta_{ij}\}$ play a role analogous to coefficients $\{\rho_{ij}\}$ that parameterize the density matrix. However, unlike $\{\rho_{ij}\}$, coefficients $\{\beta_{ij}\}$ are all independent and do not describe a physical density matrix. In this sense, this supervector is similar to the functional in Eq. (II.58), which we used to construct observables.

The quantity formally referred to as the mean number of particles in this state is determined by the following trace:

$$\mathrm{Tr}\left[\hat{N}\,|\Lambda(\{\beta_{ij}\})\rangle\!\rangle\right] = \sum_{i=1}^{M} \beta_{ii}.$$

However, this is not a strict physical particle number, as it can generally take complex values. Notably, the normalization coefficient $e^{-\sum_i \beta_{ii}}$ in Eq. (III.6) can be interpreted as the exponential of the negative of the "mean number of particles."

Remarkably, the vector $|\Lambda(\{\beta_{ij}\})\rangle\!\rangle$ is an eigenstate of the operator $\hat{T}\hat{N}$, where $\hat{T}$ is defined in Eq. (II.67). The corresponding eigenvalue is the "mean number of particles."

Applying the bosonic superoperators combined with the factors of $\hat{N}^{\pm 1/2}$ results in the following expressions:

$$\hat{b}_{pq}\sqrt{\hat{N}}\,|\Lambda(\{\beta_{ij}\})\rangle\!\rangle = \beta_{pq}\,|\Lambda(\{\beta_{ij}\})\rangle\!\rangle, \qquad \frac{1}{\sqrt{\hat{N}}}\,\hat{b}^{\dagger}_{pq}\,|\Lambda(\{\beta_{ij}\})\rangle\!\rangle = \Big(\delta_{pq} + \frac{\partial}{\partial\beta_{pq}}\Big)|\Lambda(\{\beta_{ij}\})\rangle\!\rangle.$$

These expressions lead directly to the replacement rules provided in Eq. (III.8). Neglecting the factors of $\hat{N}^{\pm 1/2}$ changes these properties, for example:

$$\hat{b}_{pq}\,|\Lambda(\{\beta_{ij}\})\rangle\!\rangle = \frac{\beta_{pq}}{\sqrt{\hat{N}+1}}\,|\Lambda(\{\beta_{ij}\})\rangle\!\rangle,$$

and the trace of this expression will no longer simply result in β_{pq}, as in Eq. (III.7).

Standard Displacement Operator

Let us explore an alternative definition for the Λ-supervectors. Specifically, we can construct them without the additional factors of $\hat{N}^{-1/2}$, similar to the traditional non-normalized coherent states in Hilbert space:

$$|\widetilde{\Lambda}(\{\beta_{ij}\})\rangle\!\rangle = \exp\Big[\sum_{i,j=1}^{M} \beta_{ij}\,\hat{b}^{\dagger}_{ij}\Big]|\mathrm{vac}\rangle\!\rangle. \tag{III.47}$$

Using basis of these supervectors as an ansatz for the density matrix has the advantage of yielding simple expressions under the action of bosonic superoperators:

$$\hat{b}_{pq}\,|\widetilde{\Lambda}(\{\beta_{ij}\})\rangle\!\rangle = \beta_{pq}\,|\widetilde{\Lambda}(\{\beta_{ij}\})\rangle\!\rangle, \qquad \hat{b}^{\dagger}_{pq}\,|\widetilde{\Lambda}(\{\beta_{ij}\})\rangle\!\rangle = \frac{\partial}{\partial\beta_{pq}}\,|\widetilde{\Lambda}(\{\beta_{ij}\})\rangle\!\rangle. \tag{III.48}$$

However, computing expectation values requires evaluating the trace of these supervectors, which has the following cumbersome form:

$$\mathrm{Tr}\Big[|\widetilde{\Lambda}(\{\beta_{ij}\})\rangle\!\rangle\Big] = \sum_{N=0}^{\infty} \frac{(\beta_{11}+\beta_{22}+\ldots+\beta_{MM})^N}{\sqrt{N!}}. \tag{III.49}$$

This function of $\{\beta_{ii}\}$ appears in all expressions for averages as an additional weight function. The series on the right-hand side requires an extra $1/\sqrt{N!}$ factor to converge to the exponential function. In fact, if we introduce this factor into definition (III.47), the original supervectors from Eq. (III.6) are recovered, up to normalization:

$$\frac{1}{\sqrt{\hat{N}!}}\,|\widetilde{\Lambda}(\{\beta_{ij}\})\rangle\!\rangle = \exp\Big[\sum_{i=1}^{M} \beta_{ii}\Big]|\Lambda(\{\beta_{ij}\})\rangle\!\rangle.$$

This suggests that the originally proposed ansatz in Eq. (III.6) is a properly normalized, generalized coherent state expansion.

One might consider incorporating the normalization in Eq. (III.49) directly into the definition in Eq. (III.47). While this simplifies the expressions for averages, it complicates the application of bosonic superoperators, specifically:

$$\hat{b}_{pq}\,\frac{|\widetilde{\Lambda}(\{\beta_{ij}\})\rangle\!\rangle}{\mathrm{Tr}\left[|\widetilde{\Lambda}(\{\beta_{ij}\})\rangle\!\rangle\right]} = \beta_{pq}\,\frac{|\widetilde{\Lambda}(\{\beta_{ij}\})\rangle\!\rangle}{\mathrm{Tr}\left[|\widetilde{\Lambda}(\{\beta_{ij}\})\rangle\!\rangle\right]}, \tag{III.50}$$

$$\hat{b}^{\dagger}_{pq}\,\frac{|\widetilde{\Lambda}(\{\beta_{ij}\})\rangle\!\rangle}{\mathrm{Tr}\left[|\widetilde{\Lambda}(\{\beta_{ij}\})\rangle\!\rangle\right]} = \left\{\frac{\partial}{\partial\beta_{pq}} + \delta_{pq}\frac{\mathrm{Tr}\left[\sqrt{\hat{N}+1}\,|\widetilde{\Lambda}(\{\beta_{ij}\})\rangle\!\rangle\right]}{\mathrm{Tr}\left[|\widetilde{\Lambda}(\{\beta_{ij}\})\rangle\!\rangle\right]}\right\}\frac{|\widetilde{\Lambda}(\{\beta_{ij}\})\rangle\!\rangle}{\mathrm{Tr}\left[|\widetilde{\Lambda}(\{\beta_{ij}\})\rangle\!\rangle\right]}. \tag{III.51}$$

With these transformations, deriving a simple Fokker-Planck equation becomes problematic. This highlights that the supervector in Eq. (III.6) provides an elegant and straightforward approach for deriving the Fokker-Planck equation and finding observables.

5.2 Non-Normalized Λ-Supervectors

As discussed in the main text, the normalization coefficient $e^{-\sum_i \beta_{ii}}$ in Eq. (III.6) introduces Kronecker deltas into the replacement rules in Eq. (III.8). Without normalization, the creation superoperators generate only the derivatives of the P-function. In this section, we investigate the properties of the non-normalized Λ supervectors.

We neglect the normalization coefficient $e^{-\sum_i \beta_{ii}}$ and replace it with $e^{-\eta N}$, where η is defined in Eq. (III.15). This choice aligns with the variable transformation in Eq. (III.14), where all β variables are linear in η. Simply removing the normalization might lead to issues, as discussed later in this section.

The definition for the new Λ-supervectors is the following:

$$|\Lambda'(\{\beta_{ij}\})\rangle\!\rangle = \exp\Big[-\eta N + \frac{1}{\sqrt{\hat{N}}}\sum_{i,j=1}^{M}\beta_{ij}\,\hat{b}^{\dagger}_{ij}\Big]|\mathrm{vac}\rangle\!\rangle = e^{-\eta N+\sum_i \beta_{ii}}\,|\Lambda(\{\beta_{ij}\})\rangle\!\rangle, \tag{III.52}$$

where the second equality establishes the connection to the original supervectors in Eq. (III.6). We propose the following ansatz for the density matrix:

$$|\rho(t)\rangle\!\rangle = \int\prod_{i,j=1}^{M}(d^2\beta_{ij})\,P'(\{\beta_{ij}\},t)\;|\Lambda'(\{\beta_{ij}\})\rangle\!\rangle. \tag{III.53}$$

The new probability density function P' is related to the original one in a manner similar to the connection between the Λ-supervectors.

The following replacement rules hold for the P' function:

$$\hat{b}_{pq}\sqrt{\hat{N}}\;|\rho(t)\rangle\!\rangle \longrightarrow \beta_{pq}\,P'(\{\beta_{ij}\},t), \qquad \frac{1}{\sqrt{\hat{N}}}\,\hat{b}^{\dagger}_{pq}\,|\rho(t)\rangle\!\rangle \longrightarrow -\frac{\partial}{\partial\beta_{pq}}\,P'(\{\beta_{ij}\},t).$$

These replacement rules lead to a Fokker-Planck equation similar to the original one in Eq. (III.10a), but without the nonlinear drift term:

$$\frac{\partial P'(\{\beta_{ij}\},t)}{\partial t} = -\sum_{p,q}\Big[\mathscr{A}_{pq}(\{\beta_{ij}\})\,P'(\{\beta_{ij}\},t)\Big] + \frac{1}{2}\sum_{p,q,p',q'}\frac{\partial^2}{\partial\beta_{pq}\,\partial\beta_{p'q'}}\Big[\mathscr{D}_{pqp'q'}(\{\beta_{ij}\})\,P'(\{\beta_{ij}\},t)\Big]. \tag{III.54}$$

Although the nonlinear drift contribution seems absent, its effect is actually reintroduced through an additional weighting function when averaging, arising from the trace of the Λ′-supervectors.

Let us calculate expectation values using the P' function. Referring to the relation between stochastic averages and quantum-mechanical expectation values in Eq. (III.9), we obtain the following relation:

$$\sum_{\mu_1\neq\ldots\neq\mu_K} \mathrm{Tr}\left[\hat{\sigma}_{\mu_1,q_1p_1}\ldots\hat{\sigma}_{\mu_K,q_Kp_K}\,\hat{\rho}(t)\right] = \frac{\int\prod_{i,j=1}^{M}(d^2\beta_{ij})\,\beta_{p_1q_1}\,\ldots\,\beta_{p_Kq_K}\,e^{-\eta N+\sum_i\beta_{ii}}\,P'(\{\beta_{ij}\},t)}{\int\prod_{i,j=1}^{M}(d^2\beta_{ij})\,e^{-\eta N+\sum_i\beta_{ii}}\,P'(\{\beta_{ij}\},t)}. \quad \text{(III.55)}$$

Next, we perform a change of variables as outlined in Eq. (III.14), reformulating the P' function in terms of the transformed variables. After this step, all statistical properties at $t = 0$ are explicitly embedded in η. Consequently, it becomes necessary to include averaging over η, which effectively replaces the averaging over the initial conditions. The explicit expression for the transformed average is provided in the next section; see Eq. (III.58).

Let's examine averaging over η. When we substitute β_{ij} with $\eta N\beta'_{ij}$, we encounter averages of the following form:

$$\left\langle e^{\pm\eta N(1-\sum_i\beta'_{ii})}\right\rangle = \left[1\pm\left(1-\sum_i\beta'_{ii}\right)\right]^N.$$

When the primed variables are close to a physical density matrix, the sum $\sum_i\beta'_{ii}$ approaches unity, causing this average to approach unity as well. However, if we omit the factor of $e^{-\eta N}$ in Eq. (III.52), this average becomes:

$$\left\langle e^{\mp\eta N\sum_i\beta'_{ii}}\right\rangle = \left(1\mp\sum_i\beta'_{ii}\right)^N,$$

which can be close to zero, potentially leading to division by zero when normalizing expectation values. Therefore, the inclusion of the factor $e^{-\eta N}$ is not merely a cosmetic adjustment, but helps to avoid such complications.

5.3 Elimination of η

In this section, we outline the steps required to eliminate η from both the initial conditions and the stochastic equations. The approach uses the representation of the non-normalized Λ-supervectors in Eq. (III.52) and the associated Fokker-Planck equation in Eq. (III.54).

We start by changing variables as described in Eq. (III.14):

$$\beta_{pq} = \eta N\beta'_{pq}. \quad \text{(III.56)}$$

This transformation redefines the function P' in terms of the new variables β'_{pq}, but we keep the same notation, $P' = P'(\{\beta'_{ij}\},t)$. At time $t = 0$, this function becomes independent of the η-object, and the variables $\beta'_{pq}(0)$ are deterministic numbers.

The Fokker-Planck equation for the new function P' has the same structure as Eq. (III.54). The corresponding Itô stochastic equations are given by:

$$\frac{d\beta'_{pq}(t)}{dt} = \mathscr{A}_{pq}(\{\beta'_{ij}(t)\}) + F_{pq}(\{\beta'_{ij}(t)\}), \quad \text{(III.57)}$$

which are entirely free of η. Thus, the function $P'(\{\beta'_{ij}\},t)$ is independent of η.

The η-object reemerges during the calculation of averages. Revisiting the average in Eq. (III.55), we change the variables as in Eq. (III.56) and reformulate the P-function in terms of

the primed variables:

$$\sum_{\mu_1\neq\ldots\neq\mu_K} \mathrm{Tr}\left[\hat{\sigma}_{\mu_1,q_1p_1}\ldots\hat{\sigma}_{\mu_K,q_Kp_K}\,\hat{\rho}(t)\right] = N^K \frac{\displaystyle\int\prod_{i,j=1}^{M}(d^2\beta'_{ij})\,\beta'_{p_1q_1}\,\ldots\,\beta'_{p_Kq_K}\left\langle\eta^K\,e^{-\eta N(1-\sum_i\beta'_{ii})}\right\rangle_\eta P'(\{\beta'_{ij}\},t)}{\displaystyle\int\prod_{i,j=1}^{M}(d^2\beta'_{ij})\left\langle e^{-\eta N(1-\sum_i\beta'_{ii})}\right\rangle_\eta P'(\{\beta'_{ij}\},t)}, \quad \text{(III.58)}$$

where $\langle\ldots\rangle_\eta$ denotes averaging over the η-object, whose statistical moments are defined in Eq. (III.15). We can explicitly average over η, yielding:

$$\sum_{\mu_1\neq\ldots\neq\mu_K} \mathrm{Tr}\left[\hat{\sigma}_{\mu_1,q_1p_1}\ldots\hat{\sigma}_{\mu_K,q_Kp_K}\,\hat{\rho}(t)\right] = \frac{N!}{(N-K)!}\frac{\displaystyle\int\prod_{i,j=1}^{M}(d^2\beta'_{ij})\,\frac{\beta'_{p_1q_1}}{\sum_i\beta'_{ii}}\,\ldots\,\frac{\beta'_{p_Kq_K}}{\sum_i\beta'_{ii}}\,e^{N\ln\sum_i\beta'_{ii}}\,P'(\{\beta'_{ij}\},t)}{\displaystyle\int\prod_{i,j=1}^{M}(d^2\beta'_{ij})\,e^{N\ln\sum_i\beta'_{ii}}\,P'(\{\beta'_{ij}\},t)}. \quad \text{(III.59)}$$

Note that averaging out η did not affect $P'(\{\beta'_{ij}\},t)$ or the associated Fokker-Planck equation.

Equation (III.59) shows that quantum expectation values are represented by the variables $\beta'_{ij}/\sum_i\beta'_{ii}$. However, this change of variables cannot be directly implemented, as the weighting function $e^{N\ln\sum_i\beta'_{ii}(t)}$ depends only on the primed variables.

The weight $e^{N\ln\sum_i\beta'_{ii}(t)}$ introduces further challenges. It increases computational complexity when calculating averages and may affect convergence, as it reintroduces the nonlinear drift term via statistical correlations. To eliminate this weight, we incorporate it into the probability density function, defining a new function P'':

$$P''(\{\beta'_{ij}\},t) = e^{N\ln\sum_i\beta'_{ii}}\,P'(\{\beta'_{ij}\},t), \quad \text{(III.60)}$$

which removes the weighting function from Eq. (III.59). This transformation modifies the properties of the stochastic variables, which are now governed by equations associated with the new function P''. To reflect this change, we denote new variables as ρ'_{ij}.

From the definition of $P''(\{\rho'_{ij}\},t)$, we derive the corresponding Fokker-Planck equation:

$$\frac{\partial P''(\{\rho'_{ij}\},t)}{\partial t} = -\sum_{p,q}\frac{\partial}{\partial\rho'_{pq}}\Big[\Big\{\mathscr{A}_{pq}(\{\rho'_{ij}\}) + \frac{N}{\sum_s\rho'_{ss}}\sum_n\mathscr{D}_{pqnn}(\{\rho'_{ij}\})\Big\}P''(\{\rho'_{ij}\},t)\Big] + \frac{1}{2}\sum_{p,q,p',q'}\frac{\partial^2}{\partial\rho'_{pq}\partial\rho'_{p'q'}}\Big[\mathscr{D}_{pqp'q'}(\{\rho'_{ij}\})\,P''(\{\rho'_{ij}\},t)\Big].$$

Compared to the original Fokker-Planck equation in Eq. (III.10a), the nonlinear drift term reappears in a modified form, while the other terms remain unchanged. The corresponding Itô stochastic equations are:

$$\frac{d\rho'_{pq}(t)}{dt} = \mathscr{A}_{pq}(\{\rho'_{ij}(t)\}) + \frac{N}{\sum_s\rho'_{ss}}\sum_n\mathscr{D}_{pqnn}(\{\rho'_{ij}(t)\}) + F_{pq}(\{\rho'_{ij}(t)\},t).$$

These equations retain the structure of Eqs. (III.11), but with a modified nonlinear drift term.

Quantum expectation values are found as averages over statistical realizations of $\rho'_{pq}(t)$:

$$\sum_{\mu_1\neq\ldots\neq\mu_K}\mathrm{Tr}\left[\hat{\sigma}_{\mu_1,q_1p_1}\,\ldots\,\hat{\sigma}_{\mu_K,q_Kp_K}\,\hat{\rho}(t)\right] = \frac{N!}{(N-K)!}\left\langle\frac{\rho'_{p_1q_1}(t)}{\sum_i\rho'_{ii}(t)}\,\ldots\,\frac{\rho'_{p_Kq_K}(t)}{\sum_i\rho'_{ii}(t)}\right\rangle.$$

This formulation motivates the following final change of variables:

$$\rho_{pq}(t) = \frac{\rho'_{pq}(t)}{\sum_s \rho'_{ss}(t)}. \tag{III.61}$$

To derive equations for the new variables $\rho_{pq}(t)$, we employ Itô's lemma, which states that the total time derivative of a function $\Phi(\{\rho_{ij}(t)\}, t)$ of stochastic variables gains an additional term due to correlations between them:

$$\frac{d\Phi}{dt} = \frac{\partial\Phi}{\partial t} + \sum_{p,q} \frac{\partial\Phi}{\partial\rho'_{pq}} \frac{d\rho'_{pq}}{dt} + \frac{1}{2} \sum_{p,q,p',q'} \frac{\partial^2\Phi}{\partial\rho'_{pq}\partial\rho'_{p'q'}} \mathscr{D}_{pqp'q'}. \tag{III.62}$$

Applying Itô's lemma to the variables $\rho_{pq}(t)$ in Eq. (III.61), we derive the following stochastic equations:

$$\frac{d\rho_{pq}(t)}{dt} = \mathscr{A}_{pq}(\{\rho_{ij}(t)\}) + (N-1) \sum_n \mathscr{D}_{pqnn}(\{\rho_{ij}(t)\}) + F_{pq}(\{\rho_{ij}(t)\}, t) - \rho_{pq}(t) \sum_s F_{ss}(\{\rho_{ij}(t)\}, t).$$

These equations are discussed in the main text, see Eq. (III.17a) and subsequent discussion. This completes the process of eliminating the η-object and deriving the stochastic variables for N particles.

Notably, the appearance of additional noise terms changes the diffusion matrix of the Fokker-Planck equation, which now becomes:

$$\widetilde{\mathscr{D}}_{pqp'q'} = \sum_{n,\ell,n',\ell'} (\delta_{np}\,\delta_{q\ell} - \delta_{n\ell}\,\rho_{pq})\,\mathscr{D}_{pqp'q'}\,(\delta_{n'p'}\,\delta_{q'\ell'} - \delta_{n'\ell'}\,\rho_{p'q'}).$$

5.4 Stochastic Drift Gauges

In this section, we discuss stochastic drift gauges from the perspective of the Fokker-Planck equation [101]. We begin with the probability density function $P(\{x_i\}, t)$, which satisfies the Fokker-Planck equation:

$$\frac{\partial P(\{x_i\}, t)}{\partial t} = -\sum_p \frac{\partial}{\partial x_p}\Big[\mathscr{A}_p(\{x_i\})\,P(\{x_i\}, t)\Big] + \frac{1}{2}\sum_{p,q} \frac{\partial^2}{\partial x_p\,\partial x_q}\Big[\mathscr{D}_{pq}(\{x_i\})\,P(\{x_i\}, t)\Big],$$

where $\mathscr{D}_{pq}(\{x_i\}) \equiv \mathscr{D}_{qp}(\{x_i\})$. The concept of stochastic drift gauges involves modifying the drift components and introducing a weight function to compensate for these changes. Since we are only concerned with averages, these modifications are designed to leave expectation values unaffected.

We introduce a new function $P(\{x_i, C_0\}, t)$, which includes an additional variable C_0 and relates to the original function via the integral over C_0 with the weight e^{C_0}:

$$P(\{x_i\}, t) = \int d^2C_0\; e^{C_0}\; P(\{x_i, C_0\}, t). \tag{III.63}$$

By construction, the average of any function $f(\{x_i\})$, independent of C_0, remains unchanged regardless of the probability density function used:

$$\frac{\int \prod_i (d^2x_i)\; f(\{x_i\})\; P(\{x_i\}, t)}{\int \prod_i (d^2x_i)\; P(\{x_i\}, t)} \equiv \frac{\int d^2C_0 \int \prod_i (d^2x_i)\; e^{C_0}\; f(\{x_i\})\; P(\{x_i, C_0\}, t)}{\int d^2C_0 \int \prod_i (d^2x_i)\; e^{C_0}\; P(\{x_i, C_0\}, t)}.$$

In stochastic equations, the factor e^{C_0} assigns specific weights to trajectories.

To ensure identical expectation values for $P(\{x_i\},t)$ and $P(\{x_i,C_0\},t)$, the latter must satisfy a specific Fokker-Planck equation, which permits freedom in choosing the diffusion matrix elements, $\mathscr{D}_p(\{x_i\})$, between x_i and C_0. These functions should be independent of C_0. Then, the Fokker-Planck equation for $P(\{x_i,C_0\},t)$ has the form:

$$\begin{aligned}\frac{\partial P(\{x_i,C_0\},t)}{\partial t} &= -\sum_p \frac{\partial}{\partial x_p}\Big[\{\mathscr{A}_p(\{x_i\}) - \mathscr{D}_p(\{x_i\})\}\,P(\{x_i,C_0\},t)\Big] \\ &\quad -\frac{\partial}{\partial C_0}\Big[\mathscr{A}(\{x_i\})\,P(\{x_i,C_0\},t)\Big] \\ +\frac{1}{2}\sum_{p,q}\frac{\partial^2}{\partial x_p\,\partial x_q}\Big[\mathscr{D}_{pq}(\{x_i\})\,P(\{x_i,C_0\},t)\Big] &+ \sum_p \frac{\partial^2}{\partial C_0\,\partial x_p}\Big[\mathscr{D}_p(\{x_i\})\,P(\{x_i,C_0\},t)\Big] \\ &\quad +\frac{1}{2}\frac{\partial^2}{\partial C_0^2}\Big[\mathscr{D}(\{x_i\})\,P(\{x_i,C_0\},t)\Big].\end{aligned}$$

where $\mathscr{D}(\{x_i\}) = -2\mathscr{A}(\{x_i\})$. The functions $\mathscr{D}_p(\{x_i\})$, which modify the drift of the original variables $\{x_i\}$, are freely chosen. The functions $\mathscr{D}(\{x_i\})$ and $\mathscr{A}(\{x_i\})$ are derived from the noise terms in the equation for $C_0(t)$.

The original stochastic equations associated with $P(\{x_i\},t)$ are:

$$\frac{dx_p(t)}{dt} = \mathscr{A}_p(\{x_i(t)\}) + F_p(\{x_i(t)\},t), \tag{III.64}$$

where noise terms satisfy $\langle F_p(\{x_i\},t)\,F_{p'}(\{x_i\},t')\rangle = \mathscr{D}_{pp'}(\{x_i\})\,\delta(t-t')$. When transitioning to the new function $P(\{x_i',C_0\},t)$, the equations transform into:

$$\frac{dx_p'(t)}{dt} = \mathscr{A}_p(\{x_i'(t)\}) - \mathscr{D}_p(\{x_i'(t)\}) + F_p(\{x_i'(t)\},t), \tag{III.65a}$$

$$\frac{dC_0(t)}{dt} = \mathscr{A}(\{x_i'(t)\}) + F(\{x_i'(t)\},t), \tag{III.65b}$$

with noise correlations:

$$\langle F_p(\{x_i'\},t)\,F_{p'}(\{x_i'\},t')\rangle = \mathscr{D}_{pp'}(\{x_i'\})\,\delta(t-t'), \tag{III.65c}$$

$$\langle F(\{x_i'\},t)\,F_p(\{x_i'\},t')\rangle = \mathscr{D}_p(\{x_i'\})\,\delta(t-t'), \tag{III.65d}$$

$$\langle F(\{x_i'\},t)\,F(\{x_i'\},t')\rangle = -2\mathscr{A}(\{x_i'\})\,\delta(t-t'). \tag{III.65e}$$

The averages using old and new variables are connected as:

$$\langle f(\{x_i(t)\})\rangle = \frac{\langle f(\{x_i'(t)\})\,e^{C_0(t)}\rangle}{\langle e^{C_0(t)}\rangle}, \tag{III.65f}$$

where the brackets $\langle\ldots\rangle$ denote averaging over the respective stochastic realizations.

Chapter IV

Conclusion and Outlook

In this dissertation, we developed and tested two theoretical frameworks for modeling cooperative emission in many-body quantum systems. The first, based on the second quantization of density matrices in Liouville space, provides a computationally efficient method for studying permutation-invariant systems with incoherent processes, enabling the analysis of small to medium-sized quantum systems.

Building on this foundation, the second framework extends the positive P representation to open systems of emitters. By describing the dynamics in terms of phase-space variables, it removes the dependence of computational complexity on the number of emitters. This approach enables the sampling of quantum expectation values through stochastic trajectories, making it well-suited for analyzing macroscopic, realistic systems.

A key limitation of the stochastic approach is its numerical stability. Noise terms are effective when they act as triggers and push the system toward a predominantly semiclassical regime. However, if the noise terms have a dominating effect, they can destabilize the equations, leading to incorrect averages. As a result, while the mapping between quantum and stochastic descriptions is theoretically exact, the stochastic framework is not exact in practice.

Several opportunities to extend our second-quantization framework are discussed throughout the main text. In Sec. 4.1 of Chapter II, we show how fermionic states can be constructed using bosonic superoperators. Sec. 4.4 illustrates how the framework can be used in analyzing correlations within ensembles of identical particles, offering a potential tool for quantum information applications. Additionally, Sec. 4.3 extends the formalism to non-identical particles and Bose-Hubbard models. While the framework provides limited computational advantages in these cases, it can be combined with other approaches, such as tensor networks [172, 173], or integrated with stochastic methods, as discussed in Chapter III.

The extension of the stochastic method to spatially distributed systems is discussed in Secs. 3.5 and 3.6 of Chapter III. However, the solution is inexact due to the extreme instability of the weight function, which was omitted from our calculations. This omission may introduce errors in the initial stages of the process, where spontaneous emission plays a defining role. These issues become more pronounced in multi-color processes, as stabilizing the fields for different carrier frequencies is necessary. Neglecting the weight function in such cases leads to greater inaccuracies. Nonetheless, for two-band level structures, Ref. [198] presents a refined approach that provides a perturbative treatment of the noise terms. This method avoids instabilities and produces reliable results when the noise terms are small compared to the dissipation rates or stimulated emission.

A possible improvement to the stochastic approach involves finding an appropriate gauge to stabilize trajectories when encountering subradiant states within compact systems. These steady states, which represent many-body dark states, are of significant interest in quantum information applications due to their long-lived nature [157, 202]. Moreover, this class of steady states can potentially be exploited to engineer non-stationary dynamics [156]. While the second-quantization method reliably captures subradiance, the stochastic equations we analyzed fail in this challenging regime.

For similar reasons, stochastic equations for systems of emitters interacting with a few quantized cavity modes achieve stability only in cavities with high loss rates. This creates an opportunity to analyze open Dicke models within the stochastic approach. However, capturing strong-coupling effects requires a more effective regularization, which remains an open question in terms of both existence and practical implementation.

Exploring alternative phase-space representations is an intriguing avenue for future research. Identifying a suitable unity expansion within the Liouville-Hilbert space would enable the construction of various representations for the density matrix supervector, analogous to conventional phase-space distribution functions. Investigating the potential advantages and challenges of such representations could provide valuable insights. However, this research lies beyond the scope of this dissertation.

In all applications of the stochastic methodology, we have assumed fully factorized initial conditions. This means that, at the initial moment, all emitters are uncorrelated, the field modes are uncorrelated, and no correlations exist between the emitters and the fields. If the initial state includes correlations (e.g., non-classical states), the method must be generalized to account for them. This generalization would require determining appropriate distributions for the initial states and developing efficient sampling techniques.

Beyond the examples discussed in this dissertation, our stochastic method holds promise for modeling non-Markovian dynamics in high-dimensional systems, for example, as in Ref. [203]. The method significantly reduces the number of degrees of freedom, enabling parallelized computation. Unlike existing approaches to solving non-Markovian stochastic Schrödinger equations, which typically model the bath stochastically, our method reformulates all degrees of freedom through stochastic sampling. However, challenges related to unstable realizations may still arise.

While we have primarily focused on superradiance, subradiance, and cavity dynamics, it would be intriguing to model quantum systems strongly driven by quantum light sources, investigate other nonlinear x-ray phenomena such as collective electronic Raman scattering in molecules, and explore practical applications like pulse shaping or light generation through nonlinear crystals. Additionally, it would be interesting to determine whether these methods can offer new insights into Bose-Einstein condensates, which have already been extensively studied using stochastic equations [102].

Overall, this work represents a significant effort in analyzing and developing broadly applicable methods. In its current form, it can be used to model superradiance and cavity-mediated dynamics, enabling, for example, the simulation of superradiant lasing operating in various regimes. Its applicability extends to ensembles of dipole-dipole interacting emitters arranged in arrays or lattices, as well as single-photon superradiance.

We hope these methods will be useful in many problems beyond those addressed in this dissertation, and we wish good luck and inspiration to those striving to break the curse of dimensionality and regularize stochastic trajectories.

Acknowledgment

I would like to express my sincere gratitude to Prof. Nina Rohringer for giving me the opportunity to conduct this research and complete my doctoral studies. Our collaboration began when I was a summer student at DESY, and since then, she has been a constant source of support and mentorship.

A special thank you to my colleague and friend, Stasis Chuchurka, with whom I have co-authored numerous papers and spent countless days immersed in research. His support, contributions, and dedication have been instrumental in shaping this work.

I extend my appreciation to Nicola Baark, whose help has been invaluable. Thanks to her professionalism and friendliness, many problems that seemed unsolvable were resolved in an instant.

I am also grateful to the other members of our group. I appreciate Andrei Benediktovitch and Aliaksandr Leonau for our long and fruitful discussions. I am thankful to Emanuele Rossi for our conversations, not only about physics and chemistry but also about art, history, and cinema. A huge thank you to Daniele Ronchetti for his camaraderie, our joint experiments, and for helping me survive the slopes of the Alps by teaching me the basics of skiing.

My deep gratitude goes to Dietrich Krebs and Christina Bömer for their unwavering support, guidance, and willingness to help. I am also thankful to Fridtjof Kerker, Xenia Brockmüller, Maria Weseloh, Gemma Douilhet, Milaim Kas, and Alessandra Picchiotti for their encouragement and for fostering a friendly atmosphere in the office.

I am grateful to the University of Hamburg, particularly the Faculty of Mathematics, Informatics, and Natural Sciences. My sincere thanks go to Dr. Mathias Trabs and Prof. Armin Iske for their support.

A special acknowledgment goes to Dietrich Krebs and Christina Bömer for their insightful critique of my dissertation introduction and their proofreading of several manuscripts associated with this work.

I also wish to acknowledge the support of DASHH and CUI, especially Heike Hufnagel Martinez, Christiane Ehrt, Jutta Voigtmann, and my fellow students.

I am deeply grateful to Prof. Dieter Jaksch for the opportunity to present my work to his group and for the valuable feedback I received. Special thanks to Dr. Frank Schlawin for discussions, his thoughtful insights, and his help.

Finally, I express my heartfelt appreciation to everyone who has supported and inspired me throughout this journey—most especially, my mother, Elena, and my brother, Konstantin.

Bibliography

[1] Robert H Dicke. Coherence in spontaneous radiation processes. Physical Review, 93(1):99, 1954. doi:10.1103/PhysRev.93.99.

[2] R. H. Dicke. The Coherence Brightened Laser. In I. Agarbiceanu, A. Agafitei, L. Blanaru, N. Ionescu-Pallas, I. M. Popescu, V. Vasiliu, and V. G. Velculescu, editors, Quantum Electronics, page 35, January 1964.

[3] Joseph H. Eberly. Superradiance Revisited. American Journal of Physics, 40(10):1374–1383, October 1972. doi:10.1119/1.1986858.

[4] Lewi Tonks. Photon Avalanches from a Population Inversion. Journal of Applied Physics, 35(4):1134–1141, April 1964. doi:10.1063/1.1713580.

[5] G. Banfi and R. Bonifacio. Superfluorescence and cooperative frequency shift. Physical Review A, 12(5):2068–2082, November 1975. doi:10.1103/physreva.12.2068.

[6] R. Bonifacio and L. A. Lugiato. Cooperative radiation processes in two-level systems: Superfluorescence. Physical Review A, 11(5):1507–1521, May 1975. doi:10.1103/physreva.11.1507.

[7] R. Bonifacio and L. A. Lugiato. Cooperative radiation processes in two-level systems: Superfluorescence. II. Physical Review A, 12(2):587–598, August 1975. doi:10.1103/physreva.12.587.

[8] L. Allen and G.I. Peters. Superradiance, coherence brightening and amplified spontaneous emission. Physics Letters A, 31(3):95–96, February 1970. doi:10.1016/0375-9601(70)90168-4.

[9] Michel Gross and Serge Haroche. Superradiance: An essay on the theory of collective spontaneous emission. Physics reports, 93(5):301–396, 1982. doi:10.1016/0370-1573(82)90102-8.

[10] Barry M Garraway. The Dicke model in quantum optics: Dicke model revisited. Philosophical Transactions of the Royal Society A: Mathematical, Physical and Engineering Sciences, 369(1939):1137–1155, 2011. doi:10.1098/rsta.2010.0333.

[11] Peter Kirton, Mor M. Roses, Jonathan Keeling, and Emanuele G. Dalla Torre. Introduction to the Dicke Model: From Equilibrium to Nonequilibrium, and Vice Versa. Advanced Quantum Technologies, 2(1–2), October 2018. doi:10.1002/qute.201800043.

[12] Michael Tavis and Frederick W Cummings. Exact solution for an N-molecule—radiation-field Hamiltonian. Physical Review, 170(2):379, 1968. doi:10.1103/PhysRev.170.379.

[13] J. Larson and T. Mavrogordatos. The Jaynes-Cummings Model and Its Descendants. IOP Publishing, December 2021. doi:10.1088/978-0-7503-3447-1.

[14] Y. K. Wang and F. T. Hioe. Phase Transition in the Dicke Model of Superradiance. Physical Review A, 7(3):831–836, March 1973. doi:10.1103/physreva.7.831.

[15] Klaus Hepp and Elliott H. Lieb. Equilibrium Statistical Mechanics of Matter Interacting with the Quantized Radiation Field. Physical Review A, 8(5):2517–2525, November 1973. doi:10.1103/physreva.8.2517.

[16] N. Skribanowitz, I. P. Herman, J. C. MacGillivray, and M. S. Feld. Observation of Dicke Superradiance in Optically Pumped HF Gas. Physical Review Letters, 30(8):309–312, February 1973. doi:10.1103/physrevlett.30.309.

[17] I. P. Herman, J. C. MacGillivray, N. Skribanowitz, and M. S. Feld. Self-Induced Emission in Optically Pumped HF Gas: The Rise and Fall of the Superradiant State. In Laser Spectroscopy, page 379–412. Springer US, 1974. doi:10.1007/978-1-4613-4517-6_28.

[18] M. Gross, C. Fabre, P. Pillet, and S. Haroche. Observation of Near-Infrared Dicke Superradiance on Cascading Transitions in Atomic Sodium. Physical Review Letters, 36(17):1035–1038, April 1976. doi:10.1103/physrevlett.36.1035.

[19] Ph. Cahuzac, H. Sontag, and P.E. Toschek. Visible superfluorescence from atomic europium. Optics Communications, 31(1):37–41, October 1979. doi:10.1016/0030-4018(79)90239-6.

[20] JM Raimond, P Goy, M Gross, C Fabre, and S Haroche. Statistics of millimeter-wave photons emitted by a Rydberg-atom maser: An experimental study of fluctuations in single-mode superradiance. Physical Review Letters, 49(26):1924, 1982. doi:10.1103/PhysRevLett.49.1924.

[21] Kankan Cong, Qi Zhang, Yongrui Wang, G. Timothy Noe, Alexey Belyanin, and Junichiro Kono. Dicke superradiance in solids. Journal of the Optical Society of America B, 33(7):C80, May 2016. doi:10.1364/josab.33.000c80.

[22] R. Florian, L.O. Schwan, and D. Schmid. Superradiance and high-gain mirrorless laser activity of O_2^--centers in KCl. Solid State Communications, 42(1):55–57, April 1982. doi:10.1016/0038-1098(82)91028-6.

[23] Reinhold Florian, Lothar O. Schwan, and Dankward Schmid. Time-resolving experiments on Dicke superfluorescence of O_2^- centers in KCl. Two-color superfluorescence. Physical Review A, 29(5):2709–2715, May 1984. doi:10.1103/physreva.29.2709.

[24] Michelle S. Malcuit, Jeffery J. Maki, David J. Simkin, and Robert W. Boyd. Transition from superfluorescence to amplified spontaneous emission. Physical Review Letters, 59(11):1189–1192, September 1987. doi:10.1103/physrevlett.59.1189.

[25] Frank C. Spano and Shaul Mukamel. Superradiance in molecular aggregates. The Journal of Chemical Physics, 91(2):683–700, July 1989. doi:10.1063/1.457174.

[26] Steven De Boer and Douwe A. Wiersma. Dephasing-induced damping of superradiant emission in J-aggregates. Chemical Physics Letters, 165(1):45–53, January 1990. doi:10.1016/0009-2614(90)87010-o.

[27] Henk Fidder, Jasper Knoester, and Douwe A. Wiersma. Superradiant emission and optical dephasing in J-aggregates. Chemical Physics Letters, 171(5–6):529–536, August 1990. doi:10.1016/0009-2614(90)85258-e.

[28] Gabriele Rainò, Michael A. Becker, Maryna I. Bodnarchuk, Rainer F. Mahrt, Maksym V. Kovalenko, and Thilo Stöferle. Superfluorescence from lead halide perovskite quantum dot superlattices. Nature, 563(7733):671–675, November 2018. doi:10.1038/s41586-018-0683-0.

[29] Carlo Bradac, Mattias T. Johnsson, Matthew van Breugel, Ben Q. Baragiola, Rochelle Martin, Mathieu L. Juan, Gavin K. Brennen, and Thomas Volz. Room-temperature spontaneous superradiance from single diamond nanocrystals. Nature Communications, 8(1), October 2017. doi:10.1038/s41467-017-01397-4.

[30] Michael Scheibner, Thomas Schmidt, Lukas Worschech, Alfred Forchel, Gerd Bacher, Thorsten Passow, and Detlef Hommel. Superradiance of quantum dots. Nature Physics, 3(2):106–110, January 2007. doi:10.1038/nphys494.

[31] Daria D. Blach, Victoria A. Lumsargis, Daniel E. Clark, Chern Chuang, Kang Wang, Letian Dou, Richard D. Schaller, Jianshu Cao, Christina W. Li, and Libai Huang. Superradiance and Exciton Delocalization in Perovskite Quantum Dot Superlattices. Nano Letters, 22(19):7811–7818, September 2022. doi:10.1021/acs.nanolett.2c02427.

[32] Chenglian Zhu, Simon C. Boehme, Leon G. Feld, Anastasiia Moskalenko, Dmitry N. Dirin, Rainer F. Mahrt, Thilo Stöferle, Maryna I. Bodnarchuk, Alexander L. Efros, Peter C. Sercel, Maksym V. Kovalenko, and Gabriele Rainò. Single-photon superradiance in individual caesium lead halide quantum dots. Nature, 626(7999):535–541, January 2024. doi:10.1038/s41586-023-07001-8.

[33] Christian Liedl, Felix Tebbenjohanns, Constanze Bach, Sebastian Pucher, Arno Rauschenbeutel, and Philipp Schneeweiss. Observation of Superradiant Bursts in a Cascaded Quantum System. Physical Review X, 14(1), February 2024. doi:10.1103/physrevx.14.011020.

[34] David D. Grimes, Stephen L. Coy, Timothy J. Barnum, Yan Zhou, Susanne F. Yelin, and Robert W. Field. Direct single-shot observation of millimeter-wave superradiance in Rydberg-Rydberg transitions. Physical Review A, 95(4), April 2017. doi:10.1103/physreva.95.043818.

[35] Mitsuru Nagasono, James R. Harries, Hiroshi Iwayama, Tadashi Togashi, Kensuke Tono, Makina Yabashi, Yasunori Senba, Haruhiko Ohashi, Tetsuya Ishikawa, and Eiji Shigemasa. Observation of Free-Electron-Laser-Induced Collective Spontaneous Emission (Superfluorescence). Physical Review Letters, 107(19), November 2011. doi:10.1103/physrevlett.107.193603.

[36] James R. Harries, Hiroshi Iwayama, Susumu Kuma, Masatomi Iizawa, Norihiro Suzuki, Yoshiro Azuma, Ichiro Inoue, Shigeki Owada, Tadashi Togashi, Kensuke Tono, Makina Yabashi, and Eiji Shigemasa. Superfluorescence, Free-Induction Decay, and Four-Wave Mixing: Propagation of Free-Electron Laser Pulses through a Dense Sample of Helium Ions. Physical Review Letters, 121(26), December 2018. doi:10.1103/physrevlett.121.263201.

[37] L. Mercadier, A. Benediktovitch, C. Weninger, M. A. Blessenohl, S. Bernitt, H. Bekker, S. Dobrodey, A. Sanchez-Gonzalez, B. Erk, C. Bomme, R. Boll, Z. Yin, V. P. Majety, R. Steinbrügge, M. A. Khalal, F. Penent, J. Palaudoux, P. Lablanquie, A. Rudenko, D. Rolles, J. R. Crespo López-Urrutia, and N. Rohringer. Evidence of extreme ultraviolet superfluorescence in xenon. Physical Review Letters, 123(2), July 2019. doi:10.1103/physrevlett.123.023201.

[38] Nina Rohringer, Duncan Ryan, Richard A. London, Michael Purvis, Felicie Albert, James Dunn, John D. Bozek, Christoph Bostedt, Alexander Graf, Randal Hill, Stefan P. Hau-Riege, and Jorge J. Rocca. Atomic inner-shell X-ray laser at 1.46 nanometres pumped by an X-ray free-electron laser. Nature, 481(7382):488–491, January 2012. doi:10.1038/nature10721.

[39] Hitoki Yoneda, Yuichi Inubushi, Kazunori Nagamine, Yurina Michine, Haruhiko Ohashi, Hirokatsu Yumoto, Kazuto Yamauchi, Hidekazu Mimura, Hikaru Kitamura, Tetsuo Katayama, Tetsuya Ishikawa, and Makina Yabashi. Atomic inner-shell laser at 1.5-ångström wavelength pumped by an X-ray free-electron laser. Nature, 524(7566):446–449, August 2015. doi:10.1038/nature14894.

[40] Thomas Kroll, Clemens Weninger, Roberto Alonso-Mori, Dimosthenis Sokaras, Diling Zhu, Laurent Mercadier, Vinay P. Majety, Agostino Marinelli, Alberto Lutman, Marc W. Guetg, Franz-Josef Decker, Sébastien Boutet, Andy Aquila, Jason Koglin, Jake Koralek, Daniel P. DePonte, Jan Kern, Franklin D. Fuller, Ernest Pastor, Thomas Fransson, Yu Zhang, Junko Yano, Vittal K. Yachandra, Nina Rohringer, and Uwe Bergmann. Stimulated X-Ray Emission Spectroscopy in Transition Metal Complexes. Physical Review Letters, 120(13), March 2018. doi:10.1103/physrevlett.120.133203.

[41] Ralf Röhlsberger, Kai Schlage, Balaram Sahoo, Sebastien Couet, and Rudolf Rüffer. Collective Lamb Shift in Single-Photon Superradiance. Science, 328(5983):1248–1251, June 2010. doi:10.1126/science.1187770.

[42] Aleksandr I. Chumakov, Alfred Q. R. Baron, Ilya Sergueev, Cornelius Strohm, Olaf Leupold, Yuri Shvyd'ko, Gennadi V. Smirnov, Rudolf Rüffer, Yuichi Inubushi, Makina Yabashi, Kensuke Tono, Togo Kudo, and Tetsuya Ishikawa. Superradiance of an ensemble of nuclei excited by a free electron laser. Nature Physics, 14(3):261–264, November 2017. doi:10.1038/s41567-017-0001-z.

[43] Uwe Bergmann, Jan Kern, Robert W. Schoenlein, Philippe Wernet, Vittal K. Yachandra, and Junko Yano. Using X-ray free-electron lasers for spectroscopy of molecular catalysts and metalloenzymes. Nature Reviews Physics, 3(4):264–282, March 2021. doi:10.1038/s42254-021-00289-3.

[44] Shaul Mukamel, Daniel Healion, Yu Zhang, and Jason D. Biggs. Multidimensional Attosecond Resonant X-Ray Spectroscopy of Molecules: Lessons from the Optical Regime. Annual Review of Physical Chemistry, 64(1):101–127, April 2013. doi:10.1146/annurev-physchem-040412-110021.

[45] Aliaksei Halavanau, Andrei Benediktovitch, Alberto A. Lutman, Daniel DePonte, Daniele Cocco, Nina Rohringer, Uwe Bergmann, and Claudio Pellegrini. Population inversion X-ray laser oscillator. Proceedings of the National Academy of Sciences, 117(27):15511–15516, June 2020. doi:10.1073/pnas.2005360117.

[46] Justin G. Bohnet, Zilong Chen, Joshua M. Weiner, Dominic Meiser, Murray J. Holland, and James K. Thompson. A steady-state superradiant laser with less than one intracavity photon. Nature, 484(7392):78–81, April 2012. doi:10.1038/nature10920.

[47] Haonan Liu, Simon B. Jäger, Xianquan Yu, Steven Touzard, Athreya Shankar, Murray J. Holland, and Travis L. Nicholson. Rugged mHz-Linewidth Superradiant Laser Driven by a Hot Atomic Beam. Physical Review Letters, 125(25), December 2020. doi:10.1103/physrevlett.125.253602.

[48] Maximilian Pallmann, Kerim Köster, Yuan Zhang, Julia Heupel, Timon Eichhorn, Cyril Popov, Klaus Mølmer, and David Hunger. Cavity-Mediated Collective Emission from Few Emitters in a Diamond Membrane. Physical Review X, 14(4), December 2024. doi:10.1103/physrevx.14.041055.

[49] R. Bonifacio, P. Schwendimann, and Fritz Haake. Quantum Statistical Theory of Superradiance. I. Physical Review A, 4(1):302–313, July 1971. doi:10.1103/physreva.4.302.

[50] R. Bonifacio, P. Schwendimann, and Fritz Haake. Quantum Statistical Theory of Superradiance. II. Physical Review A, 4(3):854–864, September 1971. doi:10.1103/physreva.4.854.

[51] F. T. Arecchi and Eric Courtens. Cooperative Phenomena in Resonant Electromagnetic Propagation. Physical Review A, 2(5):1730–1737, November 1970. doi:10.1103/physreva.2.1730.

[52] F. Bloch. Nuclear Induction. Physical Review, 70(7–8):460–474, October 1946. doi:10.1103/physrev.70.460.

[53] R. H. Lehmberg. Radiation from an N-Atom System. I. General Formalism. Physical Review A, 2(3):883–888, September 1970. doi:10.1103/physreva.2.883.

[54] R. H. Lehmberg. Radiation from an N-Atom System. II. Spontaneous Emission from a Pair of Atoms. Physical Review A, 2(3):889–896, September 1970. doi:10.1103/physreva.2.889.

[55] R. Friedberg, S.R. Hartmann, and J.T. Manassah. Frequency shifts in emission and absorption by resonant systems ot two-level atoms. Physics Reports, 7(3):101–179, March 1973. doi:10.1016/0370-1573(73)90001-x.

[56] Jamal T. Manassah. Cooperative radiation from atoms in different geometries: decay rate and frequency shift. Advances in Optics and Photonics, 4(2):108, June 2012. doi:10.1364/aop.4.000108.

[57] GS Agarwal. Master-equation approach to spontaneous emission. Physical Review A, 2(5):2038, 1970. doi:10.1103/PhysRevA.2.2038.

[58] Sanaa Agarwal, Edwin Chaparro, Diego Barberena, A. Piñeiro Orioli, G. Ferioli, S. Pancaldi, I. Ferrier-Barbut, A. Browaeys, and A.M. Rey. Directional Superradiance in a Driven Ultracold Atomic Gas in Free Space. PRX Quantum, 5(4), December 2024. doi:10.1103/prxquantum.5.040335.

[59] Stuart J. Masson and Ana Asenjo-Garcia. Universality of Dicke superradiance in arrays of quantum emitters. Nature Communications, 13(1), April 2022. doi:10.1038/s41467-022-29805-4.

[60] Marlan O. Scully, Edward S. Fry, C. H. Raymond Ooi, and Krzysztof Wódkiewicz. Directed Spontaneous Emission from an Extended Ensemble of N Atoms: Timing Is Everything. Physical Review Letters, 96(1), January 2006. doi:10.1103/physrevlett.96.010501.

[61] Marlan O. Scully. Single Photon Subradiance: Quantum Control of Spontaneous Emission and Ultrafast Readout. Physical Review Letters, 115(24), December 2015. doi:10.1103/physrevlett.115.243602.

[62] S. J. Roof, K. J. Kemp, M. D. Havey, and I. M. Sokolov. Observation of Single-Photon Superradiance and the Cooperative Lamb Shift in an Extended Sample of Cold Atoms. Physical Review Letters, 117(7), August 2016. doi:10.1103/physrevlett.117.073003.

[63] Marlan O. Scully. Collective Lamb Shift in Single Photon Dicke Superradiance. Physical Review Letters, 102(14), April 2009. doi:10.1103/physrevlett.102.143601.

[64] Aviv Karnieli, Nicholas Rivera, Ady Arie, and Ido Kaminer. Superradiance and Subradiance due to Quantum Interference of Entangled Free Electrons. Physical Review Letters, 127(6), August 2021. doi:10.1103/physrevlett.127.060403.

[65] M. G. Benedict, A. M. Ermolaev, V. A. Malyshev, I. V. Sokolov, and E. D. Trifonov. Super-radiance. CRC Press, 2018. doi:10.1201/9780203737880.

[66] Q. H. F. Vrehen and M. F. H. Schuurmans. Direct Measurement of the Effective Initial Tipping Angle in Superfluorescence. Physical Review Letters, 42(4):224–227, January 1979. doi:10.1103/physrevlett.42.224.

[67] D. Polder, M. F. H. Schuurmans, and Q. H. F. Vrehen. Superfluorescence: Quantum-mechanical derivation of maxwell-bloch description with fluctuating field source. Physical Review A, 19(3):1192–1203, March 1979. doi:10.1103/physreva.19.1192.

[68] J. C. MacGillivray and M. S. Feld. Theory of superradiance in an extended, optically thick medium. Physical Review A, 14(3):1169–1189, September 1976. doi:10.1103/physreva.14.1169.

[69] J. A. Fleck. Ultrashort-Pulse Generation by Q-Switched Lasers. Physical Review B, 1(1):84–100, January 1970. doi:10.1103/physrevb.1.84.

[70] O. Larroche, D. Ros, A. Klisnick, A. Sureau, C. Möller, and H. Guennou. Maxwell-Bloch modeling of x-ray-laser-signal buildup in single- and double-pass configurations. Physical Review A, 62(4), September 2000. doi:10.1103/physreva.62.043815.

[71] Clemens Weninger and Nina Rohringer. Transient-gain photoionization x-ray laser. Physical Review A, 90(6), December 2014. doi:10.1103/physreva.90.063828.

[72] Victor Kimberg, Song Bin Zhang, and Nina Rohringer. X-ray lasing in the CO molecule. Journal of Physics B: Atomic, Molecular and Optical Physics, 46(16):164017, August 2013. doi:10.1088/0953-4075/46/16/164017.

[73] Victor Kimberg and Nina Rohringer. Amplified X-Ray Emission from Core-Ionized Diatomic Molecules. Physical Review Letters, 110(4), January 2013. doi:10.1103/physrevlett.110.043901.

[74] Chiaki Ohae, James R. Harries, Hiroshi Iwayama, Kentarou Kawaguchi, Susumu Kuma, Yuki Miyamoto, Mitsuru Nagasono, Kyo Nakajima, Itsuo Nakano, Eiji Shigemasa, Noboru Sasao, Satoshi Uetake, Tomonari Wakabayashi, Akihiro Yoshimi, Koji Yoshimura, and Motohiko Yoshimura. Simultaneous Measurements of Superradiance at Multiple Wavelength from Helium Excited States: II. Analysis. Journal of the Physical Society of Japan, 85(3):034301, March 2016. doi:10.7566/jpsj.85.034301.

[75] G.M. Slavcheva, J.M. Arnold, and R.W. Ziolkowski. FDTD Simulation of the Nonlinear Gain Dynamics in Active Optical Waveguides and Semiconductor Microcavities. IEEE Journal of Selected Topics in Quantum Electronics, 10(5):1052–1062, September 2004. doi:10.1109/jstqe.2004.836023.

[76] Andrei Benediktovitch, Vinay P. Majety, and Nina Rohringer. Quantum theory of superfluorescence based on two-point correlation functions. Physical Review A, 99(1):013839, January 2019. doi:10.1103/PhysRevA.99.013839.

[77] Gian Carlo Ghirardi, Philip Pearle, and Alberto Rimini. Markov processes in Hilbert space and continuous spontaneous localization of systems of identical particles. Physical Review A, 42(1):78–89, July 1990. doi:10.1103/physreva.42.78.

[78] Dariusz Gatarek and Nicolas Gisin. Continuous quantum jumps and infinite-dimensional stochastic equations. Journal of Mathematical Physics, 32(8):2152–2157, August 1991. doi:10.1063/1.529188.

[79] A Barchielli and V P Belavkin. Measurements continuous in time and a posteriori states in quantum mechanics. Journal of Physics A: Mathematical and General, 24(7):1495–1514, April 1991. doi:10.1088/0305-4470/24/7/022.

[80] N Gisin and I C Percival. The quantum-state diffusion model applied to open systems. Journal of Physics A: Mathematical and General, 25(21):5677–5691, November 1992. doi:10.1088/0305-4470/25/21/023.

[81] B. M. Garraway and P. L. Knight. Evolution of quantum superpositions in open environments: Quantum trajectories, jumps, and localization in phase space. Physical Review A, 50(3):2548–2563, September 1994. doi:10.1103/physreva.50.2548.

[82] Lajos Diósi and Walter T. Strunz. The non-Markovian stochastic Schrödinger equation for open systems. Physics Letters A, 235(6):569–573, November 1997. doi:10.1016/s0375-9601(97)00717-2.

[83] L. Diósi, N. Gisin, and W. T. Strunz. Non-Markovian quantum state diffusion. Physical Review A, 58(3):1699–1712, September 1998. doi:10.1103/physreva.58.1699.

[84] D. Suess, A. Eisfeld, and W. T. Strunz. Hierarchy of Stochastic Pure States for Open Quantum System Dynamics. Physical Review Letters, 113(15), October 2014. doi:10.1103/physrevlett.113.150403.

[85] Richard Hartmann and Walter T. Strunz. Exact Open Quantum System Dynamics Using the Hierarchy of Pure States (HOPS). Journal of Chemical Theory and Computation, 13(12):5834–5845, November 2017. doi:10.1021/acs.jctc.7b00751.

[86] D. Suess, W. T. Strunz, and A. Eisfeld. Hierarchical Equations for Open System Dynamics in Fermionic and Bosonic Environments. Journal of Statistical Physics, 159(6):1408–1423, March 2015. doi:10.1007/s10955-015-1236-7.

[87] C. W. Gardiner and M. J. Collett. Input and output in damped quantum systems: Quantum stochastic differential equations and the master equation. Physical Review A, 31(6):3761–3774, June 1985. doi:10.1103/physreva.31.3761.

[88] Crispin Gardiner and Peter Zoller. Quantum Noise. Springer Berlin, Heidelberg, 1985.

[89] M. J. Collett and C. W. Gardiner. Squeezing of intracavity and traveling-wave light fields produced in parametric amplification. Physical Review A, 30(3):1386–1391, September 1984. doi:10.1103/physreva.30.1386.

[90] Hai-Woong Lee. Theory and application of the quantum phase-space distribution functions. Physics Reports, 259(3):147–211, August 1995. doi:10.1016/0370-1573(95)00007-4.

[91] M. Hillery, R.F. O'Connell, M.O. Scully, and E.P. Wigner. Distribution functions in physics: Fundamentals. Physics Reports, 106(3):121–167, April 1984. doi:10.1016/0370-1573(84)90160-1.

[92] Wei-Min Zhang, Da Hsuan Feng, and Robert Gilmore. Coherent states: Theory and some applications. Reviews of Modern Physics, 62(4):867–927, October 1990. doi:10.1103/revmodphys.62.867.

[93] E. Wigner. On the Quantum Correction For Thermodynamic Equilibrium. Physical Review, 40(5):749–759, June 1932. doi:10.1103/physrev.40.749.

[94] Kôdi Husimi. Some formal properties of the density matrix. Proceedings of the Physico-Mathematical Society of Japan. 3rd Series, 22:264–314, 1940. doi:10.11429/ppmsj1919.22.4_264.

[95] E. C. G. Sudarshan. Equivalence of Semiclassical and Quantum Mechanical Descriptions of Statistical Light Beams. Physical Review Letters, 10(7):277–279, April 1963. doi:10.1103/physrevlett.10.277.

[96] Roy J. Glauber. Coherent and Incoherent States of the Radiation Field. Physical Review, 131(6):2766–2788, September 1963. doi:10.1103/physrev.131.2766.

[97] PD Drummond and CW Gardiner. Generalised P-representations in quantum optics. Journal of Physics A: Mathematical and General, 13(7):2353, 1980. doi:10.1088/0305-4470/13/7/018.

[98] PD Drummond and MG Raymer. Quantum theory of propagation of nonclassical radiation in a near-resonant medium. Physical Review A, 44(3):2072, 1991. doi:10.1103/PhysRevA.44.2072.

[99] Peter D Drummond and Mark Hillery. The quantum theory of nonlinear optics. Cambridge University Press, 2014. doi:10.1017/CBO9780511783616.

[100] P Deuar and P D Drummond. First-principles quantum dynamics in interacting Bose gases II: stochastic gauges. Journal of Physics A: Mathematical and General, 39(11):2723–2755, March 2006. doi:10.1088/0305-4470/39/11/011.

[101] Piotr Deuar. First-principles quantum simulations of many-mode open interacting Bose gases using stochastic gauge methods. arXiv:cond-mat/0507023, July 2005. arXiv: cond-mat/0507023. URL: http://arxiv.org/abs/cond-mat/0507023.

[102] Piotr Deuar, Alex Ferrier, Michał Matuszewski, Giuliano Orso, and Marzena H. Szymańska. Fully Quantum Scalable Description of Driven-Dissipative Lattice Models. PRX Quantum, 2(1), February 2021. doi:10.1103/prxquantum.2.010319.

[103] A. Gilchrist, C. W. Gardiner, and P. D. Drummond. Positive P representation: Application and validity. Physical Review A, 55(4):3014–3032, April 1997. doi:10.1103/physreva.55.3014.

[104] S Sarkar and J S Satchell. Solution of master equations for small bistable systems. Journal of Physics A: Mathematical and General, 20(8):2147–2157, June 1987. doi:10.1088/0305-4470/20/8/028.

[105] Michael Gegg and Marten Richter. Efficient and exact numerical approach for many multi-level systems in open system CQED. New Journal of Physics, 18(4):043037, 2016. doi:10.1088/1367-2630/18/4/043037.

[106] Michael Gegg. Identical Emitters, Collective Effects and Dissipation in Quantum Optics. Technische Universität Berlin, 2017. doi:10.14279/depositonce-6526.

[107] Michael Gegg and Marten Richter. PsiQuaSP – A library for efficient computation of symmetric open quantum systems. Scientific reports, 7(1):1–14, 2017. doi:10.1038/s41598-017-16178-8.

[108] V. Sukharnikov, S. Chuchurka, A. Benediktovitch, and N. Rohringer. Second quantization of open quantum systems in Liouville space. Physical Review A, 107(5), May 2023. doi:10.1103/physreva.107.053707.

[109] S. Chuchurka, V. Sukharnikov, A. Benediktovitch, and N. Rohringer. Stochastic modeling of superfluorescence in compact systems. Physical Review A, 110(5), November 2024. doi:10.1103/physreva.110.053703.

[110] U Fano. Liouville Representation of Quantum Mechanics with Application to Relaxation Processes. In Lectures on the Many-body Problems, pages 217–239. Academic Press, 1964. doi:10.1016/B978-0-12-395616-3.50017-6.

[111] Shaul Mukamel. Principles of nonlinear optical spectroscopy. Oxford Series in Optical & Imaging Sciences. Oxford University Press, New York, NY, September 1995.

[112] Marduk Bolaños and Pablo Barberis-Blostein. Algebraic solution of the Lindblad equation for a collection of multilevel systems coupled to independent environments. Journal of Physics A: Mathematical and Theoretical, 48(44):445301, 2015. doi:10.1088/1751-8113/48/44/445301.

[113] Claude Cohen-Tannoudji, Jacques Dupont-Roc, and Gilbert Grynberg. Photons and Atoms: Introduction to Quantum Electrodynamics. Wiley, March 1997. doi:10.1002/9783527618422.

[114] J. D. Jackson. From Lorenz to Coulomb and other explicit gauge transformations. American Journal of Physics, 70(9):917–928, August 2002. doi:10.1119/1.1491265.

[115] Kirk T. McDonald. The relation between expressions for time-dependent electromagnetic fields given by Jefimenko and by Panofsky and Phillips. American Journal of Physics, 65(11):1074–1076, November 1997. doi:10.1119/1.18723.

[116] V.B. Berestetskii, E.M. Lifshitz, and L.P. Pitaevskii. Quantum Electrodynamics, volume 4 of Course of Theoretical Physics. Pergamon Press, Oxford, 2nd edition, 1982.

[117] Peter W. Milonni. The Quantum Vacuum: An Introduction to Quantum Electrodynamics. Elsevier, 1994. doi:10.1016/C2009-0-21295-5.

[118] R. Guy Woolley. Power-Zienau-Woolley representations of nonrelativistic QED for atoms and molecules. Physical Review Research, 2(1), February 2020. doi:10.1103/physrevresearch.2.013206.

[119] Marlan O Scully and M Suhail Zubairy. Quantum optics, 1999. doi:10.1017/CBO9780511813993.

[120] E Ressayre and A Tallet. Markovian model for oscillatory superfluorescence. Physical Review A, 18(5):2196, 1978. doi:10.1103/PhysRevA.18.2196.

[121] Girish S Agarwal. Quantum statistical theories of spontaneous emission and their relation to other approaches. In Quantum Optics, pages 1–128. Springer, 1974. doi:10.1007/BFb0042382.

[122] Howard J Carmichael. Statistical methods in quantum optics, volume 1. Springer Berlin Heidelberg, 1999. doi:10.1007/978-3-662-03875-8.

[123] B Coffey and R Friedberg. Effect of short-range Coulomb interaction on cooperative spontaneous emission. Physical Review A, 17(3):1033, 1978. doi:10.1103/PhysRevA.17.1033.

[124] Thibault Vogt, Matthieu Viteau, Amodsen Chotia, Jianming Zhao, Daniel Comparat, and Pierre Pillet. Electric-field induced dipole blockade with Rydberg atoms. Physical Review Letters, 99(7):073002, 2007. doi:10.1103/PhysRevLett.99.073002.

[125] Daniel Comparat and Pierre Pillet. Dipole blockade in a cold Rydberg atomic sample. JOSA B, 27(6):A208–A232, 2010. doi:10.1364/JOSAB.27.00A208.

[126] GP Hildred, RR Puri, SS Hassan, and RK Bullough. Quantum theory of recent observations on Rydberg atoms in low-Q cavities. Journal of Physics B: Atomic and Molecular Physics, 17(16):L535, 1984. doi:10.1088/0022-3700/17/16/001.

[127] EV Goldstein and Pierre Meystre. Dipole-dipole interaction in optical cavities. Physical Review A, 56(6):5135, 1997. doi:10.1103/PhysRevA.56.5135.

[128] Heinz-Peter Breuer and Francesco Petruccione. The Theory of Open Quantum Systems. Oxford University Press, 2007. doi:10.1093/acprof:oso/9780199213900.001.0001.

[129] Nivaldo A Lemos. The Heisenberg picture is not privileged for the canonical quantization of dissipative systems. Physical Review D, 24(8):2338, 1981. doi:10.1103/PhysRevD.24.2338.

[130] Rui E. F. Silva and Johannes Feist. Permutational symmetry for identical multilevel systems: A second-quantized approach. Physical Review A, 105(4), April 2022. doi:10.1103/physreva.105.043704.

[131] Bradley A Chase and JM Geremia. Collective processes of an ensemble of spin-1/2 particles. Physical Review A, 78(5):052101, 2008. doi:10.1103/PhysRevA.78.052101.

[132] Minghui Xu, DA Tieri, and MJ Holland. Simulating open quantum systems by applying $SU(4)$ to quantum master equations. Physical Review A, 87(6):062101, 2013. doi:10.1103/PhysRevA.87.062101.

[133] Stephan Hartmann. Generalized Dicke states. Quantum Information & Computation, 16(15-16):1333–1348, 2016. doi:10.26421/QIC16.15-16-5.

[134] Nathan Shammah, Neill Lambert, Franco Nori, and Simone De Liberato. Superradiance with local phase-breaking effects. Physical Review A, 96(2):023863, 2017. doi:10.1103/PhysRevA.96.023863.

[135] Nathan Shammah, Shahnawaz Ahmed, Neill Lambert, Simone De Liberato, and Franco Nori. Open quantum systems with local and collective incoherent processes: Efficient numerical simulations using permutational invariance. Physical Review A, 98(6):063815, 2018. doi:10.1103/PhysRevA.98.063815.

[136] W Alvarez-Giron and P Barberis-Blostein. The atomic damping basis and the collective decay of interacting two-level atoms. Journal of Physics A: Mathematical and Theoretical, 53(43):435301, October 2020. doi:10.1088/1751-8121/abb1e2.

[137] J Schwinger, L Biedenharn, and H Van Dam. Quantum theory of angular momentum, 1965.

[138] L. Landau and E. Lifshitz. Quantum mechanics: non-relativistic theory. Elsevier, 1977. doi:10.1016/C2013-0-02793-4.

[139] Goran Lindblad. On the generators of quantum dynamical semigroups. Communications in Mathematical Physics, 48(2):119–130, 1976. doi:10.1007/BF01608499.

[140] Vittorio Gorini, Andrzej Kossakowski, and Ennackal Chandy George Sudarshan. Completely positive dynamical semigroups of N-level systems. Journal of Mathematical Physics, 17(5):821–825, 1976. doi:10.1063/1.522979.

[141] Daniel Manzano. A short introduction to the Lindblad master equation. AIP Advances, 10(2):025106, February 2020. doi:10.1063/1.5115323.

[142] Manfred Schmutz. Real-time Green's functions in many body problems. Zeitschrift für Physik B Condensed Matter, 30(1):97–106, 1978. doi:10.1007/BF01323673.

[143] Tomaž Prosen. Third quantization: a general method to solve master equations for quadratic open Fermi systems. New Journal of Physics, 10(4):043026, 2008. doi:10.1088/1367-2630/10/4/043026.

[144] Upendra Harbola and Shaul Mukamel. Superoperator nonequilibrium Green's function theory of many-body systems; applications to charge transfer and transport in open junctions. Physics Reports, 465(5):191–222, 2008. doi:10.1016/j.physrep.2008.05.003.

[145] Alan A Dzhioev and DS Kosov. Nonequilibrium perturbation theory in Liouville–Fock space for inelastic electron transport. Journal of Physics: Condensed Matter, 24(22):225304, 2012. doi:10.1088/0953-8984/24/22/225304.

[146] Ady Stern. Anyons and the quantum Hall effect—A pedagogical review. Annals of Physics, 323(1):204–249, January 2008. doi:10.1016/j.aop.2007.10.008.

[147] Abraham Klein and ER Marshalek. Boson realizations of Lie algebras with applications to nuclear physics. Reviews of modern physics, 63(2):375, 1991. doi:10.1103/RevModPhys.63.375.

[148] Sunil Kumar and CL Mehta. Theory of the interaction of a single-mode resonant radiation field with N two-level atoms. Physical Review A, 21(5):1573, 1980. doi:10.1103/PhysRevA.21.1573.

[149] Lawrence C Biedenharn, James D Louck, and Peter A Carruthers. Angular Momentum in Quantum Physics: Theory and Application. Cambridge University Press, 1984. doi:10.1017/CBO9780511759888.

[150] Salvatore Carusotto. Dynamics of processes with a trilinear boson Hamiltonian. Physical Review A, 40(4):1848, 1989. doi:10.1103/PhysRevA.40.1848.

[151] Gabriel Drobnỳ and Igor Jex. Quantum properties of field modes in trilinear optical processes. Physical Review A, 46(1):499, 1992. doi:10.1103/PhysRevA.46.499.

[152] Congjun Wu, Bin Chen, Xi Dai, Yue Yu, and Zhao-Bin Su. Schwinger-boson mean-field theory of the Heisenberg ferrimagnetic spin chain. Physical Review B, 60(2):1057, 1999. doi:10.1103/PhysRevB.60.1057.

[153] Daniel F Walls and Richard Barakat. Quantum-mechanical amplification and frequency conversion with a trilinear Hamiltonian. Physical Review A, 1(2):446, 1970. doi:10.1103/PhysRevA.1.446.

[154] Jerryman A Gyamfi. Fundamentals of quantum mechanics in Liouville space. European Journal of Physics, 41(6):063002, 2020. doi:10.1088/1361-6404/ab9fdd.

[155] Christopher Rackauckas and Qing Nie. DifferentialEquations.jl – A Performant and Feature-Rich Ecosystem for Solving Differential Equations in Julia. Journal of Open Research Software, 5(1):15, May 2017. doi:10.5334/jors.151.

[156] Berislav Buča, Joseph Tindall, and Dieter Jaksch. Non-stationary coherent quantum many-body dynamics through dissipation. Nature Communications, 10(1), April 2019. doi:10.1038/s41467-019-09757-y.

[157] D. A. Lidar, I. L. Chuang, and K. B. Whaley. Decoherence-Free Subspaces for Quantum Computation. Physical Review Letters, 81(12):2594–2597, September 1998. doi:10.1103/physrevlett.81.2594.

[158] A. Crubellier, S. Liberman, and P. Pillet. Superradiance and subradiance in three-level systems. Optics Communications, 33(2):143–148, May 1980. doi:10.1016/0030-4018(80)90181-9.

[159] William Guerin, Michelle O. Araújo, and Robin Kaiser. Subradiance in a Large Cloud of Cold Atoms. Physical Review Letters, 116(8), February 2016. doi:10.1103/physrevlett.116.083601.

[160] D. Pavolini, A. Crubellier, P. Pillet, L. Cabaret, and S. Liberman. Experimental Evidence for Subradiance. Physical Review Letters, 54(17):1917–1920, April 1985. doi:10.1103/physrevlett.54.1917.

[161] Clemens Weninger and Nina Rohringer. Transient-gain photoionization x-ray laser. Phys. Rev. A, 90:063828, Dec 2014. doi:10.1103/PhysRevA.90.063828.

[162] Evgenii B Aleksandrov. Optical measurements of the interference of nondegenerate atomic states. Soviet Physics Uspekhi, 15(4):436–451, April 1973. doi:10.1070/PU1973v015n04ABEH004991.

[163] H. Bitto and J. Robert Huber. Molecular quantum beat spectroscopy. Optics Communications, 80(2):184–198, December 1990. doi:10.1016/0030-4018(90)90382-4.

[164] Yasumasa Hikosaka, Hiroshi Iwayama, and Tatsuo Kaneyasu. Zeeman quantum beats of helium Rydberg states excited by synchrotron radiation. Journal of Synchrotron Radiation, 27(3):675–680, May 2020. doi:10.1107/S1600577520002829.

[165] A C LaForge, A Benediktovitch, V Sukharnikov, Š Krušič, M Žitnik, M Debatin, R W Falcone, J D Asmussen, M Mudrich, R Michiels, F Stienkemeier, L Badano, C Callegari, M Di Fraia, M Ferianis, L Giannessi, O Plekan, K C Prince, C Spezzani, N Rohringer, and N Berrah. Time-resolved quantum beats in the fluorescence of helium resonantly excited by XUV radiation. Journal of Physics B: Atomic, Molecular and Optical Physics, 53(24):244012, November 2020. doi:10.1088/1361-6455/abc660.

[166] E. Gerdau, R. Rüffer, R. Hollatz, and J. P. Hannon. Quantum Beats from Nuclei Excited by Synchrotron Radiation. Physical Review Letters, 57(9):1141–1144, September 1986. doi:10.1103/PhysRevLett.57.1141.

[167] Q. H. F. Vrehen, H. M. J. Hikspoors, and H. M. Gibbs. Quantum Beats in Superfluorescence in Atomic Cesium. Physical Review Letters, 38(14):764–767, April 1977. doi:10.1103/PhysRevLett.38.764.

[168] D. Bartholdtsen and R. H. Rinkleff. Superfluorescent transitions in an external magnetic field. Zeitschrift für Physik D Atoms, Molecules and Clusters, 30(4):265–273, December 1994. doi:10.1007/BF01426390.

[169] S. Haroche. Quantum beats and time-resolved fluorescence spectroscopy. In Topics in Applied Physics, pages 253–313. Springer Berlin Heidelberg, 1976. doi:10.1007/3540077197_23.

[170] A Crubellier, S Liberman, D Pavolini, and P Pillet. Superradiance and subradiance. I. Interatomic interference and symmetry properties in three-level systems. Journal of Physics B: Atomic and Molecular Physics, 18(18):3811–3833, September 1985. doi:10.1088/0022-3700/18/18/022.

[171] Govind S Agarwal. Vacuum-field Rabi oscillations of atoms in a cavity. JOSA B, 2(3):480–485, 1985. doi:10.1364/JOSAB.2.000480.

[172] Román Orús. A practical introduction to tensor networks: Matrix product states and projected entangled pair states. Annals of Physics, 349:117–158, October 2014. doi:10.1016/j.aop.2014.06.013.

[173] Román Orús. Tensor networks for complex quantum systems. Nature Reviews Physics, 1(9):538–550, August 2019. doi:10.1038/s42254-019-0086-7.

[174] Michael A. Nielsen and Isaac L. Chuang. Quantum Computation and Quantum Information. Cambridge University Press, 2012. doi:10.1017/cbo9780511976667.

[175] F. Benatti, R. Floreanini, F. Franchini, and U. Marzolino. Entanglement in indistinguishable particle systems. Physics Reports, 878:1–27, September 2020. doi:10.1016/j.physrep.2020.07.003.

[176] Till Jonas Frederick Johann and Ugo Marzolino. Locality and entanglement of indistinguishable particles. Scientific Reports, 11(1), July 2021. doi:10.1038/s41598-021-94991-y.

[177] Yu Shi. Quantum entanglement of identical particles. Physical Review A, 67(2), February 2003. doi:10.1103/physreva.67.024301.

[178] Rosario Lo Franco and Giuseppe Compagno. Indistinguishability of Elementary Systems as a Resource for Quantum Information Processing. Physical Review Letters, 120(24), June 2018. doi:10.1103/physrevlett.120.240403.

[179] N. Killoran, M. Cramer, and M. B. Plenio. Extracting Entanglement from Identical Particles. Physical Review Letters, 112(15), April 2014. doi:10.1103/physrevlett.112.150501.

[180] Susane Calegari, Antônio C. Lourenço, Gabriel T. Landi, and Eduardo I. Duzzioni. Genuine multipartite correlations in Dicke superradiance. Physical Review A, 101(5), May 2020. doi:10.1103/physreva.101.052310.

[181] José I. Latorre, Román Orús, Enrique Rico, and Julien Vidal. Entanglement entropy in the Lipkin-Meshkov-Glick model. Physical Review A, 71(6), June 2005. doi:10.1103/physreva.71.064101.

[182] M. G. M. Moreno and Fernando Parisio. All bipartitions of arbitrary Dicke states, 2018. doi:10.48550/ARXIV.1801.00762.

[183] Elie Wolfe and S. F. Yelin. Certifying Separability in Symmetric Mixed States of N Qubits, and Superradiance. Physical Review Letters, 112(14), April 2014. doi:10.1103/physrevlett.112.140402.

[184] MK Olsen, LI Plimak, S Rebić, and AS Bradley. Phase-space analysis of bosonic spontaneous emission. Optics communications, 254(4-6):271–281, 2005. doi:10.1016/j.optcom.2005.06.006.

[185] Julian Huber, Peter Kirton, and Peter Rabl. Phase-space methods for simulating the dissipative many-body dynamics of collective spin systems. SciPost Physics, 10(2), February 2021. doi:10.21468/scipostphys.10.2.045.

[186] Stephan Mandt, Darius Sadri, Andrew A Houck, and Hakan E Türeci. Stochastic differential equations for quantum dynamics of spin-boson networks. New Journal of Physics, 17(5):053018, May 2015. doi:10.1088/1367-2630/17/5/053018.

[187] LM Narducci, DH Feng, R Gilmore, and GS Agarwal. Transient and steady-state behavior of collective atomic systems driven by a classical field. Physical Review A, 18(4):1571, 1978. doi:10.1103/PhysRevA.18.1571.

[188] RR Puri and SV Lawande. Exact steady-state density operator for a collective atomic system in an external field. Physics Letters A, 72(3):200–202, 1979. doi:10.1016/0375-9601(79)90003-3.

[189] DW Barry and PD Drummond. Qubit phase space: $SU(n)$ coherent-state P representations. Physical Review A, 78(5):052108, 2008. doi:10.1103/PhysRevA.78.052108.

[190] PT Arecchi, E Gilmore, and DM Kim. Coherent states for r-level atoms. Lettere al Nuovo Cimento (1971-1985), 6(6):219–223, 1973. doi:10.1007/BF02827264.

[191] JM Radcliffe. Some properties of coherent spin states. Journal of Physics A: General Physics, 4(3):313, 1971. doi:10.1088/0305-4470/4/3/009.

[192] FT Arecchi, Eric Courtens, Robert Gilmore, and Harry Thomas. Atomic coherent states in quantum optics. Physical Review A, 6(6):2211, 1972. doi:10.1103/PhysRevA.6.2211.

[193] Piotr Deuar. Multi-time correlations in the positive-P, Q, and doubled phase-space representations. Quantum, 5:455, May 2021. doi:10.22331/q-2021-05-10-455.

[194] Stasis Chuchurka, Andrei Benediktovitch, and Nina Rohringer. Quantum stochastic trajectories for particles and fields based on positive P-representation, 2023. doi:10.48550/ARXIV.2306.17474.

[195] Stasis Chuchurka, Andrei Benediktovitch, Špela Krušič, Aliaksei Halavanau, and Nina Rohringer. Stochastic modeling of x-ray superfluorescence. Physical Review A, 109(3), March 2024. doi:10.1103/physreva.109.033725.

[196] J Gea-Banacloche, M O Scully, and M S Zubairy. Vacuum Fluctuations and Spontaneous Emission in Quantum Optics. Physica Scripta, T21:81–85, January 1988. doi:10.1088/0031-8949/1988/t21/015.

[197] A. Leonau, S. Chuchurka, V. Sukharnikov, A. Benediktovitch, and N. Rohringer. Modelling many-body quantum dynamics with stochastic trajectories: a critical test on the Tavis-Cummings model. To be submitted.

[198] S. Chuchurka, V. Sukharnikov, and N. Rohringer. Hermitian stochastic methodology for x-ray superfluorescence. Physical Review A, 109(6), June 2024. doi:10.1103/physreva.109.063705.

[199] Sergey S. Stepanov. Stochastic World. Springer International Publishing, 2013. doi:10.1007/978-3-319-00071-8.

[200] P. E. Kloeden and E. Platen. Numerical Solution of Stochastic Differential Equations. Springer Berlin Heidelberg, 1992. doi:10.1007/978-3-662-12616-5.

[201] Riccardo Mannella and Peter V. E. McClintock. Itô versus Stratonovich: 30 years later. Fluctuation and Noise Letters, 11(01):1240010, March 2012. doi:10.1142/s021947751240010x.

[202] M. D. Lukin, M. Fleischhauer, R. Cote, L. M. Duan, D. Jaksch, J. I. Cirac, and P. Zoller. Dipole Blockade and Quantum Information Processing in Mesoscopic Atomic Ensembles. Physical Review Letters, 87(3), June 2001. doi:10.1103/physrevlett.87.037901.

[203] Javier del Pino, Florian A. Y. N. Schröder, Alex W. Chin, Johannes Feist, and Francisco J. Garcia-Vidal. Tensor Network Simulation of Non-Markovian Dynamics in Organic Polaritons. Physical Review Letters, 121(22), November 2018. doi:10.1103/physrevlett.121.227401.

Eidesstattliche Versicherung

Hiermit versichere ich an Eides statt, die vorliegende Dissertationsschrift selbst verfasst und keine anderen als die angegebenen Hilfsmittel und Quellen benutzt zu haben.

Sofern im Zuge der Erstellung der vorliegenden Dissertationsschrift generative Künstliche Intelligenz (gKI) basierte elektronische Hilfsmittel verwendet wurden, versichere ich, dass meine eigene Leistung im Vordergrund stand und dass eine vollständige Dokumentation aller verwendeten Hilfsmittel gemäß der Guten wissenschaftlichen Praxis vorliegt. Ich trage die Verantwortung für eventuell durch die gKI generierte fehlerhafte oder verzerrte Inhalte, fehlerhafte Referenzen, Verstöße gegen das Datenschutz- und Urheberrecht oder Plagiate.

06-02-2025

Datum

Unterschrift der Doktorandin / des Doktoranden